CERN-THESIS-2011-280

UNIVERSIDADE TÉCNICA DE LISBOA

INSTITUTO SUPERIOR TÉCNICO

Measurement of the Gluon Polarisation from Open-Charm Production at COMPASS

Celso Filipe Correia Franco

Supervisor: Doctor Maria Paula Frazão Bordalo e Sá

Thesis approved in public session to obtain PhD Degree in
Physics

Jury final classification: Pass with distinction

Jury

Chairperson: Chairman of the IST Scientific Board

Members of the Committee:

Doctor Jorge Manuel Rodrigues Crispim Romão
Doctor Maria Paula Frazão Bordalo e Sá
Doctor Eva Maria Kabuss
Doctor Krzysztof Kurek
Doctor Sérgio Eduardo de Campos Costa Ramos
Doctor Catarina Marques Quintans

December 2011

UNIVERSIDADE TÉCNICA DE LISBOA
INSTITUTO SUPERIOR TÉCNICO

Measurement of the Gluon Polarisation from Open-Charm Production at COMPASS

Celso Filipe Correia Franco

Supervisor: Doctor Maria Paula Frazão Bordalo e Sá

Thesis approved in public session to obtain PhD Degree in
Physics

Jury final classification: Pass with distinction

Jury

Chairperson: Chairman of the IST Scientific Board

Members of the Committee:

Doctor Jorge Manuel Rodrigues Crispim Romão, Professor Catedrático do Instituto Superior Técnico, da Universidade Técnica de Lisboa

Doctor Maria Paula Frazão Bordalo e Sá, Professora Associada (com Agregação), do Instituto Superior Técnico, da Universidade Técnica de Lisboa

Doctor Eva Maria Kabuss, Professora Associada da Universidade Johannes Gutenberg Mainz, Alemanha

Doctor Krzysztof Kurek, Professor Associado da Universidade de Varsóvia, Polónia

Doctor Sérgio Eduardo de Campos Costa Ramos, Professor Auxiliar (com Agregação) do Instituto Superior Técnico, da Universidade Técnica de Lisboa

Doctor Catarina Marques Quintans, Investigadora do Laboratório de Instrumentação e Física Experimental de Partículas

Funding Institutions

FCT Fundação para a Ciência e a Tecnologia
MINISTÉRIO DA EDUCAÇÃO E CIÊNCIA

December 2011

for Carla Carriço

Acknowledgements

This work would not have been possible without the help and advice of several people. Therefore, I would like to thank to:

- My supervisor, Prof. Paula Bordalo, for her constant support and also for giving me the opportunity to have the wonderful experience of working in the COMPASS experiment at CERN.

- Prof. Sérgio Ramos for his support and for teaching me a lot about experimental particle physics.

- My colleagues from LIP, for the pleasant scientific discussions and friendly atmosphere at work: Catarina Quintans, Helena Santos, Ana Sofia Nunes, Marcin Stolarski and Luis Silva. The technical discussions I had with Marcin about my analysis were extremely valuable to me. A special thanks goes to Luis, my PhD companion, for his endless help whenever I was stuck with a problem.

- Beata Pawlukiewicz, Grzegorz Brona and Susanne Koblitz for the cross-check that they made of my analysis. I am very grateful for their hard work, which allowed the release of the results presented in this thesis.

- The Open-Charm group, especially: Florent Robinet, Jean-Marc Le Goff, Yann Bedfer, Joerg Pretz, Eva-Maria Kabuss, Barbara Badelek and Krzysztof Kurek. I am deeply indebted to Krzysztof for the countless fruitful discussions about the physics of the nucleon spin. I am grateful to him for teaching me the theoretical basis of the spin physics.

- All people in the COMPASS collaboration who put a big effort in building and running the experiment.

I would like to thank my parents for providing me all the conditions to succeed in life. I would also like to thank my sister for her patience during all these years of my learning process. Last but not the least, I wish to thank my girlfriend Carla Carriço for her love and unfailing support during all the darkest hours of my PhD. It is a pleasure sharing my life with you.

This work was partially funded by the grant SFRH/BD/62161/2009 provided by:

FCT Fundação para a Ciência e a Tecnologia
MINISTÉRIO DA EDUCAÇÃO E CIÊNCIA

Resumo

O principal propósito da experiência COMPASS no CERN é a determinação da contribuição dos gluões para o spin do nucleão. Para atingir este objectivo COMPASS utiliza um feixe de muões naturalmente polarisados, com uma energia de 160 GeV, e um alvo fixo também ele polarisado. Dois tipos de materiais foram usados como alvo: ^{6}LiD (deuterões polarisados) em 2002-2006 e NH_3 (protões polarisados) em 2007. Os gluões no nucleão podem ser directamente acedidos através do processo de fusão do fotão com o gluão (PGF). Entre os canais estudados por COMPASS, a produção de mesões com charme aberto é aquele que selecciona uma interação PGF da forma mais limpa e eficiente. Esta tese apresenta uma estimativa da polarização dos gluões, $\Delta G/G$, que é baseada numa medida da assimetria de spin resultante da produção de mesões D^0. Estes mesões são reconstruídos através da massa invariante dos seus produtos de decaímento. A pureza dos espectros de massa D^0 foi significativamente melhorada através da utilização de um novo método baseado em Redes Neuronais. O resultado de $\Delta G/G$ é também apresentado usando correcções de ordem superior (NLO-QCD) ao processo PGF. Estas correcções são relevantes e foram pela primeira vez aplicadas a uma medida experimental da polarização dos gluões.

Palavras-chave: Spin, Deuterão, Protão, PGF, Charme Aberto, Assimetria, Espectros de Massa D^0, Rede Neuronal, Polarização dos Gluões, NLO-QCD.

Abstract

The main purpose of the COMPASS experiment at CERN is the determination of the gluon contribution to the nucleon spin. To achieve this goal, COMPASS uses a naturally polarised muon beam with an energy of 160 GeV and a fixed polarised target. Two types of materials were used as a target: ^{6}LiD (polarised deuterons) in 2002-2006 and NH_3 (polarised protons) in 2007. The gluons in the nucleon can be accessed directly via the **P**hoton **G**luon **F**usion (PGF) process. Among the channels studied by COMPASS, the production of open-charm mesons is the one that tags a PGF interaction in the most clean and efficient way. This thesis presents an estimation of the gluon polarisation, $\Delta G/G$, which is based on a measurement of the spin asymmetry resulting from the production of D^0 mesons. These mesons are reconstructed through the invariant mass of their decay products. The purity of the D^0 mass spectra was significantly improved through the use of a new method based on Neural Networks. The $\Delta G/G$ result is also presented using the next-to-leading order (NLO-QCD) corrections to the PGF process. Such corrections are relevant and were for the first time applied to an experimental measurement of the gluon polarisation.

Keywords: Spin, Deuteron, Proton, PGF, Open-Charm, Asymmetry, D^0 Mass Spectra, Neural Network, Gluon Polarisation, NLO-QCD.

Contents

List of Tables

List of Figures

Chapter 1

Introduction

All matter is composed of protons, neutrons and electrons. Our present knowledge indicates a point-like structure for the latter, whereas the nucleons (protons and neutrons) do have an internal structure. The first evidence of the existence of this substructure was obtained from experiments on inelastic electron-proton scattering [1]. They revealed a complete new world inside the proton: it is made of charged point-like particles which were initially called partons. Later, the accumulated proofs led to the identification of these partons with the u (up) and d (down) quarks postulated by Gell-Mann. The quark concept was a great success in the explanation of all the properties found in hadron spectroscopy.

It is known since the twenties that the nucleons carry half integer spin, which implies that they belong to the family of fermions. This means that, according to the Pauli exclusion principle, two identical nucleons cannot occupy the same quantum state. Up to now, it is not known how the spin of 1/2 comes about in terms of the nucleon constituents. However, the knowledge that protons and neutrons are fermions is by itself of a great help for the understanding of their complex internal structure: it's like a faint light that guides us through the shadows of the unknown. Until the eighties it was believed that the nucleon spin was distributed among its three valence quarks. In fact, assuming an SU(2) flavour symmetry and an SU(2) spin symmetry, we obtain the following expression for the static wave function of the proton (the spin projection is considered to be parallel to the quantisation axis):

$$|p\uparrow\rangle = \frac{1}{\sqrt{18}}\,[\;2\;|u\uparrow u\uparrow d\downarrow\rangle\;-\;|u\uparrow u\downarrow d\uparrow\rangle\;-\;|u\downarrow u\uparrow d\uparrow\rangle\;+\;(u\leftrightarrow d)\;] \tag{1.1}$$

Eq. 1.1 allows us to calculate the contribution of the u and d quarks to the proton spin:

$$\Delta u = \langle p\uparrow|N_u\uparrow\;-\;N_u\downarrow|p\uparrow\rangle = \frac{3}{18}(10\;-\;2) = \frac{4}{3} \tag{1.2}$$

$$\Delta d = \langle p\uparrow|N_d\uparrow\;-\;N_d\downarrow|p\uparrow\rangle = \frac{3}{18}(2\;-\;4) = -\frac{1}{3} \tag{1.3}$$

where $N_q\uparrow$ ($N_q\downarrow$) represents the number of quarks of flavour q with a spin projection parallel (anti-parallel) to the proton spin. Therefore, we have:

[1] In 1968 at the **S**tanford **L**inear **A**ccelerator **C**enter (SLAC).

$$\Delta\Sigma = \Delta u + \Delta d = \left(\frac{4}{3} - \frac{1}{3}\right) = 1 \tag{1.4}$$

Indeed, from eq. 1.4 we conclude that all the nucleon spin is carried by the valence quarks. However, in 1988 the **E**uropean **M**uon **C**ollaboration (EMC) at CERN astonished the scientific community by publishing a surprising result for the total contribution of quarks to the nucleon spin ($\Delta\Sigma$). The experimental result obtained by EMC was very small ($\Delta\Sigma = 0.12 \pm 0.17$) and even compatible with zero [1]. This fact caused the so-called **spin crisis** of the nucleon because it could not be reconciled with the theoretical predictions: even if we apply relativistic corrections [2], the expectation value for $\Delta\Sigma$ is about 0.60 [4]. Since then, polarised lepton-nucleon scattering experiments were performed at CERN by SMC [3] and COMPASS [5], at SLAC [6], at DESY [7] and at JLAB [8] as well as in polarised proton-proton collisions at RICH [9, 10]. The goal is to extract the parton helicity distributions in the nucleon, using a perturbative QCD analysis [2]. The contribution of quarks to the nucleon spin is now confirmed to be 30% ($\Delta\Sigma = 0.30 \pm 0.01 \pm 0.01$ [5]). The fact that this number is still quite below to the expected one leads us to the following question: where is the remaining part of the nucleon spin? In QCD the nucleon spin projection (in units of $\hbar$) may be decomposed into the quark and gluon helicities, $\Delta\Sigma$ and ΔG_1, and also into their orbital angular momenta L_q and L_g:

$$\frac{1}{2} = J_q + J_g = \left(\frac{1}{2}\Delta\Sigma + L_q\right) + (\Delta G_1 + L_g) \tag{1.5}$$

Therefore, the best approach to solve this **spin puzzle** (eq. 1.5) is to measure the contribution of ΔG_1. This guess is strongly supported by the discovery that gluons carry half of the proton momentum. By analogy, we expect that the missing spin in the nucleon is carried by gluons (note that $\Delta G_1 = \int_0^1 \Delta G(x_g) dx_g$). The average gluon polarisation in a limited range of x_g, $\langle \Delta G/G \rangle_{x_g}$, has been determined in a model independent way, from the **P**hoton **G**luon **F**usion (PGF) process, by HERMES [11], SMC [12] and COMPASS [13, 14]. In this work it is presented the COMPASS result which was obtained from an open-charm analysis. Basically, the PGF process is tagged by the detection of the decay products of charmed mesons.

This thesis is organised as follows. The tool of polarised **D**eep **I**nelastic **S**cattering (DIS) is introduced in Chapter 2, together with the theoretical framework needed for the extraction of information on the spin structure of the nucleon. The relevant aspects of the COMPASS experiment for this analysis are described in Chapters 3 and 4. In Chapter 5, the selection and the reconstruction of open-charm mesons is presented. Thereafter, the method used to extract $\langle \Delta G/G \rangle_{x_g}$ from the data is extensively discussed in Chapters 6 and 7. Finally, the results are presented in Chapter 8 and the systematic errors are discussed throughout Chapter 9. Chapter 10 shows the interpretation of ΔG_1 in terms of the gluon polarisation.

[2] In 1979 the gluon was discovered in the Positron-Electron Tandem Ring Accelerator (PETRA) at HERA. These bosons (spin-1 particles) are the mediators of strong interactions between quarks. The theory of QCD accounts for their presence in the calculations.

Chapter 2

Theoretical Motivation

The goal of this work is to extract an experimental value for the gluon polarisation in the nucleon. Therefore, for a proper understanding of the results, a detailed introduction to the spin dependent lepton-nucleon inelastic scattering is hereafter presented. A theoretical discussion of the polarised and unpolarised structure functions of the nucleon is also included. For more details on the polarised DIS process, see the text book of Ref. [15].

2.1 DIS - Deep Inelastic Scattering

2.1.1 Event kinematics

The main process to study the internal structure of the nucleon is illustrated in Fig. 2.1. The kinematic variables corresponding to such an interaction are:

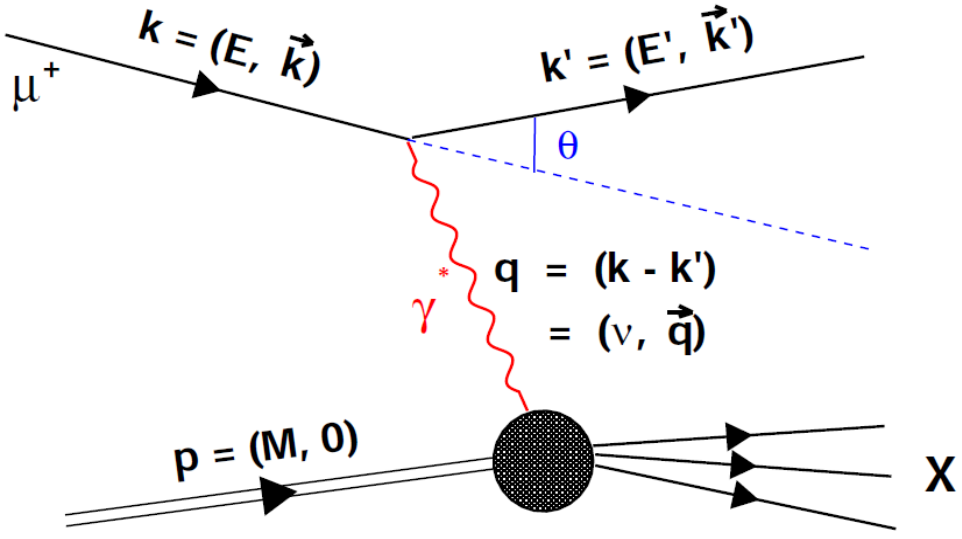

Figure 2.1: Diagram of an inclusive deep inelastic lepton-nucleon scattering. The case of COMPASS is represented: a muon beam collides in a fixed target ($\vec{p} = 0$), using the approximation of a single photon exchange. The hadronic final state is represented by X and the electromagnetic boson by γ^* (virtual-photon).

Variables	Meaning
M	Mass of the target nucleon
$\vec{p} = (0,\ 0,\ 0)$	Momentum vector of the target (COMPASS case)
$p = (M, \vec{p})$	Four-momentum of the target nucleon
E	Energy of the incident muon
$\vec{k} = (0,\ 0,\ 160\ \text{GeV/c})$	Momentum vector of the incident muon (COMPASS case)
$k = (E,\ \vec{k}) \approx E(1,0,0,1)$	Four-momentum of the incident muon
E'	Energy of the scattered muon
$\vec{k'}$ [1]$= (k'_x,\ k'_y,\ k'_z)$	Momentum vector of the scattered muon
$k' = (E',\ \vec{k'})$	Four-momentum of the scattered muon
θ	Polar angle defining the direction of the scattered muon
ϕ	Angle between the X axis and the XY projection of $\vec{k'}$
Ω	Solid angle into which the outgoing muon is scattered
$q = k - k'$	Four-momentum transfer, i.e. the four-momentum of the γ^*
$\nu = E - E' = (p \cdot q)/M$	Energy transfer from the incident muon to the γ^*
$y = \nu/E = (p \cdot q)/(p \cdot k)$	The fractional energy loss of the incident muon
$Q^2 = -q^2$ [2]$\approx 2EE'(1 - \cos\theta)$	Measure of the γ^* virtuality
$x_{Bj} = Q^2/2M\nu$	Measure of the elasticity of the process

Table 2.1: Definition of the most important DIS kinematic variables and their meaning. The muon beam is defined along the Z axis and the laboratory system is the target rest frame.

The last two variables shown in Table 2.1 are of crucial importance for the understanding of the internal properties of the nucleon. In particular, we will see in section 2.1.2 that the structure functions which describe the quarks and the gluons depend only on x_{Bj} and Q^2 (at LO-QCD they are practically independent of Q^2). Therefore it is convenient to present here a physical interpretation for these two quantities. Let's start from the definition of the invariant mass corresponding to the hadronic final state, X:

$$M_X^2 = (p+q)^2 = M^2 + 2M\nu - Q^2 \tag{2.1}$$

Since the baryon number is conserved in a DIS collision, the invariant mass of X cannot be smaller than the nucleon one. This implies that

$$M^2 + 2M\nu - Q^2 \geq M^2 \quad \Leftrightarrow \quad 2M\nu \geq Q^2 \quad \Rightarrow \quad x_{Bj} \leq 1 \tag{2.2}$$

In eq. 2.2 one sees that $x_{Bj} = 1$ if and only if Q^2 is equal to the factor $2M\nu$. Clearly, this limit

[1] $\vec{k'} = (E'\sin\theta\cos\phi,\ E'\sin\theta\sin\phi,\ E'\cos\theta)$

[2] Using $k^2 = m_\mu^2$, $k'^2 = m_{\mu'}^2$ and neglecting the muon mass.

corresponds to an elastic collision where the nucleon structure remains unchanged ($M_X = M$). Since Q^2 and ν are both positive, the allowed kinematic range for x_{Bj} is:

$$0 \leq x_{Bj} \leq 1 \tag{2.3}$$

The lepton-nucleon scattering is increasingly inelastic as it approaches the lower limit of x_{Bj}. By definition, the mass of the hadronic final state in such inelastic processes, M_X, should be larger than 4 GeV/c^2. This region of masses avoids the nucleon excited states and, consequently, implies the fragmentation of the target.

Concerning the Q^2 variable, we can interpret it as a measure of virtuality in DIS processes. The electromagnetic boson that carries the four-momentum from the lepton to the nucleon has a non-zero mass [3], $q^2 = M^2_{\gamma^*} < 0$, and therefore it cannot be considered a real photon. However, if Q^2 is close to zero, the virtuality associated to the inelastic scattering is small (quasi-real photons). This concept of the virtual-photon mass gives us a clearer physical meaning for the Q^2 variable: it can be reinterpreted as the resolving power of the virtual-photon, because its Compton wavelength is completely defined by Q^2 ($\lambda_{\gamma^*} = \hbar/M_{\gamma^*} = \hbar/\sqrt{Q^2}$). As a result, using the uncertainty principle, we can estimate the needed Q^2 to resolve the nucleon:

$$\Delta x \Delta E \sim \hbar \quad \Rightarrow \quad Q^2 \sim \left[\frac{0.197 \text{ (GeV} \cdot \text{fm)}}{\Delta x}\right]^2 \tag{2.4}$$

Inserting in eq. 2.4 the size of the proton, 1.754 fm [16], results in a Q^2 of 13 (KeV/c)^2 just to 'see' the proton. In order to be able to penetrate its structure and resolve for example a valence quark, a much higher energy is required. It is conventional to define a lower limit of 1 (GeV/c)^2 for the Q^2 of a DIS process. In this case the inelastic muon scattering results from a 'deep' interaction between the virtual-photon and one quark inside the nucleon. However, inelastic collisions with a stationary nucleon can also exist for $Q^2 < 1$ (GeV/c)^2. For these processes the interaction is simply called inelastic scattering. In the phase space of DIS, which is defined by $Q^2 > 1$ (GeV/c)^2, we can interpret x_{Bj} as the fraction of the nucleon momentum that a quark must have to absorb the virtual-photon. This is the basic assumption of the parton model which will be discussed in section 2.2. Basically, this model provides us with some structure functions that describe the probability of finding a given quark flavour (polarised or unpolarised) carrying a momentum fraction x_{Bj}. Since these functions are Lorentz invariant, we can formulate the parton model in a convenient frame of infinite momentum. The latter implies that the quarks inside the nucleon don't have time to interact (with each other) during the absorption of the virtual-photon by one of them (due to the time dilatation). Consequently, we have

$$(x_{Bj}p + q)^2 = x^2_{Bj}M^2 - Q^2 + 2x_{Bj}p \cdot q \approx 0 \quad \text{(for a mass-less quark)} \tag{2.5}$$

The previous equation reproduces the definition of x_{Bj}, given in table 2.1, provided that both Q^2 and ν are large when compared with the term $x^2_{Bj}M^2$. In the case of small Q^2, x_{Bj} can only be interpreted as a scaling variable on which the structure functions depend. This dependence is exclusive up to a leading order approximation.

[3] According to the uncertainty principle, this violation (an energy fluctuation converted into mass) is allowed during a time interval which is a fraction of the Planck constant. Nonetheless, the total energy is conserved in the process.

2.1.2 Polarised and unpolarised cross-sections

In COMPASS the centre-of-mass energy has a value of 17 GeV, which means that the scattering process is mediated by only one virtual-photon [4]. Consequently, the scattering amplitude corresponding to the spin dependent version of the process illustrated in Fig. 2.1 is given by

$$iM = (-ie)^2 \underbrace{\left(\frac{-ig_{\mu\nu}}{q^2}\right)}_{\gamma^* \text{ propagator}} \langle k'|j_l^{\mu}(0)|k, s_l\rangle \langle X|j_N^{\nu}(0)|p, s_N\rangle \tag{2.6}$$

Where s_l represents the polarisation of the incident lepton and s_N the polarisation of the stationary nucleon. The leptonic and hadronic currents are given by j_l^{μ} and j_N^{ν}, respectively. In order to obtain the total cross-section one needs to divide the description of the physical process (given by $|M|^2$) by the incident flux, which for a fixed target experiment has the value of $2E \times 2M$ [17]. In addition, an integration over all the available final states to the scattered muon is required. The phase space is defined by $d^3k'/(2\pi)^3 2E'$ and 4 delta functions are used to impose the energy-momentum conservation. Finally, after summing over all the hadronic final states, the differential cross-section is given by

$$\begin{aligned} d\sigma &= \sum_X \int \frac{d^3k'}{(2\pi)^3 2E'} (2\pi)^4 \delta^4 (k + p - k' - p_X) \frac{|M|^2}{(2E)(2M)} \\ &= \sum_X \int \frac{d^3k'}{(2\pi)^3 2E'} \frac{(2\pi)^4 \delta^4 (k + p - k' - p_X)}{(2E)(2M)} \frac{e^4}{Q^4} \\ &\times \langle p, s_{N'}|j_{N,\mu}(0)|X\rangle \langle X|j_{N,\nu}(0)|p, s_N\rangle \underbrace{\langle k, s_l|j_l^{\mu}(0)|k'\rangle \langle k'|j_l^{\nu}(0)|k, s_l\rangle}_{l^{\mu\nu}\text{: leptonic tensor}} \end{aligned} \tag{2.7}$$

The hadronic tensor is defined by the following expression [17],

$$W_{\mu\nu}(p, q, S_{NN'}) = \frac{1}{4\pi} \sum_X \left[(2\pi)^4 \delta^4 (p + q - p_X) \langle p, s_{N'}|j_{N,\mu}(0)|X\rangle \langle X|j_{N,\nu}(0)|p, s_N\rangle\right] \tag{2.8}$$

where the sum is performed over the allowed phase space for the final state X, which in turn is restricted by the four-momentum conservation imposed by the delta function. Using the definition of eq. 2.8 the differential cross-section can be written in a compact form:

$$d\sigma = \frac{e^4}{Q^4} \int \frac{d^3k'}{(2\pi)^3 2E'} \frac{4\pi l^{\mu\nu} W_{\mu\nu}}{(2E)(2M)} \tag{2.9}$$

[4] There is not enough energy for the polarised muon to emit a Z^0 with a mass of 91 GeV/c^2. In addition, since the COMPASS target is composed by deuteron/proton elements, the emission of a second photon by the incident lepton is highly suppressed. The assumption of only one photon exchange is valid for the target elements with an atomic number $Z \ll 1/\alpha$, where α is the electromagnetic coupling constant.

Explicit form of the leptonic tensor $l^{\mu\nu}$

The leptonic tensor can be easily calculated because it consists on two point-like fermions. For a polarised beam, we can sum over all the spin states that are available to the scattered muon:

$$l^{\mu\nu}(k,k',s_l) = \sum_{s'_l} \bar{u}\left(k'\right)\gamma^{\nu}u\left(k,s_l\right)\bar{u}\left(k,s_l\right)\gamma^{\mu}u\left(k'\right) \tag{2.10}$$

where $u(k,s_l)$ and $\bar{u}(k')$ represent the spinors describing the incident and scattered leptons, respectively. Instead of calculating the sum above, it is much more convenient to transform eq. 2.10 into a trace of matrices γ^{μ}. To accomplish that, two identities are used. The first one is:

$$\sum_{s'_l} u\left(k'\right)\bar{u}\left(k'\right) = \not{k}' + m_l \qquad (\text{using } \not{k}' = \gamma_{\mu}k^{\mu}) \tag{2.11}$$

The second identity uses the spin-projector operator to account for the polarisation of the incoming lepton. Thus, the product of spinors in the initial state is given by

$$\bar{u}\left(k,s_l\right)u\left(k,s_l\right) = \left(\not{k} + m_l\right) \times \underbrace{\frac{1+\gamma_5\left(\frac{\not{s}_l}{m_l}\right)}{2}}_{\text{spin-projector}} \tag{2.12}$$

The lepton mass in the spin-projector operator is a result from the chosen normalisation for s_l. We can define the spin vector as $\vec{s}_l = m_l\vec{z}$ (see Ref. [17]), for a spin-1/2 particle at rest with spin along the Z axis. This normalisation is useful to avoid unnecessary leptonic mass terms in the spin dependent cross-section (they are negligible in the relativistic domain). As a consequence, the 4-vector $s_l = (s_l^0, \vec{s}_l)$ can be written as $s_l = h_l k$, where $h_l = \pm$ represents the relativistic lepton helicity. Using those two identities, the calculation of $l^{\mu\nu}$ becomes quite simple:

$$\begin{aligned} l^{\mu\nu}(k,k',s_l) &= \mathrm{Tr}\left[\left(\not{k}' + m_l\right)\gamma^{\nu}\left(\not{k} + m_l\right)\frac{1+\gamma_5\left(\frac{\not{s}_l}{m_l}\right)}{2}\gamma^{\mu}\right] \\ &= \underbrace{2\left[k^{\mu}k'^{\nu} + k^{\nu}k'^{\mu} - g^{\mu\nu}\left(k\cdot k' - {}^{5}m_l^2\right)\right]}_{\text{symmetric part: } l^{\mu\nu(s)}} - \underbrace{2\left[i\epsilon^{\mu\nu\alpha\beta}\left(k-k'\right)_{\alpha}s_{l\beta}\right]}_{\text{anti-symmetric part: } l^{\mu\nu(a)}} \end{aligned} \tag{2.13}$$

The important detail to retain from eq. 2.13 is that the leptonic tensor can be conveniently separated into symmetric and anti-symmetric factors [18]. The anti-symmetric part results from the presence of the Levi-Civita tensor, $\epsilon^{\mu\nu\alpha\beta}$, and from its definition we can see that it absorbs completely the dependence of $l^{\mu\nu}$ on the lepton spin. Later on, we will verify that this separation is extremely useful for the study of the nucleon spin structure.

Explicit form of the hadronic tensor $W^{\mu\nu}$

[5] This term can be neglected in the relativistic domain.

Unlike the leptonic tensor which is a known quantity, the hadronic tensor cannot be calculated from QCD because of the existence of non-perturbative effects in strong interactions. Therefore, $W^{\mu\nu}$ can only be decomposed into some unknown structure functions. The latter represent our ignorance about the internal structure of the nucleon and have to be measured in experiments. The most general hadronic tensor for a polarised DIS experiment (using a spin-1/2 target) can be written in terms of p, q and s_N, together with the invariant tensors $g^{\mu\nu}$ and $\epsilon^{\mu\nu\alpha\beta}$. To accomplish this, only three requirements are needed: $W^{\mu\nu}$ must be invariant under parity and time reversal (properties of the strong interactions) and, most important, the current conservation in a real nucleon, $\partial_\mu j^\mu(x) = 0$, implies that

$$q_\mu W^{\mu\nu}(p, q, s_N) = q_\nu W^{\mu\nu}(p, q, s_N) = 0 \tag{2.14}$$

Using the above criteria, the final expression for $W_{\mu\nu}$ is (see Ref. [17]):

$$W_{\mu\nu}(p, q, s_N) = \overbrace{\left(-g_{\mu\nu} + \frac{q_\mu q_\nu}{q^2}\right) F_1\left(x_{Bj}, Q^2\right) + \left(p_\mu - \frac{p\cdot q q_\mu}{q^2}\right)\left(p_\nu - \frac{p\cdot q q_\nu}{q^2}\right)\frac{F_2\left(x_{Bj}, Q^2\right)}{p\cdot q}}^{\text{symmetric part: } W^{(s)}_{\mu\nu}} \tag{2.15}$$

$$+ \underbrace{\left(\epsilon_{\mu\nu\alpha\beta} q^\alpha s_N^\beta\right)\frac{i g_1\left(x_{Bj}, Q^2\right)}{p\cdot q} + \left(\epsilon_{\mu\nu\alpha\beta} q^\alpha \left[p\cdot q s_N^\beta - s_N\cdot q p^\beta\right]\right)\frac{i g_2\left(x_{Bj}, Q^2\right)}{(p\cdot q)^2}}_{\text{anti-symmetric part: } W^{(a)}_{\mu\nu}}$$

The total cross-section

Using the above definitions of $l^{\mu\nu}$ and $W_{\mu\nu}$, we can conveniently separate the spin dependent and the spin independent parts of the cross-section:

$$\begin{aligned}\frac{d^2\sigma}{dE' d\Omega} &= \frac{e^4}{16\pi^2 Q^4}\left(\frac{E'}{ME}\right) l^{\mu\nu} W_{\mu\nu} \\ &= \frac{\alpha^2}{Q^4}\left(\frac{E'}{ME}\right)\left[l^{\mu\nu(s)} W^{(s)}_{\mu\nu} - l^{\mu\nu(a)} W^{(a)}_{\mu\nu}\right]\end{aligned} \tag{2.16}$$

Experimentally this differential cross-section has three measurable contributions (see Ref. [19]),

$$\frac{d^2\sigma}{dE' d\Omega} = \left(\frac{d^2\sigma^{unpol}}{dE' d\Omega}\right) - h_l \times \cos\delta \left(\frac{d^2\Delta\sigma_\parallel}{dE' d\Omega}\right) - h_l \times \sin\delta \left(\frac{d^2\Delta\sigma_\perp}{dE' d\Omega}\right) \tag{2.17}$$

where δ is the polar angle of the nucleon spin vector with respect to the incident lepton direction (cf. Fig. 2.2). The first term results from an unpolarised DIS event, while the latter two correspond to the interesting configurations where the lepton spin is parallel ($\delta = 0,\ \pi$) or perpendicular ($\delta = \pi/2,\ 3\pi/2$) to the nucleon spin. The last two terms are written as a function of the following two quantities:

$$\Delta\sigma_{\parallel} = \sigma^{\overrightarrow{\Rightarrow}} - \sigma^{\overrightarrow{\Leftarrow}} \qquad \text{and} \qquad \Delta\sigma_{\perp} = \sigma^{\overleftarrow{\Downarrow}} - \sigma^{\overleftarrow{\Uparrow}} \tag{2.18}$$

with the symbols ($\rightarrow$, $\Rightarrow$) representing the orientation of the muon and nucleon spins, respectively. In the case of an unpolarised collision, the anti-symmetric part of eq. 2.16 is identical to zero. Therefore, after the contraction of the symmetric tensors (given by eq. 2.13 and eq. 2.15), the explicit expression for the differential cross section is

$$\frac{d^2\sigma^{unpol}}{dE'd\Omega} = \frac{4\alpha^2 E'^2}{Q^4}\left(\frac{2F_1(x_{Bj},Q^2)}{M}\,\sin^2\frac{\theta}{2} \;+\; \frac{F_2(x_{Bj},Q^2)}{\nu}\,\cos^2\frac{\theta}{2}\right) \tag{2.19}$$

The use of this equation allows us to extract the unpolarised structure functions $F_1(x_{Bj},Q^2)$ and $F_2(x_{Bj},Q^2)$. The only requirement is a measurement of the remaining parameters, i.e. the beam energy E, the scattered muon energy E' and the polar angle θ.

Concerning the polarised part of the cross-section, eq. 2.16 also tells us how to study the spin dependent structure functions $g_1(x_{Bj},Q^2)$ and $g_2(x_{Bj},Q^2)$. They can be obtained by subtracting the cross-sections with opposite nucleon spins (the symmetric part cancels), along an arbitrary direction. Using $\Delta\sigma_\delta = \sigma_\delta - \sigma_{\delta+\pi}$, we obtain:

$$\begin{aligned}\frac{d^2\Delta\sigma_\delta}{dE'd\Omega} &= \frac{8m_l\alpha^2E'}{q^4E}\left(\left[(q\cdot s_N)\,(q\cdot s_l) + Q^2\,(s_l\cdot s_N)\right]M\nu\;\frac{g_1\,(x_{Bj},Q^2)}{(p\cdot q)^2}\right)\\ &+ \frac{8m_l\alpha^2E'Q^2}{q^4E}\left(\left[(s_l\cdot s_N)\,(p\cdot q) - (q\cdot s_N)\,(p\cdot s_l)\right]\frac{g_2\,(x_{Bj},Q^2)}{M\nu\,(p\cdot q)}\right)\end{aligned} \tag{2.20}$$

The best way to solve eq. 2.20 is to consider the case where the beam is longitudinally polarised, i.e. the initial leptons have an helicity along or opposite their direction of motion, while the nucleons are at rest and polarised along an arbitrary direction $\vec{s}_N$ (see Ref. [18]):

$$s_l^{\mu\,\leftarrow} = -s_l^{\mu\,\rightarrow} = \left(|\vec{k}|,\;\hat{k}E\right) \qquad \text{with} \qquad \hat{k} = \frac{\vec{k}}{|\vec{k}|} \tag{2.21}$$

and

$$s_N^{\mu} = (0,\;\vec{s}) \qquad \text{with} \qquad \vec{s} = (\sin\delta\cos\beta,\;\sin\delta\sin\beta,\;\cos\delta) \tag{2.22}$$

Using these two definitions together with the ones of Table 2.1 and Fig. 2.2 ($\beta = \phi + \Phi$), results in the following polarised cross-section:

$$\frac{d^2\Delta\sigma_\delta}{dE'd\Omega} = \frac{-4\alpha^2E'}{Q^2\nu ME}\left(\left[E\cos\delta + E'\cos\Theta\right]g_1(x_{Bj},Q^2) + \frac{2EE'}{\nu}\left[\cos\Theta - \cos\delta\right]g_2(x_{Bj},Q^2)\right) \tag{2.23}$$

where

$$\cos\Theta = \sin\theta\sin\delta\cos\Phi + \cos\theta\cos\delta \tag{2.24}$$

As already stated, an experimentally interesting case is when the target is also longitudinally polarised ($\delta = 0^0,\ 180^o$ and $\theta = \Theta$). This gives a final interpretation for the parallel polarised cross-section:

$$\frac{d^2\Delta\sigma_{\parallel}}{dE'd\Omega} = -\frac{4\alpha^2 E'}{Q^2\nu ME}\left[(E + E'\cos\theta)\, g_1(x_{Bj}, Q^2) - 2x_{Bj}M g_2(x_{Bj}, Q^2)\right] \tag{2.25}$$

Similarly, for the case of a transversely polarised target ($\delta = 90^0,\ 270^o$) we obtain:

$$\frac{d^2\Delta\sigma_{\perp}}{dE'd\Omega} = -\frac{4\alpha^2 E'^2}{Q^2\nu ME}\sin\theta\cos\Phi\left(g_1(x_{Bj}, Q^2) + \frac{2E}{\nu}g_2(x_{Bj}, Q^2)\right) \tag{2.26}$$

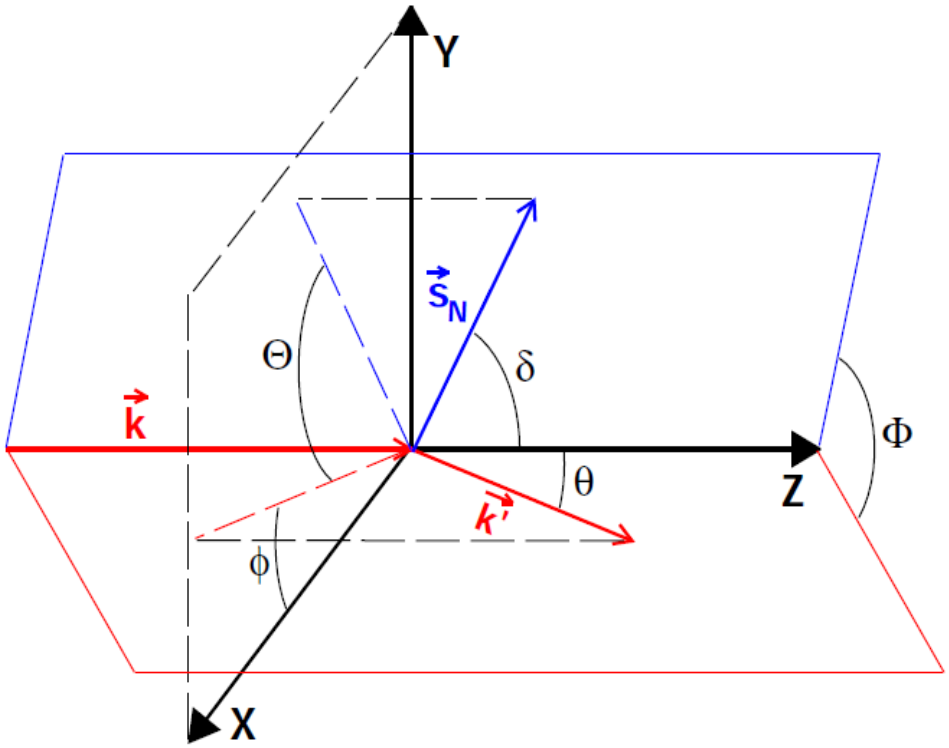

Figure 2.2: Definition of the angles δ, θ, Θ, Φ and ϕ in polarised DIS.

2.1.3 Cross-section asymmetries

In principle the spin dependent structure functions can be determined from a measurement of the two cross-section differences evidenced in eqs. 2.25 and 2.26. However, these differences are extremely sensitive to small changes in the spectrometer setup and, therefore, the following experimental asymmetries are used to study the nucleon spin:

$$A_{\parallel} = \frac{d\sigma^{\rightleftarrows} - d\sigma^{\leftrightarrows}}{d\sigma^{\rightleftarrows} + d\sigma^{\leftrightarrows}} \tag{2.27}$$

and

$$A_\perp = \frac{d\sigma^{\overleftarrow{\Downarrow}} - d\sigma^{\overleftarrow{\Uparrow}}}{d\sigma^{\overleftarrow{\Downarrow}} + d\sigma^{\overleftarrow{\Uparrow}}} \tag{2.28}$$

where $d\sigma$ is the short notation for $d^2\sigma/(dE'd\Omega)$. From the experimental point of view these asymmetries are much more reliable due to a cancellation of the systematic effects (changes in the spectrometer setup with time) in the ratio. The denominator, in both cases, corresponds to the unpolarised cross-section counted twice.

Before we proceed, it is convenient to express $A_\parallel$ and $A_\perp$ in terms of the interesting physical quantities which are the cross-section asymmetries for the photon-nucleon interaction. To accomplish this, we must rewrite eq. 2.19, eq. 2.25 and eq. 2.26 in terms of x_{Bj} and y [19]:

$$\frac{d^2\sigma^{unpol}}{dx_{Bj}dy} = \frac{8\pi\alpha^2}{Q^2}\left[\frac{y}{2}F_1(x_{Bj},Q^2) \;+\; \frac{1}{2x_{Bj}y}\left(1-y-\frac{y^2\gamma^2}{4}\right)F_2(x_{Bj},Q^2)\right] \tag{2.29}$$

$$\frac{d^2\Delta\sigma_\parallel}{dx_{Bj}dy} = \frac{8\pi\alpha^2}{Q^2}\left[\left(1-\frac{y}{2}-\frac{y^2\gamma^2}{4}\right)g_1(x_{Bj},Q^2) \;-\; \frac{y}{2}\gamma^2 g_2(x_{Bj},Q^2)\right] \tag{2.30}$$

$$\frac{d^2\Delta\sigma_\perp}{dx_{Bj}dy} = \frac{8\pi\alpha^2}{Q^2}\left[\gamma\sqrt{1-y-\frac{y^2\gamma^2}{4}}\left(\frac{y}{2}g_1(x_{Bj},Q^2) \;+\; g_2(x_{Bj},Q^2)\right)\right] \tag{2.31}$$

In the equations above the lepton mass is neglected and a new parameter, $\gamma^2 = Q^2/\nu^2 = (4M^2x_{Bj}^2)/Q^2$, is introduced. In COMPASS, a muon beam of 160 GeV/c is used. Therefore, the approximation done in these equations is completely justified. Using the equations above, we can write $A_\parallel$ and $A_\perp$ in terms of the photo-absorption cross-section asymmetries (see Ref. [20] for details):

$$A_\parallel = D(A_1 + \eta A_2) \qquad \text{and} \qquad A_\perp = d(A_2 - \lambda A_1) \tag{2.32}$$

using

$$A_1 = \frac{\sigma_{1/2}-\sigma_{3/2}}{\sigma_{1/2}+\sigma_{3/2}} \;=\; \frac{g_1-\gamma^2 g_2}{F_1}, \tag{2.33}$$

$$A_2 = \frac{2\sigma_{TL}}{\sigma_{1/2}+\sigma_{3/2}} \;=\; \frac{\gamma(g_1+g_2)}{F_1} \tag{2.34}$$

In these expressions $\sigma_{1/2}$ and $\sigma_{3/2}$ are the photo-absorption cross-sections representing the processes where the projection of the total angular momentum of the photon-nucleon system along the direction of the photon momentum is 1/2 and 3/2, respectively. The quantity σ_{TL} is the interference cross-section between the transverse and longitudinal components of the virtual-photon. The remaining quantities are the depolarisation factor, D, and the kinematics factors d, η and λ defined by:

$$D = \frac{y(2-y)(1+\gamma^2 y/2)}{y^2(1+\gamma^2)+2(1-y-\gamma^2y^2/4)(1+R)} \tag{2.35}$$

$$d = \left[\frac{\sqrt{1-y-y^2\gamma^2/4}}{1-y/2}\right] \times D \tag{2.36}$$

$$\eta = \left[\frac{1-y-\gamma^2y^2/4}{(1-y/2)(1+\gamma^2y/2)}\right] \times \gamma \tag{2.37}$$

$$\lambda = \left[\frac{1-y/2}{1+\gamma^2y/2}\right] \times \gamma \tag{2.38}$$

The variable R is the ratio of the longitudinal and transverse photo-absorption cross-sections:

$$R = \frac{\sigma_L}{\sigma_T} = \frac{F_2}{2x_{Bj}F_1}(1+\gamma^2) - 1 \tag{2.39}$$

Using eqs. 2.32-2.34, we obtain:

$$\begin{aligned} g_1 &= \frac{F_1}{1+\gamma^2} \times \left(\frac{A_\parallel}{D} + (\gamma-\eta)A_2\right) \\ &\approx \left(\frac{F_1}{1+\gamma^2}\right) \times \frac{A_\parallel}{D} = -g_2 \end{aligned} \tag{2.40}$$

The contribution of A_2 for the determination of g_1 is suppressed by the small kinematic factor $(\gamma - \eta)$. Therefore, the spin dependent structure functions can be completely determined by a measurement of $A_\parallel$ and F_1 (only at LO-QCD where we have $R \approx 0$ due to eq. 2.55). At NLO-QCD (emission of gluons), the resulting corrections to the R factor may become important and, consequently, the knowledge about F_2 is also required to calculate D.

Generalisation to the spin-1 targets

Until now the polarised target was assumed to be formed by spin-1/2 particles. In the present analysis this corresponds to the COMPASS data accumulated during the year of 2007, where the polarisable material of the target consisted on protons. However, a spin-1 deuteron target was the main polarisable material used by COMPASS during the remaining years of data taking. Therefore it is convenient to generalise the procedure discussed so far to the spin-1 targets. The unpolarised and polarised structure functions are given by [6] [20]

$$F_1 = \frac{1}{3}(\sigma_0 + \sigma_1 + \sigma_2) \tag{2.41}$$

$$g_1 = \frac{1}{2}(\sigma_0 - \sigma_2) \tag{2.42}$$

where σ_0 (σ_2) is the photo-absorption cross-section corresponding to the deuteron target polarised in the opposite (same) direction of the virtual-photon momentum. In addition to F_1

[6] Using eq. 2.33 with $\gamma^2 \approx 0$. Note that the virtual-photon is a spin-1 boson.

and g_1, the generalisation to spin-1 targets introduces a new leading-twist structure function b_1:

$$b_1 = \frac{1}{2}\left(2\sigma_1 - \sigma_0 - \sigma_2\right) \tag{2.43}$$

This structure function results from the cross-section difference obtained with a scattering from an unpolarised and a longitudinally polarised target. Clearly, b_1 is indistinguishable from g_1 in the case of a spin-1/2 target ($b_1 = 1/2[2\sigma_{1/2} - \sigma_{1/2} - \sigma_{3/2}]$). The contribution of b_1 to the photon-nucleon asymmetry is given by

$$\frac{b_1}{F_1} = \frac{1}{2}\left(\frac{2\sigma_1 - \sigma_0 - \sigma_2}{F_1}\right) = \frac{3}{2}\left(\frac{\sigma_1 - F_1}{F_1}\right) \tag{2.44}$$

This tensor asymmetry was recently measured and found to be different from zero (but small) [21]. Nonetheless, the experimental points are still compatible with zero within two standard deviations. In addition to that, the use of a solid state target in COMPASS (with $\approx 40\%$ of polarisable material) results in a small polarisation tensor [22] and, therefore, the influence of a small b_1 in the photon-nucleon asymmetry is even more suppressed. Assuming that $b_1 = 0$ ($\sigma_1 = 1/2[\sigma_0 + \sigma_2]$ from eq. 2.43), we obtain for A_1:

$$\begin{aligned} A_1 \overset{\text{eq.2.33}}{\approx} \frac{g_1}{F_1} &= \frac{3}{2}\left(\frac{\sigma_0 - \sigma_2}{\sigma_0 + \sigma_1 + \sigma_2}\right) \\ &\overset{b_1=0}{=} \frac{\sigma_0 - \sigma_2}{\sigma_0 + \sigma_2} \end{aligned} \tag{2.45}$$

From eq. 2.45 we conclude that it is sufficient to measure g_1 with parallel and anti-parallel orientation of the target spins. As a result, the expression given by eq. 2.40 is still valid for a polarised target consisting of deuterons (with $A_\parallel$ defined by eq. 2.27).

2.2 The Quark Parton Model

As it was already discussed in section 2.1.1, the **Q**uark **P**arton **M**odel (QPM) describes the internal structure of the nucleon in terms of point-like and non-interacting particles (among them) in a frame of infinite momentum. These mass-less constituents carry a fraction of the nucleon momentum ξ and they are called partons. The virtual-photon probing the internal structure of the nucleon can only interact with a charged parton and, therefore, these partons are identified with quarks. Basically the QPM provides an interpretation for the nucleon structure functions in terms of quarks, which is valid up to a leading order (LO) approximation. Using this picture of the DIS process, we just need to insert the leptonic tensor (defined by eq. 2.13) in the expression of $W_{\mu\nu}$, given by eq. 2.8, to properly describe the point-like interaction between the virtual-photon and a quark inside the nucleon. Taking also into account the charge of the quark and integrating over the phase space available to the final particle, the hadronic tensor is reduced to the following expression:

$$W^{\mu\nu}(p,q,s) = \frac{Q_q^2}{4\pi}\int \frac{d^3p'}{\xi\,(2\pi^3)\,2E_{p'}}\,(2\pi)^4\,\delta^4\,(\xi p+q-p') \times 2\left(\xi p^\mu p'^\nu+\xi p^\nu p'^\mu-g^{\mu\nu}\xi p\cdot p'\right)-2\left(i\epsilon^{\mu\nu\alpha\beta}q_\alpha s_\beta\right) \quad (2.46)$$

using the replacements: $k \to \xi p$, $k' \to p'$, $s_l \to s$ and $q \to -q$. Note that the muon mass is neglected, and the factor $1/\xi$ is introduced to normalise the parton flux to the proton flux. The integral in the definition of $W^{\mu\nu}$ is easily computed using the following identity [17]

$$\int \frac{d^3p'}{(2\pi)^3\,2E_{p'}} = \int \frac{d^4p'}{(2\pi)^4\,2p\cdot q}\,(2\pi)\,\delta\left(\xi+\frac{q^2}{2p\cdot q}\right) \quad (2.47)$$

Neglecting all the mass terms of the target and using $p' = (\xi p + q)$ together with $s_\beta = h\xi p_\beta$, with h representing the helicity of the parton, results in the final expression for the hadronic tensor:

$$W^{\mu\nu}(p,q,s) = \frac{Q_q^2}{2\xi p\cdot q}\left(2\xi^2 p^\mu p^\nu - g^{\mu\nu}\xi p\cdot q + ih\xi\epsilon^{\mu\nu\alpha\beta}q_\alpha p_\beta\right)\delta\,(\xi - x_{Bj}) \quad (2.48)$$

The comparison of eq. 2.48 with the general expression of the hadronic tensor, shown in eq. 2.15, gives us an interpretation for the structure functions of the nucleon. The target spin, s_N, is replaced by the product of the target helicity with the nucleon momentum, i.e. Hp. In addition to that, all terms involving q_μ and q_ν in eq. 2.15 are neglected. The reason for that relies in the fact that the leptonic current is also conserved, i.e. the following two equations must be verified:

$$q_\mu l^{\mu\nu} = q_\nu l^{\mu\nu} = 0 \quad (2.49)$$

Since the hadronic and leptonic tensors are contracted in the cross-section (defined by eq. 2.16), the above simplification of $W^{\mu\nu}$ is completely justified. As a result, the polarised and unpolarised structure functions have the following meaning in the frame of the parton model:

$$F_1(x_{Bj}) = \frac{Q_q^2}{2}\delta(\xi - x_{Bj}), \qquad F_2(x_{Bj}) = Q_q^2\xi\delta(\xi - x_{Bj}) \quad (2.50)$$

$$g_1(x_{Bj}) = \frac{Q_q^2}{2}hH\delta(\xi - x_{Bj}), \qquad g_2 = 0 \quad (2.51)$$

Integrating these structure functions over all point-like interactions, results in

$$F_1(x_{Bj}) = \sum_i \frac{Q_{q_i}^2}{2}\left[q_i(x_{Bj}) + \bar{q}_i(x_{Bj})\right], \quad F_2(x_{Bj}) = \sum_i Q_{q_i}^2 x_{Bj}\left[q_i(x_{Bj}) + \bar{q}_i(x_{Bj})\right] \quad (2.52)$$

$$g_1(x_{Bj}) = \sum_i \frac{Q^2_{q_i}}{2} \left[\Delta q_i(x_{Bj}) + \Delta \bar{q}_i(x_{Bj})\right] \tag{2.53}$$

using

$$q_i(x_{Bj}) = \left[q_i^+(x_{Bj}) + q_i^-(x_{Bj})\right] \qquad \text{and} \qquad \Delta q_i(x_{Bj}) = \left[q_i^+(x_{Bj}) - q_i^-(x_{Bj})\right] \tag{2.54}$$

The new functions $q_i^{\pm}(x_{Bj})$ $\left[\bar{q}_i^{\pm}(x_{Bj})\right]$ represent the probability to find a given quark [anti-quark] i carrying a momentum fraction x_{Bj} and with an helicity equal $(+)$ or opposite $(-)$ to the nucleon one. The latter corresponds to the case where $hH = -$, while the case of same helicities is defined by $hH = +$. These probability functions are identified with the following photo-absorption cross-sections:

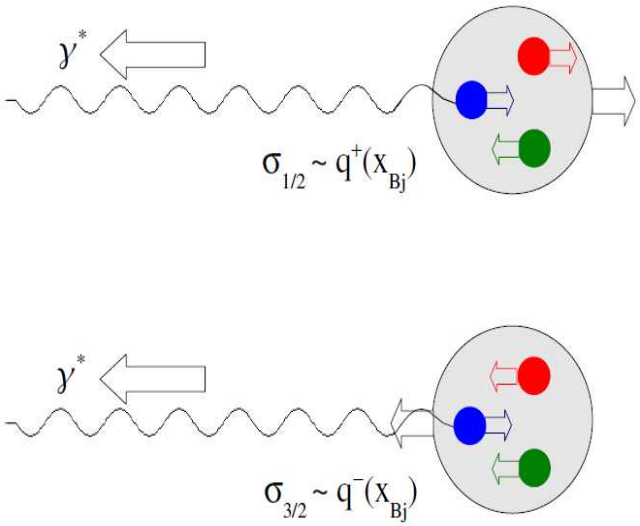

Figure 2.3: Simplified picture of a polarised DIS process in the frame of the parton model. Due to helicity conservation, the virtual-photon can only interact with a quark which is polarised in the opposite direction. Therefore if the quark is oriented in the same direction as the nucleon spin, the symbol $(+)$ is used in the probability function. In this case the total angular momentum in the photon-nucleon system has a value of 1/2 (cf. top).

The Callan-Gross relation

In the parton model the unpolarised structure function F_1 can be interpreted as the probability to find a quark carrying a momentum fraction x_{Bj} of the nucleon. For the polarised case, g_1 represents the difference in probabilities to find a given quark carrying a momentum fraction x_{Bj} with its spin parallel and anti-parallel to the nucleon one. The model implies the Q^2 independence of the structure functions and the validity of the Callan-Gross relation:

$$F_2(x_{Bj}) = 2x_{Bj}F_1(x_{Bj}) \tag{2.55}$$

In fact the expression shown in eq. 2.55 is only valid in the Bjorken limit, i.e. when $\nu, Q^2 \to \infty$.

In this case, the scattering process can be interpreted as an elastic collision between the lepton and a free quark. As a result, the structure functions of the nucleon can be conveniently interpreted as quark distribution functions. It is important to note that the sums in eq. 2.52 and in eq. 2.53 run only over those quark flavours that are light when compared with the magnitude of Q^2. The scaling of the structure functions, i.e. their exclusive dependence in x_{Bj}, was confirmed by the experiments performed at SLAC during the sixties. This was a stunning achievement of the QPM. One of the major implications of the model is that only two independent measurements of the nucleon structure functions are needed: F_1 or F_2 (cf. eq. 2.55) and g_1 to completely describe the nucleon structure. However, the next generation of experiments showed a small dependence in Q^2 of F_1 and F_2 (of the order of 10%). The scaling was approximately confirmed but it was not complete. The implications of this discovery will be discussed in section 2.3. Nevertheless, the QPM is able to describe well enough the experimental results using a LO approximation [7] (cf. Fig. 2.4).

2.2.1 The first moment of g_1

Up to now the theoretical models that describe a polarised nucleon are only capable of making predictions for the first moment of the spin dependent structure function. It is defined by

$$\Gamma_1 = \int_0^1 g_1(x_{Bj})dx_{Bj} = \frac{1}{2}\sum_i Q_{q_i}^2 \left[\Delta\hat{q}_i + \Delta\hat{\bar{q}}_i\right] \tag{2.56}$$

where

$$\Delta\hat{q}_i = \int_0^1 \left[q_i^+(x_{Bj}) - q_i^-(x_{Bj})\right] dx_{Bj} \quad \text{and} \quad \Delta\hat{\bar{q}}_i = \int_0^1 \left[\bar{q}_i{}^+(x_{Bj}) - \bar{q}_i{}^-(x_{Bj})\right] dx_{Bj} \tag{2.57}$$

Therefore, with the help of eq. 2.56 we can write explicitly the expressions for the first moments of the proton and the neutron (u = up-quark, d = down-quark and s = strange-quark):

$$\Gamma_1^p = \frac{1}{2}\left[\frac{4}{9}\left(\Delta\hat{u} + \Delta\hat{\bar{u}}\right) + \frac{1}{9}\left(\Delta\hat{d} + \Delta\hat{\bar{d}}\right) + \frac{1}{9}\left(\Delta\hat{s} + \Delta\hat{\bar{s}}\right)\right] = \frac{1}{9}a_0 + \frac{1}{12}\left[a_3 + \frac{1}{\sqrt{3}}a_8\right] \tag{2.58}$$

$$\Gamma_1^n = \frac{1}{2}\left[\frac{1}{9}\left(\Delta\hat{u} + \Delta\hat{\bar{u}}\right) + \frac{4}{9}\left(\Delta\hat{d} + \Delta\hat{\bar{d}}\right) + \frac{1}{9}\left(\Delta\hat{s} + \Delta\hat{\bar{s}}\right)\right] = \frac{1}{9}a_0 + \frac{1}{12}\left[-a_3 + \frac{1}{\sqrt{3}}a_8\right] \tag{2.59}$$

using

$$a_0 = \left[\left(\Delta\hat{u} + \Delta\hat{\bar{u}}\right) + \left(\Delta\hat{d} + \Delta\hat{\bar{d}}\right) + \left(\Delta\hat{s} + \Delta\hat{\bar{s}}\right)\right] \tag{2.60}$$

$$a_3 = \left[\left(\Delta\hat{u} + \Delta\hat{\bar{u}}\right) - \left(\Delta\hat{d} + \Delta\hat{\bar{d}}\right)\right] \tag{2.61}$$

$$a_8 = \frac{1}{\sqrt{3}}\left[\left(\Delta\hat{u} + \Delta\hat{\bar{u}}\right) + \left(\Delta\hat{d} + \Delta\hat{\bar{d}}\right) - 2\left(\Delta\hat{s} + \Delta\hat{\bar{s}}\right)\right] \tag{2.62}$$

[7] Here LO means the absence of gluon emissions by the quarks. It will be shown in section 2.3 that the Q^2 dependence is introduced by the existence of gluons. A radiated gluon is interpreted as a NLO process.

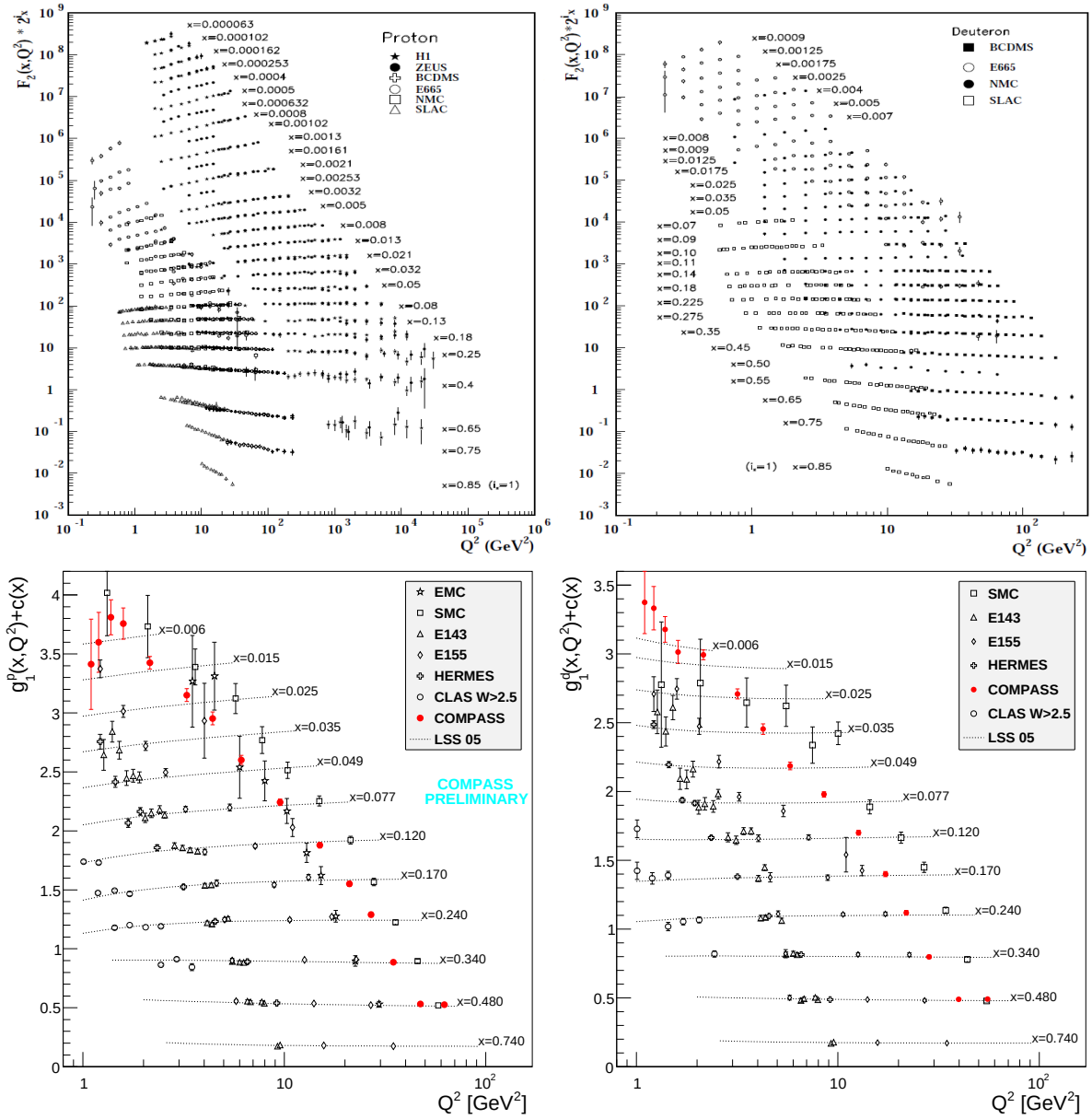

Figure 2.4: Compilation of several DIS measurements on F_2 (up) and g_1 (down) as a function of Q^2, and for fixed values of x_{Bj}. Both proton (left) and deuteron (right) data are shown. The dashed lines illustrated in the figures of g_1 correspond to a NLO fit to the world data. The measurements clearly show the scaling property of the structure functions for high Q^2 values. However, in the low Q^2 regime small scaling violations start to appear (see top-left). They are related with a harder resolution of some gluon emissions by the virtual-photon and, therefore, the momentum of the interacting quark is overestimated (cf. section 2.3). The data were obtained from H1 [23] , ZEUS [24] , BCDMS [25] , E665 [26] , NMC [27] , SLAC [28], EMC [1], SMC [3], E143 [29], E155 [6], HERMES [7], CLAS [30] and COMPASS [31, 32].

The coefficients a_0, a_3 and a_8 correspond to some of the proton matrix elements that can be calculated from the SU(3) flavour octet axial-vector currents, $J^i_{5\mu}$,

$$\langle p,s|J^i_{5\mu}|p,s\rangle = Ma_i s_\mu, \qquad i = 1...8 \tag{2.63}$$

and from the flavour singlet axial-vector current $J^0_{5\mu}$. These proton currents are given by

$$J^0_{5\mu} = \bar{\Psi}\gamma_\mu\gamma_5\Psi \qquad \text{and} \qquad J^i_{5\mu} = \bar{\Psi}\gamma_\mu\gamma_5\frac{\lambda_i}{2}\Psi \tag{2.64}$$

where λ_i are the Gell-Mann matrices (generators of the flavour SU(3) [33]) and $\Psi = (\Psi_u, \Psi_d, \Psi_s)$ is a vector in the quark flavour space. The matrix elements defined in eqs. 2.60-2.62 result from eq. 2.63 if and only if the point-like quarks are assumed as free particles inside the nucleon. The coefficients a_3 and a_8 can be obtained from the parameters F and D, which in turn are measured from the hyperon β-decays ($\Lambda \to p$, $\Sigma \to n$, etc.). The following relations are verified (g_A and g_V are the axial and the vector coupling constants, respectively) [16, 18]:

$$a_3 = \left|\frac{g_A}{g_V}\right| = F + D = 1.270 \pm 0.003 \tag{2.65}$$

$$a_8 = \frac{1}{\sqrt{3}}(3F - D) = 0.579 \pm 0.025 \tag{2.66}$$

Therefore the contribution of quarks to the nucleon spin, $\Delta\Sigma \equiv a_0$ (in the QPM), can be determined by an additional measurement of Γ_1^p. This procedure was followed by the collaboration EMC which obtained the shocking result of $\Delta\Sigma = 0.12 \pm 0.09 \pm 0.14$ [1]. Such an unexpected contribution from the quarks to the nucleon spin caused the so called spin crisis of the nucleon. This result triggered a new generation of experiments to measure $\Delta\Sigma$ in a NLO approximation (i.e., by taking also into account the gluons as mediators of the strong interactions between quarks) and, posteriorly, the obtained results motivated experiments like COMPASS to measure also the gluon polarisation, $\Delta G/G$. In Fig. 2.5 the world measurements of g_1 are presented as a function of x_{Bj}:

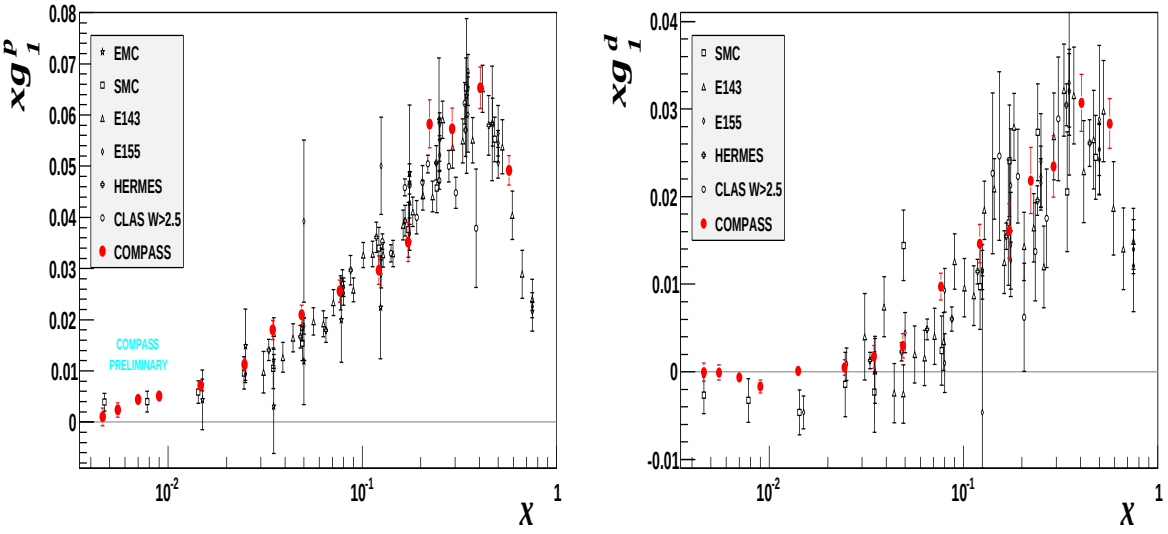

Figure 2.5: Results for the polarised structure function, xg_1, using a proton (left) or a deuteron (right) target. The first moment Γ_1^p is given by the integral of the fit to the world data shown in the left figure.

Anomalous gluon contribution

At LO all the proton currents are conserved (for mass-less quarks), i.e:

$$\partial^\mu J^j_{5\mu} = 2im_j \bar{\Psi}_j \gamma_5 \Psi_j \overset{m_j \to 0}{\to} 0 \tag{2.67}$$

However, the consideration of gluons in the nucleon dynamics gives rise to the following contribution to the proton matrix elements [18, 20, 34, 35]:

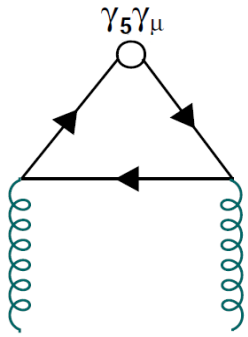

Figure 2.6: The anomalous gluon contribution to the singlet axial-vector current. It is given by the illustrated triangle (only at NLO).

The diagram of Fig. 2.6 affects only the singlet axial-vector current, while it cancels between flavours in the conserved octet axial-vector currents. We have for this process:

$$\partial^\mu J^0_{5\mu} = \frac{\alpha_s}{2\pi} n_f \mathrm{Tr}\left(G_{\mu\nu}\hat{G}^{\mu\nu}\right) \tag{2.68}$$

using

$$\hat{G}_{\mu\nu} = \frac{1}{2}\epsilon_{\mu\nu\alpha\beta}G^{\alpha\beta} \quad \text{and} \quad n_f = 3 \tag{2.69}$$

where $G_{\mu\nu}$ is the gluonic field tensor and n_f the number of active flavours. It is clear from eq. 2.68 (which is still valid for higher order corrections) that $J^0_{5\mu}$ is not conserved. As a result, the expectation value of a_0 is dependent of Q^2. However, a conserved current can be constructed by subtracting the gluon axial current, K_μ, from the quark current:

$$\hat{J}^0_{5\mu} = J^0_{5\mu} - n_f \frac{\alpha_s}{2\pi} K_\mu \qquad \text{using} \qquad \partial_\mu K_\mu = \mathrm{Tr}\left(G_{\mu\nu}\hat{G}^{\mu\nu}\right) \tag{2.70}$$

The gluon axial current is identified with ΔG_1, i.e. the gluon contribution to the nucleon spin. Therefore, at NLO, eq. 2.63 gives for $\hat{a}_0$

$$\hat{a}_0 = a_0 + n_f \frac{\alpha_s}{2\pi} \Delta G_1 \tag{2.71}$$

or in terms of the quark contribution to the nucleon spin, $\hat{a}_0 \equiv \Delta\Sigma$:

$$a_0(Q^2) = \Delta\Sigma - n_f \frac{\alpha_s(Q^2)}{2\pi} \Delta G_1(Q^2) \tag{2.72}$$

Therefore, the existence of a large gluon contribution could explain why the experimental $a_0(Q^2)$ was found so small. This was a strong motivation to measure ΔG_1 in dedicated experiments like COMPASS. However, a direct measurement of $\Delta\Sigma$ in NLO approximation was also obtained using the formalism discussed in the next section.

2.3 QCD corrections to the QPM

The gluons are as important as quarks to the understanding of the internal structure of the nucleon. This was confirmed by unpolarised DIS experiments, which have shown that quarks carry only about half of the total nucleon momentum. The remaining part of the momentum is assigned to the quanta of the strong interactions between quarks, i.e. the gluons. Accordingly, these bosons are also responsible by the breaking of the scale invariance of the nucleon structure functions. In fact, one can see in Fig. 2.4 that the Q^2 independence of the unpolarised and polarised structure functions is only approximately fulfilled. The theory of Quantum Chromodynamics (QCD) explains the small Q^2 dependence of F_2 and g_1, for fixed values of x_{Bj}, by considering that the quarks exchange coloured gluons between them (instead of being free point-like particles). According to the theory, each valence quark in the nucleon is surrounded by a cloud of gluons and sea-quark pairs ($q\bar{q}$). Such gluon cloud is better resolved with an increasingly larger Q^2:

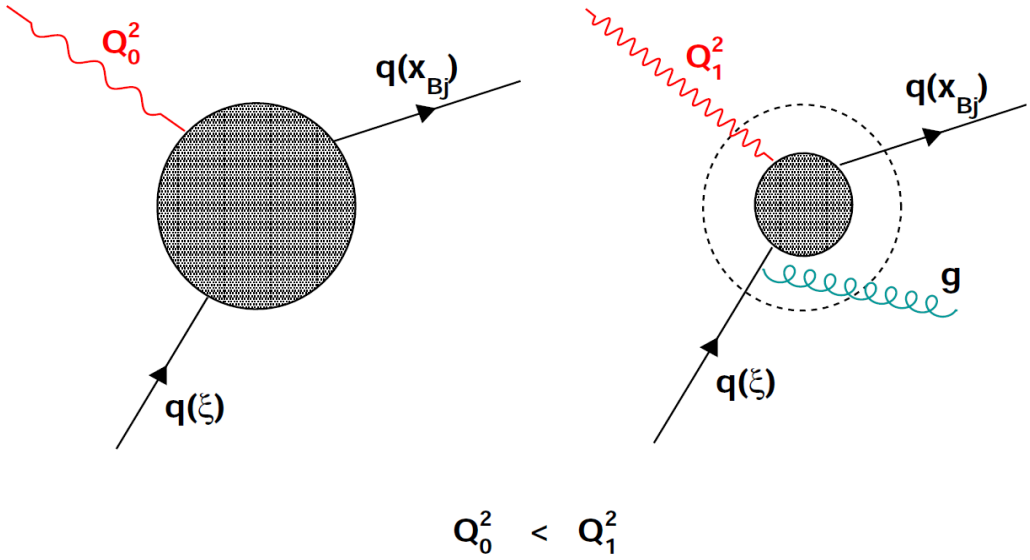

Figure 2.7: Illustration of a DIS process between a virtual-photon (γ^*) and a quark. One can see that the γ^* with a $Q_1^2 > Q_0^2$ is able to resolve the gluon emission of quark carrying a momentum ξ. Consequently, the quark is observed with a smaller momentum x_{Bj} (right) when compared to the momentum ξ which is resolved with Q_0^2 (left).

As a result, the consideration of NLO processes (gluon emissions) leads to a Q^2 dependence of the parton distributions, $\Delta q(x_{Bj}, Q^2)$, and therefore to the scale dependence of the structure functions. Is is clear from Fig. 2.7 that the momentum at which a quark is probed is dependent on Q^2: a virtual-photon with a higher resolving power can probe the same quark at a lower x_{Bj} (after a gluon emission).

The QCD evolution in the polarised case

The evolution of the quark and gluon distribution functions with Q^2, at a fixed x_{Bj}, is described by the **D**okshitzer-**G**ribov-**L**ipatov-**A**ltarelli-**P**arisi (DGLAP) equations:

$$\frac{\mathrm{d}\Delta q^{NS}\left(x_{Bj}, Q^2\right)}{\mathrm{d}\ln Q^2} = \frac{\alpha_s\left(Q^2\right)}{2\pi}\Delta P_{qq}^{NS}\left(\frac{x_{Bj}}{\xi}\right) \otimes \Delta q^{NS}\left(\xi, Q^2\right) \tag{2.73}$$

$$\frac{\mathrm{d}}{\mathrm{dln}Q^2}\begin{pmatrix}\Delta\Sigma\left(x_{Bj},Q^2\right)\\ \Delta G_1\left(x_{Bj},Q^2\right)\end{pmatrix}=\frac{\alpha_s\left(Q^2\right)}{2\pi}\begin{pmatrix}\Delta P_{qq}^S\left(\frac{x_{Bj}}{\xi}\right) & 2n_f\Delta P_{qg}^S\left(\frac{x_{Bj}}{\xi}\right)\\ \Delta P_{gq}^S\left(\frac{x_{Bj}}{\xi}\right) & \Delta P_{gg}^S\left(\frac{x_{Bj}}{\xi}\right)\end{pmatrix}\otimes\begin{pmatrix}\Delta\Sigma\left(\xi,Q^2\right)\\ \Delta G_1\left(\xi,Q^2\right)\end{pmatrix}$$

using

$$\left(\Delta P\otimes\Delta F\right)\left(x_{Bj},Q^2\right)=\int_{x_{Bj}}^1\frac{d\xi}{\xi}\Delta P\left(\frac{x_{Bj}}{\xi}\right)\Delta F\left(\xi,Q^2\right) \tag{2.74}$$

where ΔF represents a polarised parton distribution function (quark or gluon). Analogous equations can be written for the unpolarised case (see Ref. [36]). It is convenient to separate the singlet and non-singlet distributions of polarised quarks, in order to profit from a gluon independent evolution by the latter. They are defined as (using $Q_q = e$):

$$\Delta q^{NS}\left(x_{Bj},Q^2\right) = \sum_{i=1}^{n_f}\left(\frac{e_i^2}{\frac{\sum_{i=j}^{n_f}e_j^2}{n_f}}-1\right)\left[\Delta\hat{q}_i\left(x_{Bj},Q^2\right)+\Delta\hat{\bar{q}}_i\left(x_{Bj},Q^2\right)\right] \tag{2.75}$$

$$\Delta\Sigma\left(x_{Bj},Q^2\right) = \sum_{i=1}^{n_i}\left[\Delta\hat{q}_i\left(x_{Bj},Q^2\right)+\Delta\hat{\bar{q}}_i\left(x_{Bj},Q^2\right)\right] \tag{2.76}$$

The DGLAP equations contain five polarised splitting functions, ΔP, which are obtained from the following unpolarised ones:

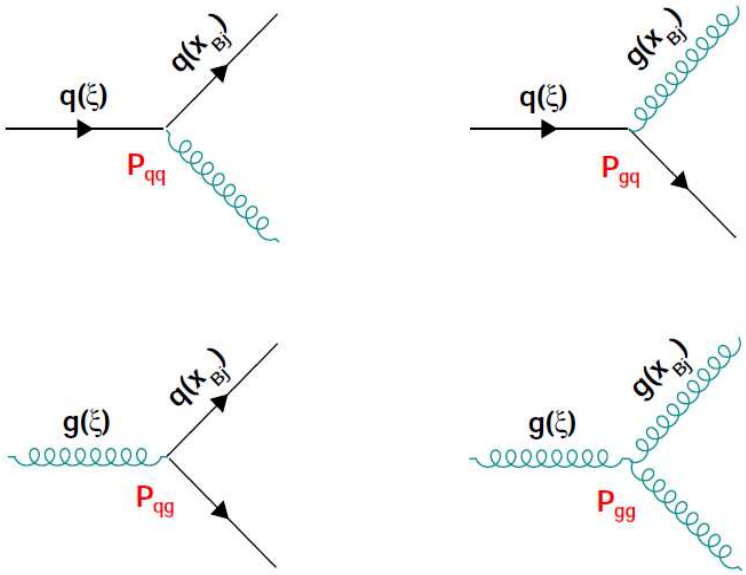

Figure 2.8: These functions account for the probability of a quark (gluon) with momentum fraction x_{Bj} to come from a parent quark with a larger momentum fraction ξ, due to a gluon radiation by the latter (top). Similarly, P_{qg} and P_{gg} take into account the probability of a quark (gluon) with momentum x_{Bj} to come from a gluon which carries a higher momentum ξ (bottom). The latter illustrate two of the gluon properties: conversion into $q\bar{q}$ and gg pairs.

In the polarised scenario we have $\Delta P_{ij}(x_{Bj}/\xi) = P_{i^+j^+}(x_{Bj}/\xi) - P_{i^-j^+}(x_{Bj}/\xi)$, with the latter term representing the probability of a parton j with positive helicity and momentum fraction ξ to radiate another parton i with negative helicity and momentum fraction x_{Bj}. The consideration of these QCD corrections to the parton model leads also to the introduction of corrections in the nucleon structure functions. In particular, the NLO expression for g_1 is given by

$$\begin{aligned} g_1\left(x_{Bj},Q^2\right) &= \left(\frac{\sum_{i=1}^{n_f} e_i^2}{2n_f}\right)\left[\Delta C_q^{NS}\left(x_{Bj},Q^2\right)\otimes\Delta q^{NS}\left(x_{Bj},Q^2\right)\right. \\ &+ \left.\Delta C_q^{S}\left(x_{Bj},Q^2\right)\otimes\Delta\Sigma\left(x_{Bj},Q^2\right) + 2n_f\Delta C_G\left(x_{Bj},Q^2\right)\otimes\Delta G_1\left(x_{Bj},Q^2\right)\right] \end{aligned} \tag{2.77}$$

The corresponding first moment of the proton is

$$\begin{aligned} \Gamma_1^p\left(Q^2\right) &= \left(\frac{\sum_{i=1}^{n_f} e_i^2}{2n_f}\right)\left[\,\Delta C_q^{NS}\left(Q^2\right)\Delta q^{NS}\left(Q^2\right) + \Delta C_q^{S}\left(Q^2\right)\Delta\Sigma\left(Q^2\right)\right. \\ &+ \left.2n_f\Delta C_G\left(Q^2\right)\Delta G_1\left(Q^2\right)\,\right] \end{aligned} \tag{2.78}$$

where C_q^{NS}, C_q^S and C_G are the coefficient functions describing the photon-parton scattering process. These three functions are calculable in perturbative QCD and are also well known up to the NLO approximation [37, 38, 39]. The same is true for the DGLAP splitting functions, $P_{ij}(x_{Bj}/\xi)$.

Each of the three factors shown in eq. 2.78 has two separate contributions: the hard part of the photon-parton interaction is included in the coefficient functions whereas the soft part, i.e. the structure of the nucleon, is absorbed in the parton distribution functions. The soft parts cannot be calculated directly from QCD and thus they have to be measured by experiments. However, the separation of these two contributions is not strict. Different factorisation schemes and scales are allowed. The latter indicates the scale at which the separation takes place. Two common choices are the **M**odified **M**inimal **S**ubtraction ($\overline{MS}$) scheme and the **A**dler-**B**ardeen (AB) scheme. The two schemes differ in how they treat some of the soft contributions. In the $\overline{MS}$ scheme these soft corrections are applied to the coefficient functions and, as a result, the first moment of $\Delta C_G(x_{Bj},Q^2)$ vanishes up to the NNLO (next-to-next-to-leading order). Consequently, the first moment of $g_1(x_{Bj},Q^2)$ is decoupled from the gluon distribution ΔG_1. Concerning the AB scheme, all the soft contributions are absorbed by the parton distribution functions, which implies the dependence of Γ_1^p in ΔG ($\Delta C_G(x_{Bj},Q^2) \neq 0$ in the NLO approximation). Therefore, at NLO, the following relation is verified (note that $\Delta\Sigma^{\overline{MS}} = a_0$ and $\Delta\Sigma^{AB} = a_0 \; + \; [(n_f\alpha_s)/2\pi]\Delta G_1$):

$$\Delta\Sigma^{\overline{MS}}(Q^2) = \Delta\Sigma^{AB} - \frac{n_f\alpha_s(Q^2)}{2\pi}\Delta G_1(Q^2) \tag{2.79}$$

where the independence of Q^2 in the AB scheme is ensured by the Adler-Barden theorem [40], which states that the gluon anomaly (discussed in section 2.2.1) does not receive any higher order corrections.

2.4 Determination of $\Delta\Sigma$ at NLO

The DGLAP equations can be used to perform a NLO-QCD analysis of the g_1 data. Four ingredients are needed to obtain the polarised parton distributions: DGLAP splitting functions, coefficient functions (shown in eq. 2.77), experimental measurements of g_1 in the (x_{Bj}, Q^2) plane and a parameterisation of $\Delta\Sigma$, Δq^{NS} and ΔG at a reference Q^2 $(= Q_0^2)$. The latter is needed as an input to the DGLAP equations in order to allow for the Q^2 evolution of the polarised parton distribution functions. The knowledge of how these distributions evolve with Q^2 provides us a tool to extract the quark and gluon contributions to the nucleon spin. In COMPASS this analysis is done using the following parameterisation:

$$\Delta F_k = n_k \frac{x_{Bj}^{\alpha_k}(1-x_{Bj})^{\beta_k}(1+\gamma_k x_{Bj})}{\int_0^1 x_{Bj}^{\alpha_k}(1-x_{Bj})^{\beta_k}(1+\gamma_k x_{Bj})dx_{Bj}} \qquad @Q_0^2 = 3\ (\mathrm{GeV/c})^2 \tag{2.80}$$

where ΔF_k represents each of the polarised parton distribution functions, namely $\Delta\Sigma$, Δq^{NS} and ΔG, and n_k is the integral of ΔF_k. A reference value of $Q_0^2 = 3\ (\mathrm{GeV/c})^2$ is chosen because it is close to the average Q^2 of the COMPASS DIS data. The above parameterisation is then evolved to the Q^2 of an existing $g_1(x_{Bj}, Q^2)$ measurement, and thereafter the parameters are optimised through the use of the following χ^2 minimisation:

$$\chi^2 = \sum_{i=1}^{N=230} \frac{\left[g_1(x_{Bj_i}, Q_i^2)^{\mathrm{calc}} - g_1(x_{Bj_i}, Q_i^2)^{\mathrm{exp}}\right]^2}{\left[\sigma\left(g_1(x_{Bj_i}, Q_i^2)^{\mathrm{exp}}\right)\right]^2} \tag{2.81}$$

Here the errors σ are the statistical ones for all the 230 experimental data points. Using these NLO-QCD fits, we obtain for the integral of $\Delta\Sigma$ [8]:

$$n_\Sigma = 0.30 \pm 0.01(\mathrm{stat}) \pm 0.02(\mathrm{evol}) \tag{2.82}$$

The quark contribution to the nucleon spin is determined from the following two hypotheses: $\Delta G > 0$ $(n_\Sigma = 0.27 \pm 0.01)$ and $\Delta G < 0$ $(n_\Sigma = 0.32 \pm 0.01)$. This result uses the world data on the polarised proton, neutron and deuteron targets. The consideration of the 43 COMPASS points on the $g_1^d(x_{Bj}, Q^2)$ measurement allowed the reduction of the error by a factor of 2 in the region of $x < 0.02$ [31].

This NLO-QCD analysis is done using the $\overline{MS}$ factorisation scheme. The high precision value obtained for n_Σ confirmed the early conclusion made upon the EMC results, i.e. the quark contribution to the nucleon spin is unexpectedly small. Therefore, the missing spin was assumed to come from the polarised gluons. It is well known from unpolarised DIS experiments that gluons carry approximately half of the nucleon momentum and, by analogy, they were also seen as the best candidates to solve this spin puzzle (cf. eq. 1.5). A value for n_G (ΔG_1) can also be obtained from the NLO-QCD fitting procedure described above. The main problem is that this analysis is extremely dependent on how extensively the g_1 structure function was measured in the (x_{Bj}, Q^2) kinematic plane. One can see from Fig. 2.4 that in the unpolarised case the coverage and statistical accuracy in this plane are very good and, consequently, the unpolarised parton distributions can be determined rather well. However the situation is completely different for the polarised case, where the available data have not yet reached the same kinematic extent because it comes mainly from fixed target experiments. As a consequence

[8] Note that in eq. 1.5 we have (for simplicity of notation): $\Delta\Sigma = \eta_\Sigma$.

the polarised parton distributions are less well constrained. In particular, the uncertainty in ΔG_1 is large. In addition to that, two equally good solutions are found for the polarised gluon distribution, one positive and one negative. Both solutions describe very well the experimental data (cf. Fig. 2.9) with a first moment of $|n_G| \approx 0.3$, but the shapes of their distributions are very different. The results of these two fits can be seen in Fig. 2.10.

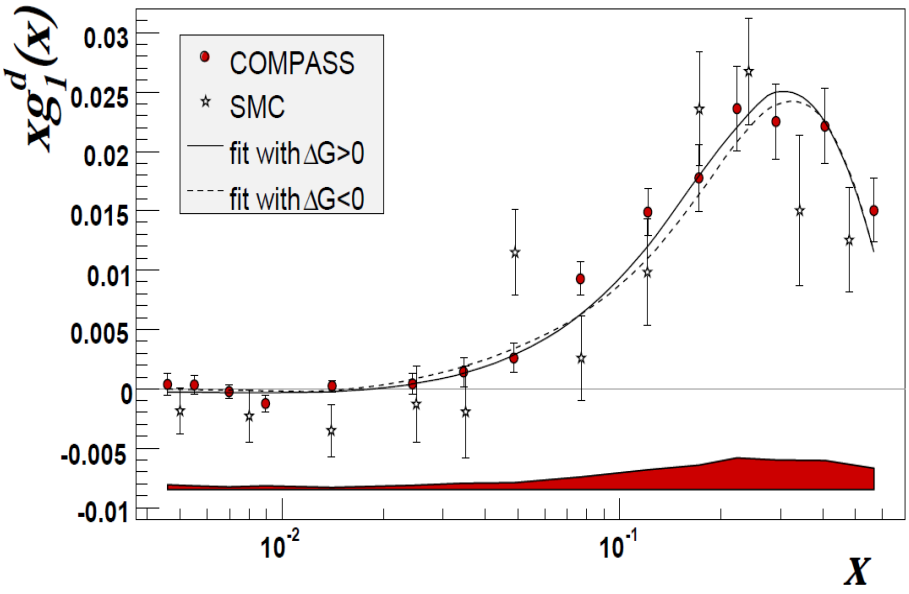

Figure 2.9: Values of $xg_1^d(x_{Bj}, Q^2)$. The COMPASS points are given at the $\langle Q^2 \rangle$ where they are measured. The SMC points have been moved to the Q^2 of the COMPASS points. Only statistical errors are shown with the data points. The shaded band at the bottom shows the systematic errors of COMPASS. The curves show the results of the QCD fits with $\Delta G > 0$ and $\Delta G < 0$. Both fits describe very well the existing data (also true for the $g_1^p(x_{Bj}, Q^2)$ points shown in Fig. 2.5 and $g_1^n(x_{Bj}, Q^2)$ using the world data). Plot taken from [31]

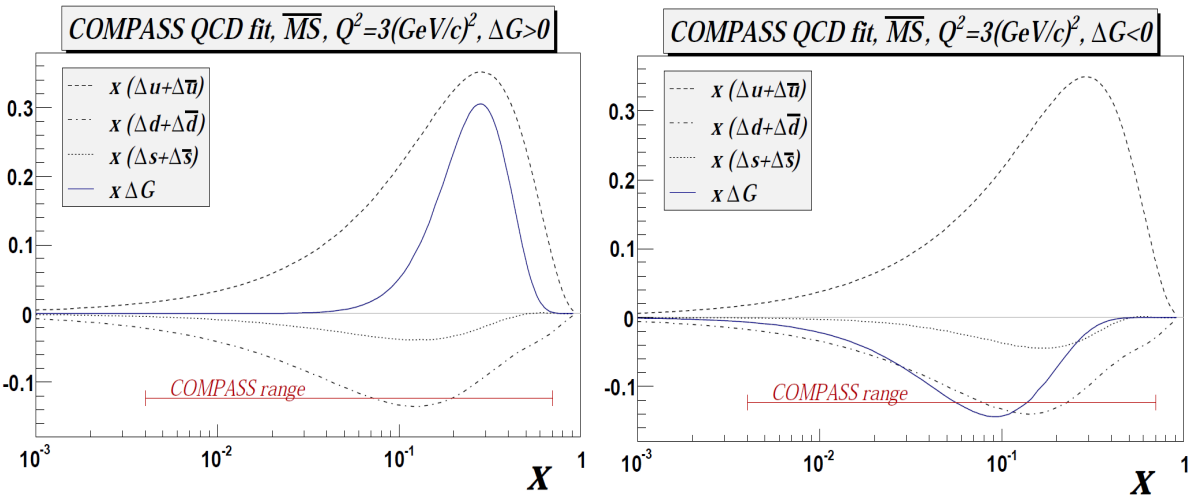

Figure 2.10: Results of the NLO-QCD fits for the polarised quarks and gluons as a function of x. All solutions obtained with $\Delta G > 0$ and $\Delta G < 0$ are shown on the left and right plots, respectively. The distributions of $x(\Delta q + \Delta \bar{q})$ reveal a very small sensitivity to $x\Delta G$.

There are two ways to improve our knowledge about ΔG. The first one is to enlarge the kinematic range of the $g_1(x_{Bj}, Q^2)$ measurements in order to better constrain the QCD fits. This could be achieved by taking data with polarised (leptonic) beams in colliders, but unfortunately this is not foreseen for the near future. The second option is to measure directly $\Delta G/G$ from a process called **P**hoton-**G**luon **F**usion (PGF).

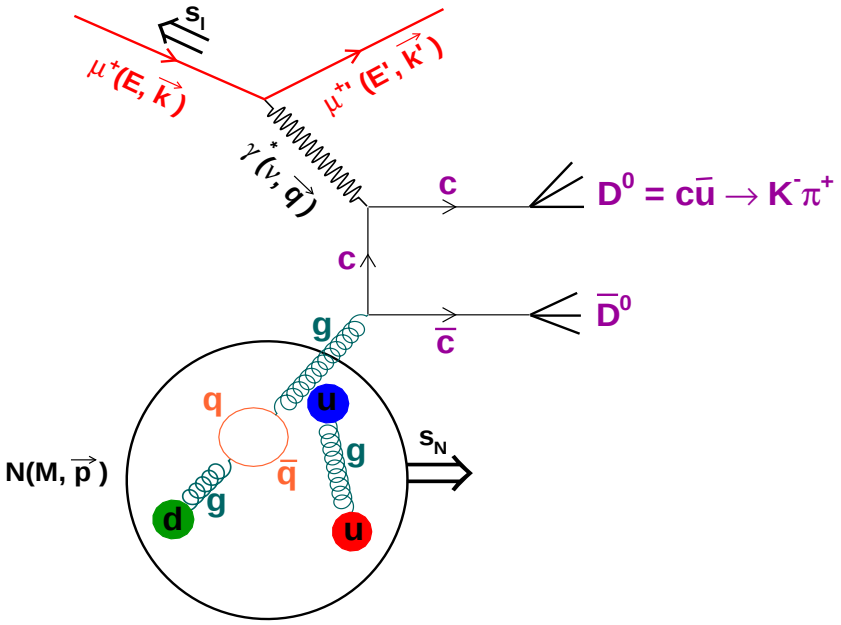

Figure 2.11: The Photon-Gluon Fusion process at LO. The diagram corresponds to the process used as a reference for the open-charm analysis.

2.5 Direct measurement of ΔG/G

The best way to obtain a direct measurement of the gluon polarisation is to make use of electromagnetic probes. It is clear from Fig. 2.11 that the PGF mechanism is the simplest process to use in order to access the polarised gluon distribution in the nucleon: the virtual-photon interacts with a gluon in the polarised nucleon via exchange of a virtual-quark, resulting in a $q\bar{q}$ pair that is produced back-to-back in the centre-of-mass frame. There are two strategies of analysis. The first one uses the open-charm method, which was applied for the first time in COMPASS (in polarised experiments). It takes advantage of the fact that in the COMPASS kinematic domain the intrinsic-charm content of the nucleon is negligible and, therefore, at LO, an open-charm hadron can only be produced as the outcome of a PGF process. Thus, the reconstruction of these hadrons provides a clean signature of events originating from interactions with gluons. The fusion process is in this case mediated by a charm quark. The "final state" quarks fragment to an open-charm hadron with the following probabilities (only the most relevant are shown):

1.) $c \overset{50\%}{\rightarrow} D^0(c\bar{u})$ (includes also the parent process $D^* \rightarrow D^0\pi_{slow}$)
2.) $c \overset{20\%}{\rightarrow} D^+(c\bar{d})$
3.) $c \overset{20\%}{\rightarrow} D_s^+(c\bar{s})$

4.) $c \overset{10\%}{\rightarrow} \Lambda_c^+(udc)$

As it is clear from the above fragmentation processes, the D^0 meson is the most important hadron to consider in the open-charm analysis. Nevertheless, the statistics is still quite limited (due to the difficulty of a $c\bar{c}$ production) and this represents the main drawback of the method. The diagram shown in Fig. 2.11 illustrates the fundamental process for the open-charm production in a LO-QCD approximation. Technically speaking, the diagram represents a higher order interaction of the virtual-photon. However since a photon cannot couple directly with a gluon, the illustrated process represents the lowest order allowed for a PGF interaction. The second option to probe the polarisation of gluons is to select hadron pairs with high transverse momentum regarding to the virtual-photon direction. In this approach it is assumed that a large transverse momentum (p_T) can only be generated by the PGF and QCD-Compton ($\gamma^* q \rightarrow gq$) processes. For the PGF part, the diagram is the same as represented in Fig. 2.11 but with the charm quark replaced by a light-quark (u, d, s). This is the high-p_T method for hadron pairs and its main advantage is the large statistics available. The drawback is the existence of physical background and therefore the method is extremely model dependent. The details about the high-p_T analysis of COMPASS are given in the Refs. [41, 42, 43].

2.5.1 The open-charm method

The open-charm analysis is the one used to obtain the results shown in this thesis. This approach is completely free from physical background (in a LO approximation) and, therefore, it is the most direct way to access ΔG. We can check in Fig. 2.12 and in Fig. 2.13 that the intrinsic-charm contamination is indeed negligible in the COMPASS kinematic domain (cf. also the top-right of Fig. 5.19).

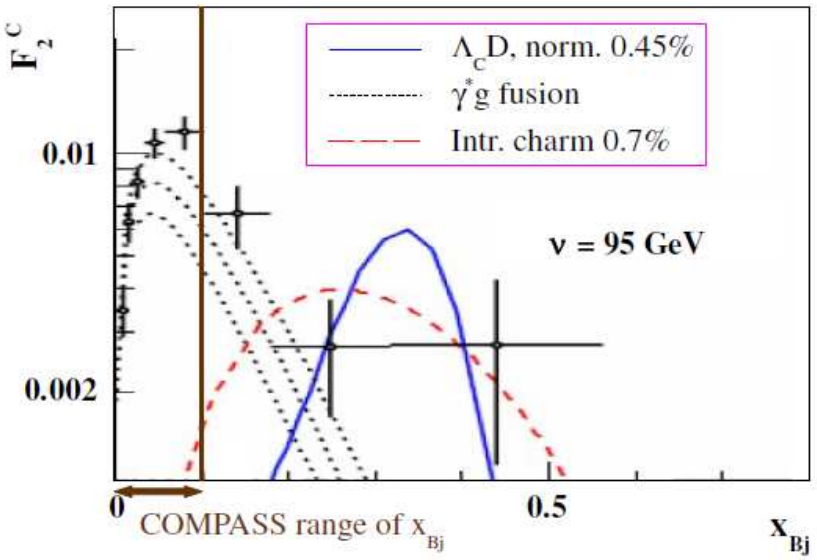

Figure 2.12: Intrinsic-charm predictions obtained for the $\langle\nu\rangle$ in COMPASS. The experimental points represent measurements of the charm structure function by the collaboration EMC [44], and the black dotted curves are theoretical fits for the PGF process using different renormalisation and factorisation schemes [45]. The blue curve shows the intrinsic-charm prediction assuming a nucleon fluctuation into charmed meson-hadron pairs [46]. The red dashed curve shows the intrinsic-charm prediction assuming charm fluctuations at the partonic level [47].

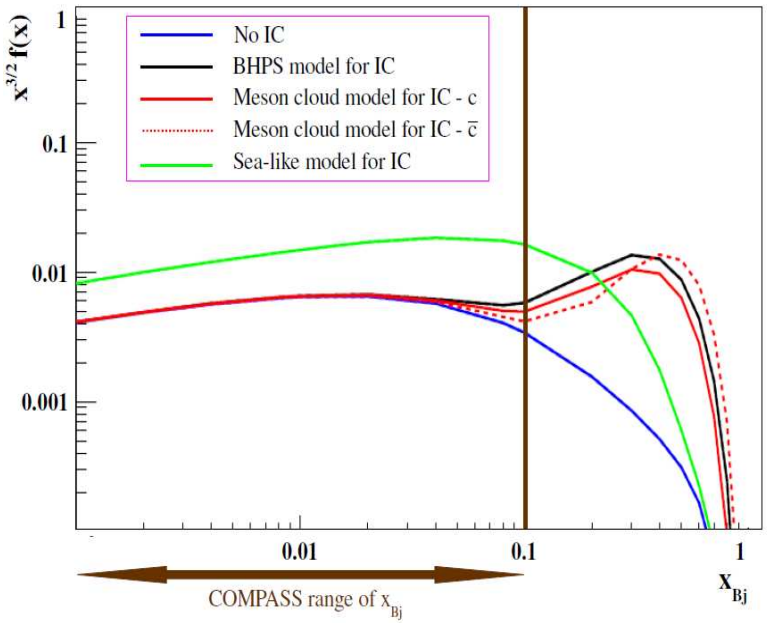

Figure 2.13: Intrinsic-charm predictions obtained by the CTEQ collaboration (CTEQ 6.5c). The theory driven predictions show that the COMPASS data is not sensitive to the nucleon intrinsic-charm. They are the meson cloud models (for c and $\bar{c}$ separately), which account for the probability that the nucleon can fluctuate into an intermediate state composed by a charmed baryon plus a charmed meson, and also the BHPS model. The latter calculates the probability of finding the nucleon in a higher Fock state of $|qqqc\bar{c}>$. The remaining prediction uses a phenomenological approach, which is based on the assumption that some charm already exists in the nucleon sea even before the DGLAP evolution of the initial gluon distribution.

We can see in Fig. 2.13 that the sea-like model predicts the existence of some intrinsic-charm in the x_{Bj} range of the COMPASS data. However, this assumption (without any theory basis) was not yet proven and therefore it is neglected in the present analysis. In addition to that, the mass of the charm quark, $m_c \approx 1.5$ GeV/c^2, is much higher than the mass of the u, d and s quarks. Therefore, the charm content of the nucleon can be safely neglected in COMPASS. The creation of charm quarks during the fragmentation of the nucleon caused by non-PGF processes is also highly suppressed (in the kinematic domain of COMPASS).

Extraction of ΔG/G in a LO-QCD approximation

As explained in section 2.1.3, it is much more convenient to extract asymmetries from experiments than to measure cross-section differences. Therefore a measurement of $\Delta G/G$, instead of ΔG, is obtained. This can be accomplished by a measurement of the experimental spin asymmetry for the open-charm production [9]. This asymmetry is defined by

$$A^{\text{exp}} = \frac{N_{c\bar{c}}^{\rightleftarrows} - N_{c\bar{c}}^{\leftleftarrows}}{N_{c\bar{c}}^{\rightleftarrows} + N_{c\bar{c}}^{\leftleftarrows}} \tag{2.83}$$

where $N_{c\bar{c}}$ represents the number of reconstructed charmed mesons coming from a polarised muon-nucleon interaction. In COMPASS, these mesons are produced with a parallel ($N_{c\bar{c}}^{\rightleftarrows}$) and

[9] Recall that an open-charm meson is a clean tag for a PGF process (c.f. Fig. 2.11).

anti-parallel ($N^{\Leftrightarrow}_{c\bar{c}}$) orientation of the beam and target spins. The relation between $A^{\rm exp}$ and the physical asymmetry, $A^{\mu N}_{c\bar{c}}$, is given by the following equation (using the definitions of $N_{c\bar{c}}$ presented in Chapter 6, with $\hat{A}_{bg} = 0$):

$$A^{\rm exp} = (f P_\mu P_t) \times A^{\mu N}_{c\bar{c}} \tag{2.84}$$

We can see that the physical asymmetry is diluted by three experimental factors: the fraction of polarisable material inside the target, f (also called the dilution factor), the beam polarisation P_μ and the target polarisation P_t. These quantities are experimentally measurable and will be further discussed in Chapter 3. In COMPASS, the selection of open-charm mesons is done via reconstruction of the invariant mass obtained from their decay products (namely, kaons and pions). Therefore, in the mass spectrum also exists some combinatorial background underlying the reconstructed resonance (D^0 mesons). If we take into account a possible contribution from the background asymmetry, $\hat{A}_{bg}$, eq. 2.84 is rewritten as

$$A^{\rm exp} = f P_\mu P_t \left(\frac{S}{S+B}\right) A^{\mu N}_{c\bar{c}} + f P_\mu P_t \left(\frac{B}{S+B}\right) \hat{A}_{bg} \tag{2.85}$$

where S and B represent the differential unpolarised cross-sections of the signal and background events folded with the experimental resolution. The quantity $S/(S+B)$ can be interpreted as a PGF probability, i.e. the probability that a given event is indeed an open-charm meson (cf. Chapter 7). Consequently, we have $B/(S+B) = [1 - S/(S+B)]$. At LO-QCD, the muon-nucleon asymmetry is given by

$$\begin{aligned}
A^{\mu N}_{c\bar{c}} &= D \times A^{\gamma^* N}_{c\bar{c}} = D \times \left(\frac{\Delta\sigma_{\gamma^* N \to c\bar{c}}}{\sigma_{\gamma^* N \to c\bar{c}}}\right) \\
&= D \times \frac{\int \Delta\hat{\sigma}_{\gamma^* g \to c\bar{c}}(\hat{s}) \Delta G(x_g, \hat{s})\ d\hat{s}}{\int \hat{\sigma}_{\gamma^* g \to c\bar{c}}(\hat{s}) G(x_g, \hat{s})\ d\hat{s}} \\
&= D \times \frac{\int \frac{\Delta\hat{\sigma}_{\gamma^* g}(\hat{s})}{\hat{\sigma}_{\gamma^* g}(\hat{s})} \frac{\Delta G(x_g,\hat{s})}{G(x_g,\hat{s})} \hat{\sigma}_{\gamma^* g}(\hat{s}) G(x_g, \hat{s})\ d\hat{s}}{\int \hat{\sigma}_{\gamma^* g}(\hat{s}) G(x_g, \hat{s})\ d\hat{s}} \\
&\approx D \times \langle \hat{a}^{\gamma^* g}_{LL} \rangle \frac{\Delta G}{G}(\langle x_g \rangle) \qquad \text{with} \qquad \hat{a}^{\gamma^* g}_{LL} = \left(\frac{\Delta\hat{\sigma}_{\gamma^* g \to c\bar{c}}}{\hat{\sigma}_{\gamma^* g \to c\bar{c}}}\right)
\end{aligned} \tag{2.86}$$

where D is the depolarisation factor defined in eq. 2.35 (with R = 0), and $\hat{s}$ is the centre-of-mass energy at the partonic level. The equality in the second line is ensured by the factorisation theorem which allows for the separation of the hard part of the process, i.e. the interaction $\gamma^* g \to c\bar{c}$, from the gluon structure function. The partonic asymmetry, $\hat{a}^{\gamma^* g}_{LL}$, is calculated at LO from the diagrams shown in Fig. 2.14. The final expression is given by [48]

$$\hat{a}^{\gamma^* g}_{LL} = \frac{\Delta\hat{\sigma}_0 + (\cos\hat{\phi})\ \Delta\hat{\sigma}_1}{\hat{\sigma}_0 + (\cos\hat{\phi})\ \hat{\sigma}_1 + (\cos 2\hat{\phi})\ \hat{\sigma}_2} \tag{2.87}$$

where

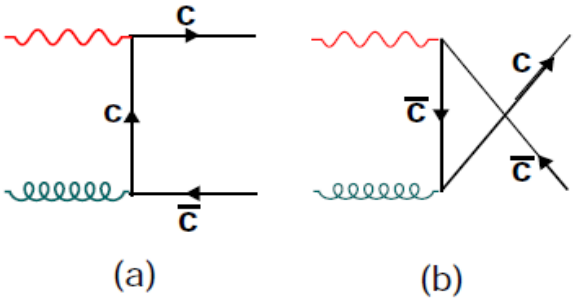

Figure 2.14: Feynman diagrams for the PGF process at LO-QCD.

$$\begin{aligned}\hat{\sigma}_0 &= \frac{\alpha_s\left(1-y\right)}{4\pi}\left(8\left(1-x_p\right)x_p-\frac{2\beta x_p}{\left(1-z_q\right)z_q}\right)+\frac{\alpha_s}{8\pi}\left(\left(1-y\right)^2+1-\frac{2m_\mu^2y^2}{Q^2}\right)\\ &\times\left[\frac{\left(x_p^2+\left(1-x_p\right)^2\right)\left(z_q^2+\left(1-z_q\right)^2\right)+\beta\left(1-2x_p\right)}{\left(1-z_q\right)z_q}+\frac{\beta\left(2x_p-\beta\right)}{4\left(1-z_q\right)^2z_q^2}\right]\end{aligned} \tag{2.88}$$

$$\begin{aligned}\hat{\sigma}_1 &= \frac{\alpha_s}{2\pi}\left(2-y\right)\sqrt{1-y-\frac{m_\mu^2y^2}{Q^2}}\left(1-2x_p-\frac{\beta}{2\left(1-z_q\right)z_q}\right)\left(1-2z_q\right)\\ &\times\sqrt{\frac{\left(1-x_p\right)x_p}{\left(1-z_q\right)z_q}-\frac{\beta x_p}{4\left(1-z_q\right)^2z_q^2}}\end{aligned} \tag{2.89}$$

$$\hat{\sigma}_2 = \frac{\alpha_s}{\pi}\left(1-y-\frac{m_\mu^2y^2}{Q^2}\right)\left(\left(1-x_p\right)x_p+\frac{\left(1-2x_p\right)\beta}{4\left(1-z_q\right)z_q}-\frac{-\beta^2}{16\left(1-z_q\right)^2z_2^2}\right) \tag{2.90}$$

$$\Delta\hat{\sigma}_0 = \frac{\frac{\alpha_s y}{2\pi}\left(2-y-\frac{2m_\mu^2y}{Q^2\left(1-x_{Bj}y\right)}\right)\left(\frac{\beta}{2(1-z_q)^2z_q^2}+\frac{2x_p-1}{(1-z_q)z_q}\right)\left((1-z_q)^2+z_q^2\right)}{\sqrt{1-\frac{4m_\mu^2\left(1-x_{Bj}\right)x_{Bj}y^2}{Q^2\left(1-x_{Bj}y\right)^2}}} \tag{2.91}$$

$$\Delta\hat{\sigma}_1 = \frac{\frac{\alpha_s y}{2\pi}\sqrt{1-y-\frac{m_\mu^2y}{Q^2}}\left(1-2z_q\right)\sqrt{\frac{x_p(1-x_p)}{z_q(1-z_q)}-\frac{\beta}{4z_q^2(1-z_q)^2}}}{\sqrt{1-\frac{4m_\mu^2\left(1-x_{Bj}\right)x_{Bj}y^2}{Q^2\left(1-x_{Bj}y\right)^2}}} \tag{2.92}$$

and

$$\beta=\frac{4x_pm_c^2}{Q^2},\qquad x_p=\frac{x_{Bj}}{\xi},\qquad z_q=\frac{p\cdot p_q}{p\cdot q},\qquad \hat{\phi}=\frac{\left(\vec{p}\times\vec{k}\right)\cdot\left(\vec{p}\times\vec{p}_q\right)}{\left|\left(\vec{p}\times\vec{k}\right)\right|\cdot\left|\left(\vec{p}\times\vec{p}_q\right)\right|} \tag{2.93}$$

In eq. 2.93 ξ is the momentum fraction of the incoming parton, m_c is the mass of the charm

quark, and p_q is the four-momentum of the final quark. Therefore, the use of eq. 2.86 in eq. 2.85 allows us to extract the gluon polarisation inside the nucleon, i.e. $\Delta G/G$. To accomplish that, the experimental asymmetry for the open-charm production is measured and, in addition, the following factor needs to be determined for every event (considering $\hat{A}_{bg} = 0$ for illustration):

$$f P_\mu P_t \left(\frac{S}{S+B} \right) \underbrace{D a_{LL}^{\gamma^* g}}_{a_{LL}^{\mu g}} \tag{2.94}$$

In Fig. 2.15 one can see a big dispersion of values for the partonic asymmetry, $a_{LL}^{\mu g} = \langle \hat{a}_{LL}^{\mu g} \rangle$, obtained as a function of the centre-of-mass energy of the muon-gluon collision. Moreover, the fact that $a_{LL}^{\mu g}$ changes sign is a strong motivation for using this quantity as an event weight. Therefore, a weighted analysis was developed in order to minimise the statistical error of the $\Delta G/G$ extraction (cf. chapter 6). In addition to that, the reconstruction of the open-charm mesons shows a clear anti-correlation between the PGF purity, $S/(S+B)$ (obtained from the D^0 mass spectra), and the asymmetry $a_{LL}^{\mu g}$: more combinatorial background events are reconstructed for high $a_{LL}^{\mu g}$ values, and vice-versa. Since these two factors are simultaneously used inside the event weight, a proper multi-dimensional kinematic parameterisation is needed, for each of them, in order to avoid any bias in the analysis.

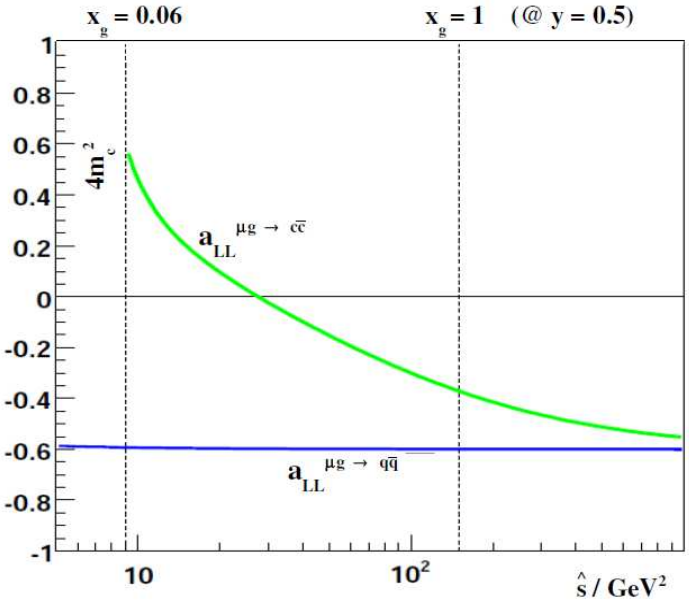

Figure 2.15: Partonic asymmetry $a_{LL}^{\mu g}$ as a function of the photon-gluon centre-of-mass energy, $\hat{s}$, for fixed values of $y = 0.5$, $Q^2 = 0.01$ (GeV/c)^2 and integrated over the polar angle [49].

The goal of this method is to extract the gluon polarisation in the most model independent way, and with the best possible precision. To accomplish that, the requirements are:

1. The reconstruction of open-charm mesons $\Rightarrow$ clean signature of a PGF process.
2. The use of a weighted method for the simultaneous extraction of $\Delta G/G$ and A_{bg} $\Rightarrow$ best possible precision in the determination of $\Delta G/G$.
3. Multi-dimensional kinematic parameterisations for $a_{LL}^{\mu g}$ and also for $S/(S+B)$. The latter reduces to a minimum the contamination of the PGF sample by the combinatorial

background (enhancing $S/(S+B)$ for the real PGF events) and, simultaneously, it ensures the experimental anti-correlation between $S/(S+B)$ and a_{LL}.

The previous three topics form the core of the present work and, therefore, they will be extensively discussed in the chapters 5, 6, and 7. Finally, $\Delta G/G$ can be translated to ΔG through the use of the unpolarised gluon structure function. Just for indicative purposes I show an example of the xG distribution in Fig. 2.16:

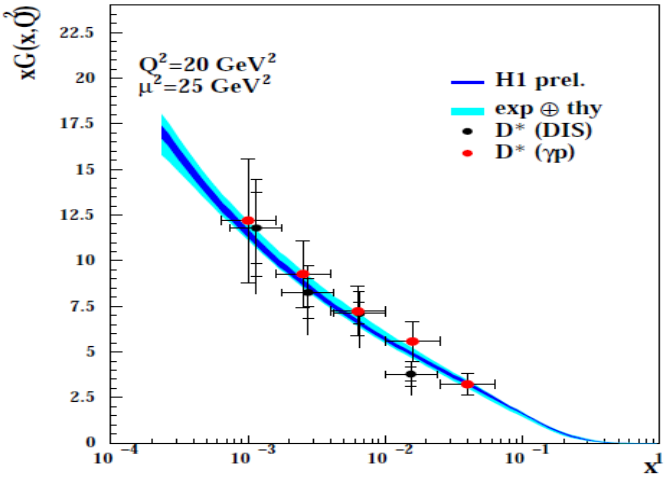

Figure 2.16: Comparison of the gluon momentum distribution (determined from a QCD fit to the NMC and H1 data) with the measurements of $xG(x, Q^2)$ obtained from an open-charm analysis [50]. For the DIS study a $Q^2 > 2$ (GeV/c)^2 was used whereas for the photo-production limit a $Q^2 < 0.01$ (GeV/c)^2 was considered.

For a proper comparison with the experimental results, the QCD fits of $\Delta G/G$ are also determined by COMPASS (using the same Q^2 as the scale of the measurements):

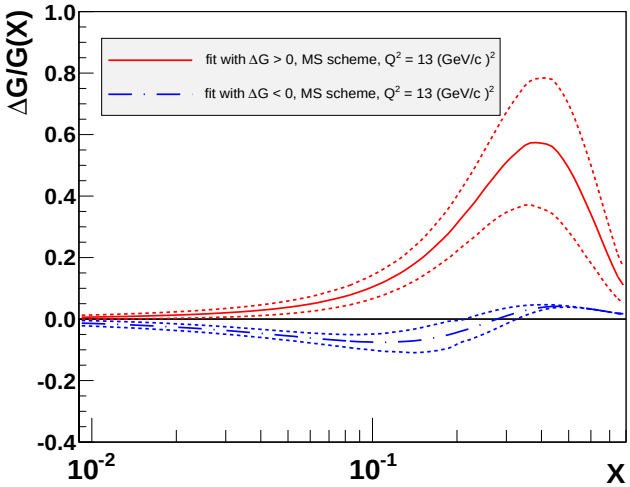

Figure 2.17: Distributions of ΔG/G at $Q^2 = 13$ (GeV/c)^2 obtained from the COMPASS NLO-QCD analysis [31, 51]. The error bands correspond to the statistical errors estimated from the error matrix on the fitted parameters. The variable x denotes the fraction of the nucleon momentum carried by a gluon.

In Ref. [52] it is shown that the NLO corrections to the PGF process may be important for the production of heavy flavours. We can see in Fig. 2.18 the comparison of the unpolarised and polarised cross-sections, obtained in a LO-QCD and NLO-QCD approximations. The shapes of the LO and NLO distributions are significantly different and, in some cases, the asymmetry $a_{LL}^{\gamma^* g}$ changes by almost a factor of two (for example, in $\eta \approx 0.4 \rightarrow$ right figure). Therefore, and for the first time, the extraction of $\Delta G/G$ is also performed at NLO. The obtained results are presented in this thesis.

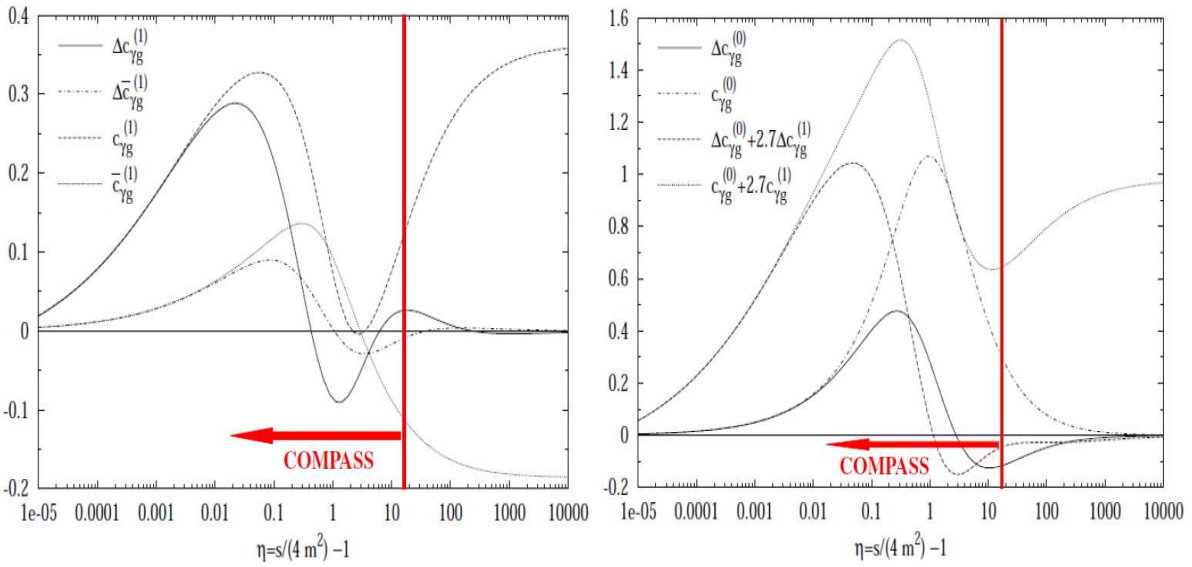

Figure 2.18: Left: distributions of the NLO cross-sections for the charm production as a result of a polarised $\left(\Delta c_{\gamma g}^{(1)}\right)$ or unpolarised $\left(c_{\gamma g}^{(1)}\right)$ photon-gluon interaction. Similar distributions are also shown for the anti-charm production. Right: comparison of the LO cross-sections, $\Delta c_{\gamma g}^{(0)}$ and $c_{\gamma g}^{(0)}$, with the ones accounting also for the NLO corrections, $\Delta c_{\gamma g}^{(0)} + 2.7\Delta c_{\gamma g}^{(1)}$ and $c_{\gamma g}^{(0)} + 2.7 c_{\gamma g}^{(1)}$. Note that $s \equiv \hat{s}$ and $a_{LL}^{\gamma^* g}(\text{NLO}) = \left(\frac{\Delta c_{\gamma g}^0 + 2.7\Delta c_{\gamma g}^1}{c_{\gamma g}^0 + 2.7 c_{\gamma g}^1}\right)$.

The main disadvantage of a NLO analysis is the existence of physical background contributing to the $c\bar{c}$ production. The Feynman diagrams responsible for these non-PGF processes are:

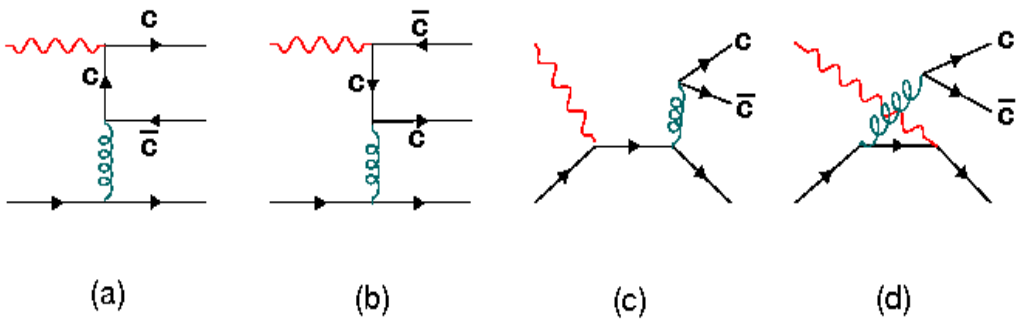

Figure 2.19: Charm production via a polarised $\gamma^* q$ interaction.

We can see in Fig. 2.19 that, at NLO, the production of an open-charm meson is not an exclusive characteristic of a PGF process. For example, in the diagram (c) the virtual-photon interacts with a light-quark in the nucleon which posteriorly creates a $c\bar{c}$ pair after the radiation of a gluon. These processes do not probe directly a gluon and, therefore, they contribute as a physical background to the measurement of the gluon polarisation. In addition to them, we have also to account for the NLO corrections to the PGF process:

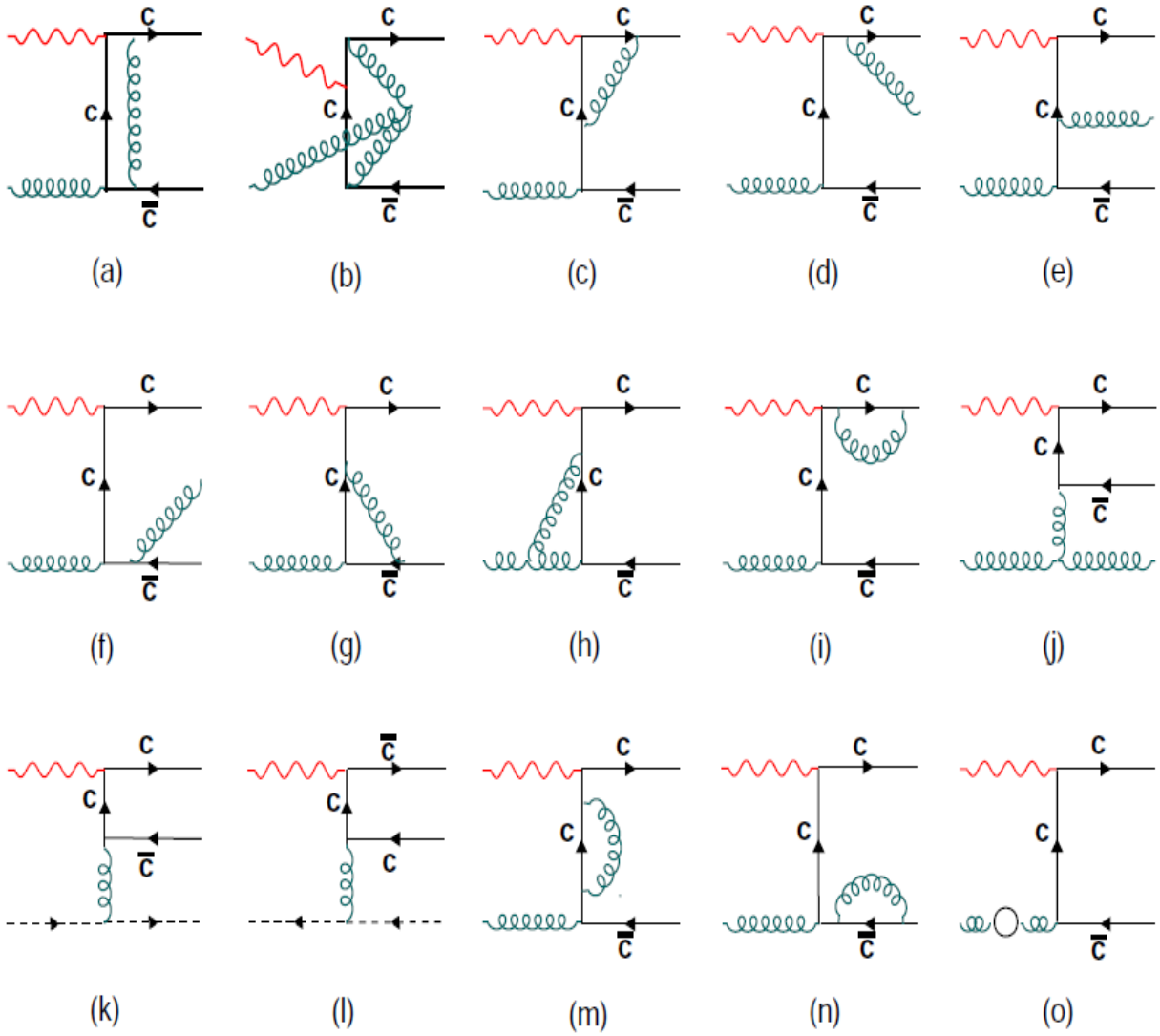

Figure 2.20: The diagrams (a), (b), (c), (g), (h), (i), (m), (n) and (o) show the NLO virtual corrections to PGF via the $\gamma^* g \rightarrow c\bar{c}$ process. The diagrams (d), (e), (f), (j), (k) and (l) represent the NLO gluon bremsstrahlung corrections that are accounted in the $\gamma^* g \rightarrow c\bar{c}g$ process [(k) and (l) are ghost diagrams]. With exception of (b), reversing the heavy quark lines yields the remaining NLO diagrams.

Therefore, in order to be able to extract $\Delta G/G$ at NLO from the open-charm asymmetries, we just need to modify the LO interpretation of $A_{c\bar{c}}^{\mu N}$ to account for the contributions shown in Fig. 2.19 and in Fig. 2.20:

$$A_{c\bar{c}}^{\mu N}(\text{NLO}) = D\left[a_{LL}^{\gamma^* g}\,\frac{\Delta G}{G} \;+\; a_{LL}^{\gamma^* q}\,A_1\right] \tag{2.95}$$

where

$$a_{LL}^{\gamma^* g} = \left(\frac{\Delta\hat{\sigma}_{\gamma^* g \to c\bar{c}}(\mathrm{LO}) + \Delta\hat{\sigma}_{\gamma^* g \to c\bar{c}}(\mathrm{NLO}) + \Delta\hat{\sigma}_{\gamma^* g \to c\bar{c}g}(\mathrm{NLO})}{\hat{\sigma}_{\gamma^* g \to c\bar{c}}(\mathrm{LO}) + \hat{\sigma}_{\gamma^* g \to c\bar{c}}(\mathrm{NLO}) + \hat{\sigma}_{\gamma^* g \to c\bar{c}g}(\mathrm{NLO})} \right) \tag{2.96}$$

$$a_{LL}^{\gamma^* q} = \left(\frac{\Delta\hat{\sigma}_{\gamma^* q \to c\bar{c}}}{\hat{\sigma}_{\gamma^* q \to c\bar{c}}} \right) \tag{2.97}$$

$$A_1 \approx \frac{g_1}{F_1} = \left(\frac{\sum_q e_q^2 \Delta q}{\sum_q e_q^2 q} \right) \tag{2.98}$$

All the diagrams shown in Fig. 2.14, in Fig. 2.19 and in Fig. 2.20 are considered in eq. 2.95. However, the results of the NLO calculations are extremely long and cumbersome to be presented here. They are partly available in [52, 53, 54, 55, 56] and also upon request [57]. The general formula shown in eq. 2.85 is still valid in the NLO-QCD approximation. The only difference, besides $A_{c\bar{c}}^{\mu N}$, is that the signal S also contains open-charm mesons originating from non-PGF processes ($S = S^g + S^q$). The proper way to correct these contaminations, for the simultaneous extraction of $\Delta G/G$ and A_{bg} ($\hat{A}_{bg} = DA_{bg}$), will be discussed in the Chapters 6 and 8.

Range of Q^2 for the open-charm analysis

In polarised DIS, we can interpret the muon beam as a source of photons. This leads to the following factorisation of the muon-nucleon cross-section:

$$\frac{d^2\sigma_{\mu N \to c\bar{c}X}}{dQ^2 d\nu} = \Gamma\left(E, Q^2, \nu\right) \sigma_{\gamma^* N \to c\bar{c}X}\left(Q^2, \nu\right) \tag{2.99}$$

where we have for the virtual-photon flux

$$\Gamma\left(E, Q^2, \nu\right) = \frac{\alpha}{2\pi} \left(\frac{2\left(1-y\right) + y^2 + \frac{Q^2}{2E^2}}{Q^2\sqrt{Q^2+\nu^2}} \right) \tag{2.100}$$

It can be seen from eq. 2.100 that the flux is higher for quasi-real photons; i.e. for $Q^2 \to 0$. Therefore, the COMPASS spectrometer was optimised to make use of the low Q^2 region. Possible contributions from resolved photons (in $Q^2 < 1$) to the open-charm production were verified to be unimportant in the COMPASS kinematic domain. Thus, they are neglected in this analysis. The perturbative treatment of the $\gamma^* g$ cross-section is ensured by the square of the transverse mass associated to the charm quarks, $\mu^2 = (2m_c^T)^2 = 4(m_c^2 + p_T^2) = 13$ GeV/c^2 (scale of the open-charm measurement).

2.6 Strong probes for the extraction of ΔG/G

The polarised gluon structure inside the nucleon can also be probed through the use of the following reactions:

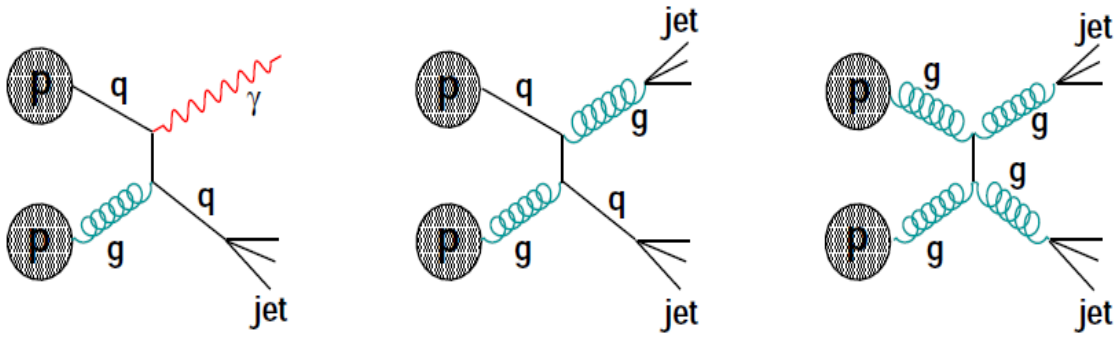

Figure 2.21: Schematic view of the prompt photon production ($qg \rightarrow \gamma q$) and of the jet production ($qg \rightarrow gq$ and $gg \rightarrow gg$).

The above processes are studied by the STAR and PHENIX experiments using the polarised proton-proton collisions at RHIC [10]. The main advantage of using strong probes is the existence of a significantly higher production of gluon interactions as compared to the lepton-nucleon processes. However, the main drawback of this analysis is the existence of reactions that contribute as physical background (eg., $q\bar{q} \rightarrow \gamma g$ in the prompt photon production). The double spin asymmetry that results from proton-proton collisions is given by (for a specific reaction i):

$$A_i^{pp} = \hat{a}_{LLi} \left(\frac{\Delta F_{i1}}{F_{i1}} \cdot \frac{\Delta F_{i2}}{F_{i2}} \right) \tag{2.101}$$

where $\Delta F_{i(1,2)}$ and $F_{i(1,2)}$ are the polarised and unpolarised distributions of partons taking part in the interaction, and $\hat{a}_{LLi}$ is the partonic asymmetry corresponding to the reaction considered. We can see from eq. 2.101 that one of the big disadvantages of using strong probes is that we have to consider an additional parton density in the initial state of the interaction, i.e. the desired measurement is sensitive only to a convolution of the gluon density and another parton density (which may be another gluon). In addition to that, the experimental asymmetry A^{exp} is a sum of all the A_i that lead to a given final hadronic state (weighted with their respective fractions and multiplied by the diluting factors). Consequently, the extraction of $\Delta G/G$ from this sum is a complex and difficult task. Therefore, instead of extracting $\Delta G/G$ directly from the data, another method is used. Different distributions of ΔG are assumed, and then the A^{exp} corresponding to a given final state is calculated. Finally, the results obtained are compared with the measured asymmetries. Thereafter, the scenarios of ΔG that do not agree with the measurements are discarded. The measurements done at RHIC cover a wide range of x_g, $0.01 < x_g < 0.3$, and they predict a small value of the gluon polarisation which is compatible with zero [58, 59] ($A^{\text{exp}} = A_{LL} = A_{\parallel}$ in the References.).

[10] **R**elativistic **H**eavy **I**on **C**ollider which is located at the Brookhaven National Laboratory (BNL) in USA.

Chapter 3

The COMPASS Experiment

The COMPASS collaboration, NA58, is formed by nearly 240 physicists from 11 countries (Europe, Russia, Japan and India) and 28 institutions. It is the successor of a long chain of muon scattering experiments at CERN, namely EMC (NA28), NMC (NA37) and SMC (NA47). COMPASS is an acronym for **CO**mmon **M**uon and **P**roton **A**pparatus for **S**tructure and **S**pectroscopy and, as the name implies, it is the result of merging two experimental proposals (HMC and CHEOPS) with different physics programs. The first one is dedicated to the study of the nucleon spin and the other is mainly focused on the hadron spectroscopy. In the former a polarised muon beam and a polarised target are used whereas the latter is based on different nuclear targets and hadron beams. The experiment was approved in 1998 and the first physics data was recorded in the year of 2002. Since then until now, 2011, COMPASS is taking data with exception of the year of 2005 during which the SPS accelerator was shutdown at CERN. The analysis presented in this thesis concerns the data collected in 2002-2007 using a naturally polarised muon beam. During these years, a longitudinally/transversely polarised deuteron (2002-2006) and proton (2007) targets were used. Only the longitudinally polarised targets are considered in the open-charm analysis, which corresponds to approximately 70% of the data recorded in those years. The data for the hadron spectroscopy program was collected in 2008 and 2009.

In this experimental chapter only the relevant topics for the open-charm analysis will be addressed: the polarised beam, the polarised target and the most important parts of the COMPASS spectrometer. In the latter mainly the **R**ing **I**maging **C**herenkov detector (RICH) will be discussed. The detailed information about the COMPASS spectrometer can be found in Ref. [60].

3.1 The Beam

The COMPASS spectrometer is located in the CERN North Area, at the end of the M2 beam-line of the **S**uper **P**roton **S**ynchrotron (SPS) accelerator. This beam-line can be tuned to deliver a muon or a hadron beam and, therefore, it is ideally suited for the two physics programmes of COMPASS. A scheme representing the production of a polarised muon beam is presented in Fig. 3.1. The first step is the acceleration of protons in the SPS to an energy of 400 GeV. Thereafter they are extracted into the M2 beam-line, during 4.8 s in a cycle of 16.8 s (spill structure of the beam), and then their collision with a thick beryllium target (T6) is imposed.

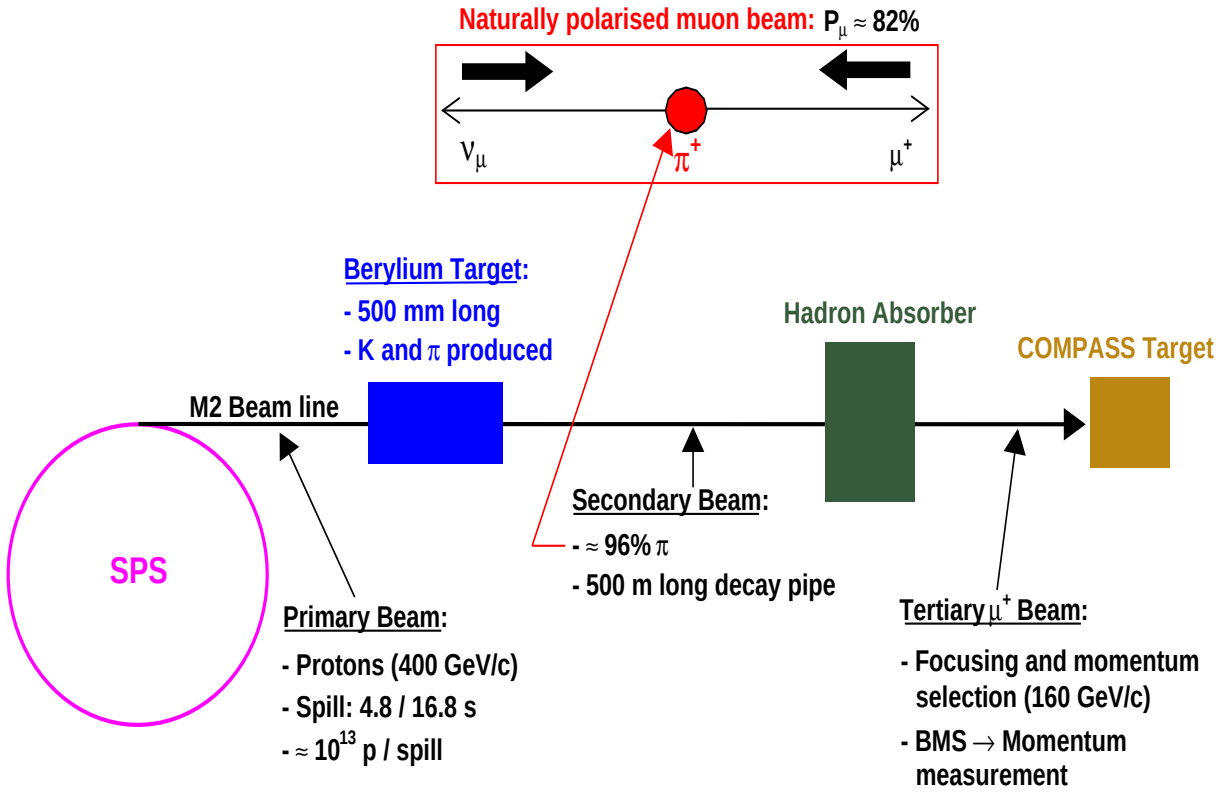

Figure 3.1: Sketch of the production of a polarised muon beam for COMPASS. The resulting leptons, μ^+, are the probes used to scan the gluon polarisation.

As a result, a secondary beam of kaons and (mainly) pions is produced: K^+, K^-, π^+ and π^-. The positive particles of the beam are then selected by bending magnets and directed into a decay pipe of 500 meters long. Basically only π^+ mesons enter into the tunnel, and then most of them decay into $\mu^+\nu_\mu$ pairs while travelling through this 500 m section of the M2 line. Therefore in the rest frame of π^+ the resulting μ^+ are 100% polarised, with negative helicity, due to the presence of a left-handed neutrino in the final state (owing to the angular momentum conservation). The thickness of the solid beryllium target can also be adjusted in order to provide a specific intensity for the muon beam. For a nominal intensity of 2.8×10^8 μ^+/spill, a target length of 500 mm is needed for T6. Finally, at the end of the tunnel is placed a heavy hadron absorber to remove the remaining hadrons from the beam. The polarised muons pass through this absorber with a minimum loss of their initial energy. Thereafter, they enter into a new section of 400 meters long, where particles of a given energy are selected and focused using a set of magnets. The out-coming muons are then delivered directly to the COMPASS experimental hall, where they will collide on a fixed polarised target (cf. Fig. 3.3 and Fig. 3.5). The contamination of the beam by hadrons is less than 10^{-6}.

Due to the Lorentz boost, the muon beam is no longer 100% polarised in the laboratory frame. Instead, the magnitude of its polarisation is given as a function of the muon energy and also as a function of the energy of its parent particle:

$$P_\mu = -\frac{m^2_{\pi,K} + \left(1 - \frac{2E_{\pi,K}}{E_\mu}\right) m^2_\mu}{m^2_{\pi,K} - m^2_\mu} \tag{3.1}$$

Therefore, the selection of the momentum for π^+/K^+ (and also for μ^+) allows us to adjust the polarisation of the muon beam. However, the momentum selection for the latter is also constrained by three important parameters that must be taken into account: the experimental acceptance of events (which varies with the muon energy), the beam intensity and most important the cross-section for the PGF process. Dedicated Monte Carlo studies have shown that the optimal momentum for μ^+ is 160 GeV/c [61]. Thereafter, a parameterisation of the beam polarisation as a function of the muon momentum was obtained from a Monte Carlo simulation of the M2 beam-line. This line was also used by the SMC experiment, which measured the polarisation of the muon beam with a good precision [62, 63]. It was found that the results of these measurements agree very well with the ones obtained from the Monte Carlo parameterisations (cf. Fig. 3.2) and, therefore, it was decided to use the latter to determine the polarisation of the muon beam at COMPASS. For the data collected in 2002 and 2003, an average muon polarisation of $\langle P_\mu \rangle = -0.76$ is obtained. To accomplish that, the momentum of π^+/K^+ is selected to be $p_{\pi^+,K^+} = 177$ GeV/c. For the years of 2004, 2006 and 2007 the momentum of the secondary beam is changed to $p_{\pi^+,K^+} = 172$ GeV/c, resulting in a larger polarisation of $\langle P_\mu \rangle = -0.82$.

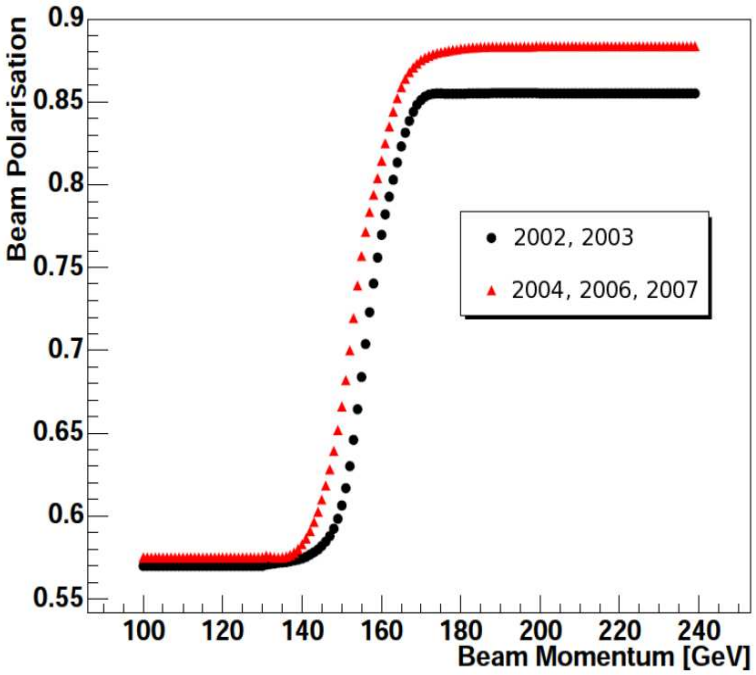

Figure 3.2: Monte Carlo parameterisation of the muon beam polarisation as a function of the beam momentum (p_{μ^+}). In 2002 and 2003, a momentum of $p_{\pi^+,K^+} = 177$ GeV/c is selected for the secondary beam (circles). For the years of 2004, 2006 and 2007 it was decided to use $p_{\pi^+,K^+} = 172$ GeV/c in order to increase the polarisation of the muon beam (triangles).

We can see in Fig. 3.2 that P_μ is obtained for every μ^+ event, provided that its momentum is known. The momenta of these particles are measured up to an accuracy of 0.5% by the **B**eam **M**omentum **S**tation, BMS, which is located 100 meters upstream of the COMPASS target.

The muon polarisation, P_μ, is one of the important factors used in the open-charm analysis. It enters as a dilution factor in eq. 2.85, and because of that it will also be used as an event weight for the extraction of $\Delta G/G$ (see Chapter 6).

3.2 The Polarised Target

The COMPASS target used in 2002, 2003 and 2004 consists on two solid state cells, each 60 cm long and 3 cm in diameter, separated by a gap of 10 cm. For the study of the gluon polarisation, the cells are longitudinally polarised in opposite directions (in order to allow for the extraction of the spin asymmetries). The experimental acceptance for the resulting events is limited to an angular range of ±70 mrad. However, in the years of 2006 and 2007 the target setup was upgraded to a 3-cell system with an angular acceptance of ±180 mrad. These two improvements represent the only differences compared to the setup used until 2004. In 2006 and 2007 the upstream and downstream cells are 30 cm long, and are both 5 cm away from a central cell of 60 cm long (their diameter is 4 cm). The former cells are longitudinally polarised in the opposite direction of the middle cell, cf. Fig. 3.3:

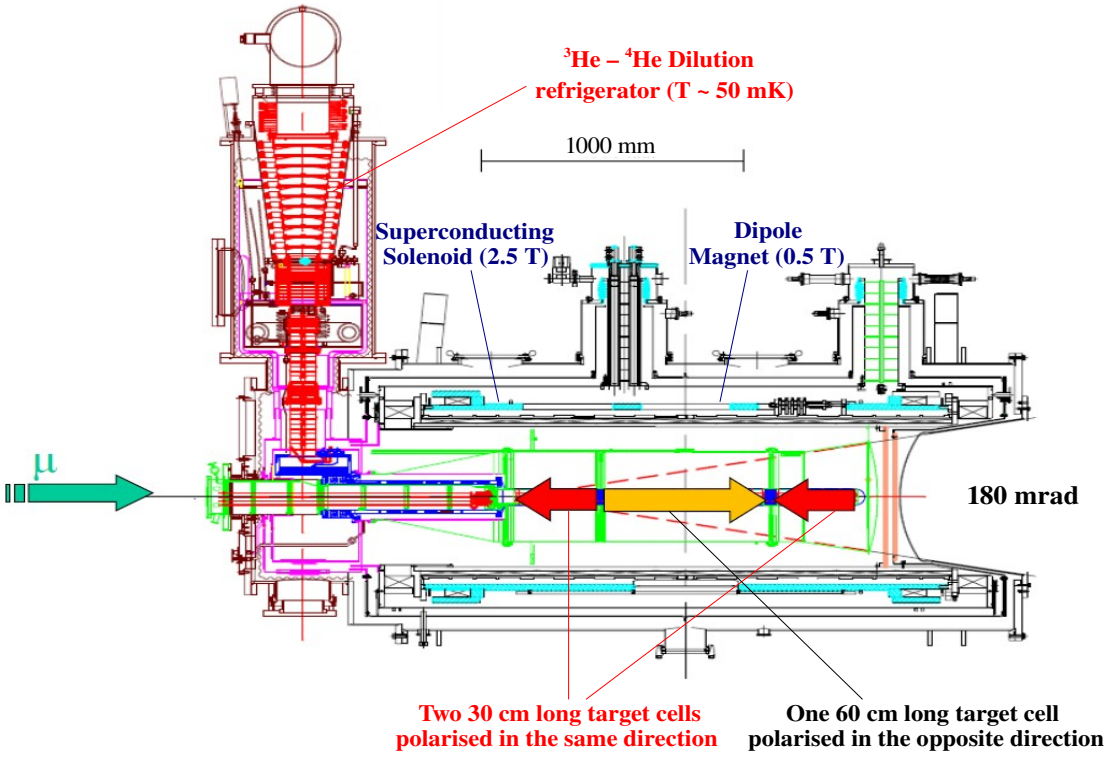

Figure 3.3: Setup of the COMPASS target as it was used during the years of 2006 and 2007. The arrows indicate the orientation of the beam and target spins. The spins of the latter may be reversed by the dipole magnet without any loss of polarisation. The experimental acceptance of events is limited by the radius of the surrounding solenoid and has a value of ±180 mrad.

Solid state targets are used, for all years of data taking, in order to achieve the high luminosity required for the physics programme of COMPASS. The target material used to study

the spin structure of deuterons and protons is ^{6}LiD (2002-2006) and NH_3 (2007), respectively. The target cells are surrounded by a powerful superconducting solenoid which is used for their polarisation. Therefore, the solenoid defines the aperture through which the resulting events are accepted for detection. During the years of 2002-2004, the old solenoid of SMC (with an aperture of ± 70 mrad) was used in the setup of the COMPASS target.

DNP - The Dynamic Nuclear Polarisation method

The first requirement for the study of the nucleon spin is to have a proton (or deuteron) target with a very high level of polarisation [1]. This can be achieved by the superconducting solenoid which provides a homogeneous longitudinal magnetic field of 2.5 T. However, even with such a field-strength and with a temperature of 1 K the polarisation that one can reach for these nuclei is less than 1%. Under the same conditions the electrons can be polarised up to 96%. This big difference is explained by a much higher magnetic moment of electrons in comparison with the atomic nuclei. Therefore, a technique based on the **D**ynamic **N**uclear **P**olarisation method [64] is used to polarise the target. Basically the trick consists in the transfer of the large electron polarisation to the nuclei. This method takes into account the fact that the electrons interact with the nucleus, in the atomic system, through the electromagnetic field. In other words, they need to be treated as a complex quantum system and cannot be considered separately. Let us consider, for illustration, an atomic system composed by one proton and one electron. Therefore, for a given electron spin projection we have two possible states for the proton spin (cf. Fig 3.4):

1. $|A\rangle = \left(+\frac{1}{2}, +\frac{1}{2}\right) \quad \& \quad |C\rangle = \left(-\frac{1}{2}, +\frac{1}{2}\right)$
2. $|B\rangle = \left(+\frac{1}{2}, -\frac{1}{2}\right) \quad \& \quad |D\rangle = \left(-\frac{1}{2}, -\frac{1}{2}\right)$

where in 1. (2.) the electron spin is oriented parallel (anti-parallel) to the magnetic field. Inside the strong solenoid field, the atomic system is divided among the two quantum states defined by $|B\rangle$ and $|D\rangle$. Then, after polarising the electrons with the solenoid field, the target cells are irradiated with a microwave radiation. The frequency of the radiation is tuned to the exact value that allows for a simultaneous flip of the electron and proton spins. We can verify in Fig. 3.4 that the selection of the proper frequency $\omega_e + \omega_p$ allows for a complete polarisation of the proton spin in the direction anti-parallel to the magnetic field. This frequency has no impact in those atomic systems where the proton spin is already anti-parallel to the solenoid field ($|D\rangle$), i.e. both spins of the system remain unchanged. However, for those atoms that are in the state $|B\rangle$ the electron and the proton spins are reversed by 180^o degrees. Soon after this spin flip the electrons relaxate to a lower energy state, defined by $|D\rangle$, while the protons maintain their spin orientation. The latter is justified by the long relaxation time of protons (low magnetic moment). Therefore after this procedure almost all nuclei will be polarised in the same direction, which is anti-parallel to the magnetic field ($|D\rangle$). Analogously, if we want to polarise the target parallel to the solenoid field, we just need to irradiate the cells with a frequency of $\omega_e - \omega_p$. During the polarisation of electrons, the ^{3}He-^{4}He dilution refrigerator provides a temperature of about 0.4 K (c.f Fig. 3.3). In this way the magnitude of the polarisation that one can achieve is maximised, because the thermal motion of the system is reduced to a minimum. Then, after polarising the nuclei with the microwave radiation, the

[1] Information about the neutron spin can be obtained from the combined results on the proton and deuteron targets.

spin configuration is frozen by cooling the target material to 50 mK. Thereafter we can benefit from a long relaxation time which exceeds 1000 hours.

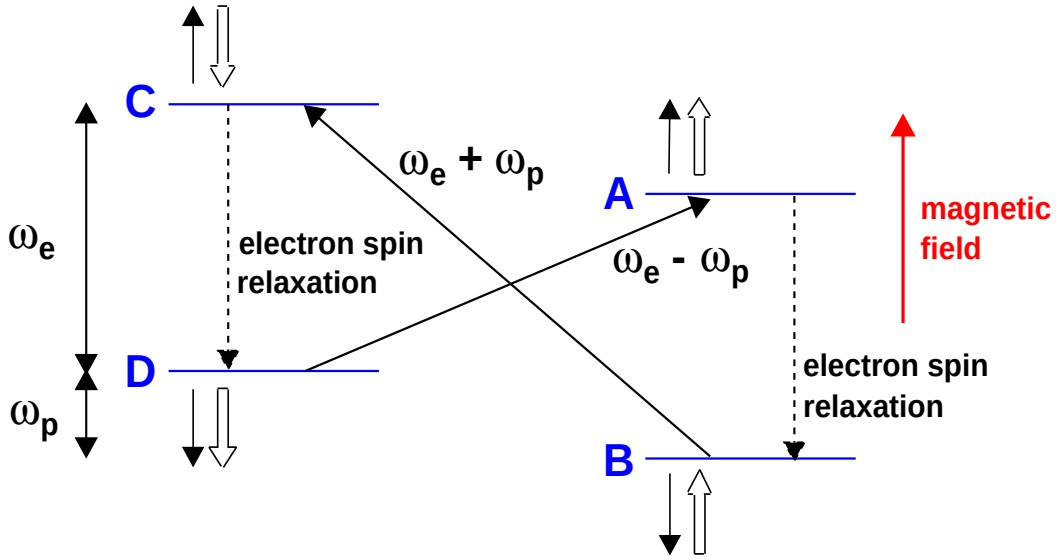

Figure 3.4: Diagram representing the four energy levels defined by the spin projections of an electron-nucleon pair. Transitions between the levels are possible using the following microwave frequencies: $\omega_e + \omega_p$ and $\omega_e - \omega_p$. Arrows $\Uparrow$ and $\uparrow$ represent the nucleus and electron spin projections.

There is a separate microwave system for each of the target cells: one for the middle cell and another one for the upstream plus downstream cells[2]. In this way we can polarise the cells in opposite directions by providing the two microwave frequencies shown in Fig. 3.4. To accomplish that, the target cells are placed inside a microwave cavity. They are separated by a gap containing a microwave stopper, which prevents the radiation intended for one cell from leaking into the other one. This microwave system ensures the attainment of the desired spin configuration with a very high level of polarisation. The result can be seen in Fig. 3.3 (red and yellow arrows). We can see that the cells are installed one after the other along the beam and, consequently, they are exposed to the same muon flux. This fact is important to avoid the measurement of false spin-asymmetries related to variations of the beam flux. However, we can also see that the experimental acceptance is different for the events coming from separate cells. This difference is even larger for the 2002-2004 setup (2-cell system). Here lies the main reason for the target upgrade to a 3-cell system: the average acceptance for the events coming from the upstream + downstream cells is approximately the same as the acceptance experienced by events coming from the middle cell. Nonetheless, possible contributions from this kind of false asymmetries are easily eliminated by the application of a dipole field of 0.5 T. This field is perpendicular to the solenoid one, and it is capable of reversing the target spins (in 30 minutes) without any loss of their polarisation. This procedure ensures the cancellation of false spin-asymmetries originating from the different experimental acceptances. However, small false asymmetries correlated with the application of the dipole field can also be generated. Therefore in 2006 and 2007, the spin reversal is done only once every 24 hours. For the years of 2002, 2003 and 2004 the polarisation is flipped every 8 hours due to the absence of a 3-cell system.

[2]For the 2002-2004 setup, the two cells have also a separate microwave system.

The polarisation of the target is measured by the method of **N**uclear **M**agnetic **R**esonance. It is constantly monitored by five NMR-coils along each cell. The maximum polarisation obtained is +57% and -53% for the target based on the ^{6}LiD material (2002-2006). For the ammonia target, NH_3 (2007), the maximum polarisation achieved is +95% and -95%. The results of these measurements give us the second dilution factor present in eq. 2.85 (needed for the extraction of $\Delta G/G$), i.e. the target polarisation P_t. The final $\langle P_t \rangle$ is about 50% for the ^{6}LiD target and about 86% for NH_3 target. The justification for the lower polarisation of the former is found in the magnetic moment of the deuterons, which is significantly smaller than the magnetic moment of protons. The fact that only deuterons (protons) are polarisable in the ^{6}LiD (NH_3) target implies that the polarisation values shown above are not true for all interactions of the muon beam at the target. This is correctly taken into account by the third dilution factor appearing in eq. 2.85, f, which accounts for the fraction of polarisable material inside the target.

The dilution factor f

The ^{6}LiD molecule can be considered as formed by a ^{6}Li-nucleus plus deuteron. The ^{6}Li-nucleus can again be thought of as a ^{4}He-nucleus, i.e. an alpha particle, and yet another deuteron. Therefore with this simple picture of ^{6}LiD we get an average value for f around 0.5 (4 polarisable nucleons out of a total of 8 nucleons):

$$f = \frac{\overbrace{n_D^{\text{nuc}}}^{4}}{\underbrace{n_D^{\text{nuc}} + n_{^4He}^{\text{nuc}}}_{8}} = 0.5 \tag{3.2}$$

In a similar way we can obtain $\langle f \rangle \approx 0.17$ for the NH_3 target (three polarisable nucleons out of 17). However, in reality the target cells contain a certain amount of impurities contaminating the above materials. In particular, for the ^{6}LiD target, half of the cylindrical cells is filled with the ^{3}He-^{4}He cooling-mixture fluid. By taking into account these two elements, we get a dilution factor with the approximate value of $\langle f \rangle = 0.43$. However, the target has also traces of 6 different isotopes: ^{1}H, ^{6}Li, C, F, Ni and Cu. In addition, the NMR coils are made of cooper-nickel (CuNi) with a Teflon coating containing carbon and fluor. All these elements need to be taken into account in the analysis since they dilute the polarisable material inside the target. The proper formula for the calculation of the dilution factor is:

$$f = \frac{n_{(D/P)}^{\text{nuc}}}{n_{(D/P)}^{\text{nuc}} + \sum_A n_A^{\text{nuc}} \left(\frac{\bar{\sigma}_{(A)}}{\bar{\sigma}_{D/P}} \right)} \tag{3.3}$$

where $n_{(D/P)}^{\text{nuc}}$ is the number of polarisable nucleons in the ^{6}LiD/NH_3 target. The sum runs over all the remaining isotopes contaminating the cells and $\bar{\sigma}$ represents the unpolarised muon-nucleon cross-section. The final results give the values of $\langle f(^6LiD) \rangle \approx 0.36$ and $\langle f(NH_3) \rangle \approx 0.15$ for the two targets used in COMPASS [65].

3.3 The Spectrometer

The COMPASS detector consists on a two-stage forward spectrometer (cf. Fig. 3.5). The spectrometer is divided in two separate parts in order to optimise the resolution of the momenta associated to the reconstructed tracks of particles. The first one is a **L**arge **A**ngle **S**pectrometer (LAS) and, as the name implies, it was designed to perform accurate measurements of tracks

emitted at large angles (up to 180 mrad) with respect to the beam direction. The LAS encom-

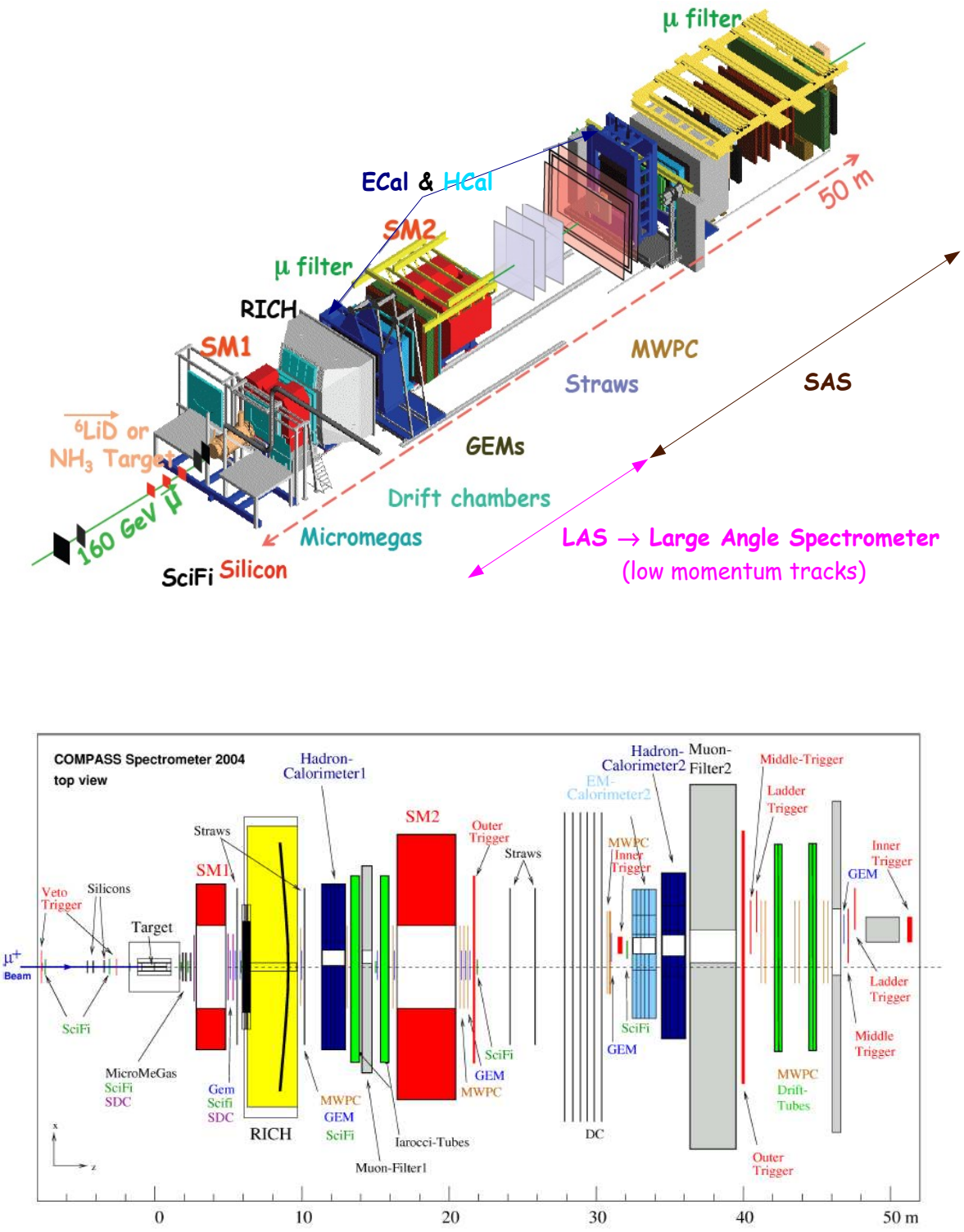

Figure 3.5: The artistic view (top) and top view (bottom) of the COMPASS spectrometer during the 2004 data taking. The polarised muon beam enters from the left, and after being tracked by a set of SciFi and Silicon detectors collides in the polarised target. The products of the reaction are detected by a two-stage spectrometer, which are separated by the SM2 magnet.

passes all detectors between the polarised target and the SM2 magnet. On the other hand,

the **S**mall **A**ngle **S**pectrometer (SAS) is intended for the reconstruction of high momentum tracks emitted at smaller angles (up to 30 mrad). Both spectrometers contain dipole magnets, SM1 and SM2. The SM1 is located 4 meters downstream of the target and has a field integral of 1.0 Tm. Its main purpose is to allow for a measurement of the low momenta associated to the particles emitted at large angles in the LAS. In order to accomplish that, the magnet was built with a wide angular acceptance: it has a central hole with dimensions of 2.29 $\times$ 1.52 m^2. The drawback of using such a wide magnet, in that position, is that it leads to a non-negligible fringe-field in the zone between the target solenoid and the SM1. Nevertheless, for some cases, this fringe-field is useful to estimate the momenta of those particles that do not cross the dipole magnet (p $<$ 400 MeV/c). This can be done by measuring the tracks deviation in the fringe-field. However, the reconstruction efficiency of particles with a momentum smaller than 2 GeV/c is quite low[3] (cf. Chapter. 4). Fortunately these missing tracks have a little impact on the open-charm analysis (see section 5.5). Concerning the SAS, the SM2 magnet is located 18 m downstream of the target. It has a field integral of 4.4 Tm and a central hole with dimensions 2 $\times$ 1 m^2. Particles need to have at least 4 GeV/c to pass through the SM2.

Each spectrometer is equipped with several tracking detectors, before and after each magnet, in order to permit the reconstruction of tracks associated to the particles coming from a polarised DIS event. The tracks are reconstructed by segments, i.e. each tracking zone (field-free regions) reconstructs a segment of the original track, and then all the segments are bridged through the magnetic field. The measured deflection allows us to estimate the momentum associated to each reconstructed track. Thereafter, the identity of the final state particles can be revealed by measuring their velocity with the RICH detector (cf. section 3.3.2). This detector is located in the first spectrometer. To complement the experimental apparatus, a set of electromagnetic and hadronic calorimeters also exists in both spectrometers. Since the hadronic calorimeters absorb most of the particles whose energy they are intended to measure, they are placed at the end of each spectrometer. For the identification of muons, a set of muon filters is used at the very end of the LAS and SAS. Particles with large momenta are able to cross the LAS due to the existence of holes in the calorimeters and in the muon filter.

The positions of all detectors are defined in a reference system where the Z axis is oriented along the direction of the beam. The X axis is pointing horizontally (in the magnetic bending plane) and the Y axis is pointing upwards. In 2002-2004 the upstream cell of the polarised targed is located between Z = $-$100 cm and Z = $-$40 cm whereas the downstream cell is between Z = $-$30 cm and Z = 30 cm. In 2006 and 2007 the upstream cell is placed between Z = $-$65 cm and Z = $-$35 cm, the middle cell between Z = $-$30 cm and Z = 30 cm, and the downstream cell is located between Z = 35 cm and Z = 65 cm.

3.3.1 Tracking detectors used in the LAS and in the SAS

Both spectrometers are equipped with three types of tracking detectors: **V**ery **S**mall **A**rea **T**rackers (VSAT), **S**mall **A**rea **T**rackers (SAT) and **L**arge **A**rea **T**rackers (LAT). The former were designed to handle the high intensity of the beam and therefore they are suited to detect particles emitted at small angles. On the other hand, the LAT detectors were made to cover large angles and because of that they don't need to be optimised for high rates of particles. The purpose of these detectors is to measure the impact point (hit) of a charged particle. Typically

[3]The fringe-field hinders the reconstruction of low momentum tracks in that zone. In most cases these particles are not reconstructible at all, even if their tracks are well reconstructed downstream of SM1: their momenta cannot be estimated because the corresponding tracks were not reconstructed in the fringe-field, i.e. it is not possible to measure the deflection imposed by the SM1 on these particles.

one plane of a tracking device measures the X or Y coordinate of the impact point. Several segments can then be reconstructed by connecting all the hits along the spectrometer. In order to solve ambiguities, the detectors are sub-divided in consecutive planes (at different Z) with their wires oriented in different projections (Y (0°), 45°, X (90°) and 135°). Two planes are needed to reconstruct a space-point. The most important tracking detectors used in COMPASS are presented in Tab. 3.1.

Detector	**Active area (mm^2)**	**Dead zone (mm)**	**Time resolution (ns)**	**Space resolution (μm)**
SciFi	39×39 (pre-target)	–	0.50	130
SciFi	123×123 (spectro.)	–	0.35	210
Silicons	50×70	–	3	14
Micromega	400×400	r = 50	9	90
GEM	316×316	r = 50	12	70
Drift Chamber	1800×1275	r = 30	–	220
Straw Tubes	3230×2800	197×197	–	250
MWPC	1780×1200	r = 220	–	500

Table 3.1: Characteristics of the most important tracking detectors used in COMPASS. The three rows divide the VSAT, SAT and LAT. In the latter only the larger dimensions of the detectors are shown (they have multiple sizes along the spectrometer). In total COMPASS has 8 SciFi with 24 projection planes (3 per detector), 3 Silicons with 12 projections, 11 GEM with 44 projections, 3 Micromegas with 12 projections, 3 Drift Chambers with 12 projections, 4 Straws with 15 projections and 11 MWPC with 34 projections. The efficiency of these detectors is 99% for the VSAT and around 97% for the remaining ones.

Micromegas

One of the detectors used by COMPASS to handle high rates of particles is the **M**icro **M**esh **G**as detector (Micromega). The detector and its working principle are shown in Fig. 3.6. It is chosen as an example to illustrate the tracking technologies used in COMPASS. Each Micromega is a gas chamber that is divided in two regions of different voltages. The separation of the conversion gap from the amplification gap is made by Micromesh wires subjected to a voltage of 500 V. As the names imply, the ionisation caused by the passage of a charged particle is produced in the conversion gap, whereas the avalanche of electrons takes place in the amplification gap. In the latter, the configuration of the electric field ensures a quick evacuation of the ions to the Micromesh. Note that the rate of particles that a gaseous detector can stand is inversely proportional to the drift time of the ions (the drift is, in general, very slow). Therefore, the trick consists in the reduction of the distance between the beginning of the amplification process and the cathode. In Micromegas the anode strips are separated from the Micromesh by an impressive 0.1 mm. This fact combined with a reduced diffusion of electrons makes the detector capable to withstand high intensities of particles. Therefore, with the help of Micromegas COMPASS is able to reconstruct tracks with high precision at very small angles. This design results in a time resolution of about 9 ns and a space resolution of 90 μm for the detector. In total, three stations of Micromegas are used in the LAS (between the target and the SM1). Each station is composed by 4 planes with the following orientation of the wires: 135° (at a fixed Z), 45° (Z + 1 cm), 90° (Z + 9 cm) and 0° (Z + 10 cm). The last two measure the coordinates Y and X (respectively) of the hits produced by a passing particle.

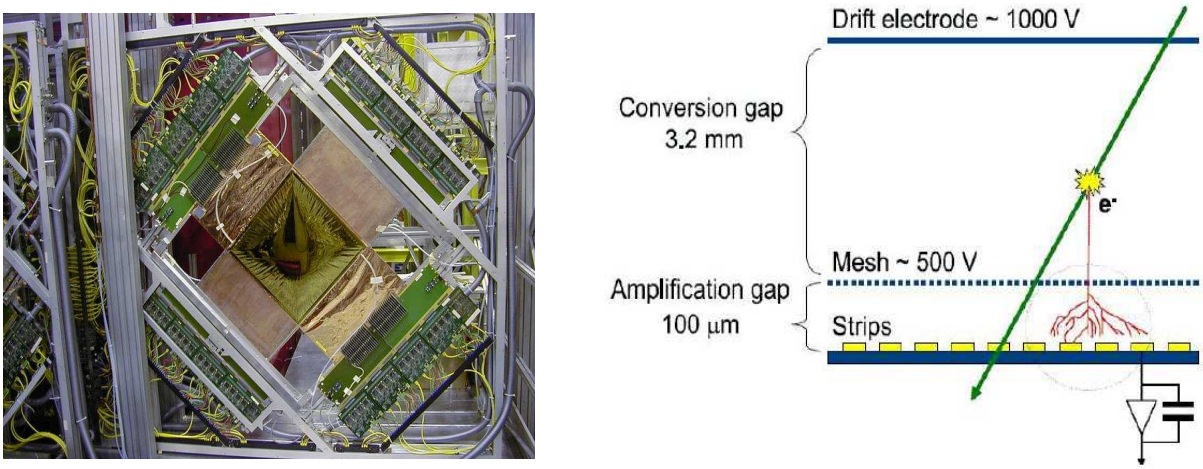

Figure 3.6: One plane of the Micromega detector (left) and its working principle (right). The active area is represented by the central green square (left). The ions resulting from the ionisation of the gas are subjected to a potential difference of 50 kV/cm in the amplification gap. In the conversion gap the potential difference is of 1 kV/ cm.

3.3.2 The RICH detector

The LAS is equipped with a **R**ing **I**maging **CH**erenkov (RICH) whose purpose is the identification of charged particles (cf. Fig 3.7). The working principle is based on the Cherenkov effect: a charged particle crossing a medium with a speed greater than the speed of the light in that medium emits photons at an angle θ_C. The use of this effect to identify charged particles is extensively discussed in section 5.2.1. Here we are only interested in the description of the main characteristics of the detector. All particles that reach the RICH within its wide acceptance [4]

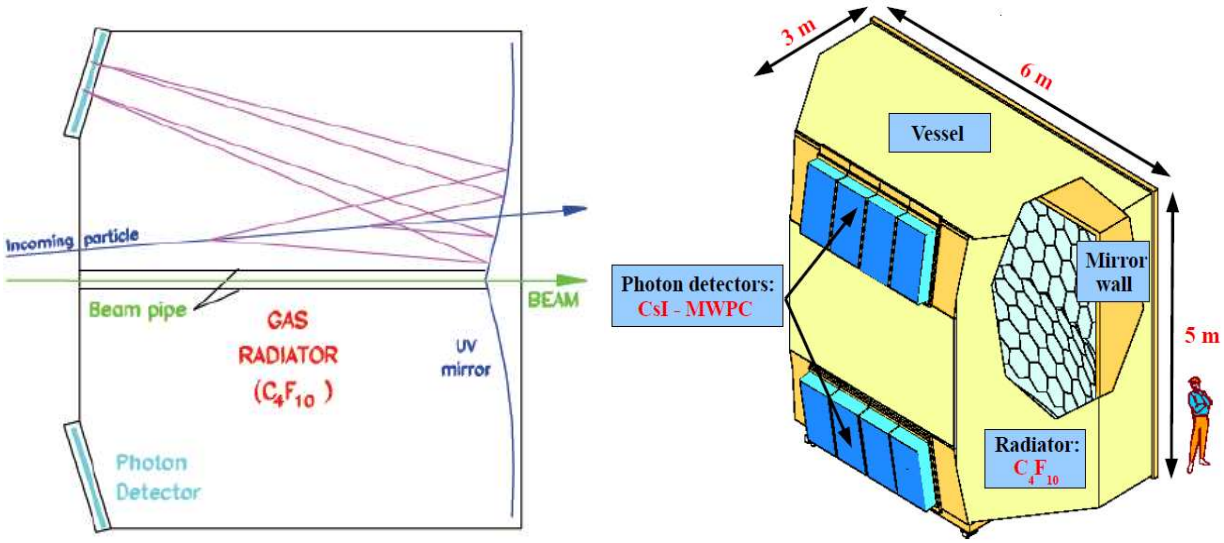

Figure 3.7: Scheme of the working principle (left) and an artistic view (right) of the RICH.

[4]RICH acceptance: ± 250 mrad in the horizontal direction and ± 200 mrad in the vertical direction.

have to cross 3 m of a C_4F_{10} gas. The detector was designed to ensure a constant pressure for the gas and also its transparency to the visible and UV photons [5]. These are crucial requirements for the correct operation of the RICH. The radiator gas system keeps the gas pressure constant within 10 Pa and ensures its transparency by a continuous filtering of contaminants. The biggest problem is the presence of O_2 and H_2O inside the gas, due to their large absorption cross-section in the UV range. Therefore these molecules are continuously removed from the cavity of the RICH.

All photons produced in the radiator are reflected by a 21 m^2 wall, formed by 116 spherical UV mirrors, and focused onto photon detectors. The mirror wall is divided in two spherical systems, with their centres vertically displaced in order to be able to focalise outside the spectrometer acceptance. In this way the photon detectors can be installed so that they are protected by the SM1 magnet. In Fig. 3.7 one can see that parallel rays are focused into the same point by the mirror system. As a result, the photons emitted by a given particle produce a ring in a plane of the photon detectors. The radius of this ring is proportional to the focal length f of the mirror system:

$$r = \theta_C \times f \tag{3.4}$$

where f has the value of 3.3 m. An example of these reconstructed rings is given in Fig. 3.8. If we determine their radius, r, we can access the value of the corresponding Cherenkov angle θ_C. In section 5.2 we will see that this angle allows us to obtain the mass of a given particle as long as we know its momentum. Particles are, therefore, identified in this way.

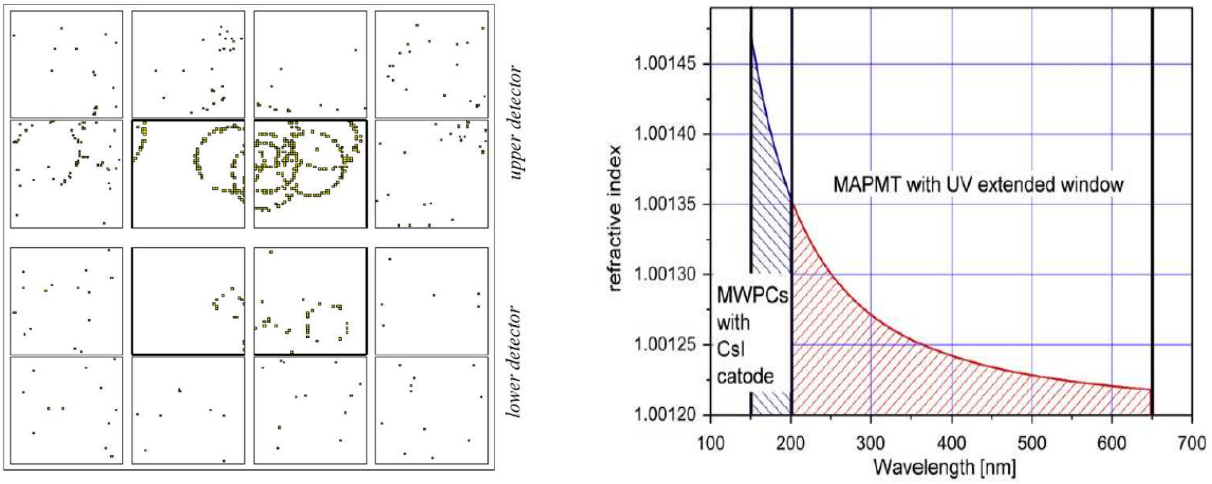

Figure 3.8: Left: examples of rings (made by the impact of Cherenkov photons) reconstructed in the central part of the photon detectors (MAPMT). The outer parts are made of MWPC detectors. Right: refractive index of C_4F_{10} as a function of the Cherenkov wavelength. The visible photons are only detected by the MAPMT. These figures are made for the 2006 setup.

During the years 2002-2004 the photo-detection in the RICH has been performed with **M**ulti**W**ire **P**roportional **C**hambers (MWPC). The Cherenkov photons enter the chambers via a quartz window and hit their photocathod (made of CsI). These photons are then converted to electrons and thereafter multiplied in the MWPC. The main drawback of the system is its electronic

[5] The intensity of the Cherenkov photons emitted by a given particle increases with decreasing the photon wavelength. Therefore, the detector was optimised to work also in the very **U**ltra-**V**iolent (UV) range.

readout which, unfortunately, generates a considerable amount of dead time due to its long integration time (around 3.5 μs). Consequently, the four central pads of the photon detectors are highly populated by uncorrelated background images (until 2004). Major sources for this background are pile-up muons (non-interacting beam particles) crossing the RICH: the Cherenkov images produced by the high momentum particles are detected in those four pads. This contamination was reduced by the installation of a stainless steel beam pipe (10 cm in diameter), which shielded the photon detectors from photons originating from the muon beam. However, not all the beam can be contained in the pipe. Therefore these halo muons contribute to a substantial amount of background. To overcome these limitations the RICH detector was upgraded from 2006 onwards. The main update is the replacement of the central part of the photon detectors by **M**ulti **A**node **P**hoto **M**ultiplier **T**ubes (MAPMT). These tubes have a considerably higher detection efficiency and a much faster response. The latter is important to account for the high intensity of Cherenkov photons emitted by the halo muons. For the outer parts the readout electronics was also refurbished, allowing a significant reduction of the background. In total, the MAPMT system allows to detect four times more Cherenkov photons than in the peripheral MWPC detectors. The use of two different detectors results in the detection of photons in two different wavelength regions (cf. Fig. 3.8). Consequently, the average values of the corresponding refractive indexes are also different. From now on they will be referred as n_{UV} (MWPC) and n_{VS} (MAPMT). This extended wavelength range also helps to distinguish a given particle from halo muons (they emit mainly UV photons). The result of the RICH upgrade can also be seen in Fig. 3.8: photon rings are very well reconstructed by the MAPMT detectors.

We will see in section 5.2 that the threshold condition for the Cherenkov effect is:

$$\beta \geq \frac{1}{n} \tag{3.5}$$

where n is the refractive index and $\beta = \sqrt{1 + (M^2c^2)/p^2}$. In the latter, M and p are the mass and momentum of the detected particle. Using the average value of the two refractive indexes belonging to the C_4F_{10} gas (c.f Fig. 3.8), we obtain the following thresholds for the **P**articles **ID**entification (PID): 2.5 GeV/c for pions, 9 GeV/c for kaons and 17 GeV/c for protons.

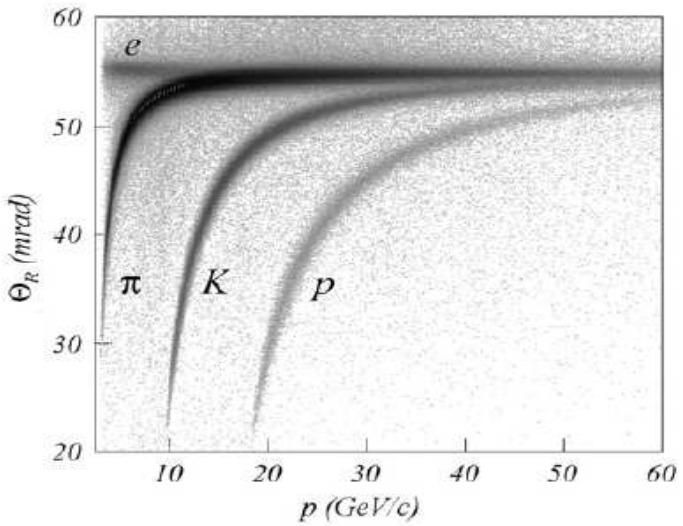

Figure 3.9: The measured Cherenkov angle θ_C versus the particle momentum p. Pions, kaons and protons are clearly distinguished below a momentum of 50 GeV/c.

For growing momenta we approach the asymptotic limit of $\beta = 1/n$ (small angles for the Cherenkov photons), which means that it is more difficult to separate the different kinds of particles. By design, the RICH detector of COMPASS has a limit around 50 GeV/c for PID. All these limits can be confirmed in Fig. 3.9.

To finalise this section, Fig. 3.10 shows the impact of the RICH upgrade in the analysis. Clearly, the RICH detector is now much more efficient in the identification of kaons. The number of kaons, per incoming muon, is bigger by almost a factor of three, in 2006. One can also see the impact of the increased acceptance of the target solenoid for the year of 2006: the reconstruction of pions at larger angles is significantly improved. These two mesons are of crucial importance for the present analysis. They are the decay products used to reconstruct the open-charm mesons and, therefore, they are the primary seeds for the definition of a PGF process.

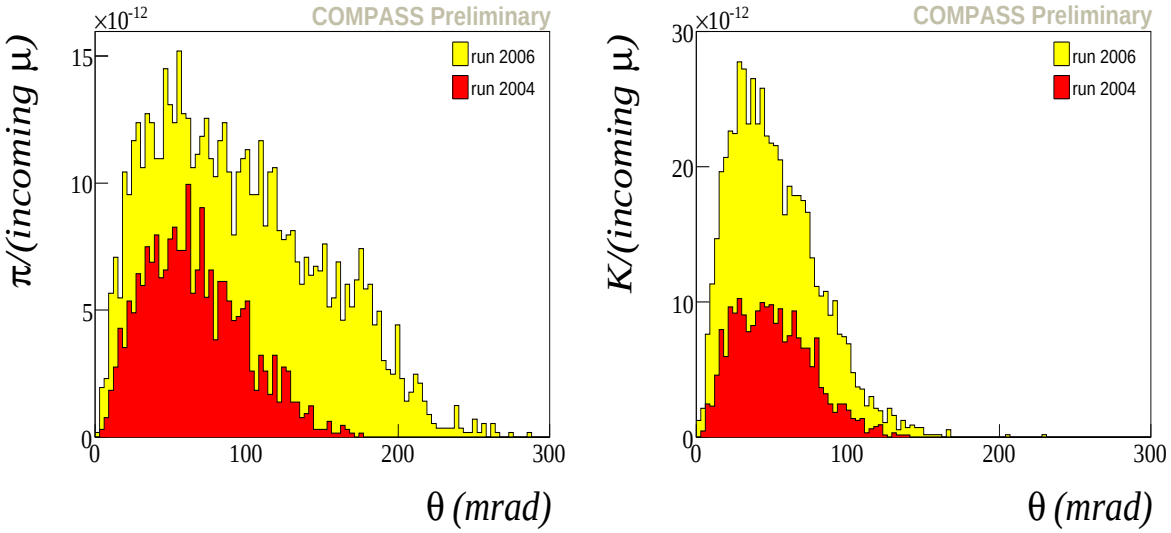

Figure 3.10: Number of identified pions (left) and kaons (right) per incident muon, as a function of the polar angle θ. The comparison is done between the target and spectrometer setups of the years 2004 (red) and 2006 (yellow). All events are required to be identified by the RICH detector.

Chapter 4

Reconstruction of Tracks in the LAS

As already stated in section 3.3, the reconstruction of low momentum tracks is strongly hindered by the fringe-field that exists upstream the SM1 magnet. A scheme of this particular zone of the LAS is shown in Fig. 4.1. Although only the equipotential lines of the individual magnetic fields (solenoid and SM1) are represented, we should not forget that interferences between the two fields also exist. This fact introduces an additional difficulty for the reconstruction of tracks, because it may generate subtle effects (small instabilities in the apparatus) that cannot be predicted. In the presence of such fringe-field the trajectories of low momentum particles are expected to deviate significantly from straight lines. Therefore, the standard-method [1] for the reconstruction of tracks cannot be applied in this zone of the LAS.

The reconstruction program of COMPASS uses the so-called projection method [66, 67]. The track-candidates are first searched in the XZ and YZ planes, separately, and thereafter they are associated in space with the help of inclined detector planes (U and V). The X and Y projections represent the axes of reference used for the reconstruction of tracks. A pair of hits in two reference planes with the same projection provides the x (or y) coordinates and the slope dx/dz (or dy/dz). These planes are well separated in order to allow for a reasonable accuracy on the obtained line direction. Lines are defined for each of the reference planes by connecting the corresponding hits. In the non-bending plane, YZ (the dipole fields of SM1 and SM2 are oriented in the Y direction), all the accepted lines are required to point to the target within a tolerance accounting for a possible residual curvature. The same is demanded for the lines defined in the X projection after the SM1. Finally, the obtained 3-d segments (combination of lines from the orthogonal projections X and Y) are extrapolated to the remaining U and V planes of the same tracking zone. The hits that are found within a given distance around the impact point, in those planes, are added to the track-candidate. The validation of these segments just requires the existence of a minimum number of planes with selected hits.

The majority of tracks have their origin before the SM1 magnet. Therefore, most of the downstream segments need to be connected to their counterparts in the fringe-field zone. The measurement of the deflection caused by the SM1 allows us to measure the particles momentum. However, due to the existence of a fringe-field (upstream the SM1), the reconstruction of particles with a momentum smaller than 2 GeV/c is somewhat inefficient. To counter this fact, a different approach is used to collect the track-candidates in that zone. It is based on the use

[1] Typically the tracking detectors are installed in free-field zones where straight lines (containing several hits) can be defined. Then, the particles momentum is estimated by bridging two matching lines through a magnetic field.

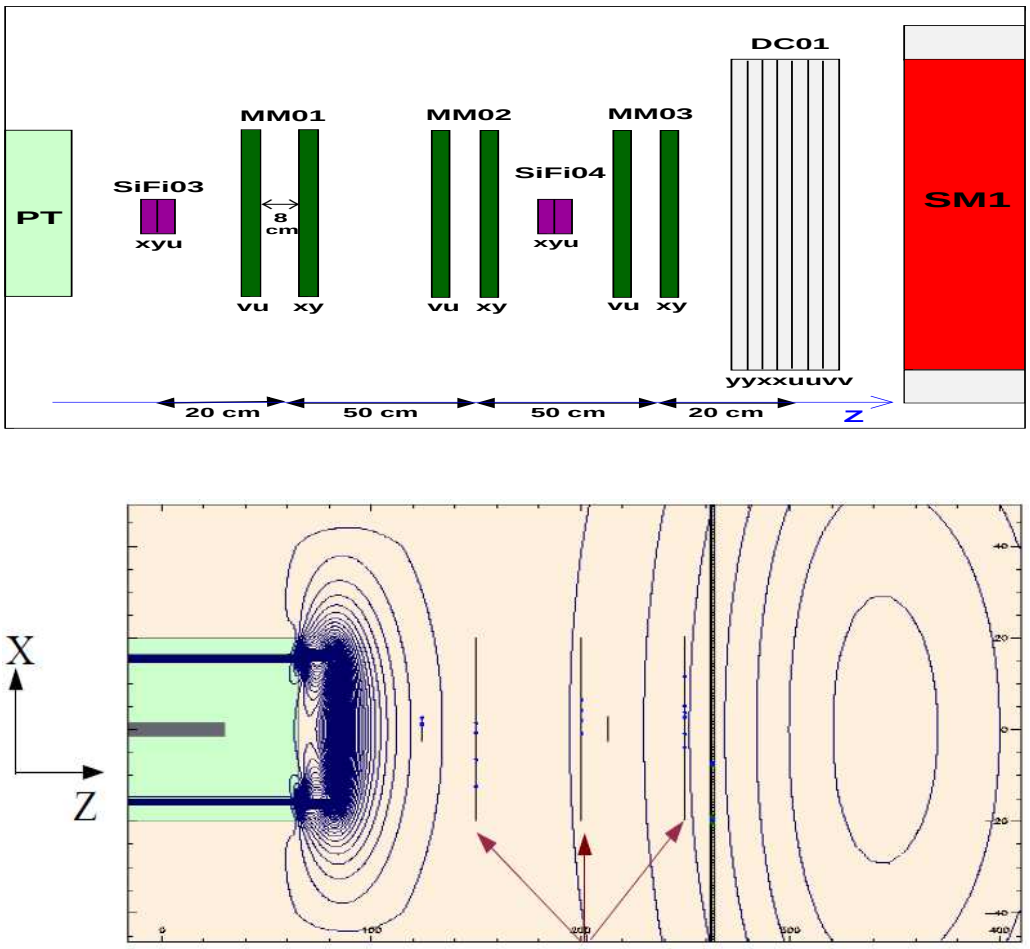

Figure 4.1: Schematic representation of the LAS spectrometer, between the target solenoid and the SM1 magnet, as it was used during the year of 2003 (top figure). All tracking detectors of the zone are represented. The number of detection planes are given by the vertical lines. The orientation of the wires have the following convention: Y (top-bottom direction), U (45°), X (90°) and V (135°). A scaled representation of the projection-plane defined by the X coordinate is also shown (bottom figure). The blue lines illustrate the fringe-field, whereas the red arrows point to the 3 Y planes of Micromegas that measure the X coordinate of the hits.

of a dictionary containing all the possible tracks through the COMPASS spectrometer. This dictionary maps the 2 representations of tracks into each other, i.e. a set of hits is connected to a vector in a 5-dimension phase space. The latter contains the following 5 parameters: x, y, t_x (dx/dz), t_y (dy/dz) and Q/p (charge / momentum). The dictionary is organised as a look-up table, thus allowing a very fast calculation of the χ^2 of a given 5-vector with respect to a set of hits. The lines defined in the YZ plane of the fringe-field zone follow the same procedure described above (for lines in the SAS). However, for the X projection, lines are selected by comparison with the dictionary of particles. The chosen lines are those containing the values of x and t_x corresponding to the smallest χ^2. This selection of segments is possible as long as we know the magnetic field map in the fringe-field zone (note that y and t_y are available a priori). Finally, the fringe-field segments that are kept are those that can be bridged through the SM1 to a more downstream segment. Despite the efforts done for a good reconstruction in the fringe-field, the overall efficiency achieved is $\langle\epsilon\rangle = 89.8\%$. The latter is obtained from a Monte Carlo simulation using the number of generated and the actually reconstructed tracks.

A minimum number of 8 hits in the fringe-field zone is required for the reconstruction. The detection efficiency of the Micromegas is 97% (main detectors in the fringe-field). Therefore, the justification for a lower efficiency of reconstruction is found in the contributions of low momentum particles. The efficiency ϵ drops to about 75% for $p = 1.5$ GeV/c and below 50% for $p \leq 0.5$ GeV/c. In the frame of this scenario, a new method based on a cellular automaton approach is developed. The goal is to raise the reconstruction efficiency for the low momentum particles. However, before we come to that, lets summarize how the measurements of the fringe-field are done.

Magnetic field in the fringe-field zone:

The field map of SM1 was measured at the beginning of the experiment. This was accomplished through the use of Hall probes, moved step-wise, systematically, over the volume of the zone. Thereafter a file with three field components and three space-point coordinates was produced. The grid size of these measurements is $4 \times 8 \times 8$ cm. Concerning the solenoid, only two field components (z and r) are stored in the field map. This is justified by the cylindrical symmetry of the homogeneous field provided by the solenoid. Apart from the latter, the target dipole magnet is also able to generate a field of 0.5 T in the Y direction. For this mode of operation the field map is provided in cartesian coordinates. The final field evaluation is performed by a linear interpolation between all measurements.

4.1 Cellular Automaton for fringe-field tracking

An algorithm based on Cellular Automata is developed in an attempt to overcome the difficulties of reconstruction of particles with low momentum. Cellular Automata have become particularly popular in the seventies with the creation of the **Game of Life** [68] by the british mathematician John Horton Conway. The idea was to use a fixed set of rules under which a simple system could evolve into complex structures capable of simulating some aspects of real life. Basically, Conway built a zero-player game: its evolution is completely determined by the initial state, without further inputs. The universe of the game is an infinite two-dimensional grid of square cells. Each cell can assume only one out of two possible states: live or dead. The set of rules for this system is very simple (rules are applied locally to each cell):

1. A cell with less than 2 living neighbours dies from isolation.
2. A cell with 2 living neighbours stays alive for the next generation.
3. A cell is born if it has exactly 3 living neighbours.
4. A cell with more than 3 living neighbours dies from overpopulation.

The initial pattern constitutes the seed of the system. Thereafter, all cells in the grid evolve simultaneously, in discrete amounts of time, to a new generation of cells. The new created structures continue to evolve, originating increasingly complex structures that are capable to simulate all kinds of behaviour. The evolution continues until stable structures are found. Structures with about 4000 cells capable of simulating logical behaviours (like memory) and movements through space were already observed. Cellular Automata are not learning algorithms (like the ones typified by Neural Networks) but, as explained above, they are a good

model for a large number of artificial life simulations. They can be considered as a particular case of a Neural Network. The use of the latter implies that the system is able to assume continuous states during its evolution. Here, the evolution proceeds in discrete amounts of time with the system assuming only those states that are allowed by the simple set of local rules.

The application of Cellular Automata to the track reconstruction in particle physics is pretty straightforward. Analogously to the cells used in the Game of Life, we can define 3d-segments as the basic ingredients of a Cellular Automaton algorithm for tracking. These segments will be called from now on as cells. Looking back to Fig. 4.1 we see that 3 different types of detectors coexist in the fringe-field zone. Unfortunately, due to their inhomogeneity, the performance of the algorithm is severely disturbed. Therefore, the reconstruction of tracks is performed in two stages:

1. **Track-searching part** → The procedure involving Cellular Automata is applied only to the Micromegas. The goal is to create seeds of very good quality.

2. **Track-following part** → The seeds selected in the track-searching are extrapolated (using a Kalman Filter [69, 70]) to the remaining detectors, and also to the Micromegas projections that were not used. The goal is to catch more hits and to remove ghost tracks.

In this chapter we focus our attention on the track-searching part. The full procedure is illustrated in Fig. 4.2:

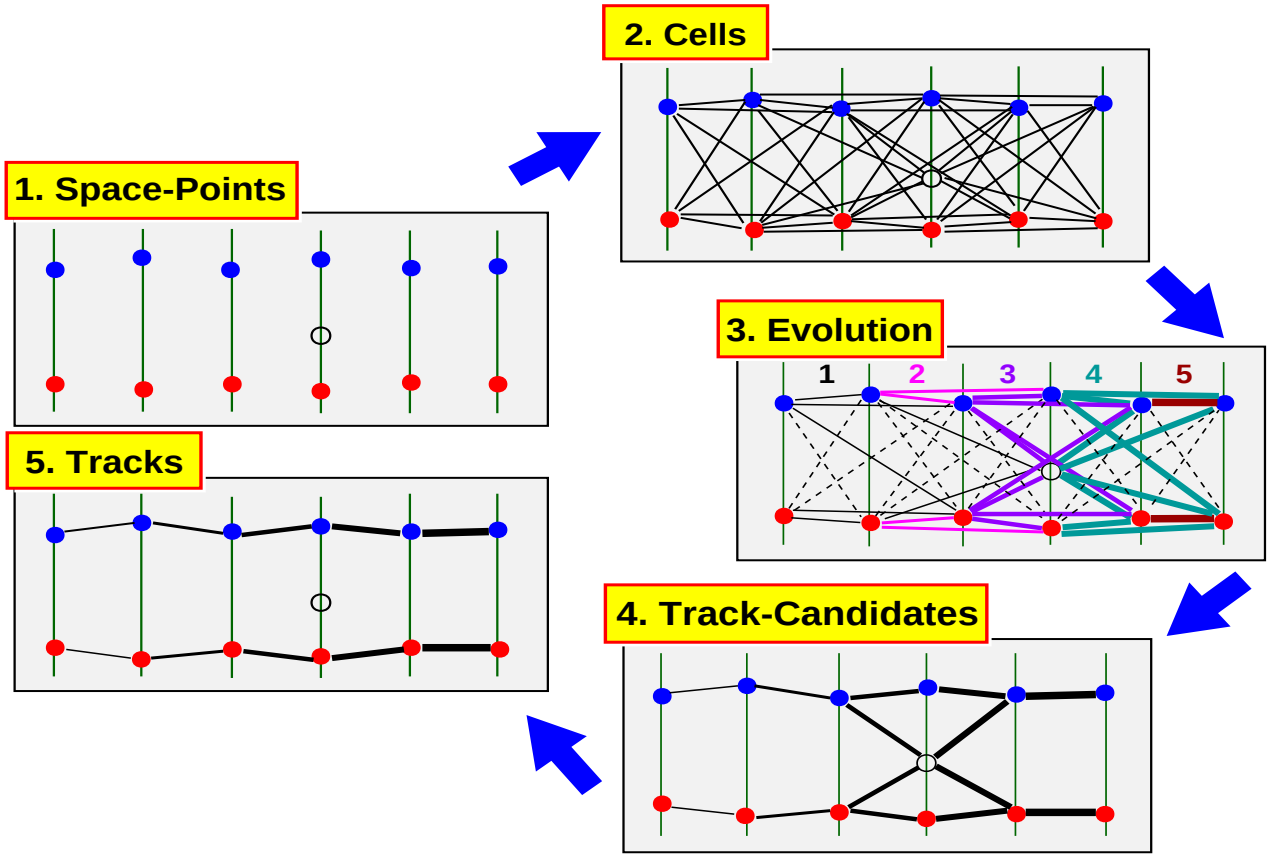

Figure 4.2: The track-searching procedure using all 6 Micromega stations. Each station is formed by 2 neighbouring projection-planes (cf. top of Fig. 4.1). The space-points are defined by the combination of 2 neighbouring hits in orthogonal planes.

A typical Cellular Automaton is built accordingly to the following algorithm. First we define elementary cells along with their possible discrete states. After that we need to define the concept of neighbour and, in addition, a set of communication rules between all cells. Finally, the last step of the algorithm encompasses the definition of time evolution for the system.

We are now in conditions to describe the track-searching algorithm presented in Fig 4.2:

1. **Definition of Space-Points** → All hits in neighbouring planes of Micromegas are combined in space-points. These points are reconstructed on the average Z coordinate corresponding to the planes used. They are only accepted if their location in space is compatible with the active area of the detectors.

2. **Definition of Cells and the Cellular Automaton initialisation** → A cell is identified with a straight-line segment connecting two neighbouring space-points (from two adjacent stations). To account for possible inefficiencies of the Micromegas, we have also to define cells that skip one station. The only criterium for their selection is that they point in the direction of the target: a safe cut of 0.2 is demanded for the t_x and t_y (cf. Fig. 4.3-left) of all accepted cells. This cut accounts for the curvature introduced in the tracks by the fringe-field. The algorithm is initialised by attributing to all cells a discrete value of 1.

3. **Definition of Neighbours and Rules of Evolution** → Cells with a common Space-Point are likely to be considered neighbours. The second requirement for that to be possible is the following: two cells are indeed neighbours if they obey the upper limit defined for their angular difference (cf. Fig. 4.3-right). These angles owe their existence to the multiple scattering in the detectors and also to the fringe-field. A cut of 0.02 is imposed to the t_x and t_y differences of all cells that share the same Space-Point. In Fig. 4.2, the dashed cells have no neighbours. The rules of evolution are as follows. At each discrete moment of time, all cells look to their preceding neighbours and increase their value by one unit if they find a neighbour in the same state (i.e., with the same value). Since the time evolution is discrete, all cells change their state simultaneously. The evolution stops when there are no more neighbouring cells in the same state. In COMPASS the maximum value that can be attributed to a cell is 5. These numbers are associated with the position of cells on the track, and are represented by different thicknesses and colours in Fig. 4.2.

4. **Collection of Track-Candidates** → The selection of candidates starts from cells with the highest position values (5 in the present case). Thereafter, tracks are collected by adding cells with lower position values of one unit. All neighbouring cells with a position value which differs by more than one are removed. After the selection of all track-candidates consisting of 5 cells, all hits that make up their Space-Points are marked as used. The selection procedure is once again repeated, but now starting with the cells in position 4. The only requirement is that none of the hits belonging to such a track of 4 cells are already in use (by a higher level track). Tracks with a minimum of 2 cells are accepted for reconstruction [2].

5. **Reconstruction of Tracks** → A final quality test is applied to all track-candidates of the same level who share hits or Space-Points among them. A Kalman Filter [3] [69, 70] is used

[2] A minimum of 3 Space-Points is required to estimate the momentum.

[3] All hits belonging to a given track are fitted twice: one in the forward direction and another one in the backward direction. As a result, we obtain a helix for the last and first measured points of the track. A helix consists of: x, y, t_x, t_y and Q/p. The latter is randomly initialised and then evaluated by the fit. After some

to fit these tracks and the one with the lowest χ^2 is chosen. The remaining competing tracks are killed. In practice, this quality test is done before the selection of track-candidates with a lower number of cells. In this way we ensure that the hits belonging to the latter are not marked as used by a ghost track of higher level. By definition, a ghost track is a reconstructed track formed by less than 85% of hits belonging to a real track (the remaining hits belong to other tracks or are fake hits). This procedure allows us to avoid the fake point (open circle in Fig. 4.2) in the reconstruction of the two real tracks.

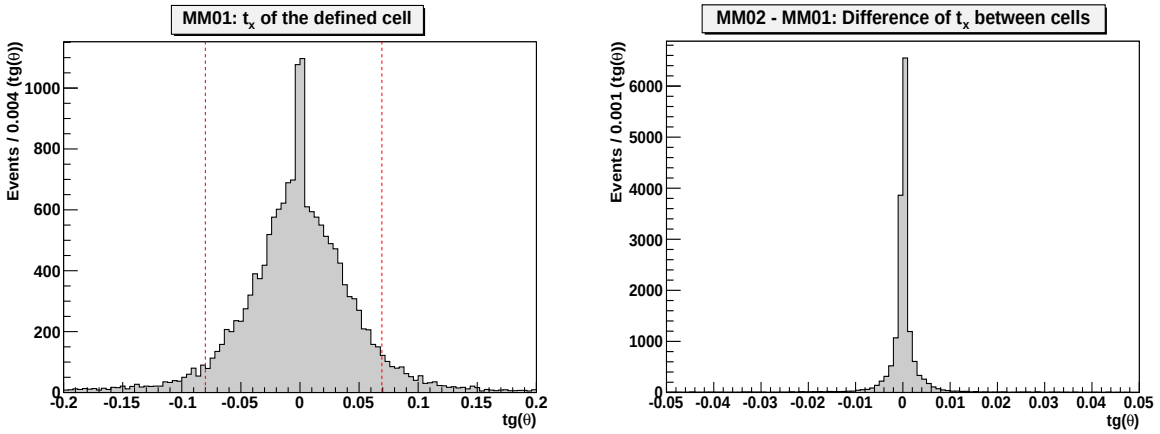

Figure 4.3: Left: slope distribution of all generated tracks in the magnetic bending plane. Only the piece of each track defined by the MM01 (1^{st} cell) is illustrated here. The target acceptance is represented by the red vertical bars (as it was in 2003). Right: angular difference between neighbouring cells corresponding to the same generated track. The first 3 Micromega stations are used in this example. Similar distributions are obtained for t_y.

In Fig. 4.4 we can verify the impact introduced by the Cellular Automaton algorithm in the reconstruction of low momentum tracks:

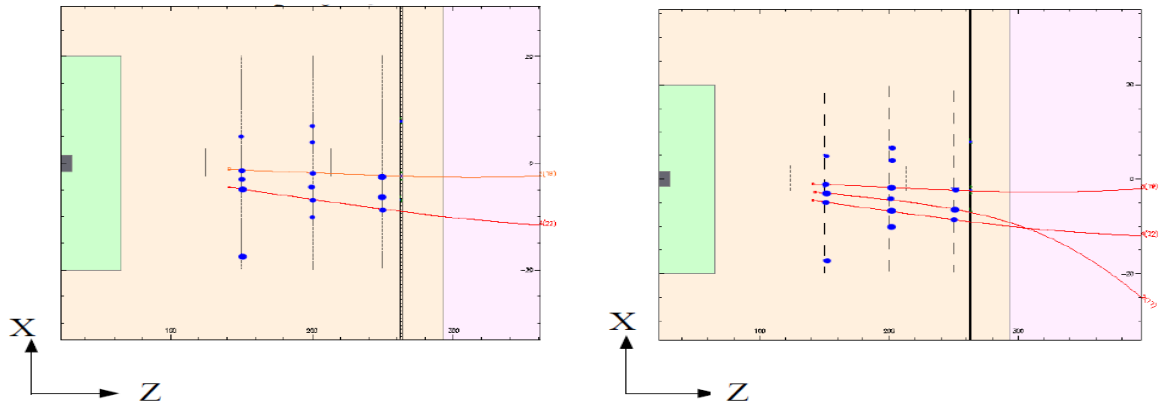

Figure 4.4: Illustration of a given event containing 3 generated particles in the fringe-field zone. All hits are shown in the projection corresponding to the magnetic bending plane. To the left, the tracks are reconstructed using the projection method. To the right, the Cellular Automaton algorithm is applied. The remaining points represent fake hits in the Micromegas.

tests, it was decided to use three fits to compensate the considerable error obtained for Q/p after the first fit. The multiple-scattering (estimated from the detectors radiation length given in the material maps) is accounted for during the fit.

Clearly, for this particular event, the Cellular Automaton algorithm is the only one that is able to reconstruct the track that bends the most in the fringe-field of SM1 (track with low momentum). The main advantage of a method based on Cellular Automata lies in its local and parallel nature. Basically, this means that the rules are only applied to the individual cells (locality) and that their evolution is simultaneous. The fact that the decisions for the evolution of the system are made locally, between neighbours, is a valuable aid for the reconstruction of tracks that reveal a non-negligible curvature. Also, by being essentially parallel and local the algorithm avoids extensive combinatorial searches (good for the online triggering). The drawback of this method is related to the characteristics of the detectors used (Micromegas): hits are provided in projections, which means that we need two registered impacts in two neighbouring planes to reconstruct a Space-Point. Therefore, the inefficiencies introduced in the reconstruction of the latter are considerably higher compared with the use of a 2D pixel detector. The ideal solution for an efficient reconstruction in the fringe-field would be the replacement of each Micromega projection-plane by a pixel detector. All 2D planes should be equally spaced apart and, if possible, the use of detectors with different geometric acceptances should also be avoided [4] (Micromegas and Drift Chamber). These modifications would allow us to use only the track-searching part for the total reconstruction of tracks in the fringe-field.

4.1.1 Results

Results of the application of Cellular Automata for the reconstruction of particles in the fringe-field are summarised in Fig. 4.5:

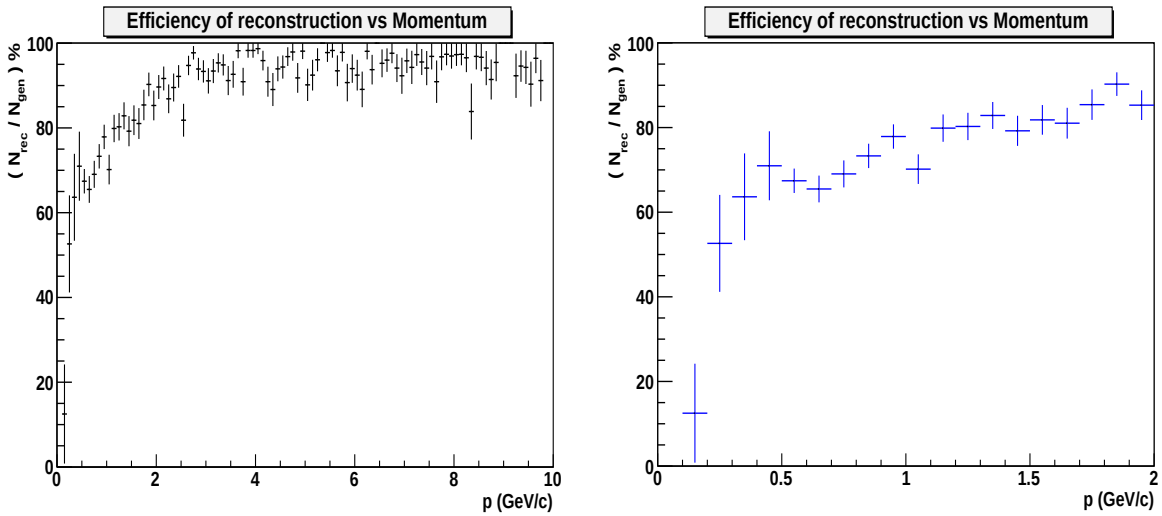

Figure 4.5: Left: the efficiency of reconstruction, $\epsilon = N_{rec}/N_{gen}$ (ratio between the number of reconstructed and generated tracks), as a function of the tracks momentum. Right: zoomed version of the figure shown in the left.

The overall efficiency of reconstruction achieved is $\langle\epsilon\rangle = 90.06\%$, using a sample of 5000 generated events. The efficiency drops to about 75% if we consider only generated particles with a momentum $p \leq 2$ GeV/c. At 1.5 GeV/c the efficiency has a value of $\epsilon \approx 80\%$, while for particles with a momentum $p \leq 0.5$ GeV/c we have an average efficiency of $\langle\epsilon\rangle \approx 50\%$. Unfortunately, these values correspond roughly to those obtained using the projection method (cf.

[4] The exception to this argument are the SciFi detectors. They are needed for the detection of high momentum particles surrounding the beam.

discussion after Fig. 4.1). The main reason for this fact can be derived from the analysis of Fig. 4.7. In this figure we can observe a proper comparison between the generated particles and the reconstructed tracks. In other words, the quality of the reconstruction can be seen from the pulls of the following 5 parameters (obtained from the last helix): x, y, t_x, t_y and Q/p. A very good reconstruction is characterized by a gaussian distribution centred in 0 and with a standard deviation of 1. We can conclude from the pulls on the X and Y coordinates that at least for some tracks the error is overestimated. The main sources of $\sigma \sim 0.85$ are the reconstructed tracks that correspond to the slow-moving particles. For most of these tracks the momentum is reconstructed with a deviation in Q/p which greater than 1 GeV/c (regarding the generated particles). These cases represent 18% of the total statistics. The remaining tracks are reconstructed with an average deviation of 0.2 GeV/c in Q/p, and 7% of them do not have any momentum associated (peak at -1 in the residual of Q/p). The latter are mostly tracks of 2-cells for which the Kalman Filter could not find any momentum.

The fact that the momentum of a slow particle is little known is strongly related to the limited spatial resolution of Micromegas (90 μm). In a fringe-field of about 0.1 T, a slow-moving particle can be easily deviated from its trajectory in a straight line. However, in most cases, the magnitude of these deviations is compatible with the resolution of the detector. If we also take into account the multiple scattering that occurs on the detection planes, we obtain a relatively large error for the momentum estimated by the Kalman Filter for those particles. As a consequence, 10% of the tracks are reconstructed with an x-residual which falls outside the illustrated range. This fact may lead to a misleading fit through the hits of some slow tracks: part of these hits may be ghost-hits which are selected in the vicinity of the real ones. As a result we may reconstruct ghost tracks which, in turn, hamper the reconstruction of real tracks with a lower level of priority [5]. Therefore, the efficiency of reconstruction is significantly reduced for particles with momentum $p < 2$ GeV/c.

In order to try to improve the determination of the particles momentum in the fringe-field, a new fitting method was also tested during the track-searching [71]. This method was specially developed to work with Cellular Automata. It makes use of an analytic formula for a fast extrapolation of tracks in an inhomogeneous magnetic field. The precision of extrapolation does not depend on the shape of the magnetic field. However, the results obtained are the same as those using the standard Kalman Filter algorithm. Therefore, we conclude that the efficiency of reconstruction associated with slow-moving particles is not likely to be improved by any method in particular. This statement is valid under the experimental conditions that were available during the year of 2003.

The relevant tracks for the open-charm analysis are the ones that cross the SM1 magnet. A proper reconstruction of the D^0 invariant mass is assured through the identification of charged particles by the RICH detector (located downstream of SM1). These particles are only reconstructed if the fringe-field tracks can find corresponding segments downstream of the SM1. These segments are very well defined by a straight-line and, therefore, they are a valuable help in the removal of ghost tracks which were defined in the fringe-field [6]. The momentum resolution for particles whose fringe-field tracks are bridged over SM1 to the downstream segments is about 1.2%.

Ghost Tracks:

As already mentioned, the Cellular Automaton algorithm reconstructs also a huge amount

[5] These kind of ghost tracks mark some hits of real tracks (containing less cells or a worse χ^2) as being already in use.

[6] Note that these segments are extrapolated to the fringe-field zone through the strong field of SM1. The measured deflection allows us to know the position of the fringe-field track with a reasonably good precision.

of ghost tracks. About 94% of the selected tracks are ghosts. This poses no problem since no attempt was made to remove such tracks during the track-searching procedure. The vast majority of ghost tracks are later on removed from the reconstruction if they do not find a corresponding segment downstream of SM1. This procedure kills most of the high-level ghost tracks (containing 4 or 5 cells), which are the most difficult ones to remove. The remaining ghost tracks need to be removed by a different method. In Fig. 4.6, we can compare the real tracks that are reconstructed with the ghost and the not-reconstructed [7] tracks:

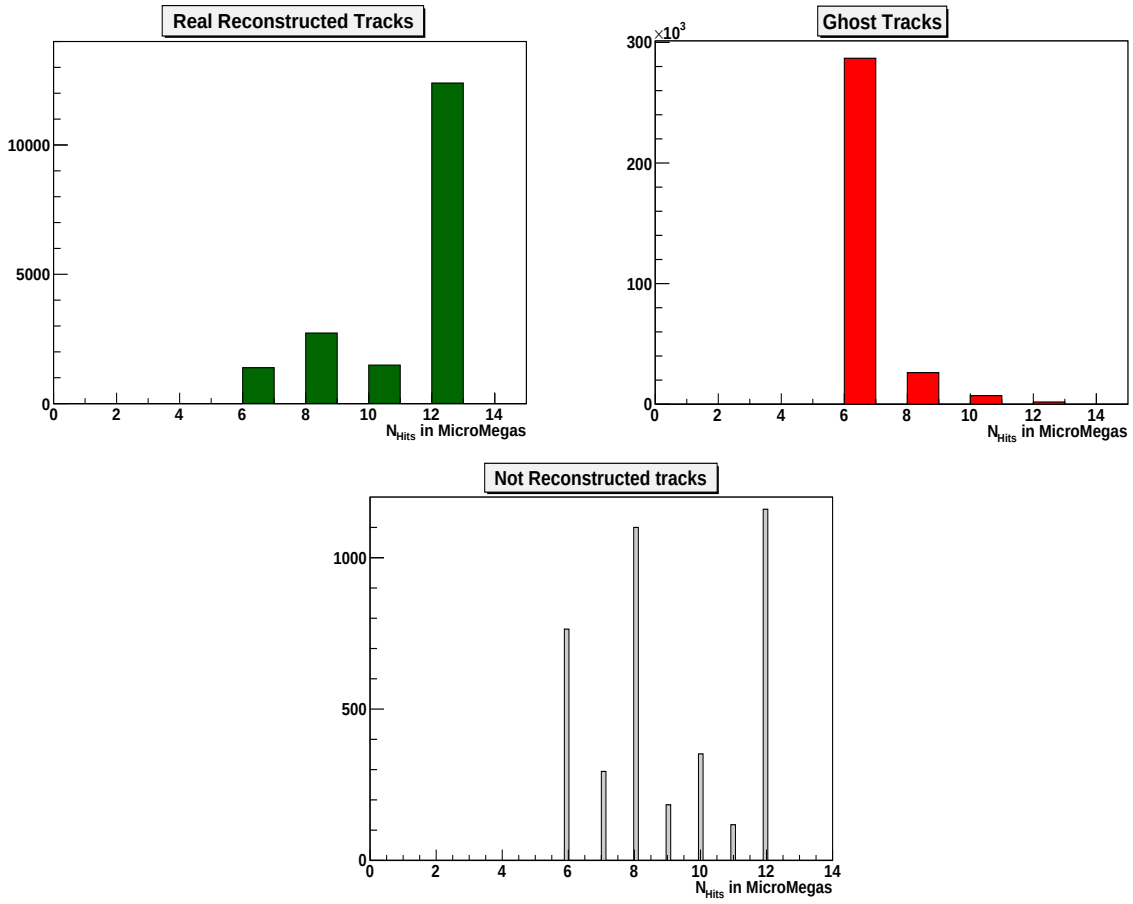

Figure 4.6: Total number of hits in the Micromegas produced by reconstructed (top-left), ghost (top-right) and missed (bottom) tracks.

From the figure above we conclude that about 90% of ghosts have their origin in the tracks of 2-cells containing 6 hits. Most of these tracks are removed from the fringe-field zone during the track-following part of the algorithm. To accomplish that, a minimum of 8 hits is demanded for the reconstruction of tracks in the fringe-field. These extra hits are added after a proper extrapolation of the track-candidates through the planes of the DC detector, and also through the missed planes of the Micromegas. The ghost contamination can be even further reduced by the application of a combined set of cuts in the momenta and in the residuals of all tracks (and also in the χ^2). We can confirm in Fig. 4.8 and in Fig. 4.9 that these quantities are significantly different for ghost tracks. After this selection, the fraction of reconstructed ghosts is kept below 10%.

[7] Note the large number of tracks with 12 hits that are not reconstructed. The justification for this lies on the poor momentum estimation for the slow-moving tracks. As a result, we may reconstruct a ghost track instead of a real one.

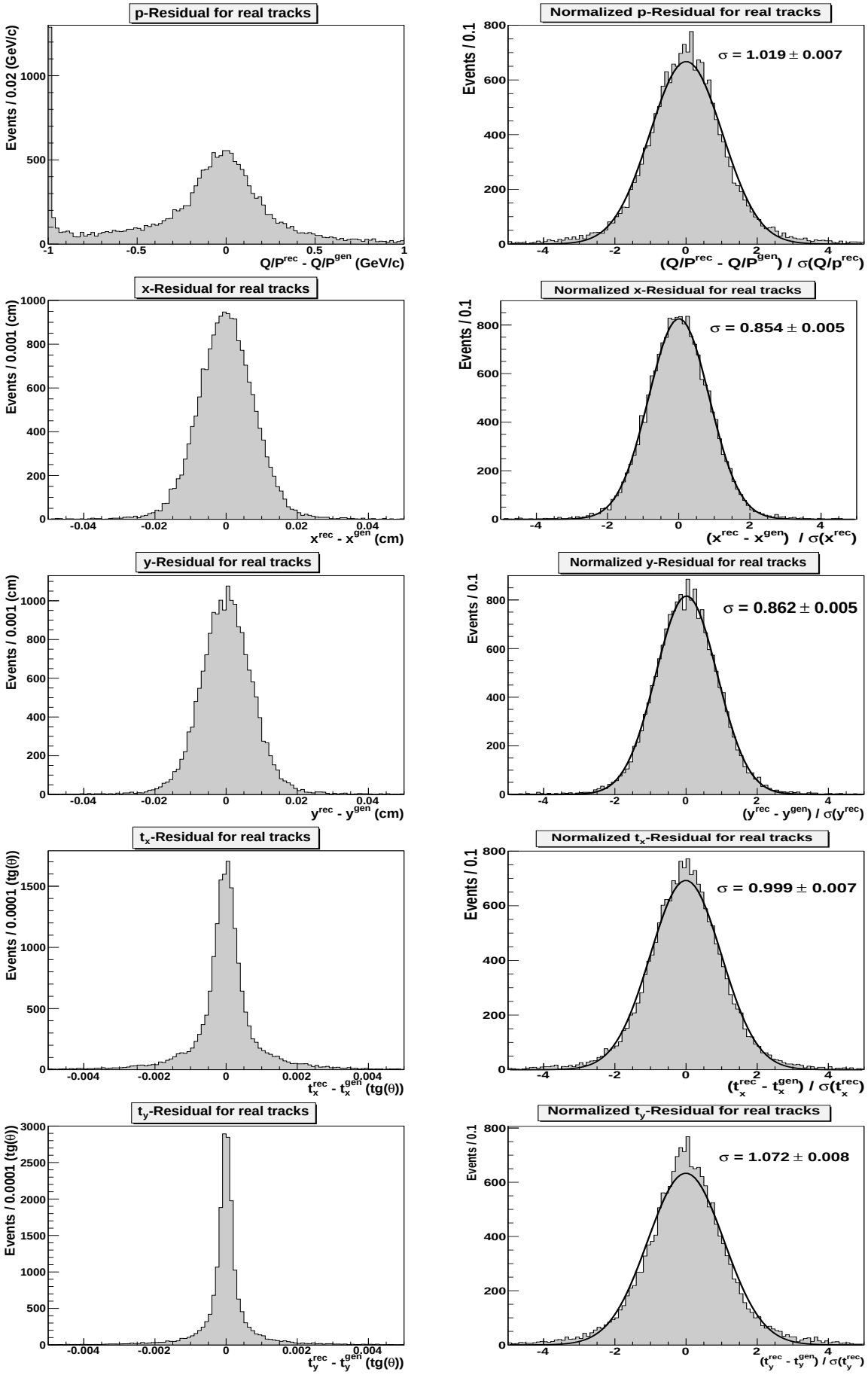

Figure 4.7: The residuals (left) and pulls (right) obtained for the relevant parameters defining a track. The definition of these two quantities can be seen on the figures.

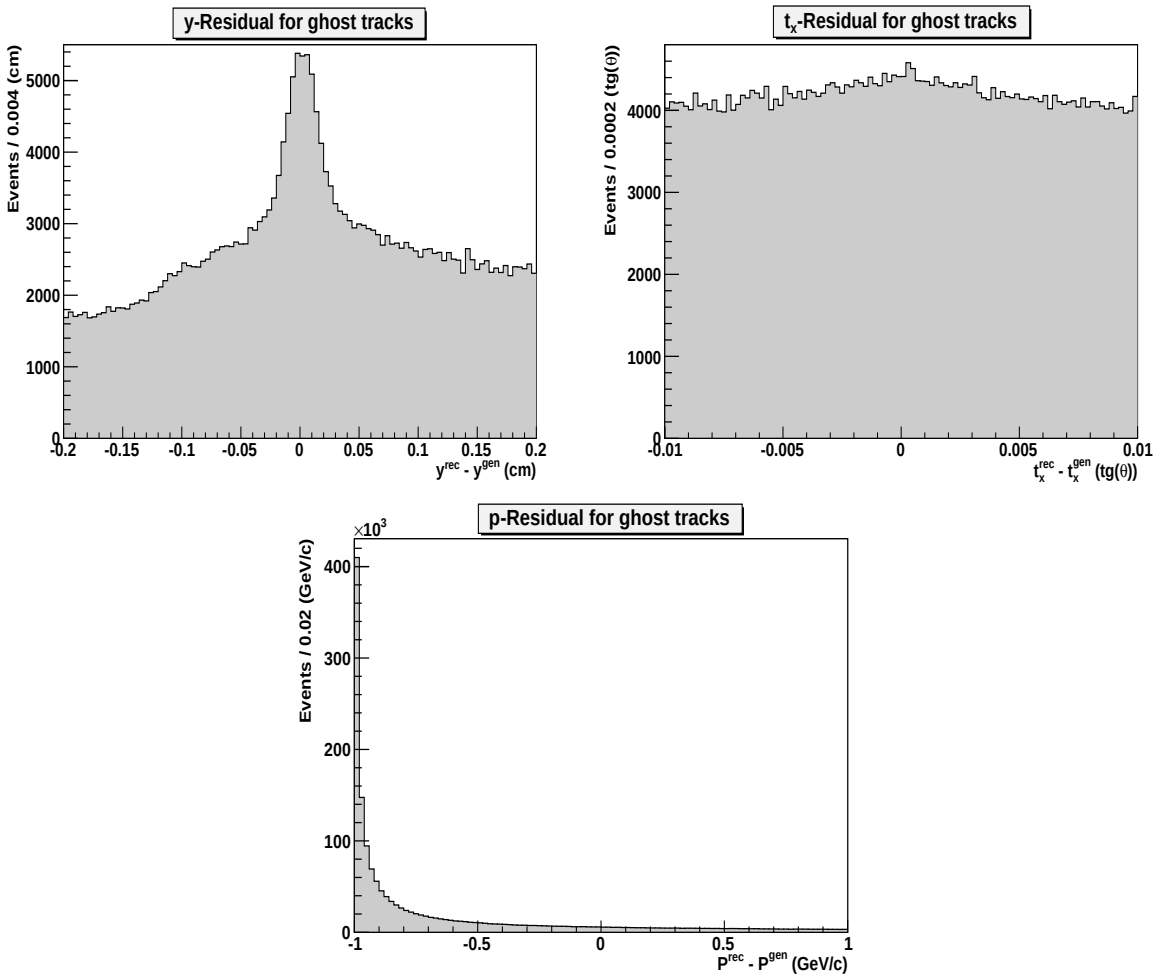

Figure 4.8: Examples of three residuals associated with ghost tracks.

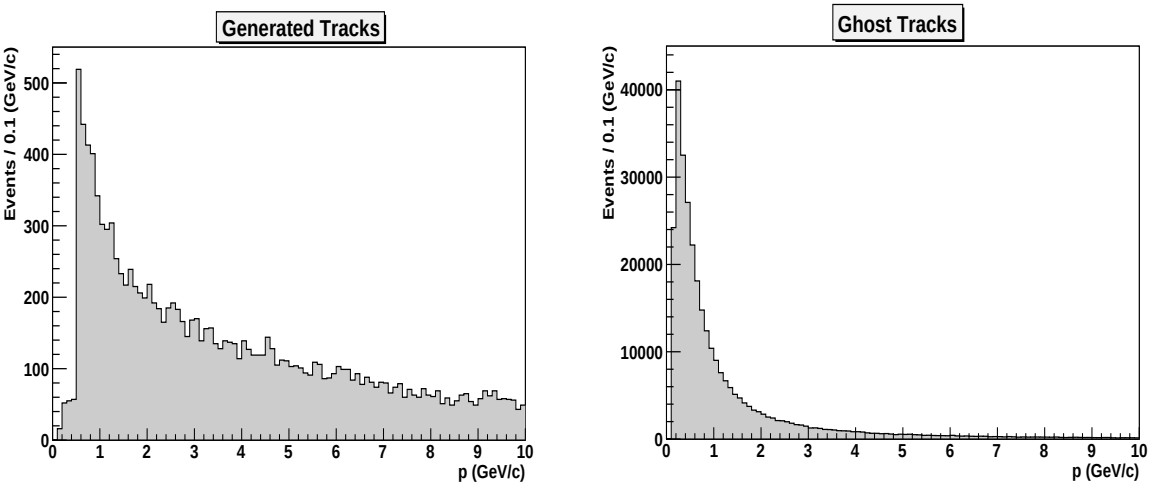

Figure 4.9: Momentum distribution of the generated tracks (left) and of the ghost tracks that are reconstructed (right).

Chapter 5

Reconstruction of D^0 Mesons

The purpose of this chapter is to provide a set of events where the fraction of those resulting from **P**hoton **G**luon **F**usion (PGF) is enhanced. In Chapter 2 it was shown that a PGF process can be distinctly tagged by the detection of a charmed meson (at LO-QCD): in the COMPASS kinematic domain the production of charm is a characteristic signature from an interaction involving a gluon (cf. Fig. 2.14) and, consequently, the gluon polarisation can be obtained from the measurable properties of the open-charm mesons that result from the fragmentation of the charm quarks. The production of these mesons is originated by the collision of the virtual-photon with one of the charm quarks[1]: due to the asymptotic-free nature of **Q**uantum **C**hromodynamics the struck quark escapes from the nucleon but, since all quarks need to be colour confined, the outcome of this interaction is the production of an open-charm meson (or baryon). At NLO-QCD, however, some of these mesons result from interactions between the virtual-photon and a light-quark of the nucleon (cf. Fig. 2.19). Nevertheless, this contamination is quite small and it can be easily taken into account in a proper NLO analysis (cf. sections 6.2 and 8.3).

The D^0 mesons are the open-charm references considered for the present analysis. Among the known open-charm hadrons, the D^0 has the best branching ratio to the most easily identifiable particles in the final state: kaons and pions. As in COMPASS there are no dedicated vertex detectors, restriction imposed by the cryogenic solid state target, it is only possible to have access to the identification of D^0 through its decay particles, pions and kaons. In the experiment, the best resolution achieved for the z component of the vertex is of the order of 1 cm, which makes it impossible to distinguish between the production and the decay vertices. Let's justify this argument by considering a D^0 with a (high) momentum of 50 GeV/c and a $c\tau$ of 122.9 μm [16] (with τ representing the D^0 proper time). Using $c = 1$, we have for the Lorentz factor:

$$\gamma = \left(\frac{E}{E_0}\right) = 26.81 \tag{5.1}$$

where

$$E_0 = M(D^0) = 1.8648 \text{ GeV} \qquad \text{and} \qquad E \overset{P^2 \gg E_0^2}{\approx} P \ (= 50 \text{ GeV})$$

Consequently, the total distance travelled by the D^0 in the spectrometer is

[1] The collision may also be seen as between a charm quark and a "polarised" gluon.

$$z = \gamma \times c\tau \overset{\text{eq.5.1}}{\approx} 3.29\ mm \qquad (\ll 1\ cm) \tag{5.2}$$

Since the reconstruction of these mesons needs be done via their invariant mass (due to the short life of D^0), an efficient identification of the particles that result from their decay is required (see section 5.2).

The following decay modes are considered for this analysis [2]:

$$D^0 \overset{3.89\%}{\rightarrow} K^-\pi^+ + cc \left(\textbf{c}\text{harge } \textbf{c}\text{onjugated} \in \overline{D}^0\right) \tag{5.3}$$

$$D^0 \overset{13.9\%}{\rightarrow} K^-\pi^+\pi^0 + cc \tag{5.4}$$

$$D^0 \overset{10.8\%}{\rightarrow} K^-\rho^+ \overset{\approx 100\%}{\rightarrow} K^-\left(\pi^+\pi^0\right) + cc \tag{5.5}$$

$$D^0 \overset{2.22\%}{\rightarrow} K^{*-}\pi^+ \overset{\approx 100\%}{\rightarrow} \left(K^-\pi^0\right)\pi^+ + cc \tag{5.6}$$

$$D^0 \overset{1.88\%}{\rightarrow} \overline{K}^{*0}\pi^0 \overset{\approx 100\%}{\rightarrow} \left(K^-\pi^+\right)\pi^0 + cc \tag{5.7}$$

$$D^0 \overset{8.09\%}{\rightarrow} K^-\pi^+\pi^+\pi^- + cc \tag{5.8}$$

$$D^0 \overset{6.76\%}{\rightarrow} K^-\pi^+\rho^0 \overset{\approx 100\%}{\rightarrow} K^-\pi^+\left(\pi^+\pi^-\right) + cc \tag{5.9}$$

In all the processes shown above, only the final particles have a sufficiently long life to be detected in the spectrometer. As a result, the different decay modes involving the same particles in the final state cannot be distinguished. Taking this fact into account, five independent data samples are defined for the study of the gluon polarisation:

	Non-tagged events	**Events tagged with a PGF D***			
Sample	$D^0_{K\pi}$	$D^*_{K\pi}$	$D^*_{K_{sub}\pi}$	$D^*_{K\pi\pi^0}$	$D^*_{K\pi\pi\pi}$
Reaction number	5.3	5.3	5.3	5.4, 5.5, 5.6, 5.7	5.8, 5.9

Table 5.1: Samples used in the analysis. The final state of a D^0 decay is indicated by a corresponding subscript. For the 'tagged' events, the D^0 is a product of a D^* decay: $D^* \overset{67.7\%}{\rightarrow} D^0\ \pi_{slow}$. For simplicity of notation the last 4 samples are referred to as D^* instead of tagged-D^0. Throughout this thesis, each sample will be referred to by the above notation.

The COMPASS RICH detector (cf. section 3.3.2 and [72]) is used to identify all particles in the final state. In this way we avoid the reconstruction of particles that are not kaons or pions. As a result, the signal purity of the D^0 mass spectra is substantially increased for all samples listed in Table 5.1. The remaining background is purely combinatorial and form a continuous underlying the reconstructed signal (see, for e.g., Fig. 5.16). This background is made

[2] They represent the reactions that can be reconstructed with enough statistics in COMPASS.

of kaons and pions that originate from other processes than PGF and that by chance have a somewhat similar kinematics to those particles coming from a D^0 meson. The only exception is the $D^*_{K_{sub}\pi}$ sample for which the kaon candidates are not directly identified. The justification for this absence of identification lies in the fact that these particles are outside the detection range for the kaon mass hypothesis: $p(K) < 9$ GeV/c (cf. Fig. 3.9) [3]. Simulations using a Monte Carlo generator for heavy flavours, AROMA [73], and a full spectrometer description based on GEANT, have shown that about 30% of kaons coming from D^0 decays have their momenta below this RICH threshold. Therefore, a considerable effort was made to recover such mesons for the analysis. However due to the existence of a higher D^0 contamination by the combinatorial background, the $D^0_{K_{sub}\pi}$ sample can only be reconstructed if their events come from a PGF D^*: the presence of an extra slow-pion in the final state allows us to significantly reduce the background through the application of a very efficient mass cut (cf. Fig. 5.12). By subtracting the pion mass to the difference obtained between the reconstructed D^* and D^0 masses, $M(D^*)^{rec} - M(D^0_{K_{sub}\pi})^{rec} - M(\pi)$, we end up only with a very small amount of available energy for the slow-pion momentum. Due to a clear domination of the pion mass over its momentum (cf. Fig. 5.21), we can measure this mass difference with a very good precision. Consequently, the purity of the $D^*_{K_{sub}\pi}$ spectrum is significantly improved. From now on this sample will be called as the RICH sub-threshold kaons sample.

For the same reason pointed out above, the samples $D^*_{K\pi\pi^0}$ and $D^*_{K\pi\pi\pi}$ are reconstructible only if they can be tagged with a D^* originating from a PGF process. However, the main causes for their low purity are different: for the $D^*_{K\pi\pi^0}$ sample the π^0 is not directly reconstructed in the COMPASS spectrometer, while for $D^*_{K\pi\pi\pi}$ the problem lies in the presence of a huge combinatorial background and a low momentum shared by four particles. In the former the signal appears in a lower mass region (compared to the real D^0 mass) of the invariant mass spectrum belonging to the $D^*_{K\pi}$ sample, as a sort of a 'bump' emerging from the combinatorial background, due to the non-identification of the neutral pion (see Fig. 5.14 and Fig. 5.15). This 'bump' also exists for the remaining samples but in those cases it is completely masked by the combinatorial background. Concerning the $D^*_{K\pi\pi\pi}$ sample, the main difficulty comes from the huge combination of the random pions that are available in the same kinematic region considered for a D^0 reconstruction. These particles are abundantly produced during the fragmentation of the nucleon caused by other processes than PGF. Also, because the number of particles in the final state is raised to four, the percentage of the RICH sub-threshold kaons is much higher. The same is true for the pions, which have an identification threshold of $p(\pi) > 2.5$ GeV/c. Consequently, and despite of the good branching ratio for this channel, the number of available D^0 mesons for reconstruction is considerably lower when compared to the $D^*_{K\pi}$ sample. The RICH sub-threshold events cannot be efficiently recovered for the $D^*_{K\pi\pi\pi}$ sample due to the enormous background contamination.

Finally, as it is clear from the above discussion, the $D^*_{K\pi}$ is the golden sample for this analysis. The corresponding mass spectrum can be reconstructed with a very good signal purity and, because of that, it also allows us to reconstruct these candidates for the untagged case: $D^0_{K\pi}$ mesons coming directly from the PGF interaction. In this chapter we will discuss the kinematic selection of all the mass spectra corresponding to the samples listed in Table 5.1. The goal is to reduce the combinatorial background as much as possible. Thereafter, in Chapter 7 we will show how to minimise the impact of the remaining background in the results. From now on all samples of Table 5.1 will be referred to as channels of analysis.

[3] Other types of particles that cannot be identified in this range are the protons. The latter can be reconstructed as kaons, and therefore the combinatorial background is significantly larger for this particular sample.

5.1 Event selection

Since the extraction of the gluon polarisation involves the measurement of small spin asymmetries, the first thing that one must control is the quality of the data. This is done by ensuring the existence of a steady performance of the spectrometer during the collection of the data under study. In fact, this is a critical condition for a reliable analysis: if the experimental apparatus is changed in such a way that the ratio of acceptances between the target cells is also changed (cf. Fig. 3.3 and Fig. 6.1), the natural consequence is the generation of false asymmetries for the corresponding data. This may also happen if some of the events used in the asymmetry calculation are collected by a certain detector which suddenly changed its efficiency. Before we proceed further, let's introduce some important definitions:

- **Event:** it is defined by the interaction of a single polarised muon in a specific target cell.
- **Spill:** corresponds to a bunch of polarised muons delivered to the COMPASS target, per unit of time. Each spill lasts for 4.8 s and has the following beam intensities:
  - 2.2×10^8 $\mu^+/16.8$ s (2002, 2003, 2004 and 2006 data: ^{6}LiD target).
  - 4.5×10^8 $\mu^+/16.8$ s (2007 data: NH_3 target).
- **Run:** a short period of data taking. Typically it includes 200 spills of data.
- **Week / Period:** defines a period of data acquisition (seven days), separated by a few hours normally used by the accelerator team for developments.

Data is considered stable if the time interval during which the spectrometer performance is tested is reasonably short. Therefore, using the definitions given above, it was decided to control the quality of the data on a spill-by-spill level. Basically, the following quantities are used to monitor the stability of the data acquisition:

- Average number of primary vertices per spill.
- Average number of beam tracks per spill.
- Average number of tracks per spill.
- Average number of tracks in the primary vertex per vertex.
- Integrated muon beam flux.

The spills in which at least one of the above quantities is more than 5 sigmas away from the main band are removed from the analysis. Spills with less than 3 times the mean number of events are also rejected, as well as a group of them which are revealing a systematic shift as compared to the neighbouring spills. Finally, a group of runs is rejected due to an online evaluation of their bad quality (e.g., relevant errors on the acquisition of some important detectors). The list of spills and runs which are removed from the analysis are summarized in Ref. [74].

In order to ensure the spectrometer stability, we should group a few runs of data and then perform a separate analysis for each of these groups. The main goal is to suppress the contributions of potential systematic effects induced by the reversal of the target spins, which for the 2-cells scheme of the target (2002, 2003 and 2004) is performed every 8 hours. This procedure is necessary to ensure an equal contribution from each spin configuration to the measured asymmetry, but unfortunately it can also disturb the stability of the experimental apparatus (e.g., by slightly moving the position of one of the cells). The impact of the dipole and solenoid fields in the spectrometer stability was studied in detail and considered in the systematic error (cf. Chapter 9). For the 2006 and 2007 data the target spins are reversed only once every 24 hours, taking advantage of the new polarised target composed by three cells. This target configuration was designed to minimise the differences in the experimental acceptance of each spin configuration (see Fig. 5.1): by adding the events produced in the upstream and downstream cells, which are longitudinally polarised along the same direction opposite to the middle cell, we can obtain the same experimental acceptance as it is experienced by those events coming from the middle cell. As a result, the need for a spin reversal in the target is much less critical for the 3-cells scheme.

During 8 hours one is able to acquire 4 to 6 runs of data but, unfortunately, for the present analysis this corresponds to an insignificant amount of the reconstructible D^0. The same is true for the 12 to 18 consecutive runs which are acquired with the same spin configuration during the years of 2006 and 2007. Therefore, due to the statistical limitations resulting from the charm production at COMPASS, this analysis is performed only on a week-by-week basis.

5.1.1 Basic cuts

After a proper run selection (as explained above), the following criteria are applied in order to enhance the selection of open-charm events from the raw data:

1. **Only the events associated with a primary vertex are considered for the D^0 reconstruction:** one and only one incoming muon must be assigned to this kind of vertices;

    - If more than one exists, the vertex with the best χ^2 fit is chosen.

2. **One scattered muon must be reconstructed from this primary vertex:** the relevant trigger hodoscopes for the open-charm analysis, which are the inner and the ladder triggers [60], should contain some hits that can be associated with this track.

3. **In addition to the scattered muon, a minimum number of outgoing particles from the primary vertex is required:**

    - 2 reconstructed tracks for the untagged $D^0_{K\pi}$ channel.
    - 3 reconstructed tracks for the following D^*-tagged channels (K, π, π_{slow}): $D^*_{K\pi}$, $D^*_{K_{sub}\pi}$ and $D^*_{K\pi\pi^0}$.
    - 5 reconstructed tracks for the $D^*_{K\pi\pi\pi}$ channel.

4. **No secondary vertices are allowed:** the D^* and D^0 mesons are too short lived to be detected through their decay vertices. Using the opposite argument, the kaons and pions are long lived enough to be directly detected by the COMPASS spectrometer.

5. **The incoming muon beam must cross all target cells:** this can be ensured after the extrapolation of the measured beam track to the beginning of the upstream cell and to the end of the downstream cell. The tri-dimensional points defined by the extrapolated positions must be inside the physical limits of the corresponding target cells. This allows us to normalise each cell to the same beam flux, for the events used in the calculation of the spin asymmetry, and at the same time it avoids the use of events coming from interactions with the halo muons.

6. **The primary vertices must be reconstructed inside of one of the target cells:** we need to ensure that the reconstructed kaons and pions result from a polarised interaction. This is the case when the ^{6}LiD (2002, 2003, 2004 and 2006 data) or NH_3 (2007 data) materials are hit by a polarised muon. So, the reconstruction of primary vertices must allow for a clear assignment of events to each of the target cells (see Fig. 5.1).

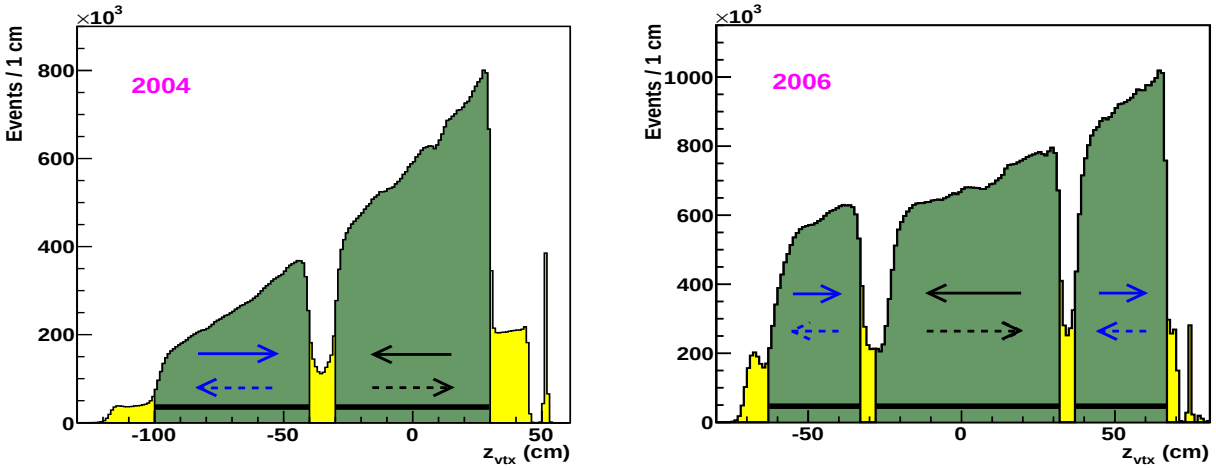

Figure 5.1: Primary vertex distribution after all cuts explained in section 5.1.1. The z component along the beam axis is chosen to illustrate that each event can undoubtedly be assigned to a specific target cell (green bands / thick bars). The arrows indicate the orientation of the target spins before (solid lines) and after (dashed lines) the reversal of the solenoid field. Also, from these figures one can see that more events are reconstructed in the downstream cells: their acceptance is larger because they are closer to the exit of the solenoid aperture.

5.2 PID: Particles identification

As it was already explained, in COMPASS the detection of a D^0 meson must be done via the reconstruction of its invariant mass. In order to obtain a good signal purity for the mass spectra we must properly identify the nature of the mesons resulting from the D^0 decay, as this significantly reduces the combinatorial background coming from the production of other types of particles. To accomplish that, a **R**ing **I**maging **CH**erenkov (RICH) detector is used to identify the relevant particles for this open-charm analysis: charged kaons and pions. The

operation of the detector is described in detail in section 3.3.2. Here the only goal is to present the method used to identify these mesons. In COMPASS, the PID algorithm [72] uses the Extended Likelihood Method which is based on the Cherenkov effect. For each particle of momentum p and mass M that reaches the RICH within its geometrical acceptance, the expected angle for the Cherenkov emission can be calculated as follows [4]:

$$\cos\theta_M = \frac{1}{n\beta} = \left(\frac{\sqrt{p^2+M^2}}{np}\right) \tag{5.10}$$

where n is the refractive index of the gaseous radiator that fills the detector. All the Cherenkov photons emitted by a given particle passing through the gas contained in the RICH vassel are expected to have the same polar angle θ_M and an uniformly distributed azimuthal angle ϕ. Taking advantage of this fact, we can use the Cherenkov equation 5.10 to determine a critical variable for the RICH PID: the refractive index n of the gaseous radiator. This important variable n is dependent on several parameters, which may change along the time, such as the purity of the gas, the atmospheric pressure, its temperature, etc. As a result, the experimental measurements of n need to be complemented with the determination of the refractive index from the data (in order to properly account for its time dependency). This is done as follows: for every charged particle entering the RICH with a measured momentum p, the refractive index is calculated for each photon associated to the particle by assuming the pion mass (using eq. 5.10). The momentum is measured with the help of the tracking system before and after the magnetic field (see section 3.3), and the assumption on the pion mass leads to a minimum bias introduced by the method. Using this approach we obtain a Gaussian-like distribution for the refractive index. The Gaussian gives the mean value for the refractive index n.

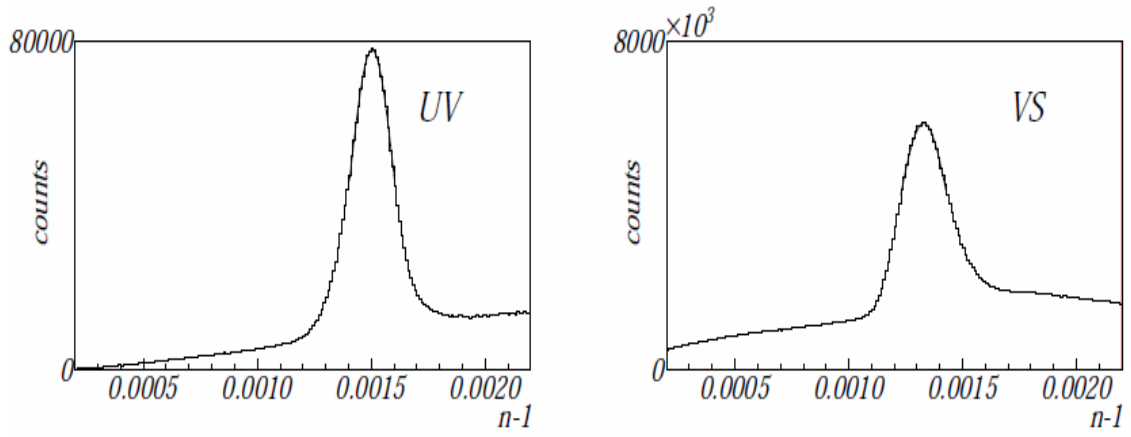

Figure 5.2: Distribution of the refractive index calculated from the reconstructed photons. To the left one can see the distribution obtained from photons with UV energies (emitted by tracks passing through the outer part of the detector), and to the right it is shown the distribution obtained from the detected photons belonging to the visible spectrum (inner part of the RICH). The solid lines correspond to the best fit of these distributions.

We can consider alternative methods, namely by using the distribution of photons associated only to identified particles (originating a cleaner peak), but unfortunately they can suffer from biases due to the selection criterium of the sample.

[4] Note that θ_M is the same variable as the θ_C defined in section 3.3.2.

The refractive indices are experimentally measured every 24 hours of data taking, and then their time evolution are determined as a function of the pressure and the temperature of the gaseous radiator (which are continuously monitored). The refractive indices which were determined from the data are then used as a correction to these experimental values but, before that, let's first describe the Likelihood algorithm for PID.

5.2.1 The Likelihood method

The Extended Likelihood Function for each mass hypothesis is written as follows:

$$L_x(M) = e^{-(S_M+B)} \times \Pi_{i=1}^{N} \left[\underbrace{\left(\frac{S_0}{\sigma_{\theta_i}\sqrt{2\pi}} \right) e^{-\frac{1}{2}\frac{(\theta_i-\theta_M)^2}{\sigma^2_{\theta_i}}} \xi(\theta_j,\phi_i)}_{s_M(\theta_i,\phi_i)} + b \right] \tag{5.11}$$

where

Variables	**Meaning**
$L_x(M)$	Likelihood for a particle x, assuming a mass hypothesis M
N	Number of detected photons
θ_i	Polar angle for each reconstructed photon
ϕ_i	Azimuthal angle for each reconstructed photon
$\xi(\theta_j,\phi_i)$	Photon probability to reach the RICH photon detectors
θ_M	Expected Cherenkov angle for a particle of mass M and momentum p (eq. 5.10)
σ_{θ_i}	Single-photon resolution
b	Background hypothesis for the origin of a single reconstructed photon
$s_M(\theta_i,\phi_i)$	Signal hypothesis for the origin of a single reconstructed photon
B	Expected number of background photons
S_M	Expected number of signal photons
S_0	Expected number of photons from the Frank-Tamm law: $S_0 = N_0 \times \sin^2\theta_M$
N_0	Number of photons at saturation ($N_{\beta\to1}/\sin^2\theta_{M,\beta\to1}$)

Table 5.2: Definition of the variables used in eq. 5.11.

The parameter b takes into account the possibility that each photon can belong to the background. Background photons have their origin in the out of time hits and also in the detector

noise: they are calculated from the integrated cluster distribution on the photon detectors, normalised to one event. Also, since the Extended Likelihood Function is used, the parameters $s_M(\theta_i, \phi_i)$ and b do not need to be normalised probabilities. Concerning the variables S_M and B, they result from the integration of the previous parameters over a region defined up to the maximum Cherenkov angle allowed by the RICH detector (70 mrad). Finally, σ_{θ_i} can be determined from a parameterisation obtained on data. This error is evaluated from two angular distributions: $\theta_i - \theta_\pi$, assuming the pion mass for all the photons associated with a given track, and $\theta_i - \theta_R$ for the photons belonging only to the reconstructed rings (see e.g. in Fig. 3.8). The distributions of the former (cf. Fig. 5.3) are parameterised as a function of the particle polar angle θ_x, the particle momentum p and the photon azimuthal angle ϕ. Using these parameterisations we can obtain the error associated to every reconstructed photon, coming from the MWPC ($\sigma_{\theta_i(UV)}$) or the MAPMT ($\sigma_{\theta_i(VI)}$) detectors.

The distribution involving θ_π has the advantage of a much clearer physical definition. However, the calculation of θ_π is also dependent on the uncertainties in the determination of the refractive indices and the particles momentum. Therefore, in order to avoid an exclusive dependence on θ_π, the distribution of $\theta_i - \theta_R$ is also used to build the final parameterisation. In Fig. 5.3 we can see the $\theta_i - \theta_\pi$ distributions, as an example, from which we can estimate a typical resolution of 2.1 mrad and 2.0 mrad for the MAPMTs and MWPCs detectors, respectively (half width of the distributions).

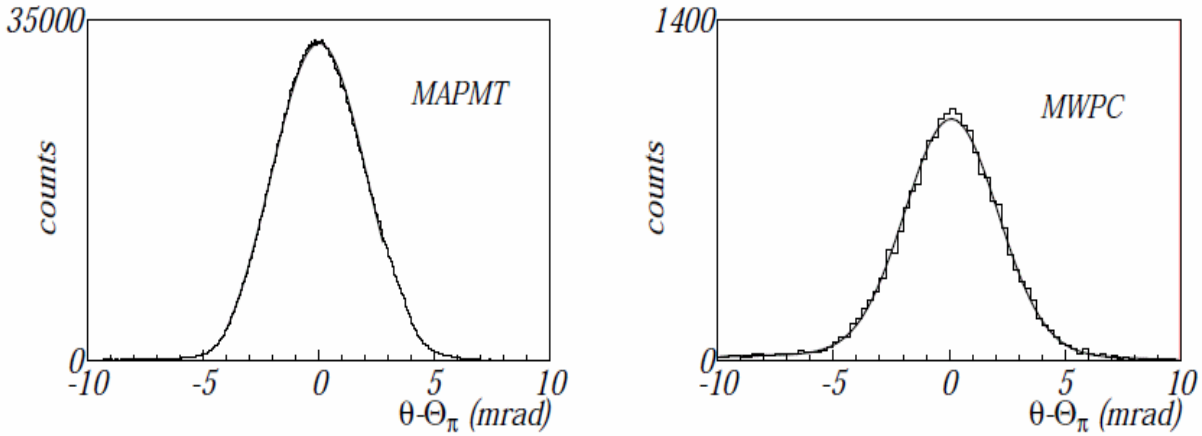

Figure 5.3: To the left one can see the $\theta_i - \theta_\pi$ distribution of the photons detected by the MAPMTs. To the right, the equivalent distribution for the MWPC detectors is shown. Typically, resolutions of 2.1 mrad and 2.0 mrad are obtained (for the left and right distributions, respectively).

The extraction of the Likelihoods for the various mass hypotheses - e, μ, K, π, Pr (proton) and also for the *background* - is done through the calculation of $L_x(M)$ for each of these cases, and, for the background hypothesis, it is assumed that $S_M(\theta_i, \phi_i)$ is zero (in eq. 5.11). The remaining variable, $\xi(\theta_j, \phi_i)$, is determined by considering that the photons can be absorbed by the beam pipe, lost because of the holes between the mirrors forming the large mirror wall, or lost due to the dead zones in the photon detectors [72]. In first order of approximation, the maximum of all the $L_x(M)$ values correspond to the best mass hypothesis. However, for the present analysis, the identification of the relevant charged particles is performed as follows:

- **Pions from a D^0 decay (π):** $\frac{L_\pi(\pi)}{L_\pi(K)} > 1$ & $\frac{L_\pi(\pi)}{L_\pi(bg)} > 1$

- **Kaons from a D^0 decay (K):** $\frac{L_K(K)}{L_K(\pi)} > 1$ & $\frac{L_K(K)}{L_K(bg)} > 1$ & $\frac{L_K(K)}{L_K(Pr)} > 1$

- **Pions from a D^* decay (π_{slow}):** $\frac{L_{\pi_s}(e)}{L_{\pi_s}(\pi)} \gg 1$ & $\frac{L_{\pi_s}(e)}{L_{\pi_s}(bg)} \gg 1$ (conditions to reject events)

  – Since typically we have $p(\pi_{slow}) < 8$ GeV/c (favourable energies for electrons), the RICH acts as an electron veto for these candidates: if there is a positive electron identification the event is rejected.

All the Likelihoods above are corrected in the following way:

$$L_x(M) = L_x(M)^{\text{tmp}} + dL_x(M)\left[n^{\text{exp}} - n^{\text{data}}\right] \tag{5.12}$$

where $L_x(M)^{\text{tmp}}$ is a temporary Likelihood calculated from eq. 5.11, $dL_x(M)$ is the Likelihood derivative for the mass hypothesis M, n^{exp} is the measured refractive index and n^{data} is the refractive index determined from the data (see Fig. 5.2). Since the identification of these particles is made by comparison of the different mass hypotheses, the term e^{-B} in eq. 5.11 is neglected (it is the same for all cases). The conditions illustrated above reflect an ideal situation, however, they are tuned per channel and year. The aim is to get the best signal-strength [5] of the resonance in the D^0 mass spectra, without removing a significant amount of signal events (cf. Fig. 5.4). The number of signal and background events are obtained from the integral of the best fit to the reconstructed peak and to the underlying background, respectively, using only those candidates within a mass window of $(M^{rec}_{D^0} - M_{D^0}) \in \pm 40$ MeV/c^2 ($\approx 2\sigma(D^0)$, cf. Fig. 5.15). Those two conditions are critical for this analysis because, as demonstrated in Chapter 6, the signal-strength obtained from the D^0 mass spectra is inversely proportional to the statistical error of the determination of the gluon polarisation. The list of all Likelihood cuts used in the analysis is shown in the next section.

5.2.2 Likelihood cuts

Years	**Kaon PID**			**Pion PID**		**Electron Rejection (π_s)**		
	$\frac{L_K(K)}{L_K(\pi)} >$	$\frac{L_K(K)}{L_K(bg)} >$	$\frac{L_K(K)}{L_K(Pr)} \geq$	$\frac{L_\pi(\pi)}{L_\pi(K)} >$	$\frac{L_\pi(\pi)}{L_\pi(bg)} >$	$\frac{L_{\pi_s}(e)}{L_{\pi_s}(\pi)} >$	$\frac{L_{\pi_s}(e)}{L_{\pi_s}(bg)} >$	$\frac{L_{\pi_s}(e)}{L_{\pi_s}(K)} >$
2007	1.05	0.99	1	0.9	0.99	1.1	2	1
2006	0.99	0.99	1	0.9	0.99	1.5	2	1
2004 (new)	1.02	0.95	1	0.9	0.99	1.5	1.8	1
2004 (old) [6]	0.97	0.97	1	0.9	0.99	1.5	1.5	1
2003	0.97	0.99	1	0.9	0.99	1.5	1.5	1
2002 (new)	0.99	0.99	1	1	1	1	1.5	1
2002 (old) [7]	/	1.01	1	1	1	/	/	/

Table 5.3: RICH coefficients for the selection of the $D^*_{K\pi}$ and $D^*_{K\pi\pi^0}$ channels.

Years	Kaon PID			Pion PID (3π)		Electron Rejection (π_s)	
	$\frac{L_K(K)}{L_K(\pi)} >$	$\frac{L_K(K)}{L_K(bg)} >$	$\frac{L_K(K)}{L_K(Pr)} \geq$	$\frac{L_\pi(\pi)}{L_\pi(K)} >$	$\frac{L_\pi(\pi)}{L_\pi(bg)} >$	$\frac{L_{\pi_s}(e)}{L_{\pi_s}(\pi)} >$	$\frac{L_{\pi_s}(e)}{L_{\pi_s}(bg)} >$
2007	0.98	0.97	1.0	0.9	0.99	1.2	1.5
2006	1.1	1.1	1.0	0.9	1.0	1.5	1.5
2004	1.0	1.0	1.0	0.9	1.0	1.3	1.5
2002+2003	1.02	1.05	1.0	0.9	1.0	1.3	1.5

Table 5.4: RICH coefficients for the selection of the $D^*_{K\pi\pi\pi}$ channel.

Years	Kaon Recovery		Pion PID		Electron Rejection (π_s)	
	$\frac{L_K(\pi)}{L_K(bg)} <$	$\frac{L_K(e)}{L_K(bg)} <$	$\frac{L_\pi(\pi)}{L_\pi(K)} >$	$\frac{L_\pi(\pi)}{L_\pi(bg)} >$	$\frac{L_{\pi_s}(e)}{L_{\pi_s}(\pi)} >$	$\frac{L_{\pi_s}(e)}{L_{\pi_s}(bg)} >$
All years	1.2	1.2	0.9	0.99	2.0	2.0

Table 5.5: RICH coefficients for the selection of the $D^*_{K_{sub}\pi}$ channel.

Years	Kaon PID			Pion PID	
	$\frac{L_K(K)}{L_K(\pi)} >$	$\frac{L_K(K)}{L_K(bg)} >$	$\frac{L_K(K)}{L_K(Pr)} \geq$	$\frac{L_\pi(\pi)}{L_\pi(K)} >$	$\frac{L_\pi(\pi)}{L_\pi(bg)} >$
2007	1.1	0.99	1	0.9	0.99
2006	1.1	0.99	1	0.9	0.99
2004 (new)	1.02	1.05	1	0.9	0.99
2004 (old)	0.98	1.15	1	0.9	0.99
2003	1.02	1.05	1	0.9	0.99
2002 (new)	0.98	1.15	1	1	1
2002 (old)	/	1.01	1	1	1

Table 5.6: RICH coefficients for the selection of the $D^0_{K\pi}$ channel.

In the tables shown above, for all channels, all cuts introduced by the Likelihood ratios are required to be fulfilled at same time (except for the electron rejection cuts): one D^0 candidate is accepted if its Likelihood ratios for the kaon and pion candidates are simultaneously true, according to the RICH coefficients which are defined for the corresponding channel/year. Concerning the slow-pion, instead of a positive identification, the RICH detector acts as an electron veto. There are two reasons justifying this approach. The first one is related to the inability of the detector to identify kaons and protons at low momentum (see Fig. 3.9), while the second reason lies on the fact that within a momentum range defined by $p < 8$ GeV/c the electron contamination is quite significant. Since the contamination introduced by other types of parti-

[5] $S^2/(S+B)$, with $S = D^0$ events and $B =$ background events.
[6] 7 periods of 2004 (out of 13) were produced with an older version of the RICH and tracking algorithms.
[7] 2 periods of 2002 (in a total of 6) were produced with an older version of the RICH code.

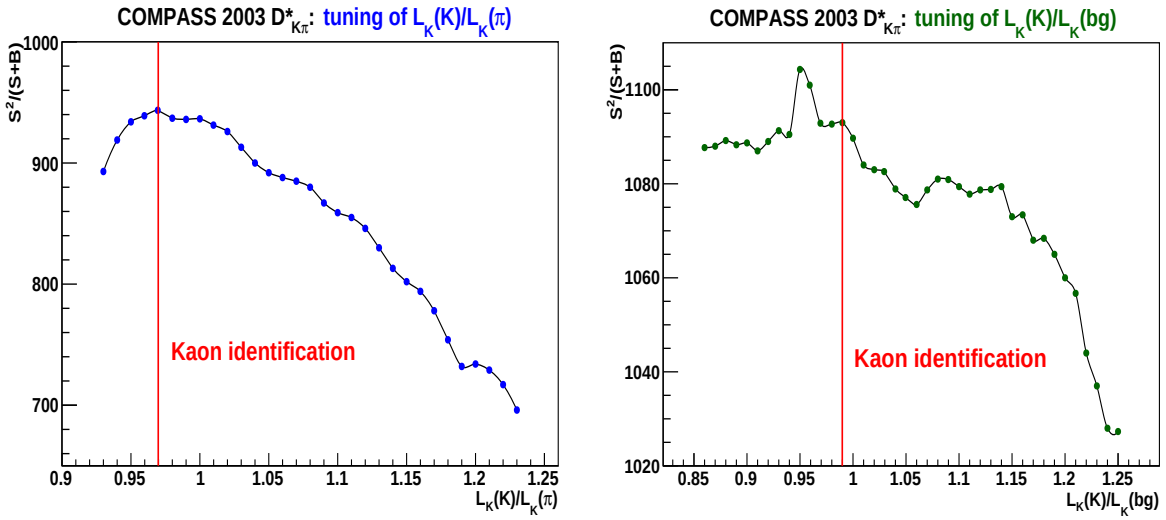

Figure 5.4: Example for the tuning of the kaon Likelihood ratios (see table 5.3). The goal is to maximise the signal-strength for the selected D^0 mesons, if and only if the signal is not reduced by more than 10%. The ratio $L_K(K)/L_K(\pi)$ is the first one to be optimized (left plot), and then the procedure is repeated iteratively until a convergence is achieved for the two ratios: $(L_K(K)/L_K(\pi))^{max}$ is used for the tuning of $L_K(K)/L_K(bg)$, and vice versa. Also, in order to avoid possible statistical fluctuations, the maximum value from each distribution is taken, instead of the absolute maximum value (cf. right plot).

cles is comparatively much smaller (due to their lower production rates), these two reasons are enough to justify the method used for the cleaning of the slow-pion sample. Therefore, if the slow-pion passes through the RICH acceptance, the corresponding D^0 candidate is accepted if and only if the particle is not identified as an electron. The events that have all the Likelihood ratios for the slow-pion simultaneously verified are rejected. For the cases where the slow-pion does not have any RICH information, the D^0 candidate is still considered in order to take advantage of the D^*-tag effect. This lack of information can happen, because particles of low momentum can be easily deviated from the experimental acceptance of the RICH by the srong magnetic field of SM1 (see Fig. 3.5).

We can verify the quality of the RICH PID in Fig. 5.5. The upper plots illustrate in a clear way the relevance of the RICH detector for a proper PGF selection. To the left, we see the invariant mass distribution for the kaon candidates considered for a D^0 selection but, as expected, this sample is strongly contaminated by pions coming mostly from other processes than PGF (blue distribution). However, after the application of the Likelihood cuts for the kaon ID, a very clean sample of kaons is obtained (cf. mean value of the zoomed spectrum of the upper-left plot). Concerning the bottom-left figure, the mass distributions, with and without Likelihood cuts, are shown for the slow-pion candidate that is used to tag a D^0 event with a PGF D^*. The clean distribution (yellow) shows a reduction of the background in the order of 65%, after the electron rejection cuts, without removing any part of the signal. To the right (gray plot), the same distribution is shown but this time with the kaon and pion Likelihood cuts applied: the background is even more suppressed, due to the constraints imposed to the other particles coming from a D^0 decay, but not completely vanished. In fact, the left wing of the peak cannot be considered as containing only background events. The majority of them have a momentum smaller than 2 GeV/c and, as a result, their momenta are measured with a large uncertainty due to the influence of the magnetic fringe-field which is present in the first

sector of the spectrometer [8] (see Chapter 4). Consequently, the invariant mass of the slow-pion will be underestimated for most of these events (cf. eq. 5.10). Due to this fact, we cannot remove more background events, by tightening the electron rejection cuts, without suppressing part of the signal belonging to the D^0 mass spectrum (the signal-strength is decreased).

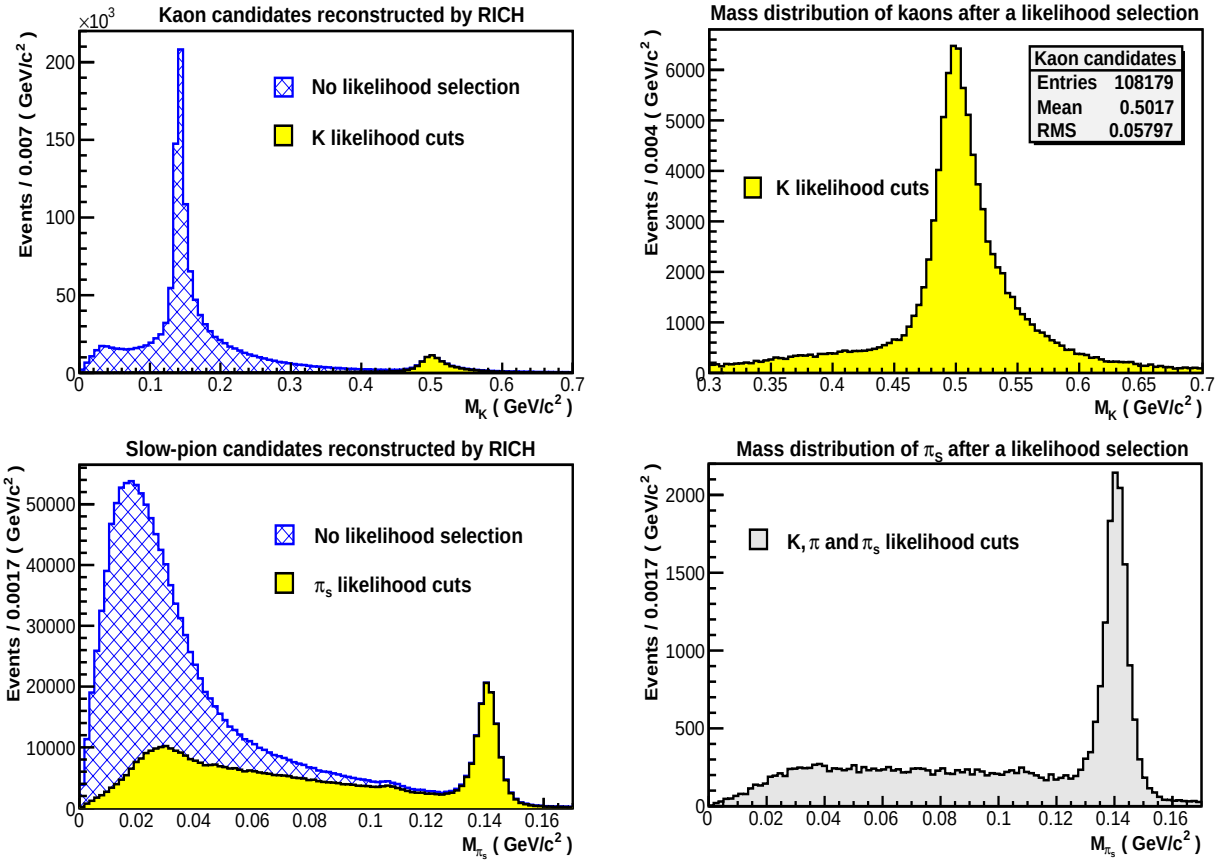

Figure 5.5: Left: the reconstructed invariant mass by the RICH detector, for the kaon (up) / slow-pion (bottom) candidates, using eq. 5.10. Right: zoomed spectrum of these candidates after the corresponding Likelihood selection.

Concerning the $D^*_{K\pi\pi\pi}$ channel the data belonging to the years of 2002 and 2003 are analysed together due to their low amount of events. For the same reason, the data from 2002 and 2004 are only separated according to the old/new productions for the main channels of analysis: tagged and untagged $D^0_{K\pi}$ samples. The cuts applied to the $D^*_{K_{sub}\pi}$ channel are tuned in a very loose way for all years. The justification for this procedure comes from the necessity of having a good amount of signal to determine the gluon polarisation with the best possible precision. However, for the sub-threshold kaons channel, the most important particle for the D^0 selection is almost unidentified. Consequently, we obtain a quite low signal-strength from the invariant mass spectra of these candidates, due to a big contamination of the kaon sample induced by the loose cuts. This difficulty can be overcome provided that the signal be preserved during the D^0 selection: the signal-strength can be greatly improved by a proper Neural Network parameterisation (see Chapter 7), which assigns a D^0 probability to each event, and therefore the impact of the background contamination is significantly reduced. For this reason, and specially for the $D^*_{K_{sub}\pi}$ channel, the RICH cuts are left loose enough in order to preserve as much sig-

[8] The description of the multi-scattering of slow-moving particles in the detectors is also quite difficult.

nal as possible. Two kinds of sub-threshold kaons are considered:

- **Kaon candidates with RICH information for the lower mass hypotheses:** they are recovered like kaons if they are not identified as pions or electrons (cf. table 5.5).

- **Kaon candidates without RICH information but within the geometrical acceptance of the detector**[9]**:** they are recovered like kaons if their momenta are above the RICH threshold for the pion identification ($p(K) > 2.5$ GeV/c).

It should be emphasised that this kaon recovery does not introduce any bias in the analysis. The only contamination with some relevance in the $D^*_{K_{sub}\pi}$ channel comes from low momentum protons that are impossible to detect (cf. Fig. 3.9). Nevertheless, in the momentum range considered, the ratio defined by the different production rates of protons and kaons is smaller than 10% (verified on Monte Carlo). This contamination appears in the invariant mass spectrum as a combinatorial background, possibly under the reconstructed D^0 peak, but since we use only the peak (where the PGF events are located) to estimate the gluon polarisation, this procedure is completely free of any bias. We can see in Fig. 5.6 and in Fig. 5.7 the impact of the RICH PID in the D^0 selection:

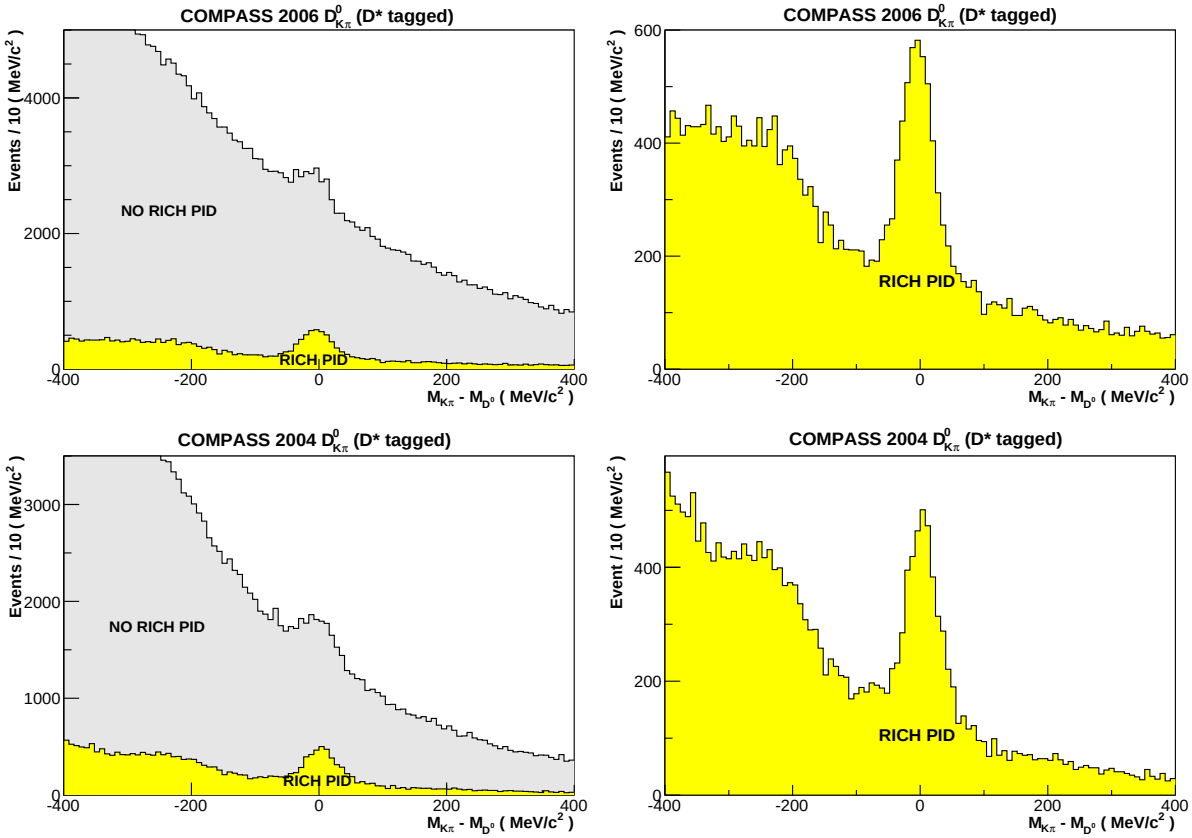

Figure 5.6: Upper line: to the left we can see the invariant mass distribution, for the golden channel, with (yellow) and without (light gray) RICH identification, for the data collected by COMPASS during the year of 2006. To the right (zoomed spectrum), one can confirm the big improvement in the signal purity achieved by the RICH PID. Bottom line: the same information is shown for the year of 2004 (smaller acceptance of the spectrometer).

[9]This can happen to those sub-threshold particles for which it is not possible to associate a single noise photon to its background hypothesis (due to a very clean environment inside the RICH).

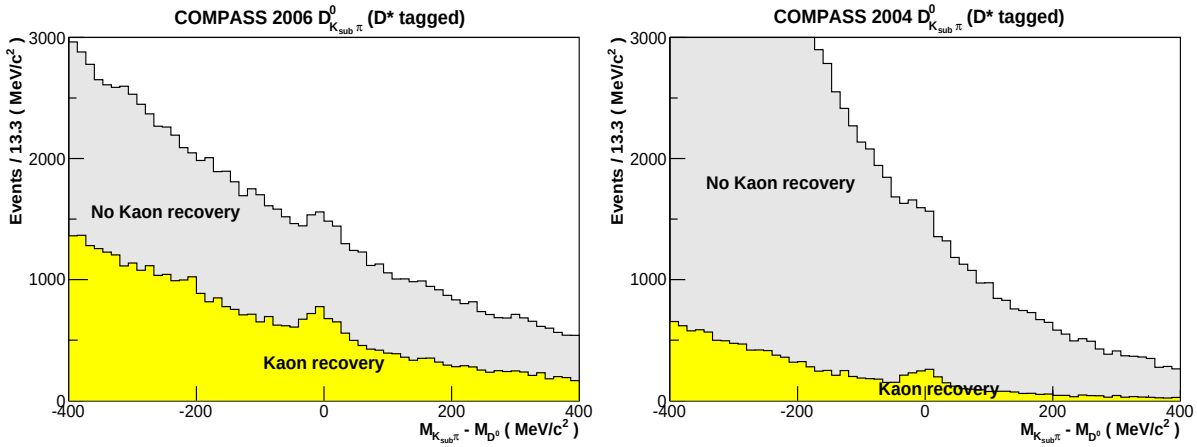

Figure 5.7: Left: invariant mass distribution for the $D^*_{K_{sub}\pi}$ channel, with (yellow) and without (light gray) kaon recovery by the RICH detector, for the data collected by COMPASS during the year of 2006. Right: the same information is shown for the year of 2004.

By fitting the signal and the background distributions of these mass spectra, we can quantify the improvement introduced by the RICH PID. This is summarized in table 5.7 for two years of data taking, 2004 and 2006.

Data		No RICH PID	RICH PID	Gain (PID/No PID)
2004	$\frac{S}{B}$	0.19	1.93	10
	$\frac{S^2}{S+B}$	437	1632	3.7
2006	$\frac{S}{B}$	0.11	1.87	17
	$\frac{S^2}{S+B}$	274	1907	7

Table 5.7: Signal-to-background ratios S/B and signal-strength $S^2/(S+B)$, for the $D^*_{K\pi}$ channel, obtained from a fit to the mass spectra shown in Fig. 5.6. These values result from an integration of the signal and background events over a mass window of ± 40 MeV/c^2 (2σ of the resonance).

The number of D^0 mesons is similar for both years but, for 2006, we can clearly see a much bigger gain in the signal-to-background ratio of the reconstructed mass spectrum. This fact is even more relevant because in 2006 the combinatorial background is significantly larger (by a factor of 1.7): more particles are detected by the COMPASS spectrometer due to the much bigger acceptance of the target solenoid. In fact, the RICH has a better performance in 2006, as compared to 2004, because an upgrade of its central part was accomplished in 2005. The new detector allows us to remove the huge combinatorial background produced by the halo muons. Finally, for the $D^*_{K_{sub}\pi}$ channel we gain a factor of 3 in the signal-strength for the year of 2006, after the kaon recovery, and a factor of 6 for the year of 2004. The gain is bigger for the latter due to the presence of a much larger background: it is a consequence from the fact that half of the periods of 2004 were produced with an old version of the RICH and tracking algorithms. As a result, we have more particles for which the RICH cannot compute the Likelihood for the kaon mass hypothesis.

5.3 Kinematic selection

5.3.1 Energy and angular cuts

The most important cuts for this analysis were discussed in the previous section. In addition to them, some kinematic cuts are also applied in order to improve the purity of the PGF samples. The most relevant quantity to consider for this kind of selection is the fraction of the virtual-photon energy carried by a D^0 candidate:

$$z_{D^0} = \left(\frac{E_{D^0}}{\nu} \right) \tag{5.13}$$

with

$$\nu = E_{\gamma^*} = (E_\mu - E_{\mu'})$$

A typical open-charm meson coming from a PGF process should have half of the virtual-photon energy: since a pair of charm quarks is produced in the centre-of-mass of the photon-gluon system (cf. Fig. 2.11), each quark tends to receive half of the virtual-photon energy. In Fig. 5.8 we can observe that PGF events are really selected: the z_{D^0} distribution obtained from the data agrees with the shape of the corresponding Monte Carlo distributions, either with parton shower on, in the initial and final states (right-plot), or with parton shower off (left-plot). Also, the the average value of these z_{D^0} distributions is close to the expected energy-fraction of 0.5.

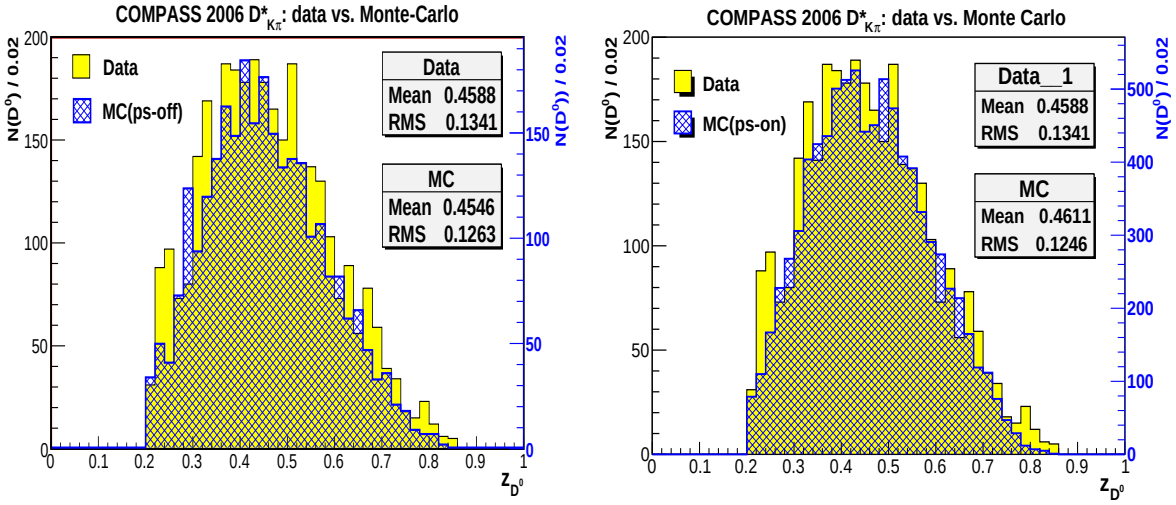

Figure 5.8: In yellow is the z_{D^0} distribution obtained from the data, using only those events belonging to a ± 80 MeV/c^2 mass window that survived to the subtraction of the background distribution. In blue is shown is the distribution for the generated D^0 mesons with (right plot - useful for a NLO analysis) and without (left plot - ideal to simulate LO processes) parton showers. The Monte Carlo distributions are obtained with the help of AROMA [73], by considering only D^0 mesons coming from a PGF interaction.

In order to accomplish a proper comparison of the data with the Monte Carlo samples, only the real reconstructed D^0 mesons are used. However, since for every channel there is also some

combinatorial background masking the D^0 signal (cf. Fig. 5.15-5.18), it is necessary to find an effective method that avoids the contamination of these events in the z_{D^0} distribution. The most obvious way to reduce the impact of the combinatorial background in this comparison is to use the channel with the highest signal purity: $D^*_{K\pi}$. The background contamination under the D^0 peak is subtracted from the mass spectrum of the $D^*_{K\pi}$ sample, in a ± 80 MeV/c^2 mass window, by using the z_{D^0} distribution from a **w**rong **c**harge **c**ombination sample (wcc). These wcc events are selected exactly in the same way as a D^0 candidate, with only one difference: the same charge is assigned to the $K\pi$ pairs and, in this way, we ensure that no D^0 mesons are reconstructed for this sample. In the upper right of Fig. 7.13 we can see the quality of the wcc sample as a background model, for the year of 2006: under the D^0 signal the wcc distribution is describing very well the real combinatorial background. It is better to use these wcc events to obtain the z_{D^0} distribution, instead of the real background [10], because it does not have the danger of dealing with the signal corresponding to the $D^*_{K\pi\pi^0}$ channel (at ≈ -240 MeV/c^2).

By subtracting the background from the reconstructed D^0 events, using the wcc sample, we can reproduce well enough the corresponding Monte Carlo distributions (cf. Fig. 5.8). Finally, from this figure we can define a z_{D^0} cut: in order to enhance the purity of the PGF sample, the events with a very high z_{D^0} value must be rejected. These events that have almost all the energy from the virtual-photon are, in general, produced during the fragmentation of a struck light-quark. Obviously, this process has nothing to do with a PGF interaction and, consequently, the resulting hadrons will contribute only to the combinatorial background (at LO-QCD). This statement is confirmed by the Monte Carlo distributions, from which we can see that no open-charm mesons are produced for $z_{D^0} > 0.85$. Moreover, we can also reject those reconstructed events with a z_{D^0} close to zero. Most of these candidates result from the hadronisation of the remnants of the nucleon fragmentation, which is caused by its DIS collision with the electromagnetic boson. In Fig. 5.8 we can see that the PGF contribution in this region is quite low and, therefore, we can safely remove some events with low z_{D^0} values in order to raise the PGF purity for the reconstructed mass spectrum. The precise values of these cuts, together with all the other kinematic cuts, are summarized in the table 5.8.

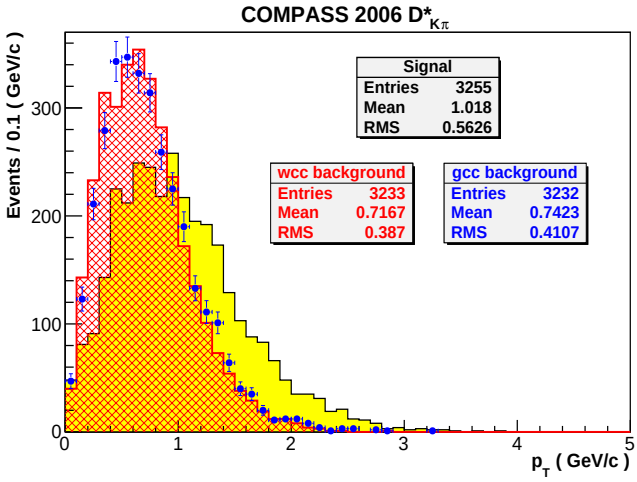

Figure 5.9: Yellow: $p_T(\mathrm{D}^0)$ distribution from data, obtained by subtracting the corresponding wcc distribution in a ± 80 MeV/c^2 mass window. Red: p_T distribution for the wcc sample in a ± 80 MeV/c^2 mass window. Blue: p_T distribution for the real combinatorial background (gcc: **g**ood **c**harge **c**ombination), obtained using the events from the sidebands of the main peak.

[10] Note that in this case the background can only be estimated from the sidebands of the mass spectrum.

As it is implicit in the above explanation for the rejection of the D^0 candidates with high z_{D^0} values, another criterium for the selection of PGF events is found on their high transverse momentum p_T regarding to the virtual-photon direction. If the D^0 candidate has a very low p_T, the most likely is that is has been produced by a hadron resulting from the fragmentation of a struck light-quark (struck by γ^*). In Fig. 5.9 we can see that indeed the signal and background events have different p_T distributions. It is clear that a typical D^0 has a larger p_T as compared to the events coming from the combinatorial background. Moreover, and despite the fact that the gcc distribution has been obtained from the sidebands of the real mass spectrum, it can be seen that the agreement with the wcc model is quite good: both distributions have an average value around 0.7 GeV/c, which is considerably lower if compared with the value of 1 GeV/c obtained for the signal events. However, there is a much better variable to use for this kind of cut: the cosine of the polar angle of kaon in the D^0 centre-of-mass regarding to the direction of the D^0 momentum.

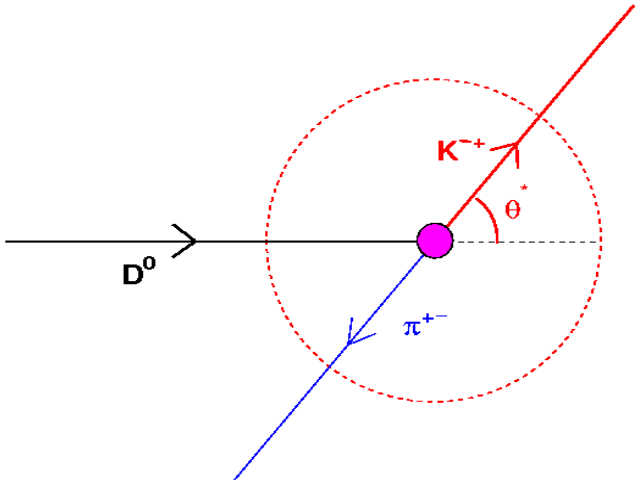

Figure 5.10: Representation of the polar angle of kaon in the D^0 centre-of-mass (example for the 2-body decay channels). The dashed circle illustrates that all angles are possible for the back-to-back D^0 decay into a kaon and a pion.

For the decay of a spin-0 particle, such as a D^0, the distribution of $\cos\theta^*$ should be flat. The combinatorial background is composed by kaons (and pions) originating from the nucleon fragmentation, obtaining only a small amount of p_T. Therefore, the background distribution should reveal a large peak for the small θ^* angles. We can take advantage of these facts to further enhance the purity of the PGF sample, by removing those candidates with $\cos\theta^*$ values close to ± 1. The cuts introduced by the RICH detector remove the kinematic range where $\cos\theta^* > 0.8$. However, it can be seen in Fig. 5.11 that the number of background events is considerably higher in the region covered by $\cos\theta^* < -0.8$. Therefore a kinematic cut in $|\cos\theta^*|$ is applied to reduce the background contamination of the PGF sample. For a low purity channel, such as the untagged D^0 (see Fig. 5.18), this angular cut is very helpful in enhancing the signal-strength.

However, another approach is used for the golden channel. Due to a mass cut (cf. section 5.3.2), the D^0 mass spectrum is already very clean (see Fig. 5.15) and, as a result, the gain introduced by an angular cut is not significant. Instead, a very loose $|\cos\theta^*|$ cut is applied, in order to preserve the underlying background (since it cannot be completely removed). The goal is to have enough statistics for a parameterisation of the probability that a D^0 candidate is indeed a D^0 meson (see Chapter 7). The outcome of this parameterisation is a clear separation of the signal events from the combinatorial background.

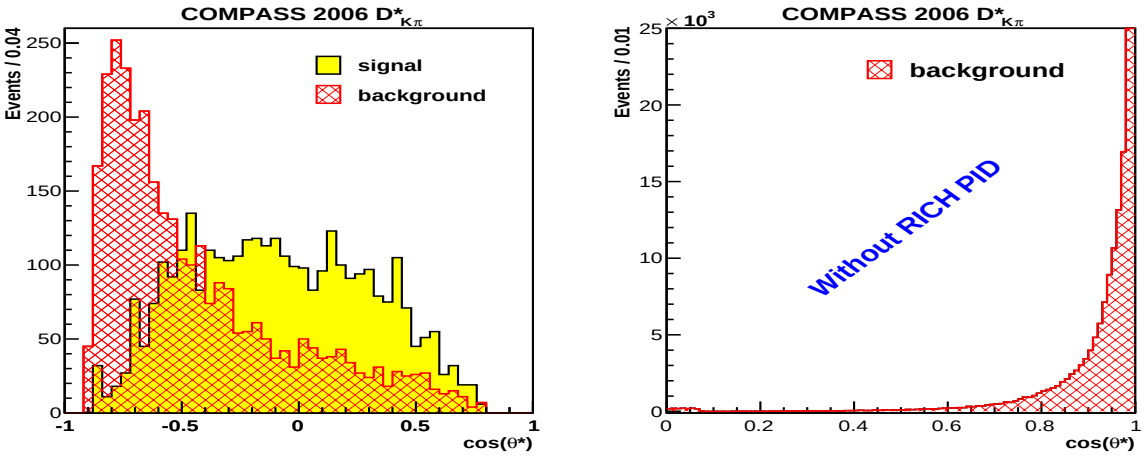

Figure 5.11: Left: distribution of $\cos\theta^*$ for the signal (after a subtraction of the background distribution) and background (wcc sample) events, after all the kinematic and RICH cuts. Right: distribution of $\cos\theta^*$, for the wcc sample, without particles identification by the RICH detector. Only those events within a mass window of ± 80 MeV/c^2 are considered.

5.3.2 The D*-tag cut

Four of the five samples of events considered in this analysis are selected through the use of a cut in the reconstructed mass difference between a PGF D^* and the resulting D^0 from its decay ($D^* \rightarrow D^0\pi_{slow}$). With the help [16], the remaining energy from the real mass difference can be easily calculated:

$$(M_{D^*} - M_{D^0}) - M_{\pi_s} \;=\; 145.92 - M_{\pi_s} \;=\; 6.35 \text{ MeV/c}^2 \tag{5.14}$$

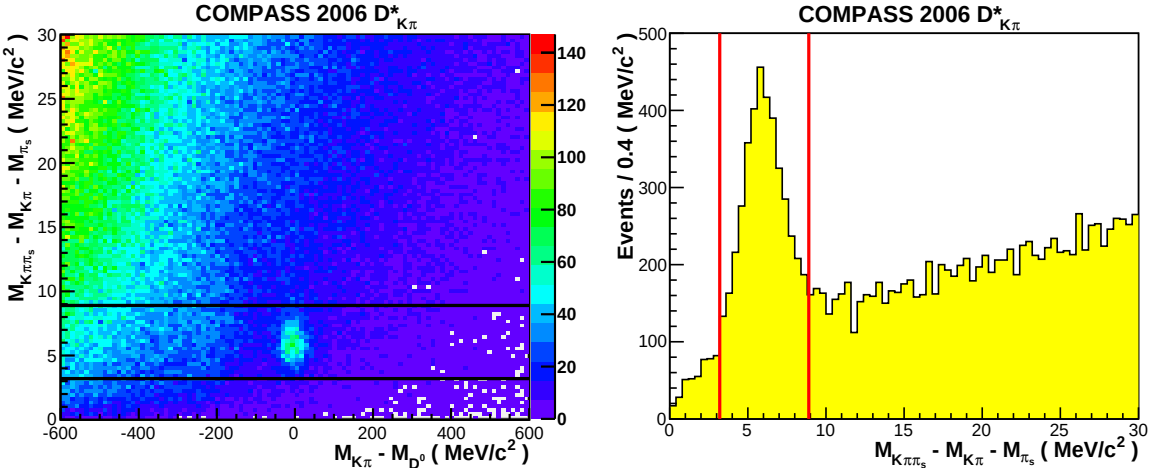

Figure 5.12: Left: the mass difference between a reconstructed D* candidate and a reconstructed D^0 candidate, $M^{rec}_{K\pi\pi_s} - M^{rec}_{K\pi}$, subtracted by the nominal pion mass, M_{π_s}, is plotted versus the reconstructed D^0 mass, $M^{rec}_{K\pi} - M_{D^0}$. A clear signal is seen around the expected value given by eq. 5.14. Right: projection of the D^0 candidates within a mass window of ± 40 MeV/c^2 (in a $M^{rec}_{K\pi}$ - M_{D^0} mass spectrum) into the $M^{rec}_{K\pi\pi_s} - M^{rec}_{K\pi} - M_{\pi_s}$ axis. The reconstructed signal peaks around 6 MeV/c^2, as expected, and the bars illustrate the mass cut chosen for this analysis.

We can see that almost all the mass difference between the two open-charm mesons is taken by the pion mass. As a result, the momenta available for the resulting particles is quite low. Therefore, the mass difference presented in eq. 5.14 is very well reconstructed (see Fig. 5.12), because possible limitations in the momentum resolution are overcome by the dominance of the slow-pion mass. The use of the mass cut, as defined in Fig. 5.12, allows us to improve significantly the signal-strength of the reconstructed mesons:

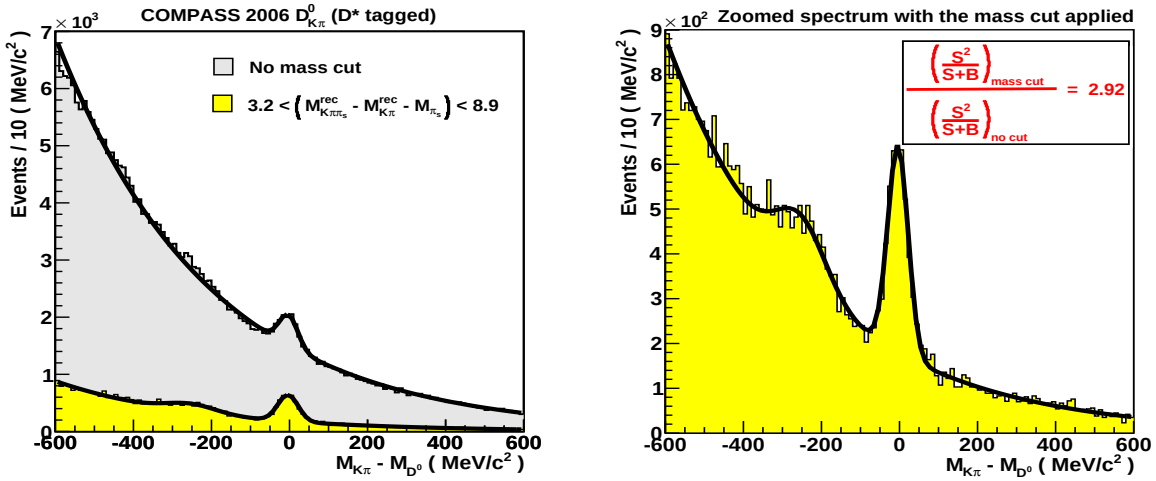

Figure 5.13: Left: comparison of the invariant mass distributions obtained with (yellow) and without (grey) the application of the mass cut. Right: a zoomed spectrum containing the mass cut is presented; a gain by a factor of 3 in the signal-strength is achieved for the golden channel.

5.3.3 Summary of the kinematic cuts

Variables	**Kinematic Cuts**				
	D^***-tagged channels**				**untagged** $D^0_{K\pi}$
	$D^0_{K\pi}$	$D^0_{K\pi\pi^0}$	$D^0_{K_{sub}\pi}$	$D^0_{K\pi\pi\pi}$	
$(M^{rec}_{K\pi} - M_{D^0})$ **[MeV/c^2]**	$\in [-600,\ +600]$		$\in [-400,\ +400]$		$\in [-400,\ +400]$
z_{D^0}	$\in [0.20,\ 0.85]$		$\in [0.25,\ 0.85]$	$\in [0.30,\ 0.85]$	$\in [0.20,\ 0.85]$
$\lvert\cos\theta^*\rvert$	< 0.90		< 0.85		< 0.65
ΔM **[MeV/c^2]**	$\in [3.2, 8.9]$			$\in [4.0, 7.5]$	——
p_K **[GeV/c]**	$\in]9.0,\ 50]$		$\in [2.5,\ 9.0]$	$\in]9.0,\ 50]$	$\in]9.0,\ 50]$
p_π **[GeV/c]**	$\in [2.5,\ 50]$				$\in [7,\ 50]$

Table 5.8: List of all kinematic cuts used in the open-charm analysis. For every channel, a D^0 candidate is accepted if it belongs simultaneously to all the specified intervals. All cuts are tuned to maximise the signal-strength without killing the D^0 mesons (cf. e.g. in Fig. 5.4). The definition of ΔM is: $\Delta M = \left(M^{rec}_{K\pi\pi_s} - M^{rec}_{K\pi} - M_{\pi_s}\right)$.

The lower cut in the pion momentum of the untagged sample, $p(\pi) < 7$ GeV/c (rejected events), is introduced to clean the electron contamination of pion candidates. In addition to that, a cut of 50 GeV/c is applied to the momentum of all particles in the analysis. This cut is necessary to avoid the kinematic region where the RICH detector is not effective in distinguishing a kaon from a pion (cf. Fig. 3.9). Finally, the following criteria is applied to the selected samples:

1. If a given channel contains a double D^0 candidate, in the same event, only one of them is considered in the analysis (chosen randomly).

2. If two channels contribute with a D^0 candidate to the same event, a priority rule is followed in their selection (only one is accepted):

   - $D^*_{K\pi\pi\pi}$, $D^*_{K\pi}$ or $D^*_{K\pi\pi^0}$, $D^0_{K\pi}$, $D^*_{K_{sub}\pi}$

The channels listed above are sorted in order of importance for the extraction of the gluon polarisation. The exception is the $D^*_{K\pi\pi\pi}$ channel: it is the first in priority because it helps in the cleaning of the golden channel when the same event is shared by them. The final samples can be seen in Figs. 5.15-5.18. We can observe that the $D^*_{K\pi\pi^0}$ and $D^*_{K\pi}$ channels share the same mass spectrum. The signal of the former emerges as a kind of a "bump" over the underlying background, centred around a mass of -240 MeV/c^2. It's origin comes from the undetected neutral pion in the COMPASS spectrometer. The effect of ignoring the π^0 in the analysis is studied by Monte Carlo and shown in Fig. 5.14. Since the π^0 is not reconstructed, the impact of the missing energy in the mass spectrum is a shift of the distribution towards the lower masses. This result confirms that the bump in Fig. 5.15 is indeed a reflection of the $D^0_{K\pi\pi^0}$ signal to that mass region.

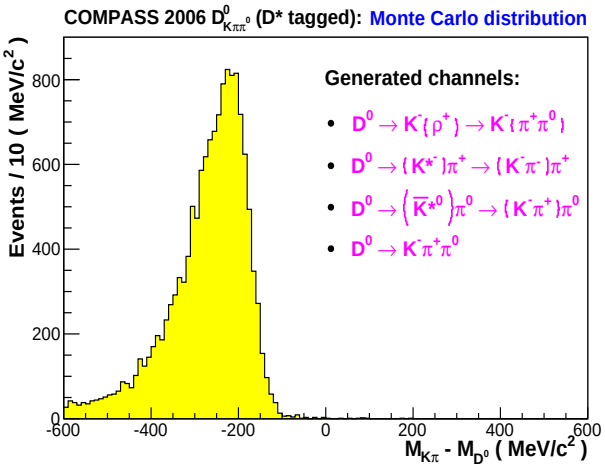

Figure 5.14: Invariant mass distribution for the $K\pi$ system. The illustrated channels are generated with AROMA [73], constrained to the COMPASS acceptance using COMGEANT [75], and finally reconstructed as real events.

5.4 The final D^0 samples

The mass spectra displayed in Figs. 5.15-5.18 are obtained by calculating the invariant mass of the system formed by D^0 decay particles (example for the $D^*_{K\pi\pi\pi}$ channel):

$$M_{K\pi\pi\pi} = \sqrt{(P_K + P_{\pi_1} + P_{\pi_2} + P_{\pi_3})^2} \tag{5.15}$$

where P_K, P_{π_1}, P_{π_2} and P_{π_3} are the four-momentum vectors defined by

$$P_K = (p_K^x,\ p_K^y,\ p_K^z,\ E_K) \quad , \quad P_{\pi_{(1,2,3)}} = \left(p^x_{\pi_{(1,2,3)}},\ p^y_{\pi_{(1,2,3)}},\ p^z_{\pi_{(1,2,3)}},\ E_{\pi_{(1,2,3)}}\right) \tag{5.16}$$

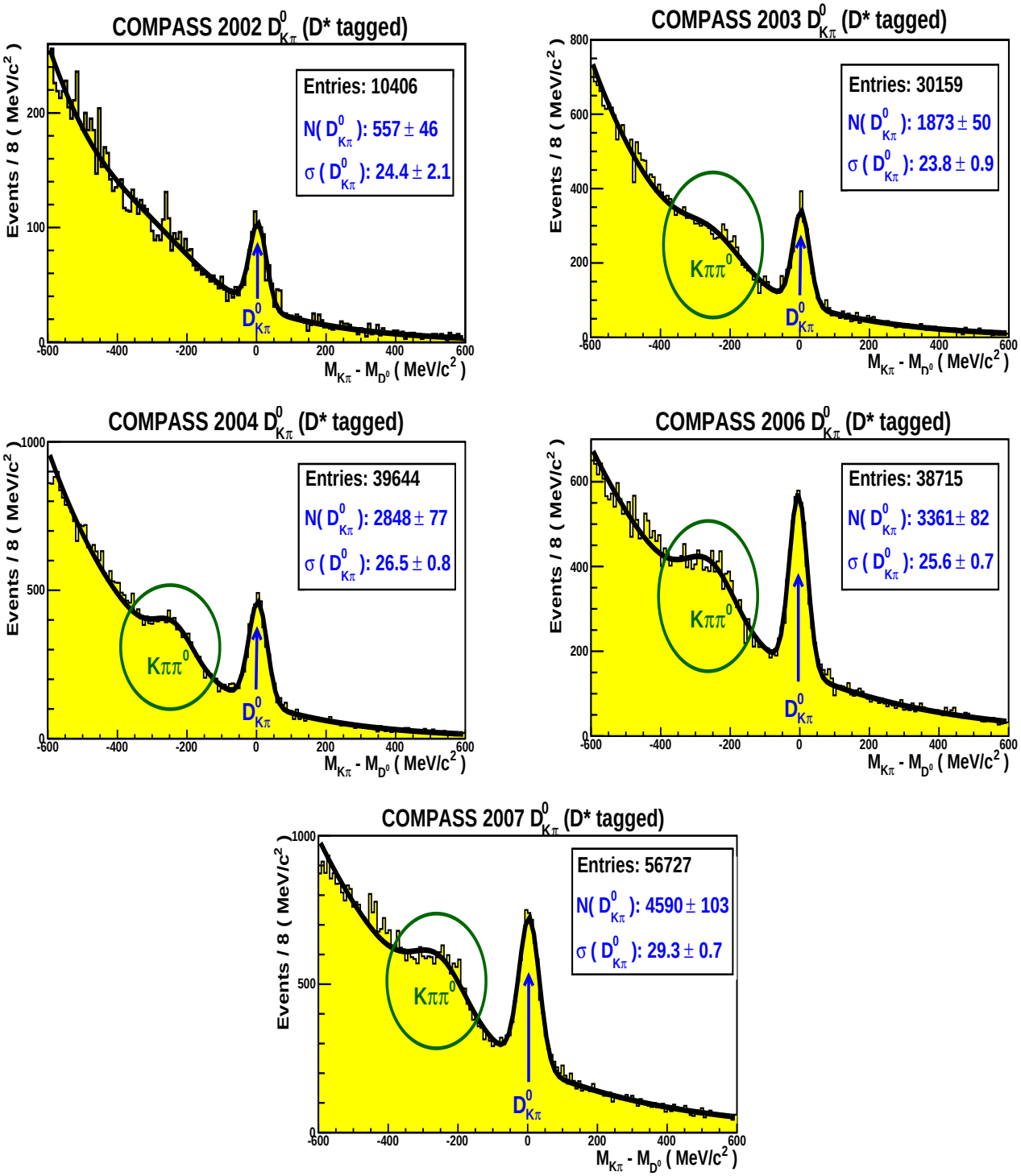

Figure 5.15: Invariant mass distributions of the $D^*_{K\pi}$ channel. After subtracting the nominal D^0 mass (cf. [16]), the signal is reconstructed, as expected, around zero. The number of D^0 mesons and the resolution of the peak are presented for these samples. To the left (highlighted in green), one can also see the signal belonging to the $D^*_{K\pi\pi^0}$ channel emerging from the combinatorial background. This resonance is seen only in these high purity spectra.

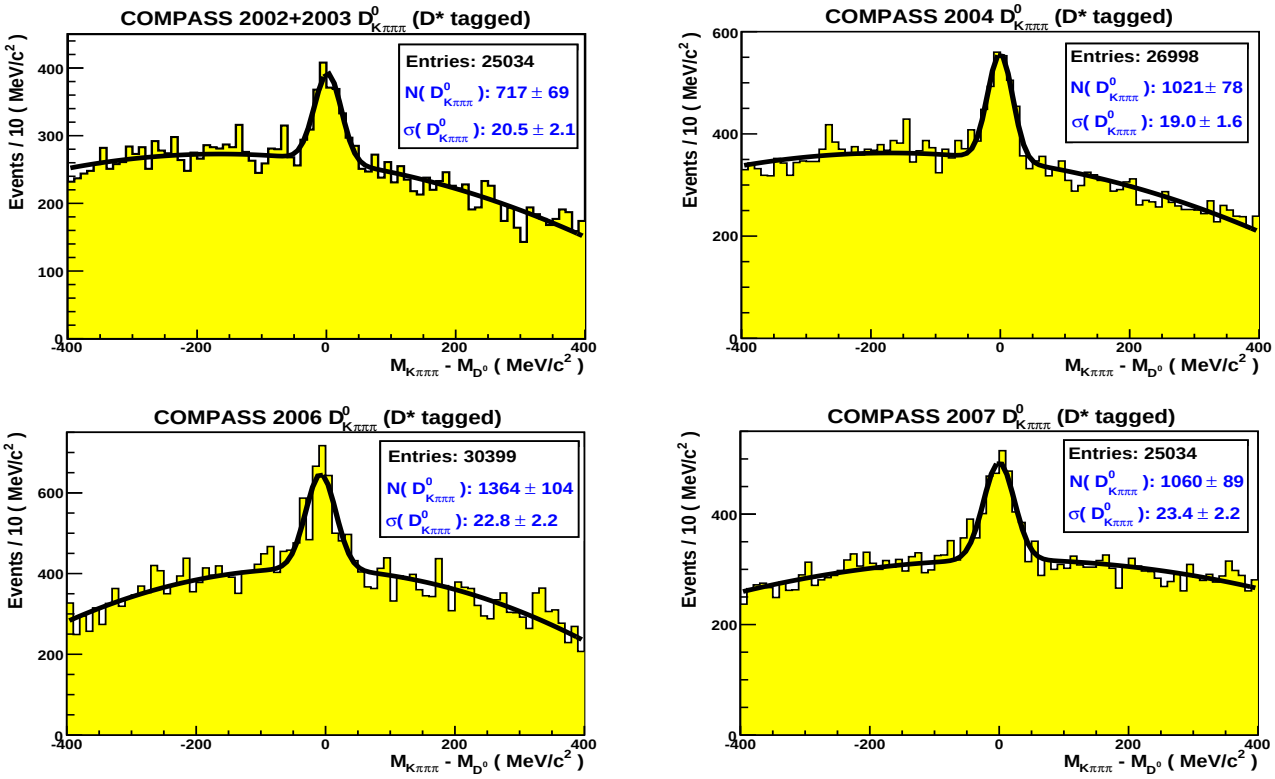

Figure 5.16: Invariant mass distributions of the $D^*_{K\pi\pi\pi}$ channel.

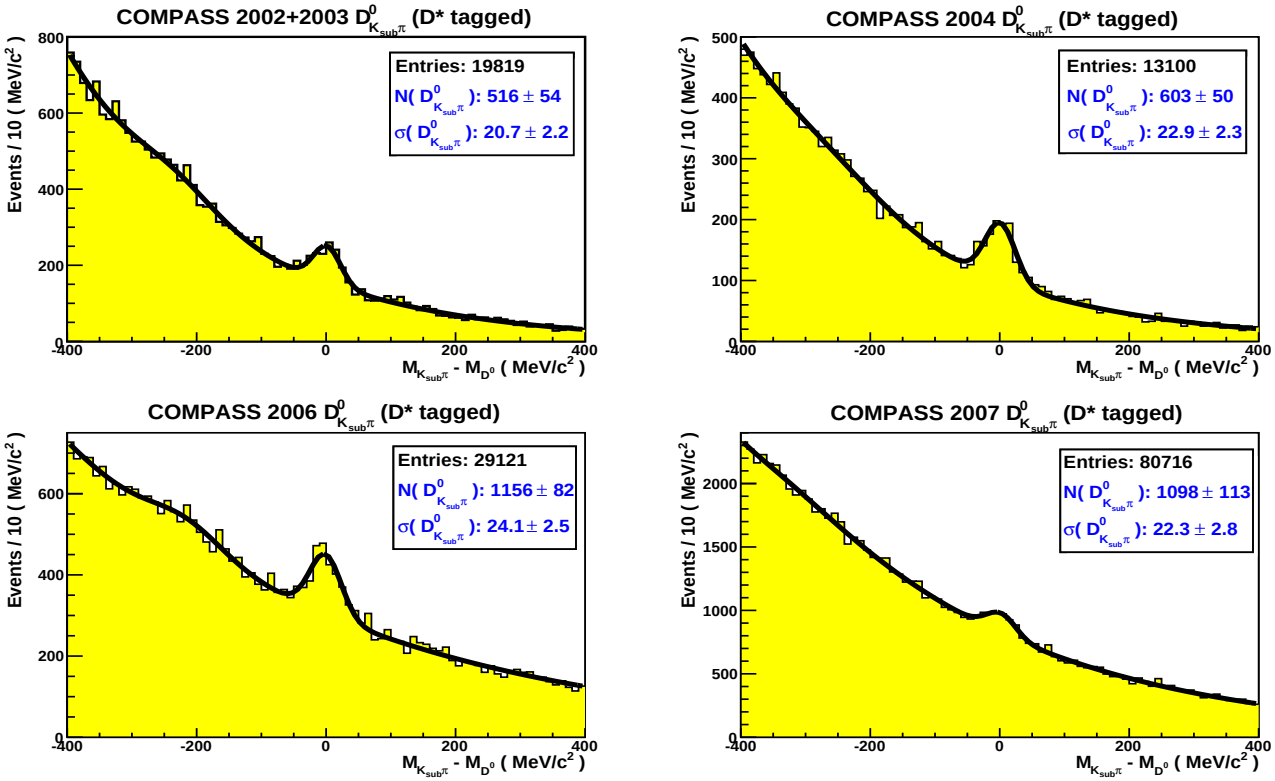

Figure 5.17: Invariant mass distributions of the $D^*_{K_{sub}\pi}$ channel.

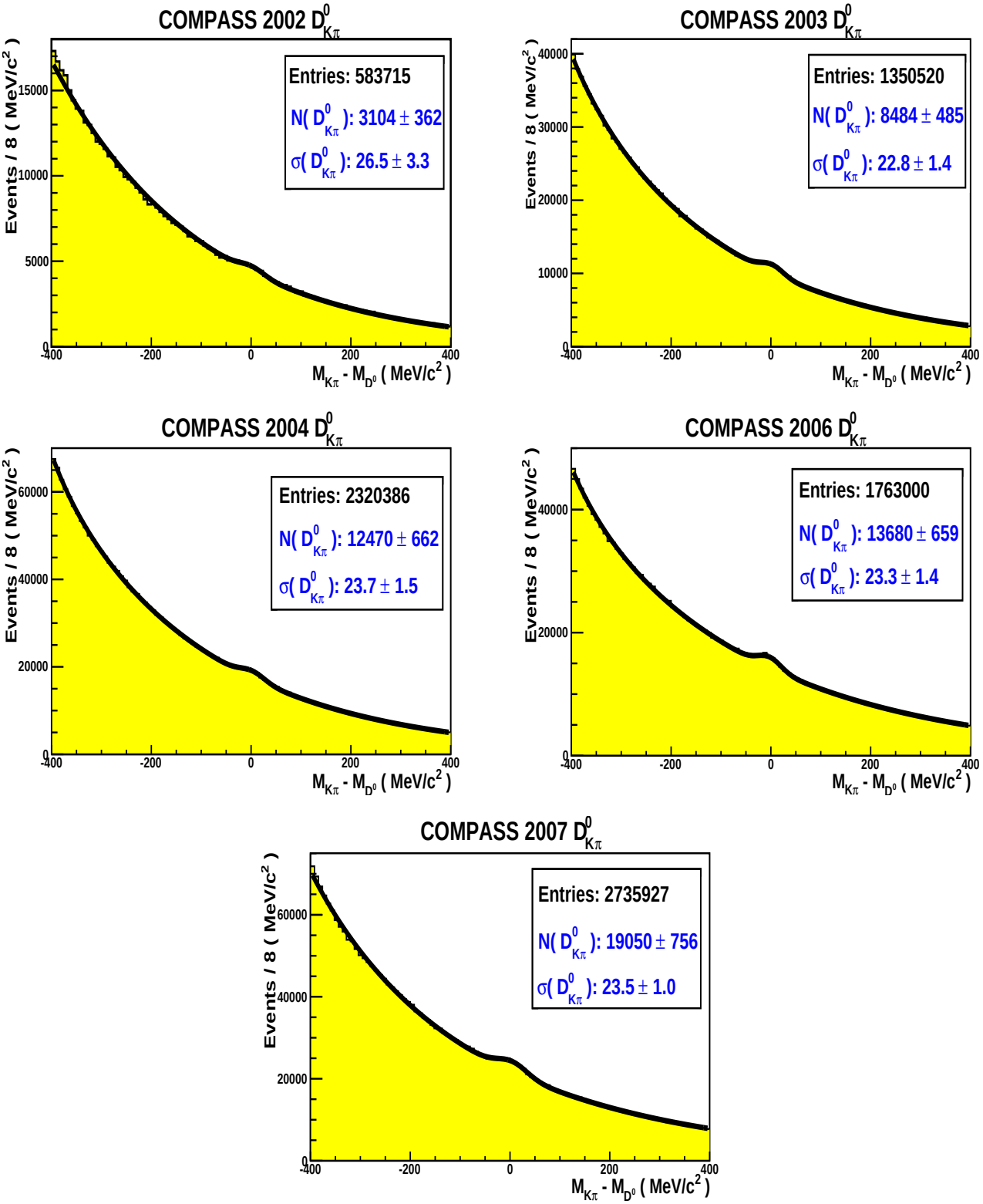

Figure 5.18: Invariant mass distributions of the $D^0_{K\pi}$ channel.

It can be seen from Fig. 5.15 that the same background is shared by the $D^*_{K\pi\pi^0}$ and $D^*_{K\pi}$ channels. However, the number of D^0 mesons and respective signal resolution are given only for the latter. The reason for that lies in the difficulty of fitting such a wide resonance of low purity (in 2002 the signal is not even seen). Therefore these results will only be presented after

an additional rejection of background events by using a Neural Network (see Chapter 7). This procedure has also a positive impact for the samples $D^*_{K\pi\pi\pi}$ and $D^*_{K_{sub}\pi}$, as shown in Fig. 5.16 and in Fig. 5.17. For the remaining channels ($D^*_{K\pi}$ and $D^0_{K\pi}$), the mass spectra displayed in Fig. 5.15 and in Fig. 5.18 correspond already to the final samples used in this work. In all figures, it is shown the mass distributions per each year of data taking.

5.5 Kinematic properties of the PGF sample

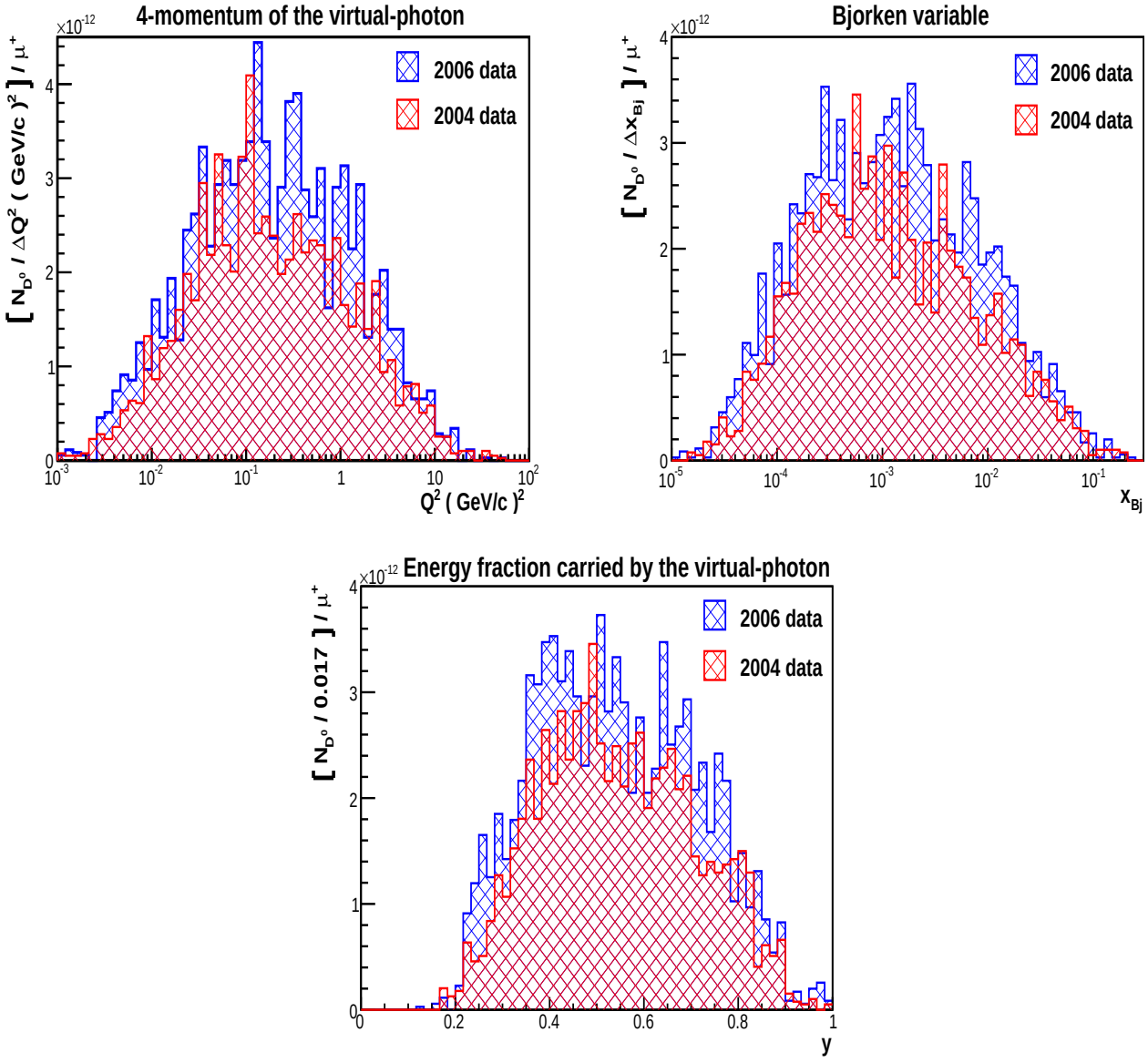

Figure 5.19: Distributions of the most important DIS variables obtained from the $D^*_{K\pi}$ channel, using only D^0 candidates within a mass window of ± 80 MeV/c^2. Note that the x_{Bj} distribution is limited to the interval defined by $x_{Bj} < 0.1$. The latter is a strong support to the assumption of no intrinsic-charm in the nucleon for the present analysis.

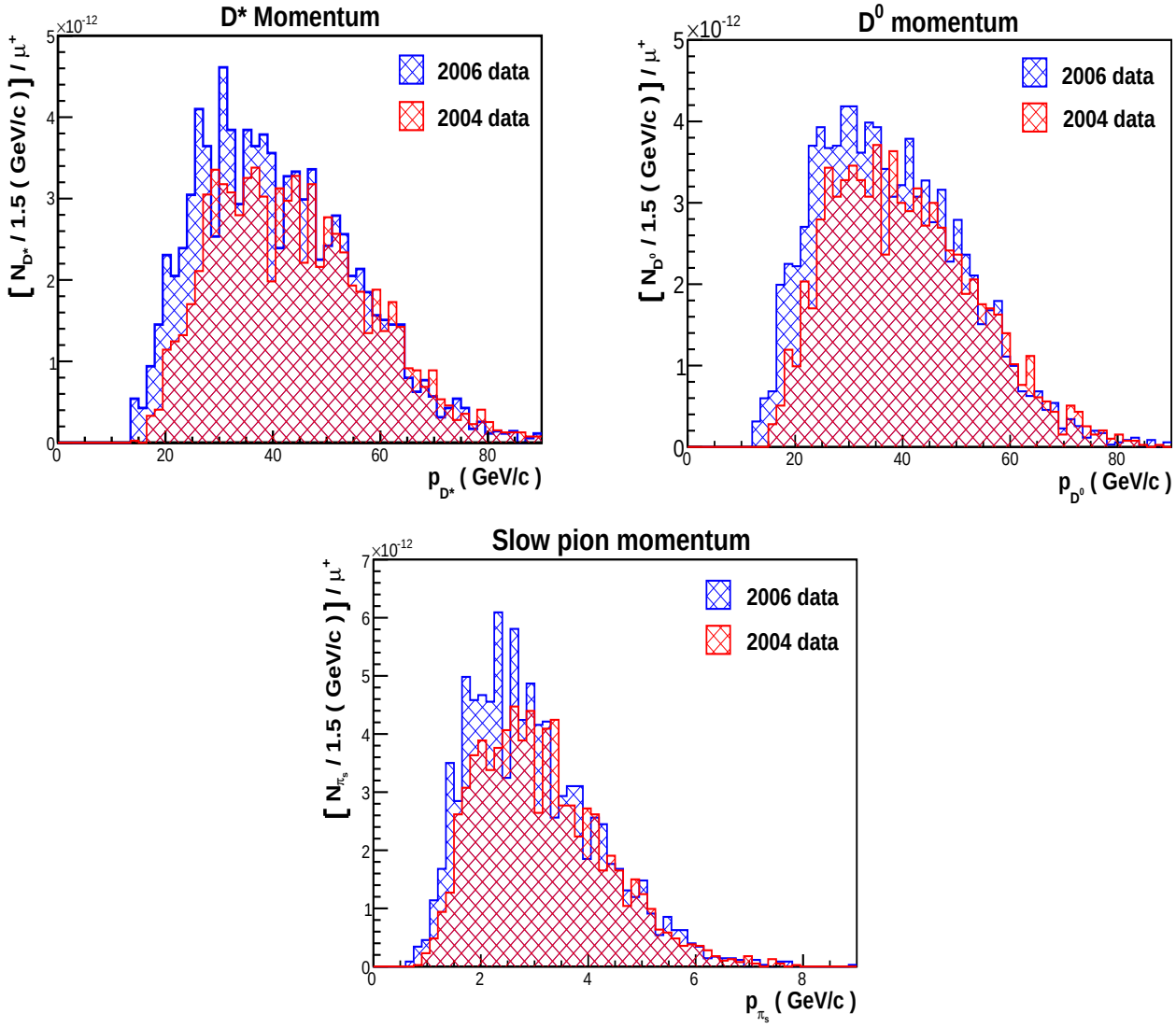

Figure 5.20: Momentum distributions of the mesons involved in a D^* decay. All distributions are obtained from the $D^*_{K\pi}$ channel, using only those events for which we have a D^0 candidate within a mass window of ± 80 MeV/c^2.

The impact of the target upgrade in this open-charm analysis is put in evidence in the upper-right of Fig. 5.21. More pions of low momentum are detected in 2006, due to the increased acceptance of the solenoid that surrounds the target. More kaons are also detected, per incoming muon, but they are uniformly distributed along the momentum range. In the bottom-left one can observe the impact of the RICH upgrade. In fact, a much cleaner sample of the Cherenkov photons in 2006 gives rise to a significant increase in the number of sub-threshold kaons recovered.

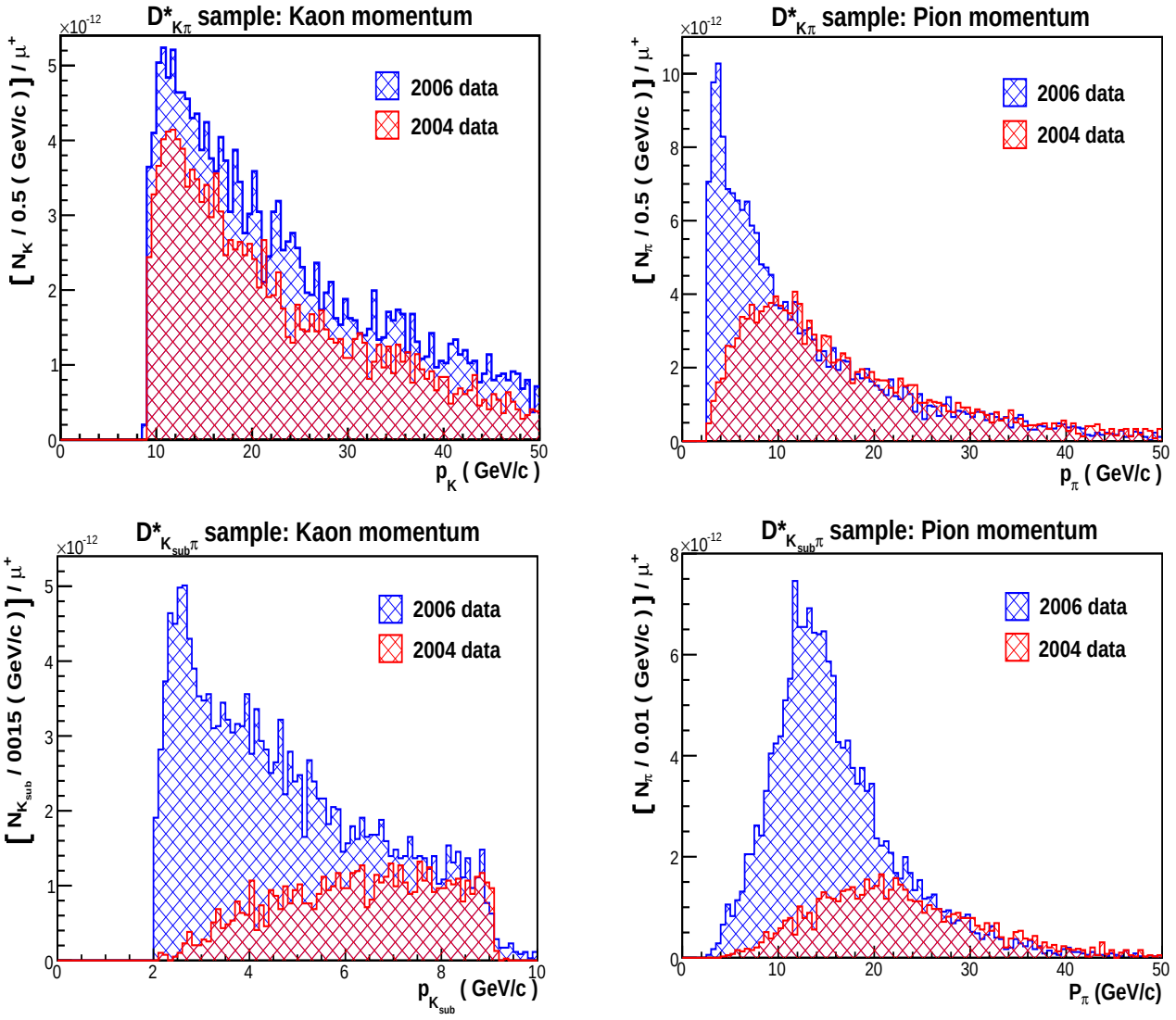

Figure 5.21: Momentum distributions of the particles that result from a D^0 decay. All distributions are obtained for the D^0 candidates within a mass window of ± 80 MeV/c^2. Two channels are represented: $D^*_{K\pi}$ (top) and $D^*_{K_{sub}\pi}$ (bottom).

Chapter 6

Extraction of the Gluon Polarisation

The gluon polarisation is proportional to the spin asymmetry that results from the production of open-charm mesons in target cells oppositely polarised (cf. eq. 2.84 and eq. 2.86). The purpose of this chapter is to demonstrate the determination of $\Delta G/G$ with the best possible accuracy. There are four types of events which are used for the experimental asymmetry calculation (see Fig. 6.1): N_u, N_d, $N_{u'}$ and $N_{d'}$, for the data taken between 2002 and 2004.

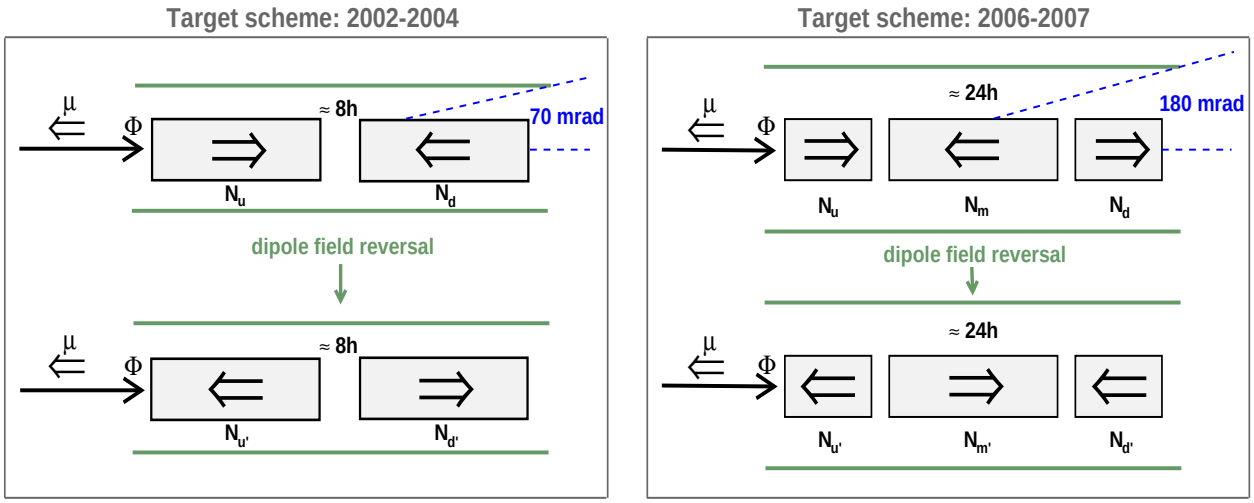

Figure 6.1: Scheme of all target configurations used in the open-charm analysis. N represents the number of D^0 candidates that are reconstructed in a given cell, with the following interpretation for the indexes: u = upstream cell, m = middle cell and d = downstream cell.

The reversal of the target spins is important to minimise the effects introduced by the different acceptances of the cells, whose origin is related to the events that are able to escape from the solenoid (that surrounds the target) to the COMPASS spectrometer. By reversing the target spins we can gather about the same amount of events for each spin configuration due to the introduction of $N_{u'}$ and $N_{d'}$ in the analysis (every 8h of data taking the solenoid field is reversed). Four event rates are also measured for the target scheme used from 2006 onwards (right plot of Fig. 6.1): $(N_u + N_d)$, N_m, $(N_{u'} + N_{d'})$ and $N_{m'}$. In fact, the target is composed by three cells in order to symmetrize the acceptance of the u and d cells regarding the m cell, and also to avoid an often reversal of the solenoid field which may cause other systematic effects (from 2006 onwards the reversal of the field is made once every 24h).

6.1 Method for the asymmetry extraction

The yield of charmed mesons is given for each cell configuration and for a defined time interval by (from now on $c\bar{c}$ will replace $\mu N \to c\bar{c}X$ for simplicity):

$$\hat{N}_t^{c\bar{c}} = a_t[\ (\Phi^{\rightarrow} n_t^{\rightrightarrows} + \Phi^{\leftarrow} n_t^{\leftleftarrows})\sigma_{c\bar{c}}^{\leftleftarrows} + (\Phi^{\rightarrow} n_t^{\leftleftarrows} + \Phi^{\leftarrow} n_t^{\rightrightarrows})\sigma_{c\bar{c}}^{\rightleftarrows} + \Phi \sum_X (n_X \cdot \sigma_{c\bar{c},X})\ ] \tag{6.1}$$

Variables	Meaning
t	Target configuration: $t = \ (u,\ d,\ u',\ d')$ or $t = \ (u+d,\ m,\ u'+d',\ m')$
a_t	Experimental acceptance for a specific t cell
$\Phi = \Phi^{\rightarrow} + \Phi^{\leftarrow}$	Total muon flux
$\Phi^{\rightarrow}$ and $\Phi^{\leftarrow}$	Integrated flux of muons with positive and negative helicity
$n_t = n_t^{\rightrightarrows} + n_t^{\leftleftarrows}$	Number of polarisable nucleons per area unit and cell configuration
$n_t^{\rightrightarrows}$ and $n_t^{\leftleftarrows}$	Number of nucleons with positive and negative spin projections
$\overline{\sigma}_{c\bar{c}} = \frac{1}{2}\left(\sigma_{c\bar{c}}^{\leftleftarrows} + \sigma_{c\bar{c}}^{\rightrightarrows}\right)$	Unpolarised cross-section of polarisable nucleons for the $c\bar{c}$ production
$\sigma_{c\bar{c}}^{\leftleftarrows}$ and $\sigma_{c\bar{c}}^{\rightrightarrows}$	Cross-sections for the parallel and anti-parallel spin configurations
n_X	Number of unpolarisable nucleons inside the target cell
$\sigma_{c\bar{c},X}$	Unpolarised cross-section for the non-polarisable nucleons
$\hat{n}_t = n_t + \sum_X n_X$	Total number of nucleons per unit area and cell configuration
$\hat{\sigma}_{c\bar{c}} = \frac{n_t\overline{\sigma}_{c\bar{c}} + \sum_X (n_X \cdot \sigma_{c\bar{c},X})}{\hat{n}_t}$	Total averaged unpolarised cross-section
$P_\mu = \frac{\Phi^{\rightarrow} - \Phi^{\leftarrow}}{\Phi^{\rightarrow} + \Phi^{\leftarrow}}$	Polarisation of the muon beam
$P_t = \frac{n_t^{\rightrightarrows} - n_t^{\leftleftarrows}}{n_t^{\rightrightarrows} + n_t^{\leftleftarrows}}$	Target polarisation for each cell configuration
$f = \frac{n_t\overline{\sigma}_{c\bar{c}}}{n_t\overline{\sigma}_{c\bar{c}} + \sum_X (n_X \cdot \sigma_{c\bar{c},X})}$	Dilution factor of the target material
$A_{\mu N \to c\bar{c}} = \left(\frac{\sigma_{c\bar{c}}^{\rightleftarrows} - \sigma_{c\bar{c}}^{\leftleftarrows}}{\sigma_{c\bar{c}}^{\rightleftarrows} + \sigma_{c\bar{c}}^{\leftleftarrows}}\right)$	Muon-Nucleon asymmetry for charmed meson events (for short $A_{c\bar{c}}$)

Table 6.1: Definition of the variables used in eq. 6.1 and in eq. 6.2.

The mass spectra of the D^0 decay particles do not represent a pure sample of PGF events. In Figs. 5.15 to 5.18 it is clear that a significant combinatorial background is masking the D^0 signal. Most of this contamination corresponds to the reconstruction of kaons and pions resulting from the fragmentation of the struck light-quarks. Since this background is part of the samples, we must also include its contribution to the event yield ($\hat{A}_{\mu N \to bg} \equiv \hat{A}_{bg}$):

$$\frac{dN_t}{dmdX} = a_t \Phi \hat{n}_t \hat{\sigma}_{tot,t} \left(1 - P_\mu P_t f \frac{\hat{\sigma}_{c\bar{c}}}{\hat{\sigma}_{tot,t}} A_{c\bar{c}} - P_\mu P_t f \frac{\hat{\sigma}_{bg}}{\hat{\sigma}_{tot,t}} \hat{A}_{bg}\right) \tag{6.2}$$

with

$$\hat{\sigma}_{tot,t} = \hat{\sigma}_{c\bar{c}} + \hat{\sigma}_{bg} \quad , \quad m \equiv M_{K\pi} \quad \text{and} \quad X = (z_{D^0},\ \cos\theta^*, ...) \tag{6.3}$$

Equation 6.2 is conveniently written in terms of the physical and background spin asymmetries, to take advantage of the fact that they are much less sensitive to the experimental changes than the cross-section differences. By assuming an equal acceptance for the signal and background events, the cross-section ratios can be expressed in the following way:

$$\frac{\hat{\sigma}_{c\bar{c}}}{\hat{\sigma}_{tot,t}} = \left(\frac{S}{S+B}\right) \quad \text{and} \quad \frac{\hat{\sigma}_{bg}}{\hat{\sigma}_{tot,t}} = \left(\frac{B}{S+B}\right) \tag{6.4}$$

The quantity $S/(S+B)$ is the signal purity, where the signal events, $S(m,X)$, are obtained from a fit to the peak of the invariant mass spectra. $S(m,X)$ and $B(m,X)$ represent the unpolarised cross-section of signal and background events folded with the experimental resolution, where X denote a set of kinematic variables defining an event. From these definitions, we see that a good kinematic parameterisation of $S/(S+B)$ is essential for an unbiased analysis (cf. section 7.3).

We now turn to the relation between the muon-nucleon asymmetry, $A_{c\bar{c}}$, and the partonic distribution that we want to measure, $\Delta G = G^{\Rightarrow} - G^{\Leftarrow}$. In the perturbative regime of LO-QCD (cf. Fig. 2.14), the $c\bar{c}$ cross-section has the following decomposition:

$$\sigma^{\overleftrightarrows}_{\mu N\to c\bar{c}} \equiv \sigma^{\overleftrightarrows}_{c\bar{c}} \quad \propto \quad \int (\hat{\sigma}^{\overleftrightarrows}_{\mu g} G^{\Leftarrow} + \hat{\sigma}^{\overleftarrows}_{\mu g} G^{\Rightarrow})\ d\hat{s} \tag{6.5}$$

$$\sigma^{\overleftarrows}_{\mu N\to c\bar{c}} \equiv \sigma^{\overleftarrows}_{c\bar{c}} \quad \propto \quad \int (\hat{\sigma}^{\overleftarrows}_{\mu g} G^{\Leftarrow} + \hat{\sigma}^{\overleftrightarrows}_{\mu g} G^{\Rightarrow})\ d\hat{s} \tag{6.6}$$

Using the above equations and the definition of $A_{c\bar{c}}$ given in Table 6.1, we obtain

$$\begin{aligned}
A_{c\bar{c}} &= \frac{\int \left[\hat{\sigma}^{\overleftrightarrows}_{\mu g}(\hat{s}) - \hat{\sigma}^{\overleftarrows}_{\mu g}(\hat{s})\right] \left[G^{\Leftarrow}(x_g,\hat{s}) - G^{\Rightarrow}(x_g,\hat{s})\right] F(z_{D^0})\ d\hat{s}}{\int \left[\hat{\sigma}^{\overleftrightarrows}_{\mu g}(\hat{s}) + \hat{\sigma}^{\overleftarrows}_{\mu g}(\hat{s})\right] \left[G^{\Leftarrow}(x_g,\hat{s}) + G^{\Rightarrow}(x_g,\hat{s})\right] F(z_{D^0})\ d\hat{s}} \\
&= \frac{F(z_{D^0}) \int \Delta\hat{\sigma}_{\mu g}(\hat{s}) \Delta G(x_g,\hat{s})\ d\hat{s}}{F(z_{D^0}) \int \hat{\sigma}_{\mu g}(\hat{s}) G(x_g,\hat{s})\ d\hat{s}} \\
&= \frac{\int \left(\frac{\Delta\hat{\sigma}_{\mu g}(\hat{s})}{\hat{\sigma}_{\mu g}(\hat{s})} \frac{\Delta G(x_g,\hat{s})}{G(x_g,\hat{s})}\right) \hat{\sigma}_{\mu g}(\hat{s}) G(x_g,\hat{s})\ d\hat{s}}{\int \hat{\sigma}_{\mu g}(\hat{s}) G(x_g,\hat{s})\ d\hat{s}} \\
&= \left\langle \hat{a}_{LL} \frac{\Delta G}{G}(x_g) \right\rangle \\
&\overset{1}{=} a_{LL} \times \frac{\Delta G}{G}(\overline{x}_g) \qquad \text{with} \qquad a_{LL} = \langle \hat{a}_{LL} \rangle \ , \ \overline{x}_g = \langle x_g \rangle
\end{aligned} \tag{6.7}$$

where $\hat{s} = (q + x_g p)^2$ is the invariant mass of the photon-gluon system, q and p are the virtual-photon and the nucleon 4-momenta, ν is the virtual-photon energy, $x_g = (\hat{s} + Q^2)/(2M\nu)$ is the gluon momentum fraction with dx_g expressed in terms of $d\hat{s}$ (the resulting Jacobian cancels in the asymmetry), M is the nucleon mass and F describes the fragmentation of c quarks into

[1] See eq. 6.37 from section 6.1.1 for the demonstration

D^0 mesons carrying an energy fraction $z_{D^0} = (E_{D^0}/\nu)$ [76]. The perturbative approach of the muon-nucleon cross-section is justified by the hard scale given by the charm mass: $(2m_c^T)^2$ for the $c\bar{c}$ production. This scale turns the assumption of the convolution between the gluon structure function and the hard fusion (photon-gluon) valid. Finally, the partonic asymmetry for the longitudinally polarised beam and target is defined by:

$$\hat{a}_{LL} = \frac{\Delta\hat{\sigma}_{\mu g}(\hat{s})}{\hat{\sigma}_{\mu g}(\hat{s})} = \left(\frac{\hat{\sigma}^{\rightleftarrows}_{\mu g}(\hat{s}) - \hat{\sigma}^{\rightleftarrows}_{\mu g}(\hat{s})}{\hat{\sigma}^{\rightleftarrows}_{\mu g}(\hat{s}) + \hat{\sigma}^{\rightleftarrows}_{\mu g}(\hat{s})} \right) \tag{6.8}$$

This asymmetry is fully dependent on the partonic kinematics, and its general expression, in a LO-QCD approximation, can be found in eqs. 2.87-2.93.

We are now in conditions to rewrite eq. 6.2 in its final form ($d\xi = dmdX$):

$$\langle N_t \rangle = \int \hat{N}_t \; d\xi = \alpha_t \left(1 \; - \; \langle \beta_{t,c\bar{c}} \rangle \frac{\Delta G}{G} \; - \; \langle \beta_{t,bg} \rangle A_{bg} \right) \tag{6.9}$$

with

$$\alpha_t = \int (a_t \Phi \hat{n}_t \hat{\sigma}_{tot,t}) \; d\xi \quad , \quad \langle \beta_t \rangle = \frac{\int (a_t \Phi \hat{n}_t \hat{\sigma}_{tot,t} \beta_t) \; d\xi}{\int (a_t \Phi \hat{n}_t \hat{\sigma}_{tot,t}) \; d\xi} \quad , \quad \hat{A}_{bg} = D A_{bg} \tag{6.10}$$

$$\beta_{c\bar{c}} = P_\mu P_t f \left(\frac{S}{S+B} \right) a_{LL} \quad \text{and} \quad \beta_{bg} = P_\mu P_t f \left(\frac{B}{S+B} \right) D \tag{6.11}$$

The new background asymmetry, A_{bg}, is a photon-nucleon asymmetry: $A_{\gamma^* N \to bg}$. The relation with $\hat{A}_{bg}$ is given through the depolarisation factor, D, which defines the amount of polarisation transferred from the muon to the virtual-photon (cf. eq. 2.35). Concerning the signal asymmetry, the depolarisation factor is hidden inside the muon-gluon asymmetry a_{LL}.

6.1.1 Extracting ΔG/G with the best possible accuracy

From now, in order to simplify the notation we will only consider the target configuration used in COMPASS until 2004: $t = (u, \; d, \; u', \; d')$ in Fig. 6.1. Assuming that the background asymmetry is negligible, we can easily solve eq. 6.9 by using the following double ratio of the number of events:

$$r = \left(\frac{N_u N_{d'}}{N_{u'} N_d} \right) = \frac{\alpha_u \alpha_{d'}}{\alpha_{u'} \alpha_d} \left[\frac{(1 - \langle \beta_u \rangle \frac{\Delta G}{G})(1 - \langle \beta_{d'} \rangle \frac{\Delta G}{G})}{(1 - \langle \beta_{u'} \rangle \frac{\Delta G}{G})(1 - \langle \beta_d \rangle \frac{\Delta G}{G})} \right] \tag{6.12}$$

where the expectation values $\langle N_t \rangle$ were replaced by the measured D^0 rates (N_t). Since with specific cuts to the data sample it is ensured that both cells are subject to the same muon flux ($\Phi_u = \Phi_d$ and $\Phi_{u'} = \Phi_{d'}$), we can solve the previous equation by assuming that (obviously, we have also: $n_u = n_{u'}$, $n_d = n_{d'}$, $\hat{\sigma}_{tot,u} = \hat{\sigma}_{tot,u'}$ and $\hat{\sigma}_{tot,d} = \hat{\sigma}_{tot,d'}$):

$$\frac{\alpha_u \alpha_{d'}}{\alpha_{u'} \alpha_d} = 1 \tag{6.13}$$

Equation 6.13 implies that the two cells are equally affected by possible changes in the experimental acceptance over time (the acceptance don't need to be the same for both cells). Consequently, the knowledge of $\langle \beta_t \rangle$ for every event allows us to solve eq. 6.12 for $\Delta G/G$:

$$B \left(\frac{\Delta G}{G} \right)^2 + C \left(\frac{\Delta G}{G} \right) + D = 0 \tag{6.14}$$

with

$$B = r \langle \beta_{u'} \rangle \langle \beta_d \rangle - \langle \beta_u \rangle \langle \beta_{d'} \rangle \tag{6.15}$$

$$C = r \left(\langle \beta_{u'} \rangle + \langle \beta_d \rangle \right) - \left(\langle \beta_u \rangle + \langle \beta_{d'} \rangle \right) \tag{6.16}$$

$$D = r - 1 \tag{6.17}$$

The solution of this second order equation is (for $B \neq 0$)

$$\frac{\Delta G}{G} = \frac{-C \pm \sqrt{C^2 - 4BD}}{2B} \tag{6.18}$$

The case where $B = 0$ is very helpful to illustrate clearly how to extract $\Delta G/G$ with the best possible precision (since $\langle \beta \rangle \ll 1$, the following definitions ensure that $B \ll D$):

$$\left(\frac{N}{4} \right) = N_u \approx N_{u'} \approx N_d \approx N_{d'} \tag{6.19}$$

and

$$\langle \beta \rangle = \langle \beta_u \rangle \approx \langle \beta_{d'} \rangle \approx -\langle \beta_{u'} \rangle \approx -\langle \beta_d \rangle \tag{6.20}$$

A more general expression of the error associated with eq. 6.18 can be found in [77]. However, this is irrelevant for the present discussion because the conclusions to draw are the same. Using these realistic approximations, the gluon polarisation is trivially extracted from eq. 6.14:

$$\left(\frac{\Delta G}{G} \right)_{B=0} = -\frac{D}{C} \tag{6.21}$$

The corresponding statistical error is given by

$$\begin{aligned} \sigma^2_{\frac{\Delta G}{G}} &= \left(\frac{\partial (\Delta G/G)}{\partial r} \right)^2 \sigma_r^2 \\ &= \frac{1}{\langle \beta \rangle^2 N} \quad \text{with} \quad \sigma_r = \frac{4}{\sqrt{N}} \end{aligned} \tag{6.22}$$

$$\overset{2}{\approx} \quad \frac{1}{\langle P_\mu P_t f\rangle^2 \left(\frac{S^2}{S+B}\right) \langle \hat{a}_{LL}\rangle^2} \tag{6.23}$$

In eq. 6.23 we have used $N = (S + B)$. The quantity FOM $\equiv S^2/(S + B)$ is the **F**igure **O**f **M**erit (or signal-strength) of the reconstructed D^0 mass spectra. One can easily see the interpretation given to the event rates, N, by looking to the mass spectra of $k\pi$ pairs (see Figs. 5.15, 5.17 and 5.18) or to the mass spectra of $K\pi\pi\pi$ combinations (cf. Fig. 5.16): they show a mass distribution containing the PGF events, S, inside the resonance that emerges over the combinatorial background B. From eq. 6.23 we can also verify that the FOM is inversely proportional to the precision of the gluon polarisation measurement. As a result, the main criterium for the selection of the final mass spectra should be the maximisation of the FOM for each reconstructed peak.

Event Weight to minimise the statistical error

It is clear from eq. 6.22 that no measurement can be made for the case where $\langle\beta\rangle^2 = 0$, because the resulting uncertainty would be infinite. Unfortunatelly, the partonic asymmetry $\hat{a}_{LL}$ assumes both positive and negative values (see Fig. 2.15). This fact may lead to a result for $\langle\beta\rangle^2$ which is very close to zero. The best way to solve this potential problem is to extract $\Delta G/G$ in bins of β. Since these measurements are independent (inside each bin), the corresponding statistical error is given by

$$\left(\sigma_{\frac{\Delta G}{G}}\right)^{N_{bin}} = \frac{1}{\sqrt{\sum_i^{N_{bin}} \left(\frac{\sum_j^N \beta_j^2}{N^2}\right)_i N_i}} \tag{6.24}$$

using

$$\begin{aligned} \langle\beta\rangle \quad &= \quad \frac{\int \beta\alpha \; d\xi}{\int \alpha \; d\xi} \\ &\overset{3}{\underset{\beta\frac{\Delta G}{G}\ll 1}{\approx}} \quad \frac{\int \beta\alpha \left(1+\beta\frac{\Delta G}{G}\right) \; d\xi}{\int \alpha \left(1+\beta\frac{\Delta G}{G}\right) \; d\xi} \quad \underset{\text{eq. 6.9}}{\overset{N\to\infty}{=}} \quad \frac{\sum_j^N \beta_j}{N} \end{aligned} \tag{6.25}$$

Ideally, an infinite number of bins should be used to allow for the best possible precision. The corresponding error is

$$\left(\sigma_{\frac{\Delta G}{G}}\right)^{N_{bin}\to\infty} = \frac{1}{\sqrt{\langle\beta^2\rangle N}} \tag{6.26}$$

Using this result, we can determine the maximum gain introduced by the binning in the signal-strength of a given D^0 mass spectrum:

$$\text{FOM(gain)} = \frac{\left(1/\left(\sigma_{\frac{\Delta G}{G}}\right)^{N_{bin}\to\infty}\right)^2}{\left(1/\sigma_{\frac{\Delta G}{G}}\right)^2} = \frac{\langle\beta^2\rangle}{\langle\beta\rangle^2} \tag{6.27}$$

[2] From $\sigma_{A_{c\bar{c}}}\left(\equiv \langle\hat{a}_{LL}\rangle \times \sigma_{\frac{\Delta G}{G}}\right) = \frac{1}{\langle P_\mu P_t f \frac{S}{S+B}\rangle\sqrt{N}} \overset{*}{=} \frac{1}{\langle P_\mu P_t f\rangle\frac{S}{\sqrt{S+B}}}$ $\quad *(\frac{S}{S+B}$ is independent of f, P_t and $P_\mu)$

[3] The approximation is justified by the observed data. A possible error made in the calculation of $\langle\beta\rangle$ has a negligible impact on $\Delta G/G$: the propagation of this error to $\Delta G/G$ is diluted by the ratio of asymmetries. Therefore, the approximation is only assumed for $\langle\beta\rangle$ (not for α).

If we define an appropriate weight for each event, ω, the ideal situation of an infinite number of bins is reached [49]. To confirm this, we must rewrite eq. 6.12 in terms of the double ratio of the weights:

$$r(\omega) = \left(\frac{W_u W_{d'}}{W_{u'} W_d}\right) = \frac{(1 - \langle\beta_u\rangle_{\omega_u}\frac{\Delta G}{G})(1 - \langle\beta_{d'}\rangle_{\omega_{d'}}\frac{\Delta G}{G})}{(1 - \langle\beta_{u'}\rangle_{\omega_{u'}}\frac{\Delta G}{G})(1 - \langle\beta_d\rangle_{\omega_d}\frac{\Delta G}{G})} \tag{6.28}$$

where we used

$$W_t = \sum_{i=1}^{N_t}\omega_i \quad , \quad \langle\beta_t\rangle_{\omega_t} = \frac{\int(\omega_t\beta_t\alpha_t)\ d\xi}{\int(\omega_t\alpha_t)\ d\xi} \ \text{ and } \ \alpha_t = \int(\omega_t a_t \Phi \hat{n}_t \hat{\sigma}_{tot,t})\ d\xi \tag{6.29}$$

Since by definition we have $\sigma\left(\sum_i^{N_t}\omega_t\right) = \left(\sum_i^{N_t}\omega_i\right)^2$, the statistical error for the weighted extraction of $\Delta G/G$ is (using again eq. 6.19 and eq. 6.20)

$$\begin{aligned}
\sigma^2_{\frac{\Delta G}{G}(\omega)} &= \left(\frac{1}{16\langle\beta\rangle^2_\omega}\right)\sigma^2_{r(\omega)} \\
&= \frac{1}{\left(\frac{16\langle\beta\omega\rangle^2}{\langle\omega\rangle^2}\right)\left(\frac{\left(\sum_i^{N_t}\omega_t\right)^2}{16\sum_i^{N_t}(\omega_t)^2}\right)} \\
&= \frac{1}{\left(\frac{\langle\beta\omega\rangle^2}{\langle\omega\rangle^2}\right)\left(\frac{N\langle\omega\rangle^2}{\langle\omega^2\rangle}\right)}
\end{aligned} \tag{6.30}$$

If we define $\omega = \beta$, we obtain:

$$\begin{aligned}
\sigma_{\frac{\Delta G}{G}(\omega)} &= \frac{1}{\sqrt{\langle\beta^2\rangle N}} \\
&= \left(\sigma_{\frac{\Delta G}{G}}\right)^{N_{bin}\to\infty}
\end{aligned} \tag{6.31}$$

In conclusion, the use of $\omega = \beta$ allows us to reach the ideal case of an infinite number of β bins. Consequently, the best possible precision for an unbiased extraction of $\Delta G/G$ is achieved by a weighted analysis [4]. The gluon polarisation can be estimated from eq. 6.14 (replacing r and $\langle\beta_t\rangle$ by $r(\omega)$ and $\langle\beta_t\rangle_{\omega_t}$), using the following factor which is evaluated for each D^0 candidate:

$$\langle\beta_t\rangle_{\omega_t} \overset{\text{eq.6.25}}{=} \frac{\sum_j^{N_t}\beta_j\omega_j}{\sum_j^{N_t}\omega_j} \tag{6.32}$$

$$\omega = f P_\mu \left(\frac{S}{S+B}\right) a_{LL} \qquad \text{and} \qquad \beta = f P_\mu P_t \left(\frac{S}{S+B}\right) a_{LL} \tag{6.33}$$

The target polarisation, P_t, was removed from the event weight because it is a time dependent quantity. This dependence results from the target re-polarisation or relaxation, and it may

[4] For a more general discussion concerning the extraction of weighted asymmetries see [78].

even be different for each cell. As explained before, to be able to extract $\Delta G/G$ from eq. 6.28 we must ensure the following identity:

$$K = \frac{\langle a_u \rangle_{\omega_u} \langle a_{d'} \rangle_{\omega_{d'}}}{\langle a_{u'} \rangle_{\omega_{u'}} \langle a_d \rangle_{\omega_d}} = 1 \qquad \text{with} \qquad \langle a_t \rangle_{\omega_t} = \frac{\int (a_t \omega_t \Phi \hat{n}_t \hat{\sigma}_{tot,t}) \; d\xi}{\int (\omega_t \Phi \hat{n}_t \hat{\sigma}_{tot,t}) \; d\xi} \tag{6.34}$$

From the above definitions we immediately see the impact of the time dependent P_t (if included in ω) in the ratio K: it may deviate from 1 even if the acceptances are perfectly stable in time. All the major sources of $K \neq 1$ are taken into account in the systematic error. However, it is wise to avoid unnecessary additional contributions such as the definition of P_t inside the event weight. All the needed ingredients for eq. 6.33 are obtained as true values, for each event, with their uncertainty being transferred to the systematic error. The determination of f, P_μ and P_t was discussed in Chapter 3, whereas the parameterisations of a_{LL} and $S/(S+B)$ will be discussed in Chapter 7.

We have now all the required information to define the remaining variable of the puzzle, $\langle x_g \rangle$, which represents the average fraction of the nucleon momentum carried by the probed gluons. Assuming a linear behaviour for $\Delta G/G$,

$$\frac{\Delta G}{G} = a \left(x_g - \langle x_g \rangle \right) + b \tag{6.35}$$

we can easily demonstrate eq. 6.7 and write a general expression for $\langle x_g \rangle$:

$$\begin{aligned}
A_{c\bar{c}} \quad &\overset{\text{eq.6.7}}{=} \quad \left\langle \; \hat{a}_{LL} \frac{\Delta G}{G}(x_g) \; \right\rangle_\omega \qquad \rightarrow \qquad \text{weighted case} \\
&= \quad \frac{\int\int \omega(\xi) \hat{a}_{LL}(\hat{s}) \left[a(x_g - \langle x_g \rangle) + b \right] \hat{\sigma}_{\mu g}(\hat{s}) G(x_g, \hat{s}) \; d\xi d\hat{s}}{\int\int \omega(\xi) \hat{\sigma}_{\mu g}(\hat{s}) G(x_g, \hat{s}) \; d\xi d\hat{s}} \qquad (6.36) \\
&\overset{x_g \,=\, \langle x_g \rangle}{=} \quad \frac{b \int \omega(\xi) \hat{a}_{LL}(\hat{s}) \hat{\sigma}_{\mu g}(\hat{s}) G(x_g, \hat{s}) \; d\hat{\xi}}{\int \omega(\xi) \hat{\sigma}_{\mu g}(\hat{s}) G(x_g, \hat{s}) \; d\hat{\xi}} \qquad (6.37) \\
&\overset{*}{=} \quad \langle \hat{a}_{LL} \rangle_\omega \frac{\Delta G}{G}(\langle x_g \rangle) \qquad (6.38)
\end{aligned}$$

* using

$$b = \frac{\Delta G}{G}(\langle x_g \rangle) \qquad \text{and} \qquad \langle \hat{a}_{LL} \rangle_\omega = \frac{\int \omega(\xi) \hat{a}_{LL}(\hat{s}) \hat{\sigma}_{\mu g}(\hat{s}) G(x_g, \hat{s}) \; d\hat{\xi}}{\int \omega(\xi) \hat{\sigma}_{\mu g}(\hat{s}) G(x_g, \hat{s}) \; d\hat{\xi}} \tag{6.39}$$

The eq. 6.37 is only obtained from eq. 6.36 if the following definition is true:

$$\langle x_g \rangle = \frac{\int x_g \omega(\xi) \hat{a}_{LL}(\hat{s}) \hat{\sigma}_{\mu g}(\hat{s}) G(x_g, \hat{s}) \; d\hat{\xi}}{\int \omega(\xi) \hat{a}_{LL}(\hat{s}) \hat{\sigma}_{\mu g}(\hat{s}) G(x_g, \hat{s}) \; d\hat{\xi}} \qquad \text{with} \qquad d\hat{\xi} = d\xi d\hat{s} \;\; , \;\; \langle x_g \rangle = \langle x_g \rangle_\omega \tag{6.40}$$

In order to complete section 6.1.1, we quantitatively verify the large gain introduced by the weighted analysis in the FOM of each spectrum (see Fig. 6.2). We can conclude that the use of ω is absolutely essential for an accurate measurement of $\Delta G/G$. Moreover, we can also verify that the FOM corresponding to an infinite number of bins is achieved even without the inclusion of P_t in the weight. These huge improvements (by a factor 3 or 4) are justified by the unfortunate shape of the β distributions. Since they peak around zero, we have:

$$\frac{\langle\beta^2\rangle}{\langle\beta\rangle^2} = \frac{\langle\beta\rangle^2 + \sigma_\beta^2}{\langle\beta\rangle^2} = \left(1 + \frac{\sigma_\beta^2}{\langle\beta\rangle^2}\right) \qquad \text{with} \qquad \frac{\sigma_\beta^2}{\langle\beta\rangle^2} \overset{\langle\beta\rangle\to 0}{\gg} 1 \tag{6.41}$$

The main reason for $\langle\beta\rangle$ being close to zero is given by the distribution of the partonic asymmetry, $\hat{a}_{LL}$, which can assume positive and negative values. Also, the purity of the reconstructed D^0 mesons, $S/(S+B)$, is much higher for low values of a_{LL} (and vice-versa). Consequently, a proper parameterisation of $S/(S+B)$ brings $\langle\beta\rangle$ even closer to zero. In the limit of $\langle\beta\rangle = 0$, an infinite improvement is obtained due to the total uncertainty that results from the standard analysis (cf. eq. 6.22). In practice, the gains are smaller than the ones shown in Fig. 6.2, because one can extract $\Delta G/G$ in several β bins. Nevertheless, the number of bins is strongly limited by the available statistics and, therefore, the weighted method corresponds to the best possible statistical precision that one can achieve. Moreover, the weighting of the charmed events allows us to measure a more reliable asymmetry: the use of ω in the analysis ensures that the D^0 candidates with a small $\langle\beta\rangle$ factor have a small impact on the final asymmetry.

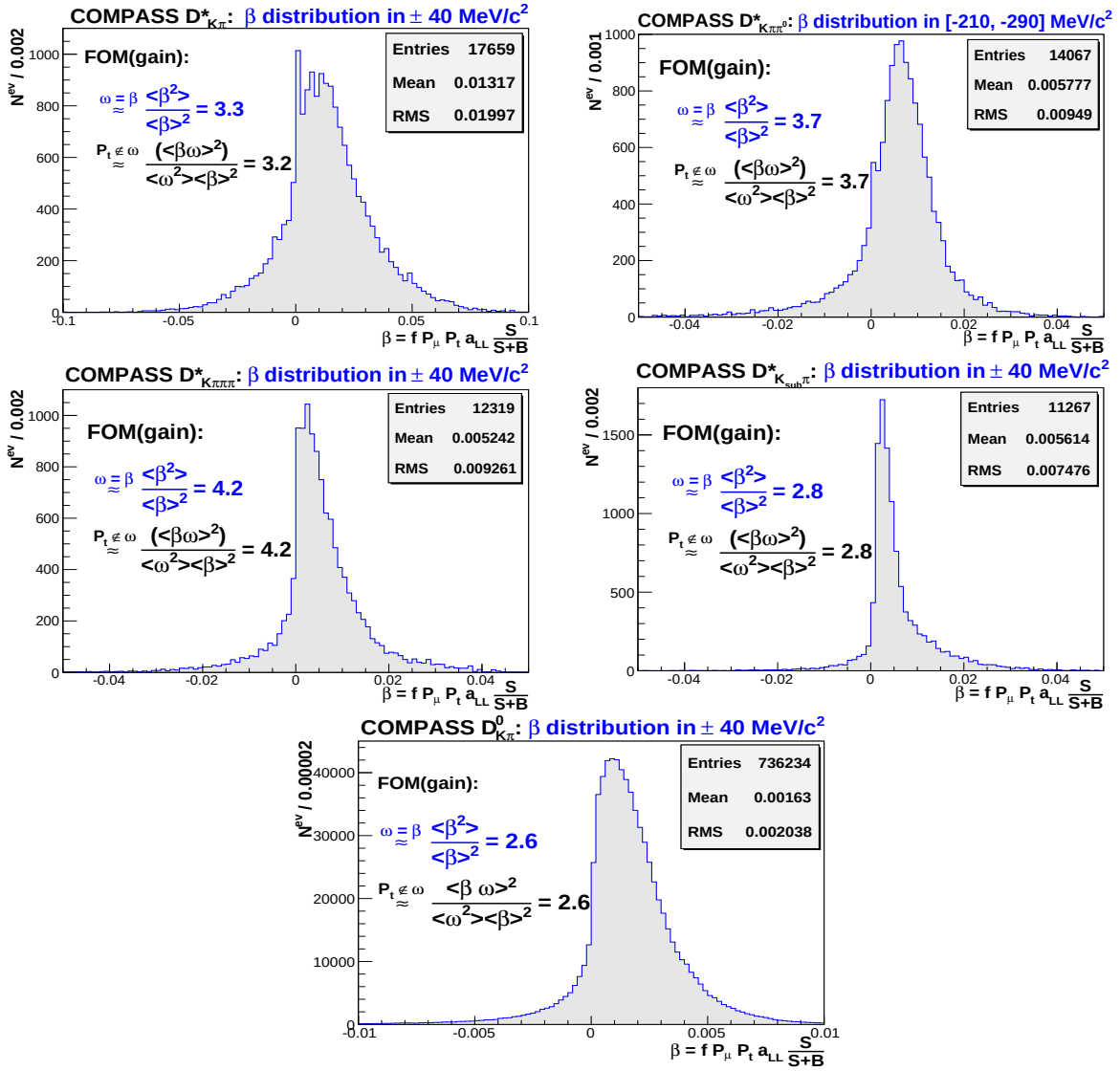

Figure 6.2: Distributions of β, per channel, using only events under the reconstructed peak. Since $\sigma_{\Delta G/G} \propto (1/\sqrt{FOM})$, the statistical gain introduced by ω range from 40% ($D^0_{K\pi}$) to 50% ($D^*_{K\pi\pi\pi}$). The FOM(gain) is calculated with the help of eqs. 6.22, 6.26 and 6.31.

6.1.2 Fit method - Simultaneous extraction of $\Delta G/G$ and A_{bg}

In the previous section we saw how to extract $\Delta G/G$ in the most optimal way. One of the two assumptions involved in the determination of $\Delta G/G$ is summarised in eqs. 6.13 and 6.34, for the unweighted and weighted methods: the possible modifications in the experimental acceptance over time affect all target cells in the same way. This is a fair assumption because it only requires that a specific cell should not significantly move its position with respect to the other cell(s) (small deviations of the target stability are considered in the systematic error).

Up to now a possible contribution from the background asymmetry A_{bg} has been neglected. However, if in reality A_{bg} is nonzero, the assumption that A_{bg} is negligible may be a bit dangerous for the validity of the procedure described in 6.1.1. One solution to this potential problem would be to correct the $\Delta G/G$ result, by subtracting a value of A_{bg} estimated from events belonging to the sidebands of the D^0 mass spectra (see Figs. 5.15-5.18). Yet, this is not the ideal solution because the events that contaminate the signal (under the reconstructed peak) are not taken into account in this correction. There is an elegant and much more efficient method that involves the simultaneous extraction of $\Delta G/G$ and A_{bg} [49]. In order to explain this method, we must write the weighted version of eq. 6.9 with $A_{bg} \neq 0$ (consequently, a weight ω_B should be considered). Using $t = (u,\ d,\ u',\ d')$, $C = (S,\ B)$ and $C' = (S,\ B)$, we obtain:

$$\sum_{i=1}^{N_t} \omega_{i,C} = \alpha_{t,C} \left(1 - \langle \beta_{t,S} \rangle_{\omega_{t,C}} \frac{\Delta G}{G} - \langle \beta_{t,B} \rangle_{\omega_{t,C}} A_{bg} \right) \tag{6.42}$$

with

$$\begin{aligned} \langle \beta_{t,C'} \rangle_{\omega_{t,C}} &= \frac{\int (\omega_{t,C} \beta_{t,C'} \alpha_t)\ d\xi}{\int (\omega_{t,C} \alpha_t)\ d\xi} \\ &\overset{\text{eq.6.25}}{\approx} \frac{\sum_{i=1}^{N_t} P_{t,i} \omega_{i,C'} \omega_{i,C}}{\sum_{i=1}^{N_t} \omega_{i,C}} \end{aligned} \tag{6.43}$$

and

$$\omega_S = f P_\mu \left(\frac{S}{S+B} \right) a_{LL} \quad , \quad \omega_B = f P_\mu \left(\frac{B}{S+B} \right) D \tag{6.44}$$

$$\alpha_{t,C} = \int (\omega_{t,C} a_t \Phi \hat{n}_t \hat{\sigma}_{tot,t})\ d\xi \tag{6.45}$$

In eq. 6.42 we have defined 8 equations with the following 10 unknown quantities:

$$\frac{\Delta G}{G},\ A_{bg},\ \alpha_{u,S},\ \alpha_{d,S},\ \alpha_{u',S},\ \alpha_{d',S},\ \alpha_{u,B},\ \alpha_{d,B},\ \alpha_{u',B},\ \alpha_{d',B}$$

These 8 equations result from the weighting procedure: we have 4 equations for each spin configuration t weighted with a signal weight, ω_S, or with a background weight, ω_B. The number of unknowns corresponding to the parameters α is reduced from 8 to 6, because $\alpha_{u',S}$ and $\alpha_{u',B}$ are fixed by the following acceptance conditions (cf. eq. 6.13):

$$\alpha_{u',S} = \left(\frac{\alpha_{u,S}\alpha_{d',S}}{\alpha_{d,S}}\right) \qquad \text{and} \qquad \alpha_{u',B} = \left(\frac{\alpha_{u,B}\alpha_{d',B}}{\alpha_{d,B}}\right) \tag{6.46}$$

Using these constraints the system 6.42 can be solved simultaneously for $\Delta G/G$ and A_{bg}, provided that we know ω_S and ω_B for every D^0 candidate. Nevertheless, one can reduce further the number of unknowns by assuming that:

$$\frac{\alpha_{d,S}}{\alpha_{d,B}} = \frac{\alpha_{d',S}}{\alpha_{d',B}} \tag{6.47}$$

The same is assumed for the u and u' configurations. These conditions imply that the number of unknowns is reduced to 7 (by fixing, for eg., $\alpha_{d',S}$). The assumption made here is even safer: the signal and background events are affected in the same way by a possible change in the position of the cell where they are produced (their ratio is the same before and after the field reversal). The reduced number of unknowns in the 8 equations allows us to extract them by the method of minimum quadratics:

$$\chi^2 = (\vec{N} - \vec{f})^T Cov^{-1} (\vec{N} - \vec{f}) \tag{6.48}$$

with

$$\vec{N} = \left(\sum_{i=1}^{N_u}\omega_{i,S},\ \sum_{i=1}^{N_d}\omega_{i,S},\ \sum_{i=1}^{N_{u'}}\omega_{i,S},\ \sum_{i=1}^{N_{d'}}\omega_{i,S},\ \sum_{i=1}^{N_u}\omega_{i,B},\ \sum_{i=1}^{N_d}\omega_{i,B},\ \sum_{i=1}^{N_{u'}}\omega_{i,B},\ \sum_{i=1}^{N_{d'}}\omega_{i,B}\right) \tag{6.49}$$

and

$$\vec{f} = (f_{u,S},\ f_{d,S},\ f_{u',S},\ f_{d',S},\ f_{u,B},\ f_{d,B},\ f_{u',B},\ f_{d',B}) \tag{6.50}$$

The components of the vector function, $\vec{f}$, are obtained from each of the 8 equations for the weighted event rates:

$$\sum_{i=1}^{N_u}\omega_{i,S} = \alpha_{u,S}\left[1 - \langle\beta_{u,S}\rangle_{\omega_{i,S}}\frac{\Delta G}{G} - \langle\beta_{u,B}\rangle_{\omega_{i,S}}A_{bg}\right] = f_{u,S}(\alpha_{u,S},\ \frac{\Delta G}{G},\ A_{bg}) \tag{6.51}$$

$$\sum_{i=1}^{N_d}\omega_{i,S} = \alpha_{d,S}\left[1 - \langle\beta_{d,S}\rangle_{\omega,S}\frac{\Delta G}{G} - \langle\beta_{d,B}\rangle_{\omega_{i,S}}A_{bg}\right] = f_{d,S}(\alpha_{d,S},\ \frac{\Delta G}{G},\ A_{bg}) \tag{6.52}$$

$$\sum_{i=1}^{N_{u'}}\omega_{i,S} = \alpha_{u',S}\left[1 - \langle\beta_{u',S}\rangle_{\omega_{i,S}}\frac{\Delta G}{G} - \langle\beta_{u',B}\rangle_{\omega_{i,S}}A_{bg}\right] = f_{u',S}(\alpha_{u',S},\ \frac{\Delta G}{G},\ A_{bg}) \tag{6.53}$$

$$\sum_{i=1}^{N_{d'}}\omega_{i,S} = \alpha_{d',S}\left[1 - \langle\beta_{d',S}\rangle_{\omega_{i,S}}\frac{\Delta G}{G} - \langle\beta_{d',B}\rangle_{\omega_{i,S}}A_{bg}\right] = f_{d',S}(\alpha_{d',S},\ \frac{\Delta G}{G},\ A_{bg}) \tag{6.54}$$

$$\sum_{i=1}^{N_u} \omega_{i,B} = \alpha_{u,B}\left[1 - \langle\beta_{u,S}\rangle_{\omega_{i,B}} \frac{\Delta G}{G} - \langle\beta_{u,B}\rangle_{\omega_{i,B}} A_{bg}\right] = f_{u,B}(\alpha_{u,B},\ \frac{\Delta G}{G},\ A_{bg}) \quad (6.55)$$

$$\sum_{i=1}^{N_d} \omega_{i,B} = \alpha_{d,B}\left[1 - \langle\beta_{d,S}\rangle_{\omega_{i,B}} \frac{\Delta G}{G} - \langle\beta_{d,B}\rangle_{\omega_{i,B}} A_{bg}\right] = f_{d,B}(\alpha_{d,B},\ \frac{\Delta G}{G},\ A_{bg}) \quad (6.56)$$

$$\sum_{i=1}^{N_{u'}} \omega_{i,B} = \alpha_{u',B}\left[1 - \langle\beta_{u',S}\rangle_{\omega_{i,B}} \frac{\Delta G}{G} - \langle\beta_{u',B}\rangle_{\omega_{i,B}} A_{bg}\right] = f_{u',B}(\alpha_{u',B},\ \frac{\Delta G}{G},\ A_{bg}) \quad (6.57)$$

$$\sum_{i=1}^{N_{d'}} \omega_{i,B} = \alpha_{d',B}\left[1 - \langle\beta_{d',S}\rangle_{\omega_{i,B}} \frac{\Delta G}{G} - \langle\beta_{d',B}\rangle_{\omega_{i,B}} A_{bg}\right] = f_{d',B}(\alpha_{d',B},\ \frac{\Delta G}{G},\ A_{bg}) \quad (6.58)$$

Finally, the covariance matrix is given by

$$\begin{pmatrix}
\sigma^2_{u,S} & 0 & 0 & 0 & \sigma_{u,SB} & 0 & 0 & 0 \\
0 & \sigma^2_{d,S} & 0 & 0 & 0 & \sigma_{d,SB} & 0 & 0 \\
0 & 0 & \sigma^2_{u',S} & 0 & 0 & 0 & \sigma_{u',SB} & 0 \\
0 & 0 & 0 & \sigma^2_{d',S} & 0 & 0 & 0 & \sigma_{d',SB} \\
\sigma_{u,SB} & 0 & 0 & 0 & \sigma^2_{u,B} & 0 & 0 & 0 \\
0 & \sigma_{d,SB} & 0 & 0 & 0 & \sigma^2_{d,B} & 0 & 0 \\
0 & 0 & \sigma_{u',SB} & 0 & 0 & 0 & \sigma^2_{u',B} & 0 \\
0 & 0 & 0 & \sigma_{d',SB} & 0 & 0 & 0 & \sigma^2_{d',B}
\end{pmatrix}$$

with

$$\sigma_{t,SB} = Cov(\sum_{i=1}^{N_t} \omega_{i,S},\ \sum_{j=1}^{N_t} \omega_{j,B}) \ \overset{5}{\approx}\ \sum_{i=1}^{N_t} \omega_{i,S}\omega_{i,B} \quad (6.59)$$

and

$$\sigma^2_{t,C} = Cov(\sum_{i=1}^{N_t} \omega_{i,C},\ \sum_{i=1}^{N_t} \omega_{i,C}) \ \approx\ \sum_{i=1}^{N_t} (\omega_{i,C})^2 \quad (6.60)$$

where $t = (u,\ d,\ u',\ d')$ and $C = (S,\ B)$. The existence of nonzero off-diagonal elements is related to the fact that the same data are used twice: once with a weight ω_S and once with ω_B.

---

[5]

$$\begin{aligned}
\sigma_{t,SB} &= \left\langle \sum_{i=1}^{N_t} \omega_{i,S} \sum_{j=1}^{N_t} \omega_{j,B} \right\rangle - \left\langle \sum_{i=1}^{N_t} \omega_{i,S} \right\rangle \left\langle \sum_{j=1}^{N_t} \omega_{j,B} \right\rangle \\
&= \left\langle \sum_{i=j}^{N_t} \omega_{i,S}\omega_{i,B} + \sum_{i\neq j}^{N_t} \omega_{i,S}\omega_{j,B} \right\rangle - \left\langle \sum_{i=1}^{N_t} \omega_{i,S} \right\rangle \left\langle \sum_{j=1}^{N_t} \omega_{j,B} \right\rangle \\
&\overset{\text{eq.6.25}}{=} \langle N\rangle \langle\omega_S\omega_B\rangle + \langle N(N-1)\rangle \langle\omega_S\rangle \langle\omega_B\rangle - \langle N\rangle^2 \langle\omega_S\rangle \langle\omega_B\rangle \\
&= \langle N\rangle \langle\omega_S\omega_B\rangle + (\ \underbrace{\overbrace{\langle N^2\rangle - \langle N\rangle^2}^{\sigma^2_N} - \langle N\rangle}_{=0 \text{ if N is Poisson distributed}}\ ) \langle\omega_S\rangle \langle\omega_B\rangle \ \approx\ \sum_{i=1}^{N_t} \omega_{i,S}\omega_{i,B}
\end{aligned}$$

This fit method is the one used to estimate the gluon polarisation. The second order weighted method (described in section 6.1.1) was also used, but only to control the results obtained by the fit method. For both cases, $\Delta G/G$ is extracted in the leading order approximation (LO-QCD, cf. Fig. 2.14) using the interpretation of $A_{c\bar{c}}$ given in eq. 6.7. However, we have seen in Chapter 2 that the next-to-leading order corrections to the PGF process may be important for the charm production (see Fig. 2.20). It can be seen from Fig. 2.18 that the partonic asymmetry may even change by a factor of 2, in the COMPASS kinematic domain. The implementation of such corrections in the fit method will be discussed in the following section.

6.2 The Fit method with NLO corrections

In addition to the several NLO corrections to the photon-gluon fusion graph (cf. Fig. 2.11 and Fig. 2.20), an unwanted process must be properly taken into account for the NLO determination of $\Delta G/G$. This process corresponds to the interaction between a virtual-photon and a light-quark in the nucleon, producing in the final state a pair of charmed quarks (see Fig. 2.19). The possible reconstruction of the resulting open-charm mesons (which are not originate from a PGF interaction) contributes to the physical background of the D^0 resonance in the mass distributions. Until now we have always treated each event belonging to the D^0 resonance as resulting from one interaction with a gluon. However, at NLO it is also necessary to take into account the contamination introduced by the physical background. The impact in the analysis caused by these events must be carefully evaluated. Since in the NLO approximation we have,

$$\frac{S}{S+B} = \left(\frac{S^{(PGF)} + S^{(q)}}{S^{(PGF)} + S^{(q)} + B} \right) \tag{6.61}$$

and

$$a_{LL} = \left[\left(a_{LL}^{0\ (PGF)\ +\ 1\ (PGF)} \right) \quad + \quad \underbrace{a_{LL}^{1\ (q)}}_{\text{physical background}} \right] \qquad \text{with} \qquad a_{LL} = \langle \hat{a}_{LL} \rangle \tag{6.62}$$

the ideal solution for the extraction of $\Delta G/G$ would be (starting from eq. 6.42):

$$\sum_{i=1}^{N_t} \omega_{i,C} = \alpha_{t,C} \left(1 - \langle \beta_{t,S^{(PGF)}} \rangle_{\omega_{t,C}} \frac{\Delta G}{G} - \tilde{A}^{(q)} - \langle \beta_{t,B} \rangle_{\omega_{t,C}} A_{bg} \right) \tag{6.63}$$

where $C = (S^{(PGF)}, B)$ and $q = (u_{quark},\, d_{quark},\, c_{quark},\, \bar{c}_{(anti)quark})$. The Feynman diagrams represented in Fig. 2.19 show two kinds of interactions that contribute to the physical background: in the first two diagrams we see an interaction between a charm quark $(c_{quark},\, \bar{c}_{(anti)quark})$ [6] and a valence quark in the nucleon, whereas the last two illustrate a direct interaction between the virtual-photon and one of the valence quarks $(u_{quark},\, d_{quark})$ [7]. Contributions from the polarised sea-quarks are negligible. Comparing eq. 6.63 with eq. 6.42 we obtain the following differences:

[6] These quarks are produced by the γ^*. One of them emits the gluon involved in the interaction and, therefore, the resulting mesons have nothing to do with the gluon polarisation in the nucleon.

[7] The charm quarks are produced by a valence quark, after or before its collision with the γ^*.

$$\omega_{S^{(PGF)}} = fP_\mu \left(\frac{S^{(PGF)}}{S^{(PGF)} + S^{(q)} + B} \right) \left(a_{LL}^{0\ (PGF)\ +\ 1\ (PGF)} \right) \tag{6.64}$$

and

$$\tilde{A}^{(q)} = \langle \beta_{t,S^{(q)}} \rangle_{\omega_{t,C}} \underbrace{\left(\frac{\sum_q e_q^2 \Delta q}{\sum_q e_q^2 q} \right)}_{A_1} \tag{6.65}$$

using

$$\langle \beta_{t,S^{(q)}} \rangle_{\omega_{t,C}} \approx \frac{\sum_{i=1}^{N_t} P_{t,i} \omega_{i,C} \left[fP_\mu \left(\frac{S^{(q)}}{S^{(PGF)}+S^{(q)}+B} \right) a_{LL}^{1\ (q)} \right]_i}{\sum_{i=1}^{N_t} \omega_{i,C}} \tag{6.66}$$

The system 6.63 has solution provided that we know the values of ω_B, $\langle \beta_{t,B} \rangle_{\omega_{t,C}}$, $\omega_{S^{(PGF)}}$, $\langle \beta_{t,S^{(PGF)}} \rangle_{\omega_{t,C}}$ and $\langle \beta_{t,S^{(q)}} \rangle_{\omega_{t,C}}$ for each D^0 candidate. Note that the asymmetry A_1 in eq. 6.65 is experimentally well known, which implies that $\tilde{A}^{(q)}$ is contributing only as a correction number. Therefore, we solve eq. 6.63 using the same 7 unknowns described in section 6.1.2.

However, there is one big disadvantage in using this method for the present analysis:

- It is not possible to distinguish $S^{(q)}$ from $S^{(PGF)}$ without increasing considerably the systematic error of the $\Delta G/G$ measurement.

Two separate Monte Carlo parameterisations are needed to obtain $S^{(q)}/(S^{(PGF)} + S^{(q)} + B)$ and $S^{(PGF)}/(S^{(PGF)} + S^{(q)} + B)$ (no distinction is possible from real data). In order to trust these two fractions we must use a full NLO Monte Carlo generator and, in addition, we need to tune it carefully so that we can perfectly describe the real data. Consequently, the advantage of having an analysis that is weakly dependent of models is drastically reduced. A method capable of solving this problem will be presented in the following section.

6.2.1 NLO extraction of ΔG/G without $S^{(q)}$ identification

First, we consider the decomposition of the muon-nucleon cross-sections. In the perturbative regime of QCD (ensured by the heavy quark mass), we have for the polarised part:

$$\begin{aligned} \Delta\sigma_{c\bar{c}} &= \left(\Delta G \otimes \left(\Delta\hat{\sigma}_{\mu g}^{0\ (PGF)} + \Delta\hat{\sigma}_{\mu g}^{1\ (PGF)} \right) + \sum_{q'} e_{q'}^2 \Delta q' \otimes \Delta\hat{\sigma}_{\mu q'}^{1\ (q')} + \sum_{q''} \Delta q'' \otimes \Delta\hat{\sigma}_{\mu q''}^{1\ (q'')} \right) \otimes F \\ &= \left(\Delta G \otimes \Delta\hat{\sigma}^{(g)} + \sum_q \Delta q \otimes \Delta\hat{\sigma}^{(q)} \right) \otimes F \end{aligned} \tag{6.67}$$

with

$$\Delta\hat{\sigma}^{(g)} = \left(\Delta\hat{\sigma}_{\mu g}^{0\ (PGF)} + \Delta\hat{\sigma}_{\mu g}^{1\ (PGF)} \right) \quad \text{and} \quad \Delta\hat{\sigma}^{(q)} \overset{8}{=} \left(\frac{5}{18} \Delta\hat{\sigma}_{\mu q'}^{1\ (q')} + \Delta\hat{\sigma}_{\mu q''}^{1\ (q'')} \right) \tag{6.68}$$

where $q' = (u_{quark}, d_{quark})$, $q'' = (c_{quark}, \bar{c}_{(anti)quark})$, $q = (q', q'')$, $\otimes$ is the convolution integral between the partonic cross-sections and the corresponding structure functions (of gluons and quarks), and F stands for the fragmentation function. All the kinematic dependencies have been omitted for simplification. For the unpolarised cross-section we have:

$$\sigma_{c\bar{c}} = \left(G \otimes \hat{\sigma}^{(g)} + \sum_q q \otimes \hat{\sigma}^{(q)} \right) \otimes F \tag{6.69}$$

The resulting asymmetry is

$$\begin{aligned} A_{c\bar{c}} = \left(\frac{\Delta\sigma_{c\bar{c}}}{\sigma_{c\bar{c}}} \right) &= \frac{\left(\frac{\Delta G}{G} G \otimes \Delta\hat{\sigma}^{(g)} + A_1^{d,c} \sum_q q \otimes \Delta\hat{\sigma}^{(q)} \right) \otimes F}{\sigma_{c\bar{c}}} \\ &= \frac{\int \left(\frac{\Delta G}{G} + \frac{A_1^{d,corr} \sum_q q\Delta\hat{\sigma}^{(q)}}{G\Delta\hat{\sigma}^{(g)}} \right) \left(\frac{G\Delta\hat{\sigma}^{(g)}}{G\hat{\sigma}^{(g)} + \sum_q q\hat{\sigma}^{(q)}} \right) \left(G\hat{\sigma}^{(g)} + \sum_q q\hat{\sigma}^{(q)} \right) F \, d\hat{s}}{\sigma_{c\bar{c}}} \\ &= \left\langle \frac{\Delta G}{G} \hat{a}_{LL}^{(g)} + A_1^{d,corr} \hat{a}_{LL}^{(q)} \right\rangle \\ &\overset{\text{eq.6.38}}{=} \underbrace{\left\langle \frac{\Delta G}{G} + A_1^{d,corr} \frac{\hat{a}_{LL}^{(q)}}{\hat{a}_{LL}^{(g)}} \right\rangle}_{A_{gq}:\ D^0 \text{ asymmetry}} \left\langle \hat{a}_{LL}^{(g)} \right\rangle \end{aligned} \tag{6.70}$$

using for the case of the deuteron target:

$$A_1^d = \frac{\sum_q e_q^2 \Delta q}{\sum_q e_q^2 q} \quad , \quad A_1^{d,corr} = \frac{A_1^d}{1 - \frac{3}{2}\omega_D} \tag{6.71}$$

and

$$\hat{a}_{LL}^{(g)} = \frac{G\Delta\hat{\sigma}^{(g)}}{G\hat{\sigma}^{(g)} + \sum_q q\hat{\sigma}^{(q)}} \quad , \quad \hat{a}_{LL}^{(q)} = \frac{\sum_q q\Delta\hat{\sigma}^{(q)}}{G\hat{\sigma}^{(g)} + \sum_q q\hat{\sigma}^{(q)}} \tag{6.72}$$

After inserting this expression for $A_{c\bar{c}}$ in eq. 6.2, it is straightforward to obtain the following system of 8 weighted equations (NLO equivalent of eq. 6.42):

$$\sum_{i=1}^{N_t} \omega_{i,C} = \alpha_{t,C} \left(1 - \langle \beta_{t,S} \rangle_{\omega_{t,C}} A_{gq} - \langle \beta_{t,B} \rangle_{\omega_{t,C}} A_{bg} \right) \tag{6.73}$$

[8] The factor $\frac{5}{18}$ is a consequence of using a deuteron target (80 % of the data): we have the same number of u_{quarks} and d_{quarks} inside the polarised target, which allows us to factorize $\sum_{q'} e_{q'}^2$ in front of the partonic cross-section $\Rightarrow \sum_{q'} e_{q'}^2 \Delta\hat{\sigma}_{\mu q'}^{(q')} = \left(\frac{(4/9)+(1/9)}{2} \right) \Delta\hat{\sigma}_{\mu q'}^{(q')}$ (averaged over the isoscalar target). The second term, $\Delta\hat{\sigma}_{\mu q''}^{(q'')}$, is needed to describe the charm production by the virtual-photon: in this case, all valence quarks contribute equally to the physical background because they are coupled to a virtual-gluon (consequently, this term is convoluted only with $\sum_{q''} \Delta q''$).

with $C = (S,\ B)$, $t = (u,\ d,\ u',\ d')$ and $S = \left(S^{(PGF)} + S^{(q)}\right)$. From this system of 8 equations and 7 unknowns, one can extract $A_{gq}(\langle x_g \rangle)$ using:

$$\omega_S = f P_\mu \left(\frac{S}{S+B}\right) a_{LL}^{(g)} \quad , \quad \omega_B = f P_\mu \left(\frac{B}{S+B}\right) D \tag{6.74}$$

and

$$a_{LL}^{(g)} = \left\langle \hat{a}_{LL}^{(g)} \right\rangle_\omega = \frac{\int \omega_S \hat{a}_{LL}^{(g)} \left(G\hat{\sigma}^{(g)} + \sum_q q\hat{\sigma}^{(q)}\right)\ d\hat{\xi}}{\int \omega_S \left(G\hat{\sigma}^{(g)} + \sum_q q\hat{\sigma}^{(q)}\right)\ d\hat{\xi}} \tag{6.75}$$

$$\langle x_g \rangle_\omega \overset{\text{eq.6.40}}{=} \frac{\int x_g \omega_S \hat{a}_{LL}^{(g)} \left(G\hat{\sigma}^{(g)} + \sum_q q\hat{\sigma}^{(q)}\right)\ d\hat{\xi}}{\int \omega_S \hat{a}_{LL}^{(g)} \left(G\hat{\sigma}^{(g)} + \sum_q q\hat{\sigma}^{(q)}\right)\ d\hat{\xi}} \tag{6.76}$$

Since this asymmetry is obtained per week of data taking (cf. section 5.1), we can safely extract the gluon polarisation from A_{gq} [9]:

$$\left(\frac{\Delta G}{G}(\langle x_g \rangle)\right)^{\text{week}} = \left[A_{gq} - \left\langle A_1^{d,corr} \frac{\hat{a}_{LL}^{(q)}}{\hat{a}_{LL}^{(g)}} \right\rangle\right]_{\langle x_g \rangle}^{\text{week}} \tag{6.77}$$

where

$$\begin{aligned} \left\langle A_1^{d,corr} \frac{\hat{a}_{LL}^{(q)}}{\hat{a}_{LL}^{(g)}} \right\rangle_{\langle x_g \rangle} &= \frac{\int \omega_S \left(A_1^{d,corr} \frac{\hat{a}_{LL}^{(q)}}{\hat{a}_{LL}^{(g)}}\right) \left(G\hat{\sigma}^{(g)} + \sum_q q\hat{\sigma}^{(q)}\right)\ d\hat{\xi}}{\int \omega_S \left(G\hat{\sigma}^{(g)} + \sum_q q\hat{\sigma}^{(q)}\right)\ d\hat{\xi}} \\ &\approx \frac{\sum_{i=1}^{N} \omega_S \left(A_1^{d,corr} \frac{\hat{a}_{LL}^{(q)}}{\hat{a}_{LL}^{(g)}}\right)}{\sum_{i=1}^{N} \omega_S} \end{aligned} \tag{6.78}$$

Finally, we have:

$$\left\langle \frac{\Delta G}{G}(\langle x_g \rangle) \right\rangle = \frac{\sum_{\text{week}} \left(\frac{(\Delta G/G)^{\text{week}}}{\sigma^2_{(\Delta G/G)^{\text{week}}}}\right)}{\sum_{\text{week}} \left(\frac{1}{\sigma^2_{(\Delta G/G)^{\text{week}}}}\right)} \quad \text{and} \quad \sigma_{\frac{\Delta G}{G}(\langle x_g \rangle)} = \sqrt{\frac{1}{\sum_{\text{week}} \left(\frac{1}{\sigma^2_{(\Delta G/G)^{\text{week}}}}\right)}} \tag{6.79}$$

Note that we don't need to decompose $S/(S+B)$ to obtain $\Delta G/G$ from eq. 6.73. The fractions of the PGF and non-PGF processes are accounted for in the new definitions of the respective partonic asymmetries (cf. eq. 6.72). The asymmetries $\hat{a}_{LL}^{(g)}$ and $\hat{a}_{LL}^{(q)}$ are estimated from Monte Carlo using only the available phase space, i.e. they are both calculated for each generated event. The inclusive asymmetry $A_1^{d,corr}$ is taken from a parameterisation of the data shown in ref [5].

[9] During these periods of time, the spectrometer conditions are stable enough to allow for a reliable correction of A_{gq} using the average contribution from the physical background.

Chapter 7

Neural Network Parameterisations

On the last few years, artificial Neural Networks are being successfully applied to a wide range of problems involving all areas of knowledge. In fact, for every situation where one is confronted with a problem of prediction or classification, the use of an artificial intelligence algorithm is highly recommended. The working principle is based on the operation of biological neural systems. In other words, it is a result from an emulation of the most powerful computer known: the human brain. The advantages of these algorithms include:

- **Nonlinear modelling:** Neural Networks are capable of modelling extremely complex functions, which are useful to describe many real life problems where the linear approximation is not valid.

- **Parallel processing:** when solving a specific task, if an individual element fails the program can go on without any problem.

- **Adaptive learning:** like for the brain that learns from experience, a Neural Network learns from examples (initial experience). The Neural Networks invoke training algorithms to automatically understand the structure of the data, and thus they are very useful to solve those problems where all the needed instructions to work out a conventional program are unavailable (not known a priori). Contrary to conventional computer programs, Neural Networks are not programed to execute a specific task.

- **Multidimensional classification of the data:** correlations between the predictor variables (input information) and their individual influences on the predicted variable (Neural Network output) are taken simultaneously. An artificial Neural Network is capable to execute extremely complex tasks, making use of a very large number of simple processing units. The analogy with the brain is obvious: complexity (e.g., human behaviour) results from simplicity (billions of simple neurons processing information in parallel).

The aim of this chapter is to explain how the parameterisations of $S/(S+B)$ and a_{LL} are obtained. As already discussed in Chapter 6, the estimation of these two quantities is critical for the extraction of the gluon polarisation, i.e. $\Delta G/G$. The best unbiased precision that one can achieve for the gluon polarisation is reached by the use of a Neural Network in the parameterisations of the signal purity and of the muon-gluon asymmetry.

7.1 Biological inspiration of a Neural Network

The brain contains about 10 billion neurons massively interconnected (thousands of connections per neuron). Each neuron has an input structure, called the dendrites, a specialised cell body, and an output structure formed by axons. The axons of one neuron connect to the dendrites of another neuron through synapses. Each neuron can fire an electrochemical signal along the axon, if the signal received from the dendrites is above a certain level (activation threshold), which in turn may activate other neurons after crossing their synaptic connections. Each synapse contains a gap, with chemical neurotransmitters ready to transmit the signals across the gap: the strength of a signal received by a neuron critically depends on the efficiency of these synaptic connections. The most important conclusion for the artificial Neural Network algorithms is that the learning process consists mainly in altering the strength of the synaptic connections: a person learns by experience to avoid obstacles, when walking, by strengthening the synaptic connections between the visual cortex and the motor cortex neurons. The same principle is applied in a Neural Network algorithm as it will be explained in the next section.

7.2 DMLP Network to improve the PGF selection

To capture the essence of biological systems a DMLP (Dynamic MultiLayer Perceptrons) Network is used [79, 80]. Each artificial neuron structure receives several inputs from real data or from other neurons. This information arrives through connections with weights associated (synaptic strength), allowing the neuron to compute an output if the weighted sum of the inputs is greater than the activation threshold. The global architecture involves the input data (sensory nerves) connected to the Network output (motor nerves), through some hidden neurons involved in the process:

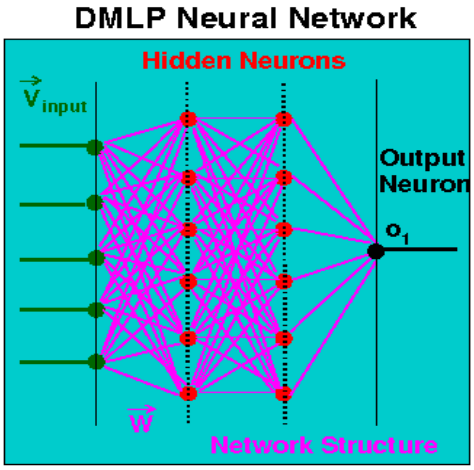

Figure 7.1: Structure of the Dynamic Neural Network used in the analysis.

The Network used in this analysis has a feed-forward nature, meaning that the information flows from the input data to the output neurons: the final response corresponds to the output of the neurons in the final layer. Each neuron computes an answer, after being activated by the input data, by using a transfer function that should be able to accept the input values in a wide range and also to compute an output in a restricted range. One good candidate to use is the sigmoid function which computes an output between [0, 1] by taking an input range in

the interval [-1, 1]. This function has a smooth nature and it is easily differentiable, facts that are essential for a good operation of the training algorithms (see Fig. 7.2).

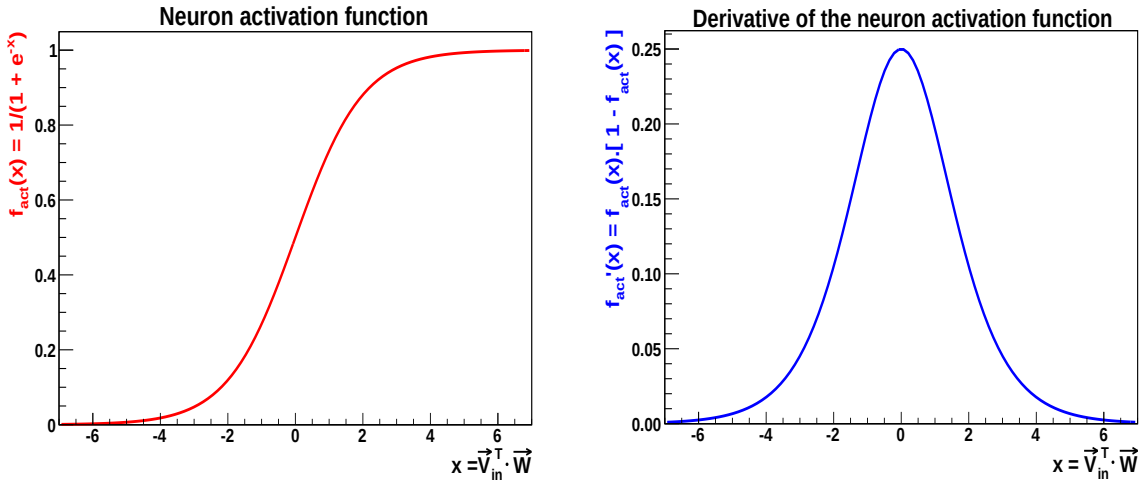

Figure 7.2: Neuron activation function (left) and its derivative (right).

Like for the biological Neural Networks, the goal is to tune the weights of the Network structure. This is achieved by the minimisation of the error obtained during the training procedure, using the expected result and the obtained output. If one defines the expected output variable as t_1, the Network will minimise the following mean squared error function (averaged over all events):

$$\delta = \frac{1}{N}\sum_{i=1}^{N}(t_{1,i} - o_{1,i})^2 \tag{7.1}$$

The learning procedure, which consists in the weights optimisation, is based on a supervised back propagation algorithm: it is supervised in the sense that the Neural Network is trained with the help of an input vector and matching output patterns. As the algorithm name implies the errors propagate backwards from the output neuron to the hidden units, and finally to the input vector. This is done by calculating the gradient of the error, for each neuron, with respect to the corresponding weights from all existing connections:

$$\Delta w_{ij} = -\frac{\partial(\delta_{ij})}{\partial w_{ij}} = -\frac{\partial(\delta_{ij})}{\partial n_i}\frac{\partial}{\partial w_{ij}}\sum_{k\in A_i}(w_{ik}x_k) = -\frac{\partial(\delta_{ij})}{\partial n_i}x_j = \delta_i x_j \tag{7.2}$$

where ω_{ij} are the weights associated to all connections between the neurons j and the neuron i, A_i is a set containing all neurons prior to the unit i, δ_i is the error signal for the neuron i and x_j is the activity in the unit i generated by all neurons j. Note that for the neurons in the first layer we have $V_j = x_j$. During each iteration the weights are infinitesimally adjusted, towards the greatest descent Δw over the error surface, until a minimisation in the output error is achieved. Therefore, for each neuron we just need to know 2 things: the activity through the incoming connections, x_j, and the error associated to the structure. By simply adjusting these weights we can model any function regardless of the exact neuron activation shape. The power of this kind of Neural Network is hidden in its dynamic structure: during the training stage a control sample is used to ensure the validity of the Neural Network parameterisation (the quality of the learning), and if the errors in the 2 samples start to diverge the Network

can readjust itself by allowing new neurons to born or neurons with redundant connections to be killed. This feature is of great importance, because it allows total independence of precise initial conditions (number of neurons) for a task that we don't know a priori how to proceed.

In the analysis, this DMLP Network is used for two important tasks:

- **Event classification:** to distinguish the signal (D^0 mesons) from the combinatorial background on a event-by-event basis.
- **Event prediction:** to obtain the PGF partonic asymmetry a_{LL}, for every event, after learning from a Monte Carlo sample.

7.3 Neural Network classification of events

The main goal here is to obtain D^0 probabilities for each of the events belonging to the Figs. 5.15-5.18. The knowledge of $S/(S+B)$ is of critical importance for this analysis (see Chapter 6), and to achieve this aim the illustrated Neural Network (cf. Fig. 7.1) is used to parameterise simultaneously its relevant kinematic dependencies. In practice, what the Neural Network does is to sort the events according to their kinematic similarities. This classification of events allows us to distinguish the signal from the combinatorial background in the D^0 mass spectra, provided that we feed the Network with a realistic background model.

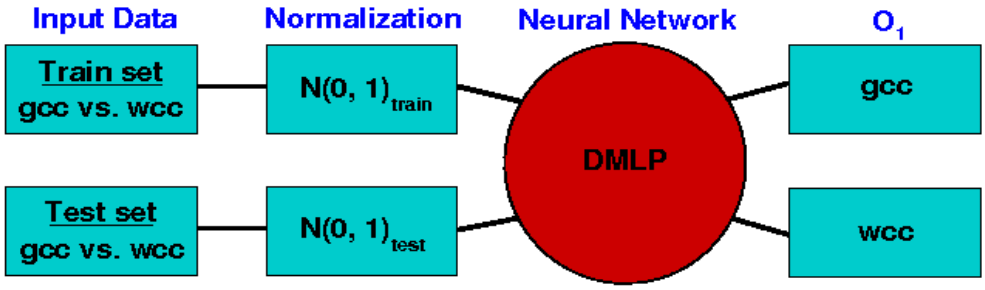

Figure 7.3: Procedure for the Neural Network classification of events.

The full procedure is represented on Fig. 7.3. The parameterisation is accomplished by feeding the DMLP Network with 2 samples: the signal model, gcc (**g**ood **c**harge **c**ombination of particles resulting from a D^0 decay), and the wcc (**w**ood **c**harge **c**ombination of kaons and pions) background model. Each channel is parameterised separately (except the $D^0_{K\pi}$) and per year of data taking:

- **gcc:**
$$\begin{cases} \textbf{1: } D^*_{K\pi} \rightarrow D^0\pi_s \rightarrow (K^-\pi^+)\pi^+_s + cc \quad \left(\textbf{charge conjugated} \in \overline{D}^0\right) \\ \textbf{2: } D^*_{K\pi\pi^0} \rightarrow D^0\pi_s \rightarrow (K^-\pi^+\pi^0)\pi^+_s + cc \\ \textbf{3: } D^*_{K\pi\pi\pi} \rightarrow D^0\pi_s \rightarrow (K^-\pi^+\pi^+\pi^-)\pi^+_s + cc \\ \textbf{4: } D^*_{K_{sub}\pi} \rightarrow D^0\pi_s \rightarrow (K^-_{sub}\pi^+)\pi^+_s + cc \end{cases}$$
- **wcc:**
$$\begin{cases} \textbf{Channel 1: } \rightarrow K^-\pi^-\pi^+_s + cc \\ \textbf{Channel 2: } \rightarrow K^-\pi^-\pi^0\pi^+_s + cc \\ \textbf{Channel 3: } \rightarrow K^-\pi^-\pi^+\pi^-\pi^+_s + K^-\pi^+\pi^-\pi^-\pi^+_s + K^-\pi^-\pi^-\pi^-\pi^+_s + cc \\ \textbf{Channel 4: } \rightarrow K^-_{sub}\pi^-\pi^+_s + cc \end{cases}$$

Each of these samples is randomly divided in 2, the train set (learning sample) and the test set (control sample), in order to ensure a universal result. The signal model corresponds to the D^0 mass spectra (after all kinematic and RICH cuts) and, therefore, contains D^0 mesons plus background events. The wcc sample is selected in a very similar way but with the additional requirement that the net charge of the final state particles is different from zero (not counting with π_s): in this way we ensure that no D^0 event is present in the background sample. After defining the expected outputs, $t_1 = 0.95$ for the gcc sample and $t_1 = 0.05$ for the wcc sample [1], the best input vector is chosen to teach the Neural Network, considering 5 variables:

$$\mathbf{V}\left(z_{D^0},\ \mathbf{cos}\,\theta^*,\ p(K),\ \frac{L_K(K)}{L_K(bg)},\ \frac{L_\pi(\pi)}{L_\pi(bg)}\right)$$

These variables are then normalised to a zero mean and to one standard deviation, in order to avoid very different ranges among them. Using this input vector, the Neural Network learns from the training set how to distinguish the D^0 events from the combinatorial background: by comparing the signal and background models in a multidimensional way, the Network is able to identify some of the combinatorial background events inside the gcc sample (due to a similar kinematics between these events and the ones belonging to wcc). The same is to say that the weights of the Network structure are tuned to minimise the error in the output neuron, $(t_1 - o_1)^2_{\text{train}}$, averaged over all events. As explained before, the validity of this trained Network structure is ensured by an independent parameterisation coming from the control sample (test set). In Fig. 7.4, we can observe the followed criterium to choose a good learning variable.

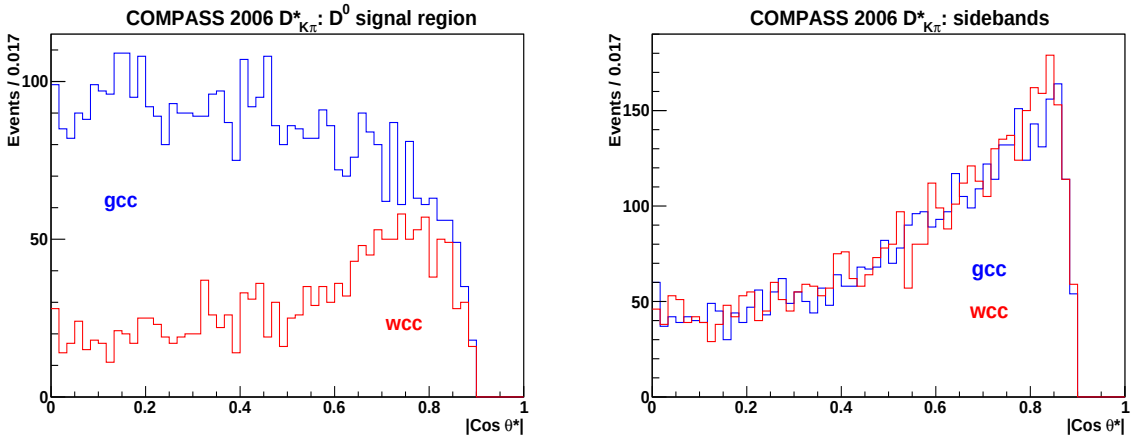

Figure 7.4: Distribution of $|\cos\theta^*|$ for the gcc (blue) and wcc (red) events, under (left) and outside (right) the $\mathrm{D}^*_{K\pi}$ peak.

The $|\cos\theta^*|$ distributions correspond to the cosine of the polar angle of kaon in the D^0 centre-of-mass regarding to the direction of the D^0 momentum. We can verify the good description of the real combinatorial background by the wcc sample (see Fig 7.4-right), both in shape and normalization, which clearly indicates that this sample is a good background model to work with. On the other hand, both distributions have different shapes under the peak, meaning that the Neural Network can learn to distinguish the D^0 events from the combinatorial background due to their different kinematic distributions.

[1] The choice of these two values simplifies the interpretation of the Neural Network result in terms of probabilities.

After the convergence of the training algorithm, the weights from the frozen structure are used to compute an answer o_1, from the output neuron, for every gcc and wcc event. However, the Neural Network output cannot be interpreted directly as a D^0 probability: for those gcc events that the Network cannot distinguish from the typical wcc kinematics, an answer o_1 around 0.5 is computed (see Fig. 7.2). In the next sections, two alternative methods to obtain $S/(S+B)$ from o_1 are presented.

7.3.1 Parameterisation of S/(S+B): Pure Neural Network method

When the available background model is good enough (same shape and similar statistics), and the existing signal purity is significant, the open-charm probabilities can be directly obtained from the Neural Network output. This fit independent method can be used to parameterise $S/(S+B)$ in the following samples: $D^*_{K\pi}$, $D^*_{K\pi\pi^0}$ and $D^*_{K\pi\pi\pi}$ from the years with more statistics (2004, 2006 and 2007). Unfortunately, as it can be seen from Fig. 7.5, the above criteria are not fulfilled for the $D^0_{K\pi}$ channel. Since this untagged sample is the major source of systematic errors (and they are all correlated among channels), it was decided to use a "hybrid method" to build all the $S/(S+B)$ parameterisations. This hybrid approach will be discussed in the next section. In any case, the statistical accuracy achieved in the extraction of $\Delta G/G$ is the

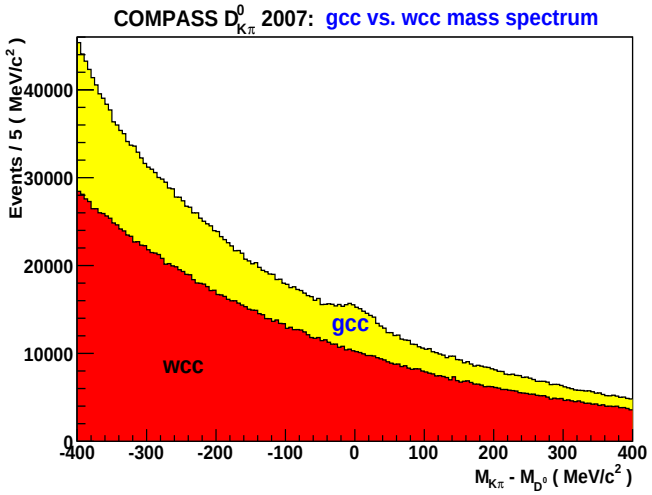

Figure 7.5: $D^0_{K\pi}(2007)$ mass spectrum (yellow plot) vs. wcc background model (red plot). In addition to the low $S/(S+B)$, the background is also poorly described by the wcc sample.

same for both methods. There are, however, two exceptions to the hybrid method used in this analysis: the $D^*_{K\pi\pi^0}$ channel obtained from the years of 2006 and 2007. These two examples are chosen to illustrate the good approximation made in the description of the broad resonance containing the $D^0_{K\pi\pi^0}$ signal in the mass spectra of the $D^*_{K\pi}$ channel (cf. Fig. 5.15): a Gaussian function is used to fit the bumpy shape, which results from the failure to identify the π^0. In the pure Neural Network approach the probabilities are extracted as explained below, in a fit independent way, and then they are validated by the Gaussian fits that are applied to the 'bump' (cf. Fig. 7.21).

The Neural Network is trained using only the events within a ± 40 MeV/c^2 mass window under the $D^0_{K\pi\pi^0}$ peak. In order to parameterise the signal purity of these two samples (using the data from the years of 2006 and 2007), an additional input is provided to the Network: $(f \cdot P_\mu \cdot a_{LL})$. This quantity is needed to ensure the known anti-correlation between $S/(S+B)$ and the

fundamental partonic asymmetry a_{LL} [2]. At the end of the learning procedure of the Neural Network we can obtain $S/(S+B)$ from its output, using the following system of equations:

$$\begin{cases} (S+B)_{gcc} & = o_1 \\ (S+B)^{o_1}_{gcc} + B^{o_1}_{wcc} & = 1 \end{cases} \tag{7.3}$$

The Neural Network computes an answer o_1 for every gcc event (an answer is also computed for each of the wcc events). If the background model is good enough, meaning that the Network can learn about the background existing in the gcc sample, the normalised sum of gcc and of wcc events, around a specific o_1 value, should be 1. The validity of the second condition in the system of equations 7.3 can be confirmed in several bins of o_1. This would prove that the Neural Network is doing what is supposed to do and, as a consequence, we can safely obtain D^0 probabilities from the parameterisation (by solving the system of equations above):

$$\left(\frac{S}{S+B}\right)_{gcc} = \frac{[(1+k)\cdot o_1 - 1]}{k \cdot o_1} \qquad \text{using} \qquad k = \left(\frac{B_{wcc}}{B_{gcc}}\right) \tag{7.4}$$

The ratio k, of crucial importance for this method, is tuned inside a few o_1 bins to fulfil the second condition of the system 7.3 (only for the samples $D^*_{K\pi\pi^0}(2006)$ and $D^*_{K\pi\pi^0}(2007)$).

Recipe to tune the background ratios (k in eq. 7.4):

1. **In order to maximise the FOM of the D^0 signal, the events coming out of the Neural Network with low o_1 values are rejected** (see Figs. 7.6, 7.7 and 7.8):

   - $D^*_{K\pi\pi^0}(2006)$ final mass spectrum $\rightarrow$ Only events with $o_1 \geq 0.50$ are accepted.

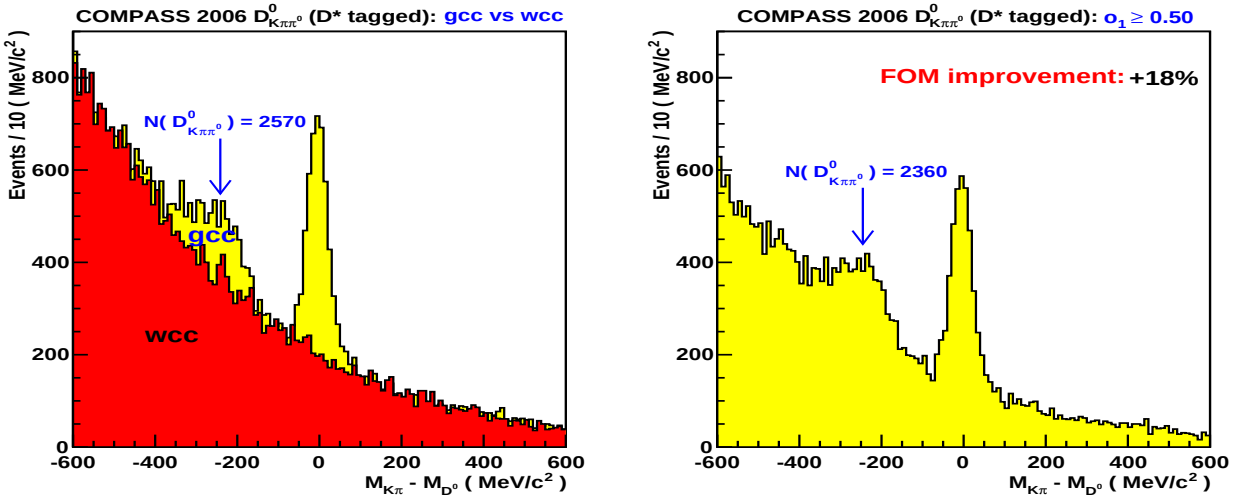

Figure 7.6: Left: gcc (yellow) and wcc (red) training samples. Right: final mass spectrum after a cut in the Neural Network response.

[2] Note that these two quantities appear in the definition of the signal weight (cf. eq. 6.33). If their proper correlation is not taken into account, the outcome will be an underestimation of the statistical error of $\Delta G/G$.

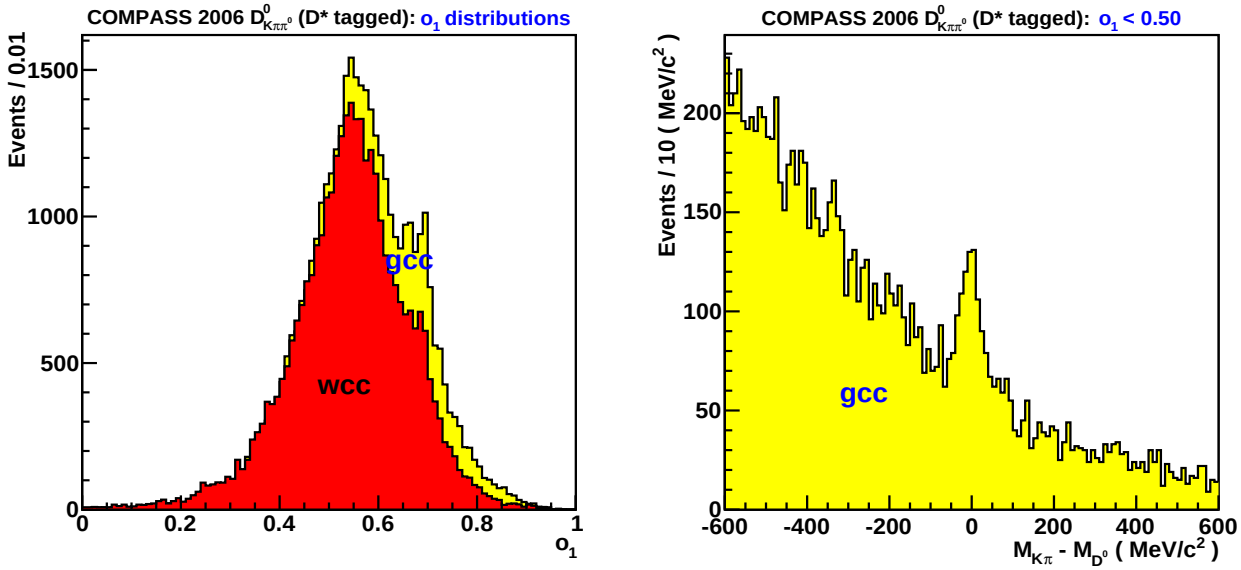

Figure 7.7: Distributions of the Neural Network o_1 (left) and rejected mass spectrum (right). One can verify that no significant signal exists in the mass spectrum containing the events with $o_1 < 0.5$, and as a consequence the FOM is increased by applying this cut in o_1.

- $D^*_{K\pi\pi^0}(2007)$ final mass spectrum $\rightarrow$ Only events with $o_1 \geq 0.53$ are accepted.

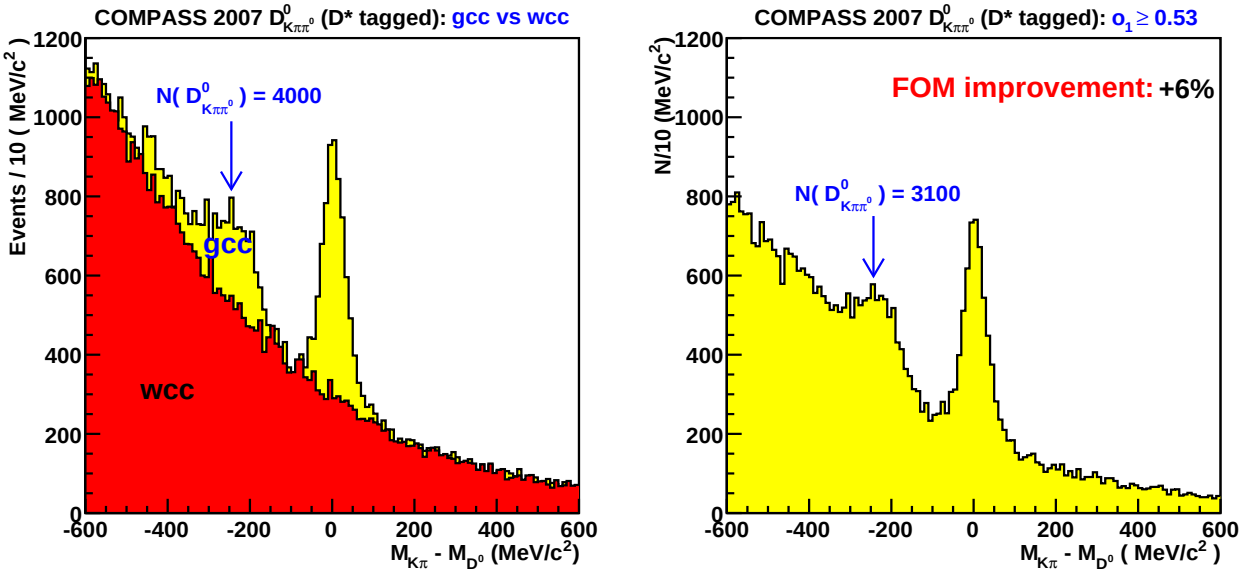

Figure 7.8: In the left plot one can see the training samples corresponding to $D^*_{K\pi\pi^0}(2007)$. To the right of, it is shown the final mass spectrum used in the analysis (after the Neural Network cut).

2. **Each final mass spectrum is divided in bins of o_1 for an optimised tuning of the k factor** (see Figs. 7.9 and 7.10):

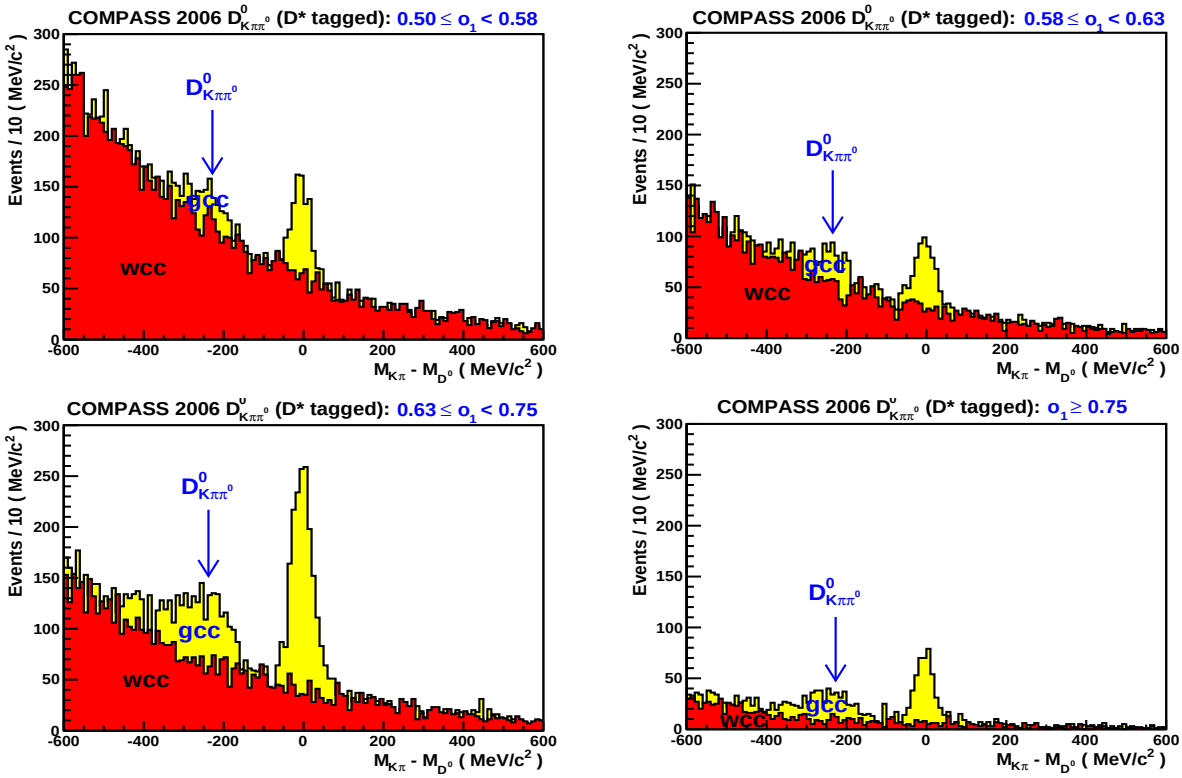

Figure 7.9: $D^*_{K\pi\pi^0}(2006)$ mass spectrum in bins of o_1. One can see a good description of the background by the wcc sample, inside all bins, together with an increasing purity of the mass spectrum due to the signal recognition by the Neural Network.

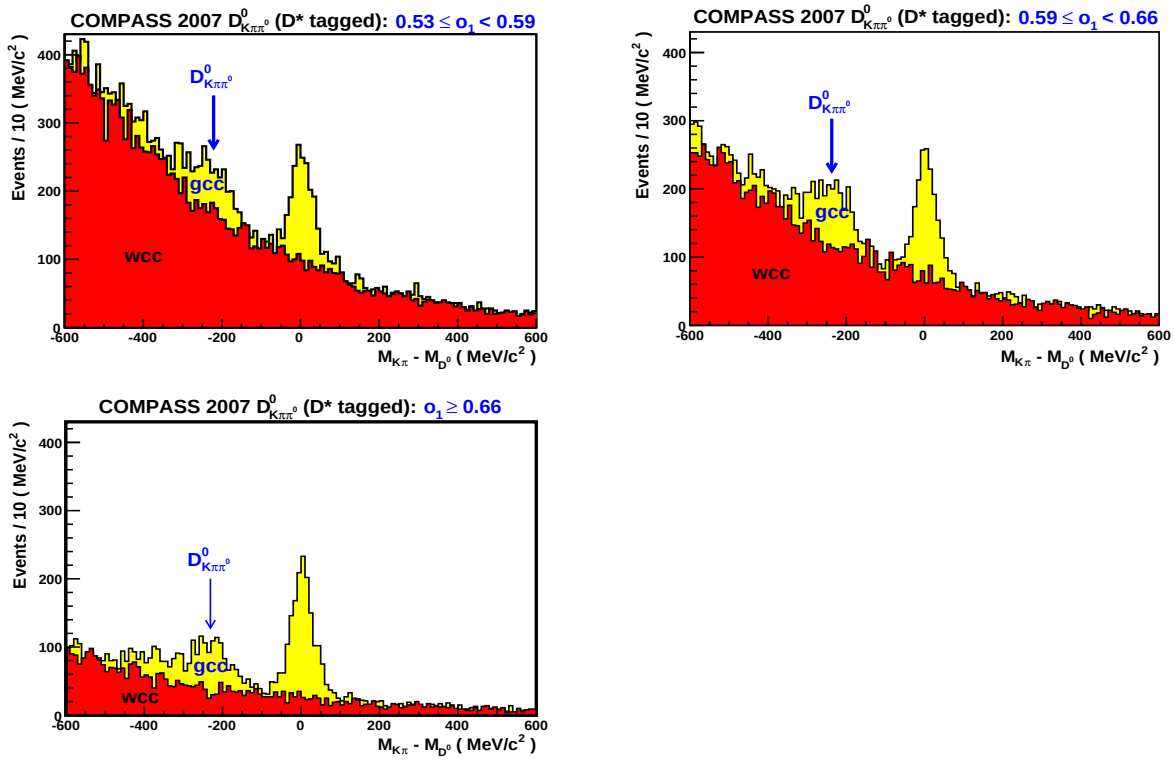

Figure 7.10: $D^*_{K\pi\pi^0}(2007)$ sample in bins of o_1.

3. **A temporary ratio k' is evaluated for each bin, using the number of gcc and wcc events outside both D^0 peaks ($D^0_{K\pi}$ and $D^0_{K\pi\pi^0}$).**

4. **Finally, a correction is applied to k' in order to satisfy the second equation of system 7.3:**

   - The average value of $o_1(wcc)$ is calculated per bin using only the events within the parameterisation window: $\langle o_1 \rangle^{\text{final}}_{wcc} = [\langle o_1 \rangle_{wcc}]^{o_1 \leq 0.5}$ or $\langle o_1 \rangle^{\text{final}}_{wcc} = [1 - \langle o_1 \rangle_{wcc}]^{o_1 > 0.5}$.

   - The final k factor is determined from the following equation (where N represents the number of events within the parameterisation window):

$$k \;=\; k' \;+\; \left| \frac{\langle o_1 \rangle^{\text{final}}_{wcc}}{\frac{N(wcc)}{N(wcc+gcc)}} - 1 \right| \tag{7.5}$$

7.3.2 Parameterisation of S/(S+B): Hybrid method

This method is the one used for 90% of the $S/(S+B)$ parameterisations. It is not so elegant as the previous one, which is totally fit independent, but it is much easier to implement since it does not depend critically on a very good Neural Network parameterisation. Moreover, as it was mentioned before, the achieved statistical precision in the measurement of the gluon polarisation is the same (one example will be given for the $D^*_{K\pi}$ channel). Each sample is parameterised independently per year of data taking (with a few exceptions for the data of 2002 and 2003): in this way we avoid the mixture of data obtained with different experimental acceptances and also with different spectrometer conditions. The process of the classification of events according to their kinematic similarities is the same as discussed in the previous section. The only difference lies on the procedure used to obtain $S/(S+B)$, per event, from the Neural Network output.

In total, 24 parameterisations of $S/(S+B)$ are built:

Data	**Channels**				
	$D^*_{K\pi}$	$D^*_{K\pi\pi^0}$	$D^*_{K\pi\pi\pi}$	$D^*_{K_{sub}\pi}$	$D^0_{K\pi}$
2002	$\Sigma(1)$	$\Sigma(7)$	$\Sigma(11)$	$\Sigma(15)$	$\Sigma(19)$
2003	$\Sigma(2)$				$\Sigma(20)$
2004(old)	$\Sigma(3)$	$\Sigma(8)$	$\Sigma(12)$	$\Sigma(16)$	$\Sigma(21)$
2004 (new)	$\Sigma(4)$				$\Sigma(22)$
2006	$\Sigma(5)$	$\Sigma(9)$ *	$\Sigma(13)$	$\Sigma(17)$	$\Sigma(23)$
2007	$\Sigma(6)$	$\Sigma(10)$ *	$\Sigma(14)$	$\Sigma(18)$	$\Sigma(24)$

Table 7.1: Parameterisations of the signal purity: $\Sigma = \left(\frac{S}{S+B}\right)[\vec{V}']$ (cf. eq. 7.13).

In 2004, two separate parameterisations are built for the channels with higher statistics. The justification for this fact lies in the existence of two different reconstruction programs for this data sample (cf. Tab 5.3). Concerning the channels of low purity and low statistics from the years of 2002 and 2003 (columns 3, 4 and 5 in Tab. 7.1), only one parameterisation is obtained due to a very small D^0 statistics collected from the 2002 data. The parameterisations $\Sigma(9)$ and $\Sigma(10)$ come directly from the corresponding Neural Network outputs as it was explained in the previous section. The remaining 22 parameterisations use a different approach to obtain the desired D^0 probabilities, for every event, as explained hereafter.

Principle: Why do we need a proper kinematic parameterisation of $S/(S+B)$?

The signal purity Σ is a very important quantity of the event weight used in the open-charm analysis, i.e. $\omega_S = fP_\mu a_{LL}\Sigma$. It is known experimentally that the dependence of Σ on the event kinematics is anti-correlated with $fP_\mu a_{LL}$ (cf. Fig. 7.11). Therefore, the naive approach to obtain the probability Σ is to calculate $\Sigma_{fP_\mu a_{LL}}(m)$ from each mass spectrum of Fig. 7.11 (example for $\Sigma(5)$). The same is to say that we are including the mass dependence in Σ from a fit to the mass spectrum sampled in bins of $fP_\mu a_{LL}$, in order to account for the anti-correlation that exists in the weight. However, if the full weight is $v\omega$ instead of ω, the use of ω as the weight gives rise to a bias if the missing term v is correlated with ω. To illustrate this point, we use the experimental open-charm asymmetry, i.e. $A^{\rm exp} = fP_\mu P_t A_{c\bar{c}}^{\mu N}$ (see eq. 2.84):

$$A^{\mu N} = \frac{1}{\langle\omega\rangle}\left(\frac{N_u - N_d}{N_u + N_d}\right) \tag{7.6}$$

$$\delta(A^{\mu N}) = \frac{1}{\langle\omega\rangle\sqrt{N}} \qquad \text{with} \qquad N = (N_u + N_d) \tag{7.7}$$

where a generic weight $\omega = fP_\mu P_t$ is defined. Note that the D^0 counting rates are represented by N_u (upstream cell) and N_d (downstream cell), using the target geometry of [2002, 2004]. Weighting each event with w is equivalent to define an infinite number of $y = (E_{\gamma^*}/E_\mu)$ bins for the extraction of $A^{\mu N}$ (the dilution factor is dependent on this kinematic variable):

$$A_\omega^{\mu N} = \frac{\sum_i \left(\frac{A_i^{\mu N}}{\delta^2(A_i^{\mu N})}\right)}{\sum_i \left(\frac{1}{\delta^2(A_i^{\mu N})}\right)} = \frac{\sum_i (A_i^{\mu N}\omega_i^2 N_i)}{\sum_i(\omega_i^2 N_i)} = \frac{\sum_i(N_{u_i}\omega_i) - \sum_i(N_{d_i}\omega_i)}{\sum_i(N_{u_i}\omega_i^2) + \sum_i(N_{d_i}\omega_i^2)} \tag{7.8}$$

The above sums can be rewritten just as the sum of ω for each target cell:

$$A_\omega^{\mu N} = \frac{\sum_u \omega - \sum_d \omega}{\sum_u \omega^2 + \sum_d \omega^2} \tag{7.9}$$

$$\delta^2(A_w^{\mu N}) = \frac{1}{\sum_u \omega^2 + \sum_d \omega^2} = \frac{1}{\langle\omega^2\rangle\, N} \tag{7.10}$$

Now, we consider that the weight is $\omega = f$ instead of the true one: $v\omega = fP_\mu P_t$. If we divide at the end the weighted asymmetry by the missing weight, $\langle v\rangle$, we obtain:

$$\left\langle A_{\omega}^{\mu N}\right\rangle = \frac{1}{\langle v\rangle}\frac{\sum_i\left(\frac{\left\langle A_i^{\mu N}\right\rangle}{\delta^2(A_i^{\mu N})}\right)}{\sum_i\left(\frac{1}{\delta^2(A_i^{\mu N})}\right)} = \frac{1}{\langle v\rangle}\frac{\sum_i(v_i\omega_i^2 N_i)}{\sum_i(\omega_i^2 N_i)}A_\theta = \frac{\langle v\omega^2\rangle}{\langle v\rangle\langle\omega^2\rangle}A_\theta \tag{7.11}$$

where the expectation value of the physical asymmetry is: $\langle A_i^{\mu N}\rangle = v_i A_\theta$. If the used weight ω is not correlated with the missing weight, v, there is no bias:

$$\left\langle v\omega^2\right\rangle = \langle v\rangle\left\langle\omega^2\right\rangle \tag{7.12}$$

Unfortunately, this is not the case for the real weight used in the analysis. We can see from Fig. 7.11 that the quantity $fP_\mu a_{LL}$ shows a well defined anti-correlation with the signal purity (due to a_{LL}), $S/(S+B)$, which in turn is strongly dependent on the event kinematics. The solution to remove this residual bias from the weight is to parameterise the dependence of $S/(S+B)$ in the relevant event kinematics, $S/(S+B)(\vec{V})$, in addition to the anti-correlation with a_{LL}:

$$\Sigma = \left(\frac{S}{S+B}\right)[\vec{V'}] \qquad \text{with} \qquad \vec{V'} = (o_1, fP_\mu a_{LL}) \tag{7.13}$$

For the present method, two variables are needed to parameterise Σ in the most optimal way. Since a_{LL} is a critical variable for this analysis, it was decided to treat $fP_\mu a_{LL}$ separately from the Neural Network output o_1 (the former variable exists independently in the weight). The inclusion of o_1 into the parameterisation is vital to remove the residual bias in the weight, as explained above, but also to allow for the best statistical precision in the measurement of the asymmetry. By comparing eq. 7.10 with eq. 7.7, we immediately see that the gain introduced by a weighted analysis is proportional to the variance of the weights (note that for $\omega = fP_\mu a_{LL}\Sigma$ we need to replace $A^{\mu N}$ by $\Delta G/G$):

$$\left(\frac{\delta(A^{\mu N})}{\delta(A_\omega^{\mu N})}\right)^2 = \frac{\langle\omega^2\rangle}{\langle\omega\rangle^2} = 1 + \frac{\sigma_\omega^2}{\langle\omega\rangle^2} \tag{7.14}$$

The largest unbiased ratio of $\sigma_\omega/\langle\omega\rangle$ is achieved after a proper parameterisation of the signal purity, over the event kinematics, and as a consequence the gain in statistical precision due to the use of the weights is maximised. This method is better because it considers the kinematic dependencies of $S/(S+B)$ in a multidimensional way. In fact, the Neural Network is able to process all the input variables at same time, meaning that possible correlations between them are correctly taken into account.

Algorithm to build Σ:

Each sample is divided in bins of o_1 (cf. Fig 7.12) and also in bins of $fP_\mu a_{LL}$ (cf. Fig. 7.11). In the illustrated example, for the $D^*_{K\pi}(2006)$ sample, we can see the nice improvement in the signal purity with o_1. The efficient parameterisation obtained by the Neural Network, as shown in Fig. 7.12, is only possible due to the existence of good background models from real data (wcc). In Figs. 7.13-7.14 all samples used for each parameterisation of Tab. 7.1 are shown, except for the mass spectra corresponding to the untagged $D^0_{K\pi}$ channel. In this case, we use the parameterisations obtained from $D^*_{K\pi}$.

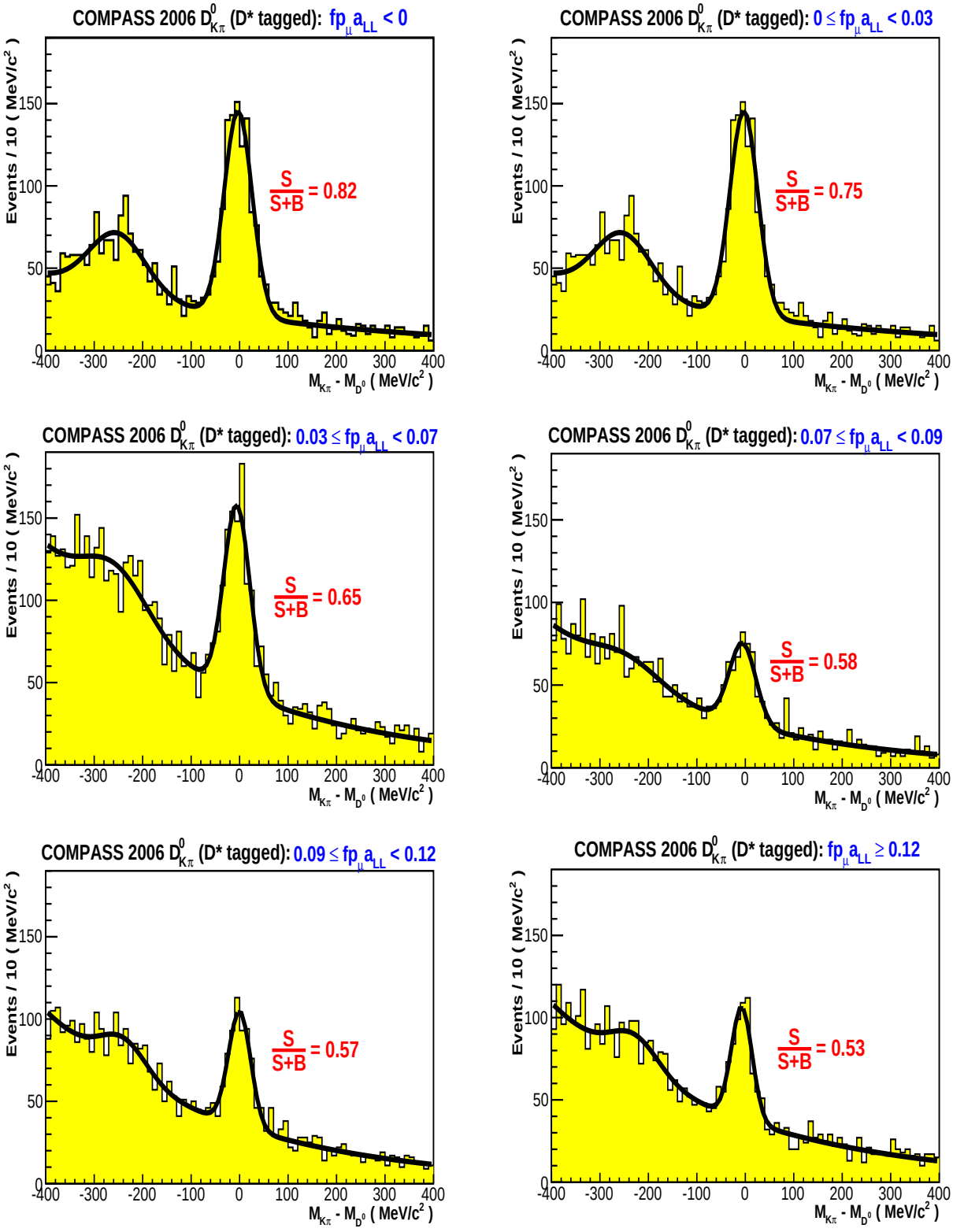

Figure 7.11: $D^*_{K\pi}(2006)$ sample in bins of $fP_\mu a_{LL}$. The anti-correlation between $S/(S+B)$ and the remaining part of the event weight is clear (these signal purities are obtained from a fit to the mass spectra in a window of ± 40 MeV/c^2).

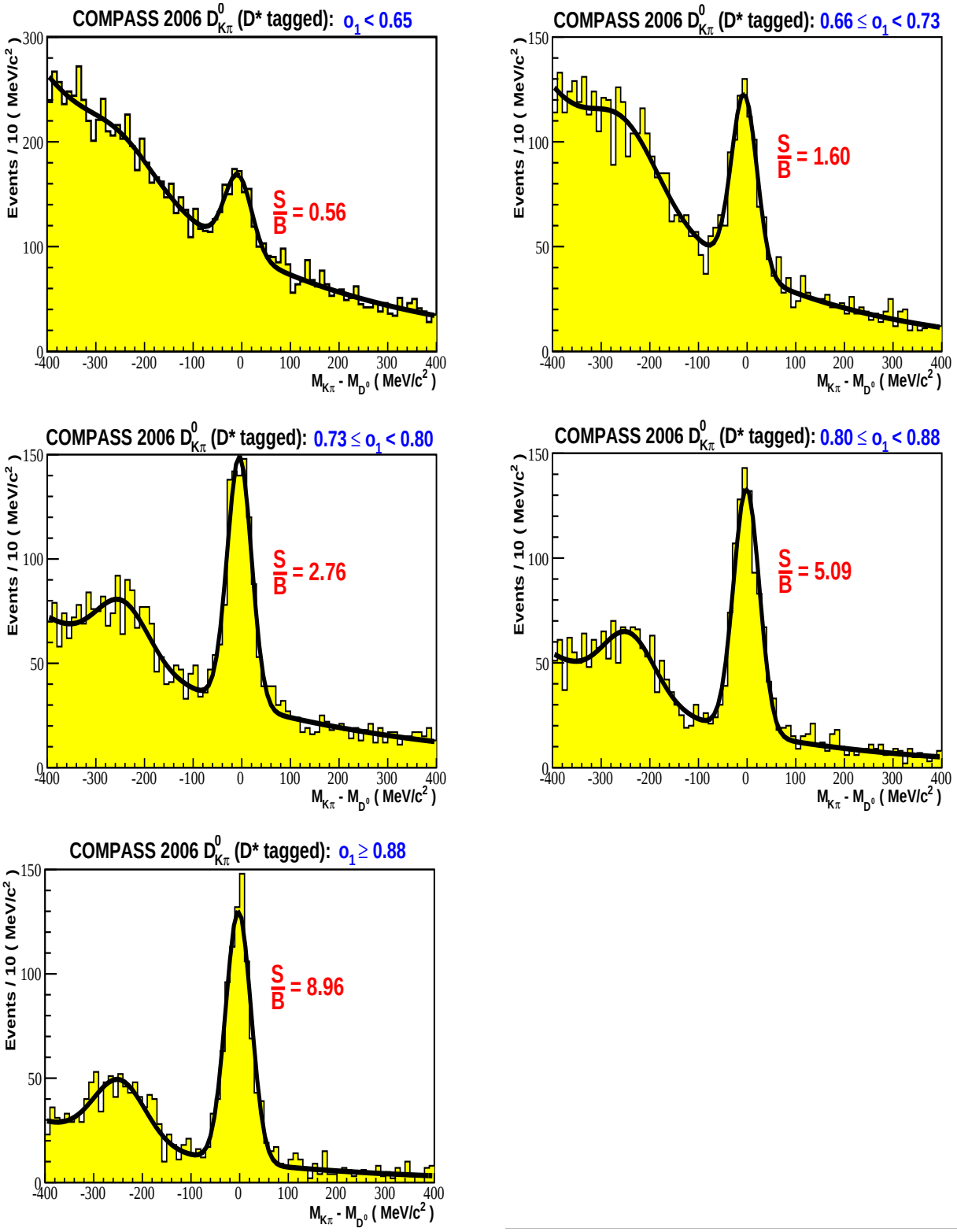

Figure 7.12: $D^*_{K\pi}(2006)$ mass spectrum in bins of o_1. The Neural Network is clearly able to recognise the signal, D^0 mesons, out of the combinatorial background.

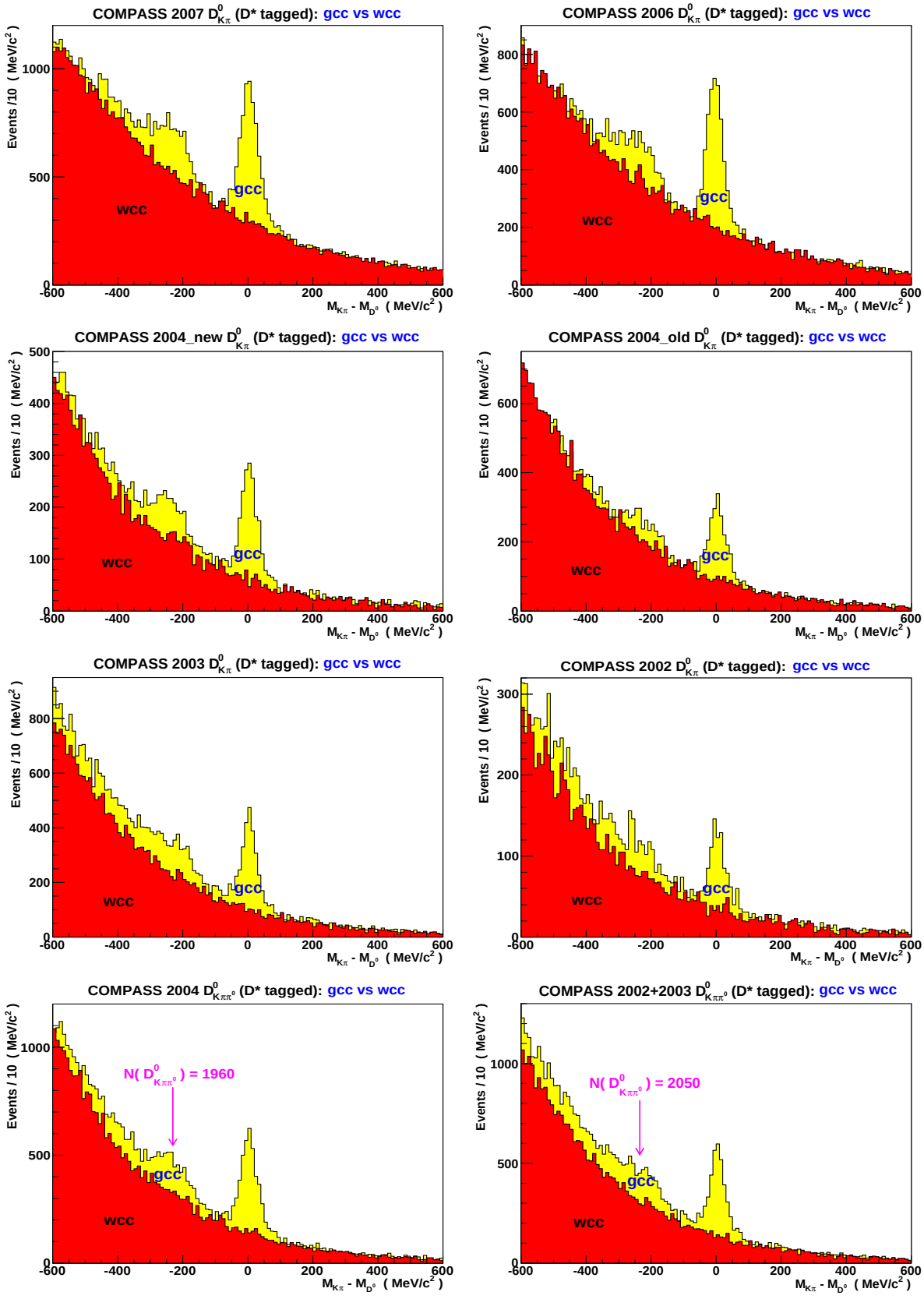

Figure 7.13: Full samples used for each Neural Network classification of the $D^*_{K\pi}$ candidates (first 3 lines). In the last line we can see the remaining samples of the $D^*_{K\pi\pi^0}$ channel (cf. Fig. 7.6 and Fig. 7.8 for the 2006 and 2007 mass spectra). The signal model is represented in yellow (gcc) and the background model in red (wcc): the multidimensional comparison is performed in a mass window of ± 40 MeV/c^2 under the corresponding D^0 peak.

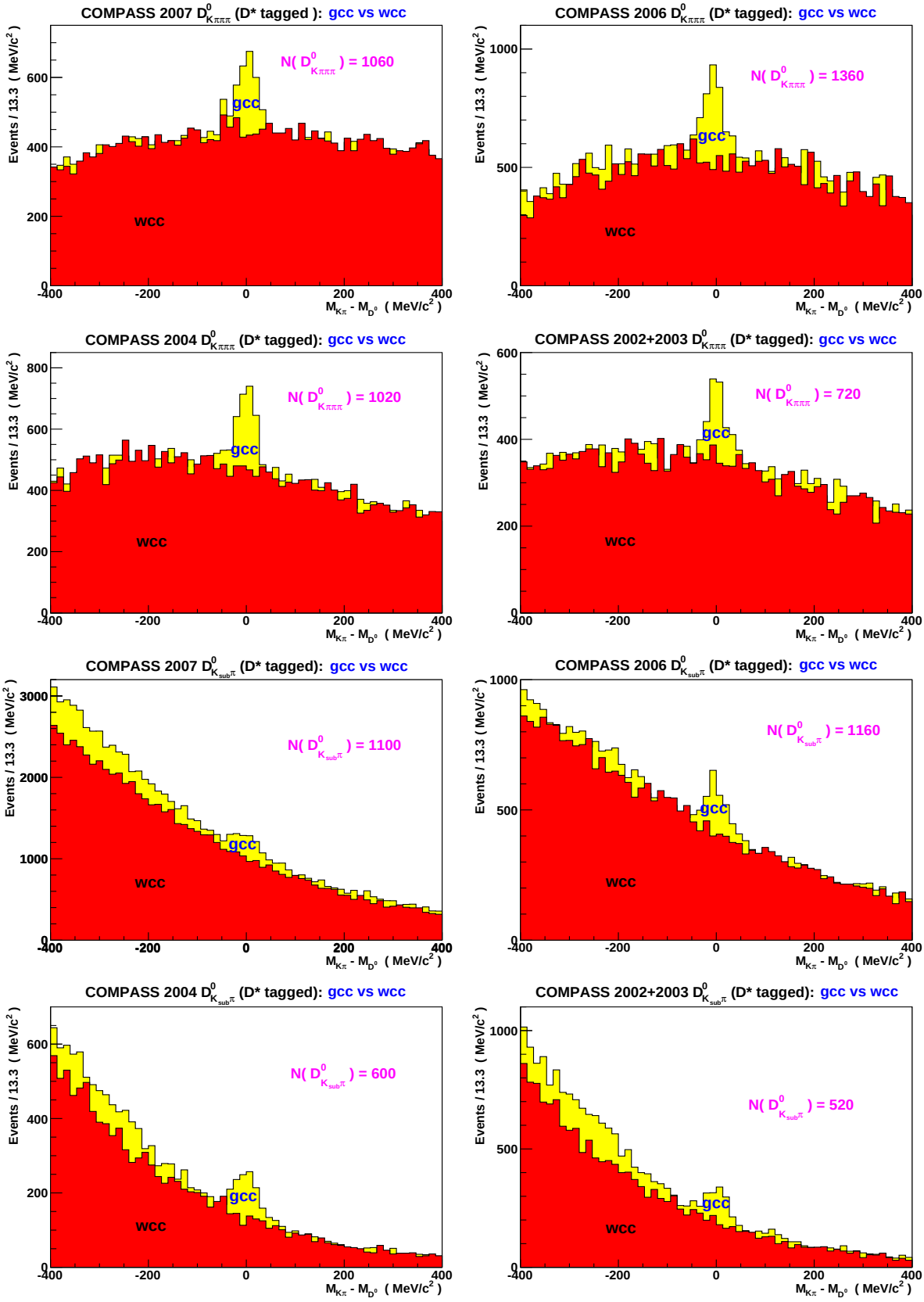

Figure 7.14: Full samples used for each Neural Network classification of the $D^*_{K\pi\pi\pi}$ (first 2 lines) and of the $D^*_{K_{sub}\pi}$ (last 2 lines) candidates. The multidimensional comparison is also performed in a mass window of ± 40 MeV/c^2 under the corresponding D^0 peak.

In Figs. 7.13-7.14 one can see the number of D^0 corresponding to the low purity samples: $D^*_{K\pi\pi^0}$, $D^*_{K\pi\pi\pi}$ and $D^*_{K_{sub}\pi}$. It turns out that for these channels the Neural Network is able to kill part of the combinatorial background under the peak, after applying a cut on the o_1 values computed by the Network. By rejecting events with low o_1 values, the FOM of these mass spectra are increased with a minimum loss of the signal content (cf. example in Fig. 7.6). This fact can be confirmed by comparing the numbers of D^0 events shown in the figures above with the numbers of D^0 events obtained from a fit to the final mass spectra (see Fig. 7.27-yellow). However, since we assign a D^0 probability to each event after the parameterisation of $S/(S+B)$, a compromise between the number of signal events and the final FOM must be established (all D^0 should be preserved in an ideal parameterisation). In the case of the $D^*_{K\pi}$ channel, despite of the good signal recognition by the Neural Network (cf. Fig. 7.12), the FOM cannot be further improved by a cut in o_1: these mass spectra are already very clean after the kinematic cuts, containing only a residual background which is hard to distinguish from the signal due to the very similar kinematics. By applying a cut in the first bin of Fig. 7.12 (for example), part of the signal is also removed in a way that the FOM can only decrease or remain the same.

The parameterisation of Σ is built in the bi-dimensional space of $\vec{V}'$, $(o_1, fP_\mu a_{LL})$, divided in $n_1 \times n_2$ bins (see Fig. 7.11 and Fig. 7.12 for $\Sigma(5)$). It is chosen to parameterise the ratio $(S/B)_{\rm par}$ (see also [81]), inside of each bin, by taking as a reference the total number of signal and background events: they are obtained from a fit to the mass spectra in a window of $\pm(40/30)$ MeV/c^2 under the corresponding peak (for the tagged/untagged mass spectra). Finally, after this parameterisation, the signal purity Σ is obtained for each event as follows:

$$\Sigma = \frac{\left(\frac{S}{B}\right)_{par}}{1 + \left(\frac{S}{B}\right)_{par}} \tag{7.15}$$

The algorithm, for the ratio parameterisation $(S/B)_{\rm par}$, uses two functions, F_1 and F_2, which are initially defined as explaind in Fig. 7.15.

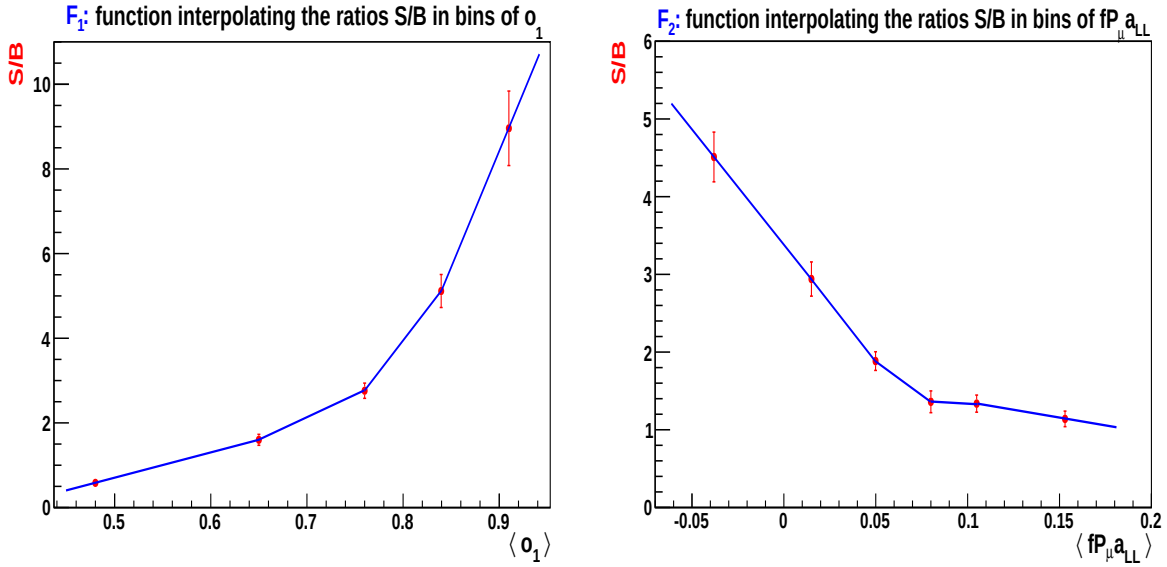

Figure 7.15: Ratios of $(S/B)_{\rm fit}$ obtained in bins of o_1 (left) and in bins of $fP_\mu a_{LL}$ (right), for the $D^*_{K\pi}(2006)$ mass spectrum. The continuous functions F_1 and F_2 are defined, for each variable, by a linear interpolation of the fit results obtained for each bin.

More specifically, the function F_1 interpolates linearly the points $\left(\langle o_1\rangle, \frac{(S/B)_{\rm fit}}{\langle (S/B)_{\rm par}\rangle}\right)^j$ from all bins j (similarly for F_2). By initialising the ratio $(S/B)_{\rm par}$ with the value of 1, for every event, the initial functions of Fig. 7.15 are reproduced. The procedure can now be easily explained:

- For each iteration i, the algorithm loops twice over all events (once per variable). The first loop of the iteration i corrects the slopes of F_1, from iteration $(i-1)$, between 2 neighbouring bins j:

$$f^{i,j}_{\rm corr}(o_1) = \frac{\left[\frac{(S/B)^{j+1}_{\rm fit}(o_1)}{\left\langle (S/B)^{i-1}_{\rm par}(o_1)\right\rangle^{j+1}} - \frac{(S/B)^{j}_{\rm fit}(o_1)}{\left\langle (S/B)^{i-1}_{\rm par}(o_1)\right\rangle^{j}}\right]}{\left[\langle o_1\rangle^{j+1} - \langle o_1\rangle^{j}\right]} \tag{7.16}$$

- With the help of the global function $f^i_{\rm corr}(o_1)$, the signal-to-background ratios are also corrected for every event:

$$\left(\frac{S}{B}\right)^{i}_{\rm par}(o_1) = f^i_{\rm corr}(o_1) \times \left(\frac{S}{B}\right)^{i-1}_{\rm par}(o_1) \tag{7.17}$$

- A second loop over all events is performed, inside the same iteration i, to account for the dependence of S/B in $fP_\mu a_{LL}$. Using $(S/B)^i_{\rm par}(o_1)$ as an input, from eq. 7.17, we can obtain the final parameterisation of S/B for the iteration i:

$$\left(\frac{S}{B}\right)^{i}_{\rm par} = f^i_{corr}(fP_\mu a_{LL}) \times f^i_{\rm corr}(o_1) \times \left(\frac{S}{B}\right)^{i-1}_{\rm par}(o_1) \tag{7.18}$$

  where

$$f^{i,j}_{\rm corr}(fP_\mu a_{LL}) = \frac{\left[\frac{(S/B)^{j+1}_{\rm fit}(fP_\mu a_{LL})}{\left\langle (S/B)^{i}_{\rm par}(fP_\mu a_{LL})\right\rangle^{j+1}} - \frac{(S/B)^{j}_{\rm fit}(fP_\mu a_{LL})}{\left\langle (S/B)^{i}_{\rm par}(fP_\mu a_{LL})\right\rangle^{j}}\right]}{\left[\langle fP_\mu a_{LL}\rangle^{j+1} - \langle fP_\mu a_{LL}\rangle^{j}\right]} \tag{7.19}$$

The procedure continues iteratively until a global convergence is achieved for all bins from both variables (cf. Fig. 7.16). The final function $F(o_1, fP_\mu a_{LL})$ describes properly $(S/B)_{\rm par}$, for every event, if it can reproduce the fit results obtained for all $n_1 \times n_2$ bins:

$$\left\langle F(o_1, fP_\mu a_{LL}) \equiv \left(\frac{S}{B}\right)_{par}\right\rangle^j = \left(\frac{S}{B}\right)^j_{fit} \tag{7.20}$$

where

$$\left(\frac{S}{B}\right)_{par} = F_2 \times F_1 \times \left(\frac{S}{B}\right)_{par}(o_1) \tag{7.21}$$

and

$$F_1 = \Pi_i^N f_{corr}^i(o_1) \quad , \quad F_2 = \Pi_i^N f_{corr}^i(fP_\mu a_{LL}) \tag{7.22}$$

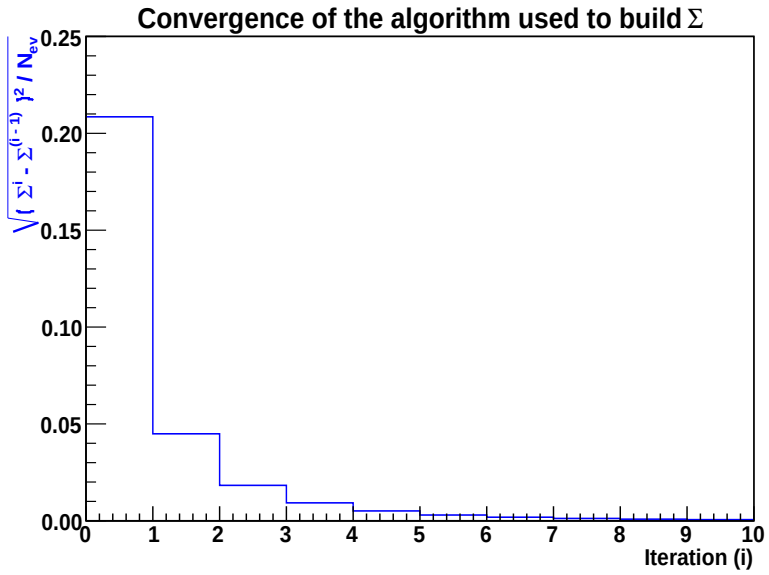

Figure 7.16: $D^*_{K\pi}(2006)$: the algorithm is stable after 5 iterations (with corrections below 0.2%). The quadratic differences of Σ, between 2 consecutive iterations, are taken as a sum over all events.

7.3.3 Validation of the Σ-parameterisations

Each parameterisation Σ from Tab. 7.1 must fulfill two conditions in order to avoid any bias. These conditions are defined with the help of the true signal purity, Σ_{true} [82]:

1. We must ensure that the missing part of the weight, $\left(\frac{\Sigma_{\text{true}}}{\Sigma}\right)$, is not correlated with the weight used in the analysis: $\omega = fP_\mu a_{LL}\Sigma$. To guarantee this, we fit the mass spectrum sampled in bins of ω, to obtain $\Sigma^\omega_{\text{true}} = \left(\frac{S}{S+B}\right)$, and finally we check that $\left(\frac{\Sigma^\omega_{\text{true}}}{\langle\Sigma\rangle^\omega}\right) = 1$ within the fitting errors (inside of each parameterisation window and for each bin).

2. In addition to the previous requirement, we must verify that Σ does not include any other dependence which is not present in Σ_{true}. This is ensured by fitting the mass spectrum sampled in bins of Σ, to obtain $\Sigma^\Sigma_{\text{true}}$, and thereafter we must control that we obtain $\left(\frac{\Sigma^\Sigma_{\text{true}}}{\langle\Sigma\rangle^\Sigma}\right) = 1$ within the fitting errors (inside of each parameterisation window and for each bin).

We can see from Fig. 7.17 to Fig. 7.21 that each of the Σ parameterisations satisfy these 2 conditions.

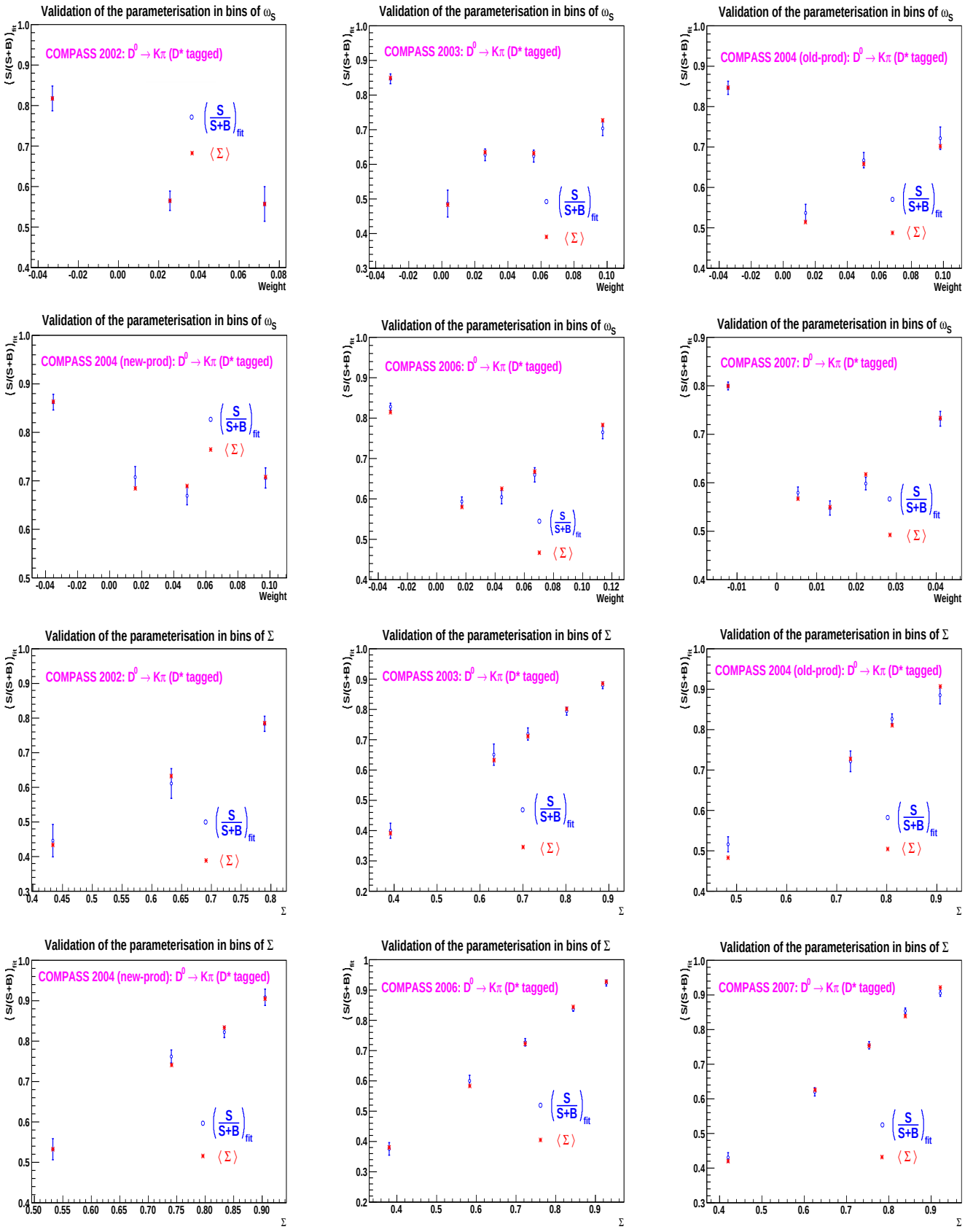

Figure 7.17: $D^*_{K\pi}$ channel: validation of all parameterisations (Σ_1, Σ_2, Σ_3, Σ_4, Σ_5, Σ_6) in bins of weight (first 2 lines) and also in bins of probability (last 2 lines). The agreement between the fits and the $\langle\Sigma\rangle$ is good enough inside all bins (within the fitting errors).

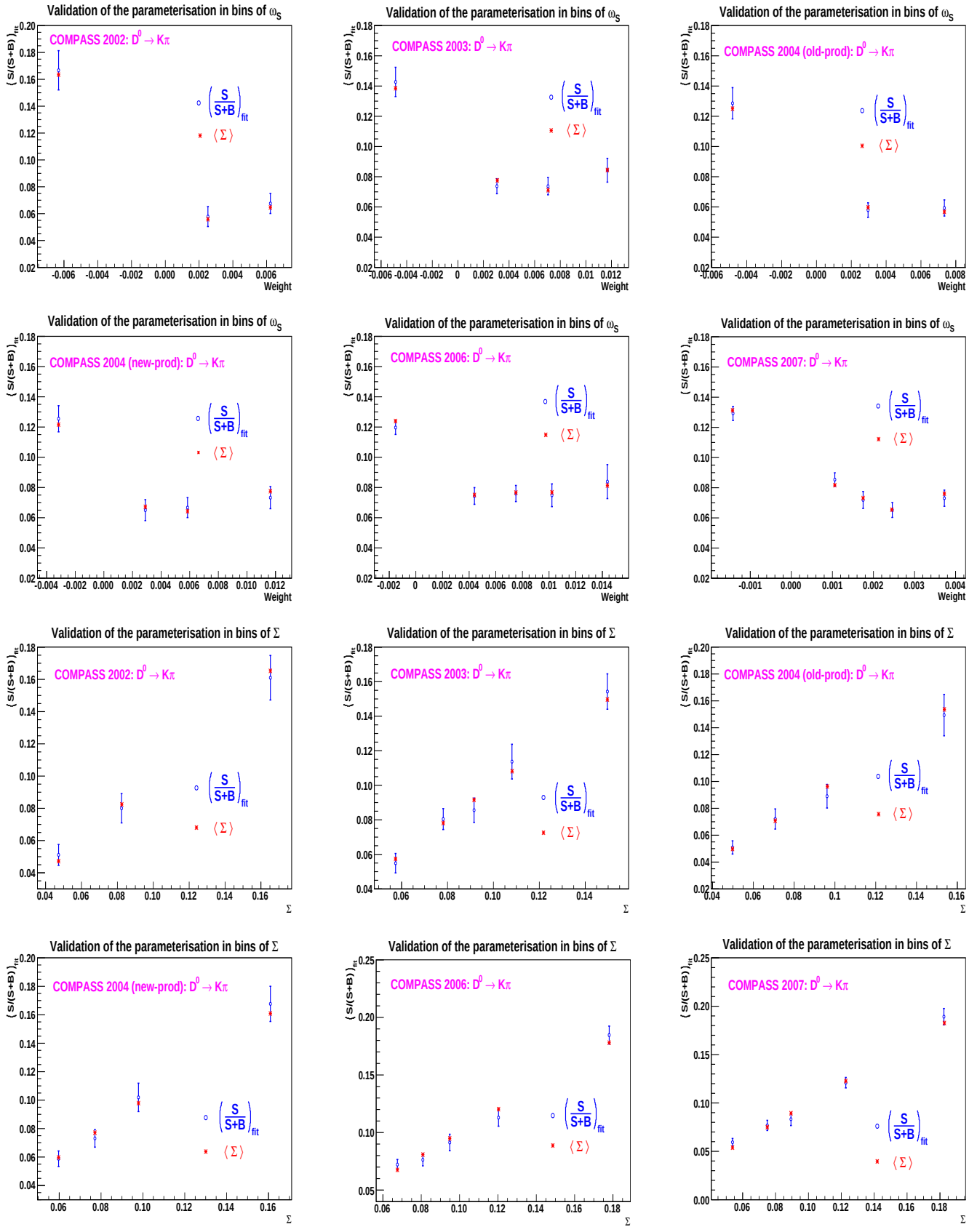

Figure 7.18: $D^0_{K\pi}$ channel: validation of all parameterisations (Σ_{19}, Σ_{20}, Σ_{21} , Σ_{22}, Σ_{23}, Σ_{24}) in bins of weight (first 2 lines) and also in bins of probability (last 2 lines).

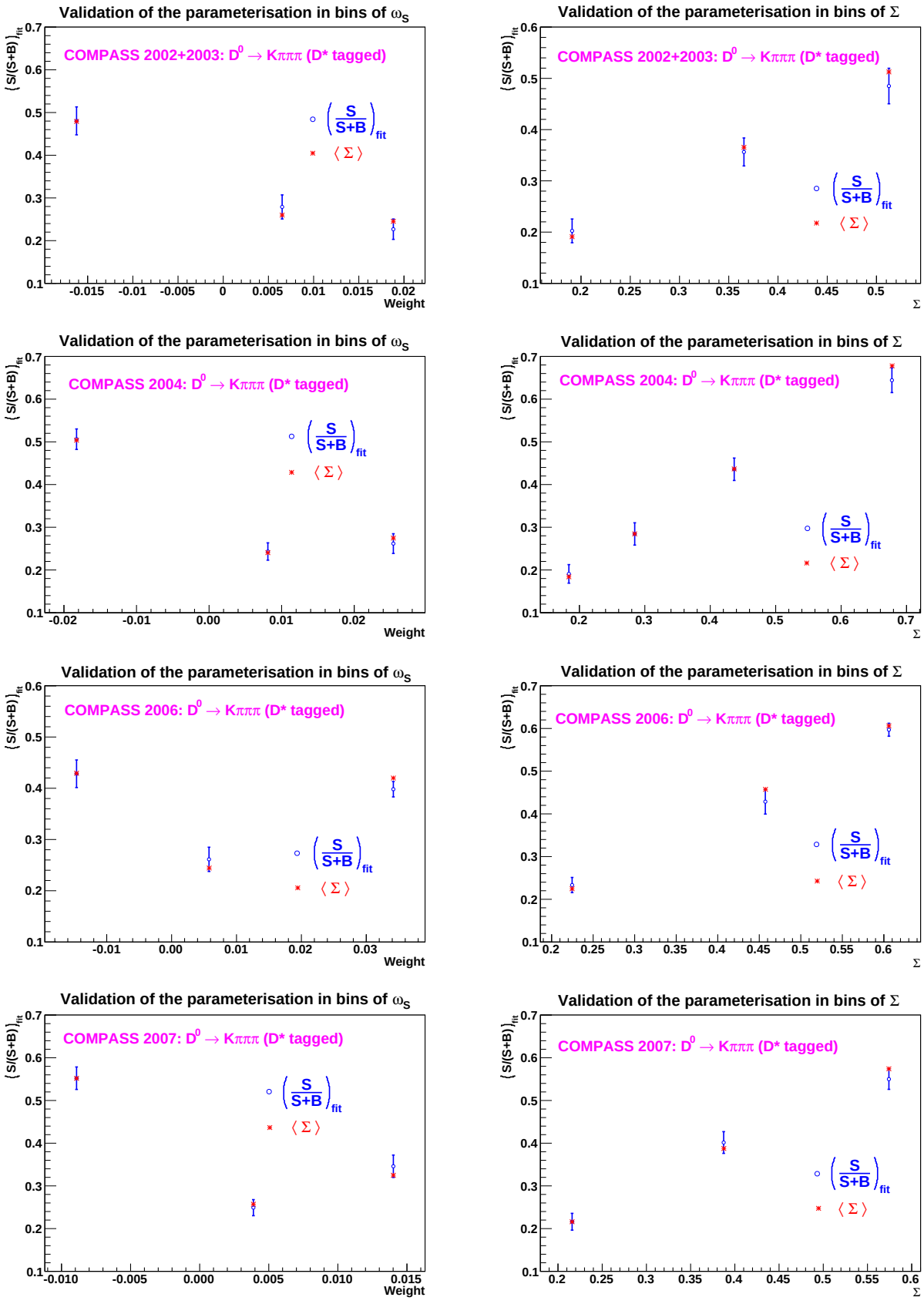

Figure 7.19: $D^*_{K\pi\pi\pi}$ channel: validation of all parameterisations (Σ_{11}, Σ_{12}, Σ_{13}, Σ_{14}) in bins of weight (first column) and also in bins of probability (second column).

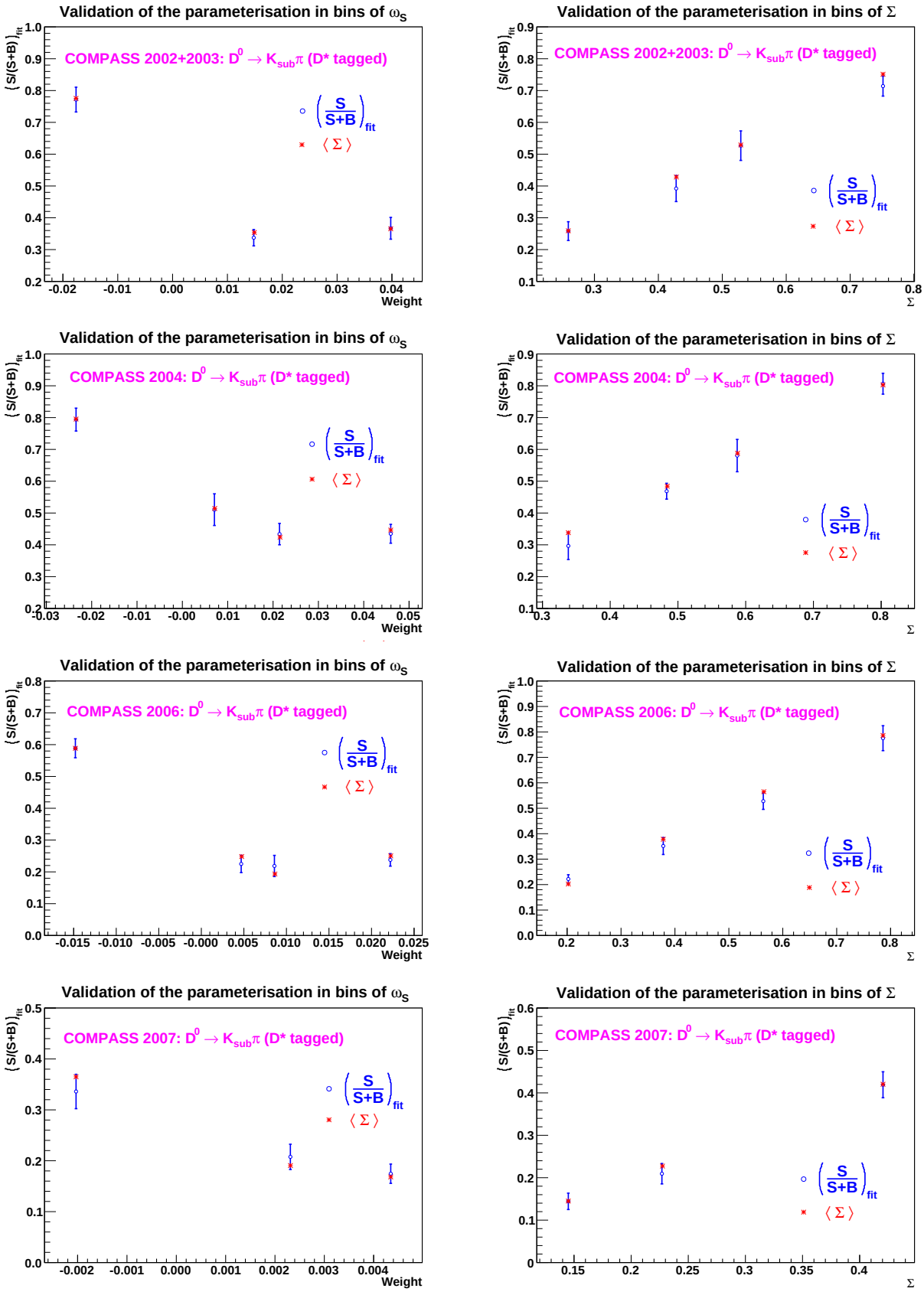

Figure 7.20: $D^*_{K_{sub}\pi}$ channel: validation of all parameterisations (Σ_{15}, Σ_{16}, Σ_{17}, Σ_{18}) in bins of weight (first column) and also in bins of probability (second column).

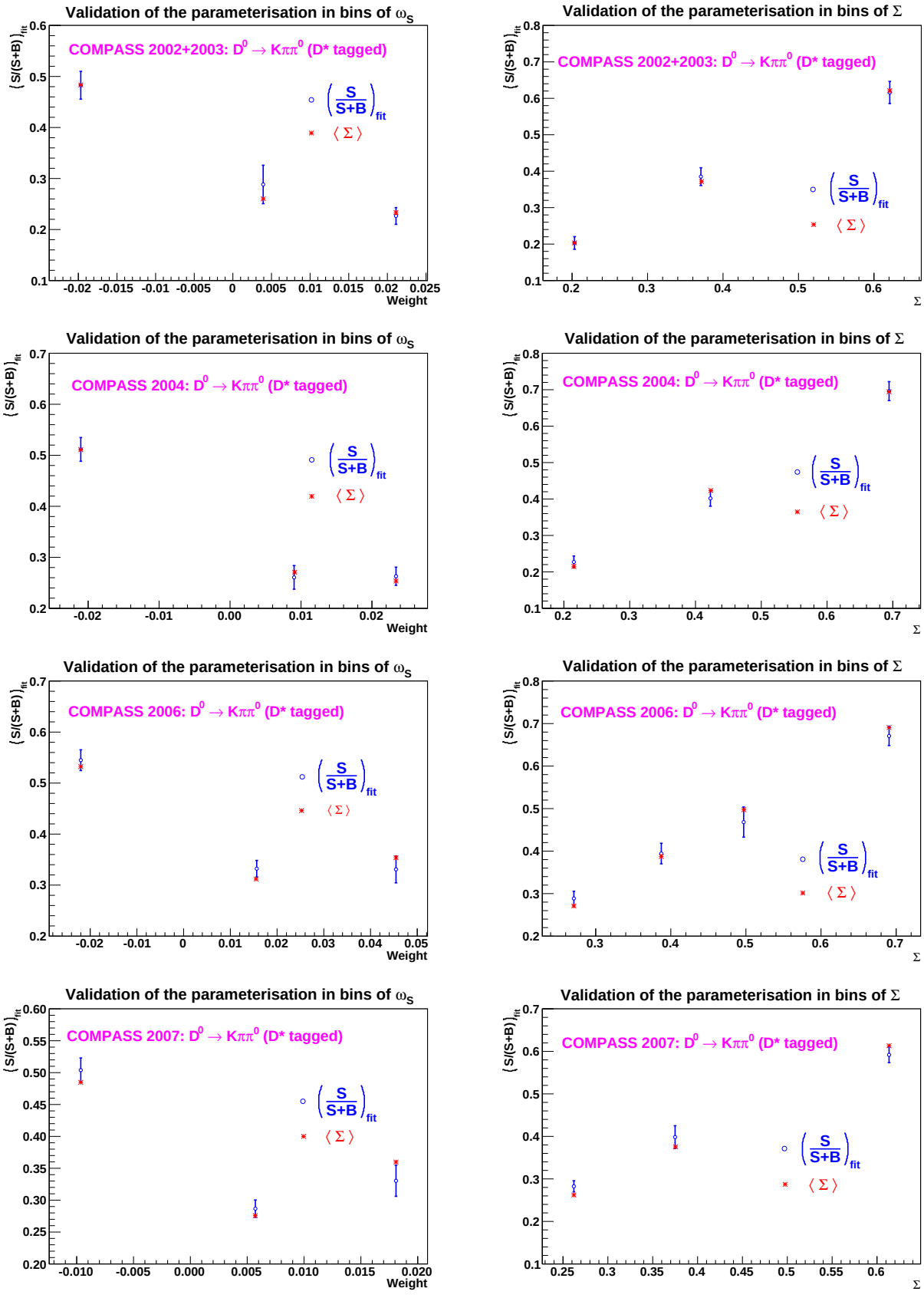

Figure 7.21: $D^*_{K\pi\pi^0}$ channel: validation of all parameterisations (Σ_7, Σ_8, Σ_9, Σ_{10}) in bins of weight (first column) and also in bins of probability (second column).

7.4 Including the reconstructed mass in Σ

In the previous sections the method used to build Σ is described in terms of kinematic variables. However, the final parameterisation must also include the dependence on the reconstructed mass, $\Sigma(m)$, before using it in the weight for the asymmetry extraction [3]. This is done in bins of the parameterised Σ (unbiased bins), according to the following equation:

$$\Sigma(m) = \left(\frac{\eta S(m)}{\eta S(m) + B(m)}\right) \tag{7.23}$$

using

$$\eta = \frac{\left(\frac{S}{B}\right)_{\text{par}}}{\left(\frac{\int_a^b S(m)}{\int_a^b B(m)}\right)_{\text{fit}}} \qquad \text{and} \qquad \left(\frac{S}{B}\right)_{\text{par}} = \left(\frac{\Sigma}{1-\Sigma}\right) \tag{7.24}$$

The mass dependence is included in eq. 7.23 by the functions S(m) and B(m). These functions are the signal and background fits to the mass spectra sampled in bins of Σ, and they are used to obtain the signal purity for every event of mass m. The final parameterisation, $\Sigma(m)$, results from these signal purity fits corrected with the parameterisation Σ (cf. eq. 7.24), where the limits of integration correspond to the training mass windows which are used for the Neural Network parameterisations (windows under the corresponding D^0 peak): $\{a, b\} = \{-40\ (-30), +40\ (+30)\}$ MeV/c^2 for the D* tagged (untagged) samples. The fits used for each channel are:

- $D^*_{K\pi}$ + $D^*_{K\pi\pi^0}$: $\begin{cases} S(m) \to \left(\frac{p[0]\cdot b_w}{\sqrt{2\pi}\cdot p[2]}\right) e^{-\frac{1}{2}\cdot\left(\frac{m-p[1]}{p[2]}\right)^2} \\ B(m) \to p[3]e^{-p[4]\cdot m} + \left(\frac{p[5]\cdot b_w}{\sqrt{2\pi}\cdot p[7]}\right) e^{-\frac{1}{2}\cdot\left(\frac{m-p[6]}{p[7]}\right)^2} \end{cases}$

- $D^*_{K\pi\pi\pi}$: $\begin{cases} S(m) \to \left(\frac{p[0]\cdot b_w}{\sqrt{2\pi}\cdot p[2]}\right) e^{-\frac{1}{2}\cdot\left(\frac{m-p[1]}{p[2]}\right)^2} \\ B(m) \to p[3] + (p[4]\cdot m) + (p[5]\cdot m)^2 \end{cases}$

- $D^*_{K_{sub}\pi}$: $\begin{cases} S(m) \to \left(\frac{p[0]\cdot b_w}{\sqrt{2\pi}\cdot p[2]}\right) e^{-\frac{1}{2}\cdot\left(\frac{m-p[1]}{p[2]}\right)^2} \\ B(m) \to p[3]e^{-p[4]\cdot m}\left[+\left(\frac{p[5]\cdot b_w}{\sqrt{2\pi}\cdot p[7]}\right) e^{-\frac{1}{2}\cdot\left(\frac{m-p[6]}{p[7]}\right)^2}\right] \end{cases}$

- $D^0_{K\pi}$: $\begin{cases} S(m) \to \left(\frac{p[0]\cdot b_w}{\sqrt{2\pi}\cdot p[2]}\right) e^{-\frac{1}{2}\cdot\left(\frac{m-p[1]}{p[2]}\right)^2} \\ B(m) \to p[4]\cdot e^{-p[3]\cdot m} + p[6]\cdot e^{-p[5]\cdot m} \end{cases}$

where b_w is the bin width in MeV/c^2, and the parameters p in the signal function are the total number of D^0, p[0], the reconstructed mass of the particle, p[1], and finally the signal width p[2].

Since the resonances of the $D^*_{K\pi}$ and $D^*_{K\pi\pi^0}$ channels are seen in the same mass spectrum, a second Gaussian is used to fit the unwanted peak as a background contribution: for example, in

[3] Note that the reconstructed mass cannot be used as a learning variable, in the Neural Network, because it will enhance the probability of a background event in the signal region to be a true D^0 meson.

the $D^*_{K\pi\pi^0}$ case the signal function is parameterised by $p[0] = N(D^0_{K\pi\pi^0})$, $p[1] = M(D^0_{K\pi\pi^0})$ and $p[2] = \sigma(D^0_{K\pi\pi^0})$; and the background function contains a Gaussian distribution describing the $D^0_{K\pi}$ peak. Concerning the $D^*_{K_{sub}\pi}$ mass sample, the Gaussian fit is only used in the background function for those bins where the $D^0_{K\pi\pi^0}$ resonance can be distinguished from the combinatorial background. All Gaussians are centred around zero, $M_{K\pi} - M_{D^0}$ or $M_{K\pi\pi\pi} - M_{D^0}$, except for the $D^0_{K\pi\pi^0}$ peak where the signal fit is centred around -240 MeV/c^2 (cf. Fig. 5.14).

In Figs. 7.22-7.26 we can see the nice probability behaviour of the mass spectra, in bins of Σ, for each channel, together with the fits used to introduce the mass dependence (one example per channel is shown). One can clearly see that in the first Σ-bin mostly combinatorial background is present, whereas the last Σ-bin contains mostly open-charm events. The beauty of this behaviour is that we can obtain a very large $\Sigma(m)$ for the events belonging to the last bins of Σ, which are also the events that reveal the biggest kinematic differences as compared to the combinatorial background (this is the reason why they are classified with higher probabilities Σ). This means that these events are a cleaner tag of the PGF process, and by isolating them from the background we are able to maximise their contribution to the weight in an unbiased way. Consequently, the statistical improvement introduced by the weights in the measured asymmetry is also maximised (cf. eq. 7.14).

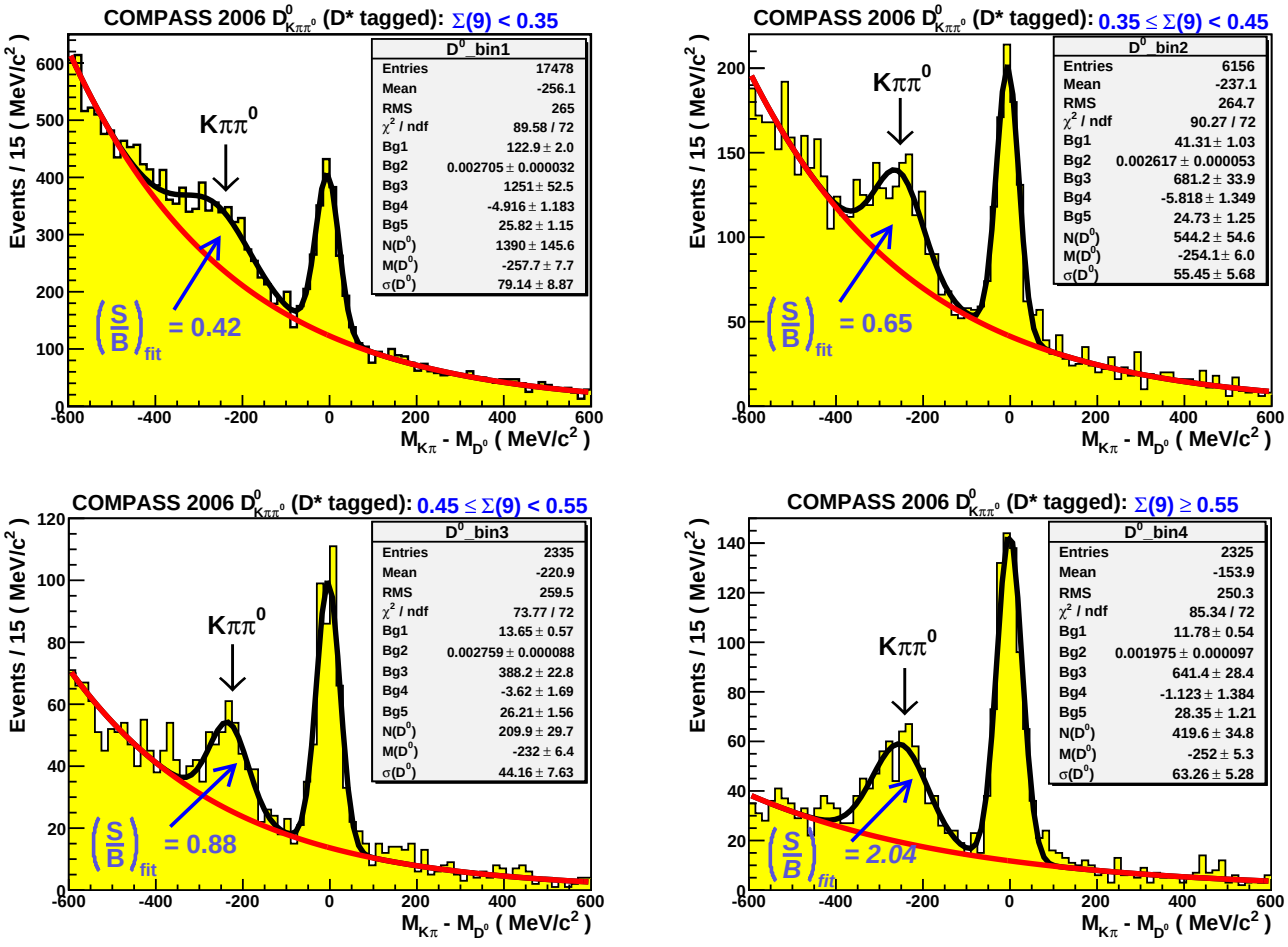

Figure 7.22: $D^*_{K\pi\pi^0}(2006)$ mass spectrum sampled in bins of D^0 probability (Σ). This specific parameterisation was built in a fit independent way (c.f. section 7.3.1), however, the agreement with the illustrated fits is good enough to trust them as a good approximation to the bumpy shape of this D^0 signal (as quantified in the 6^{th} plot of Fig. 7.21)

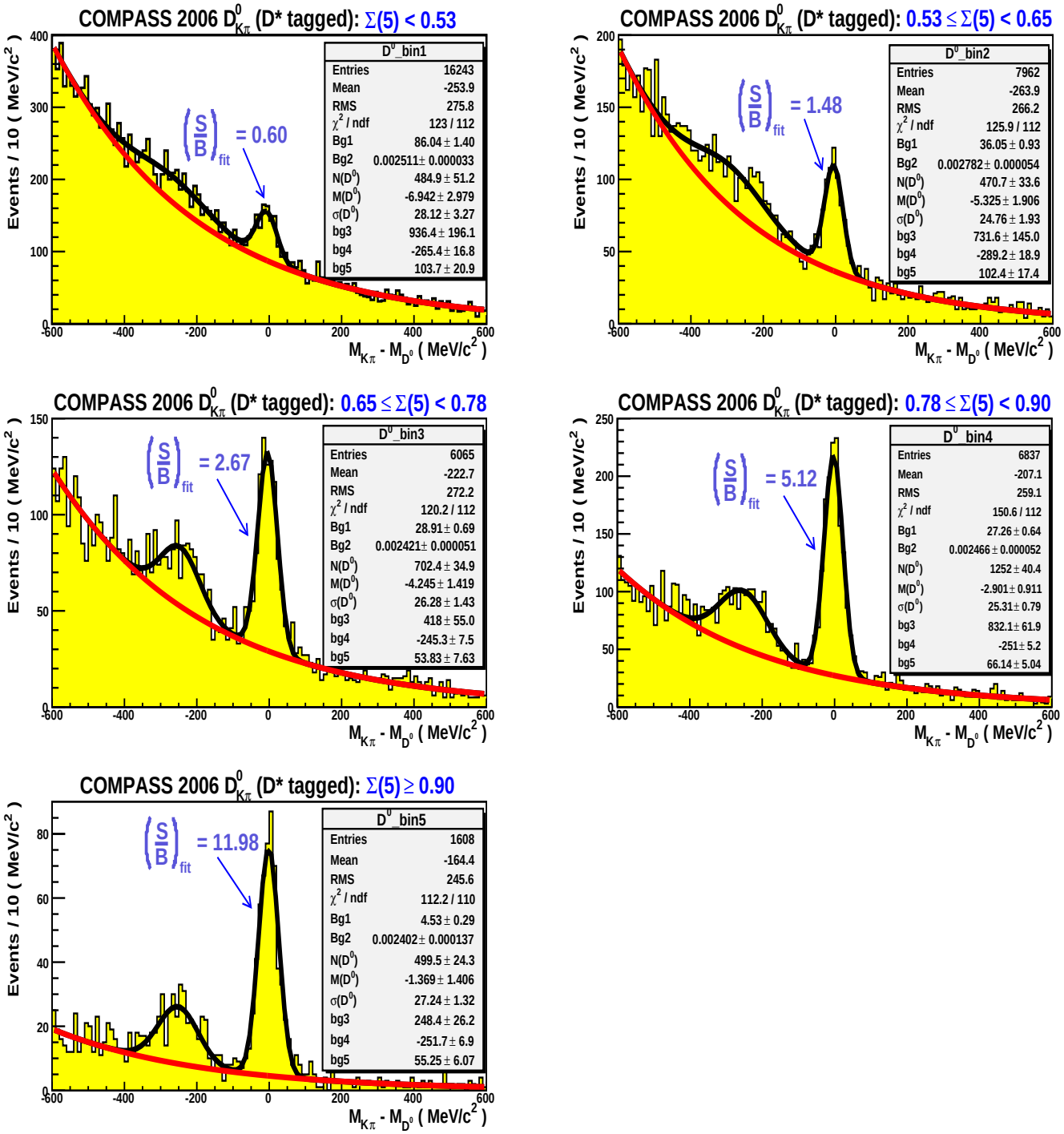

Figure 7.23: $D^*_{K\pi}(2006)$ mass spectrum in bins of D^0 probability (Σ). The fits shown are used to introduce the mass dependence in $\Sigma(5)$ and also to validate the parameterisation (11^{th} plot in Fig. 7.17)

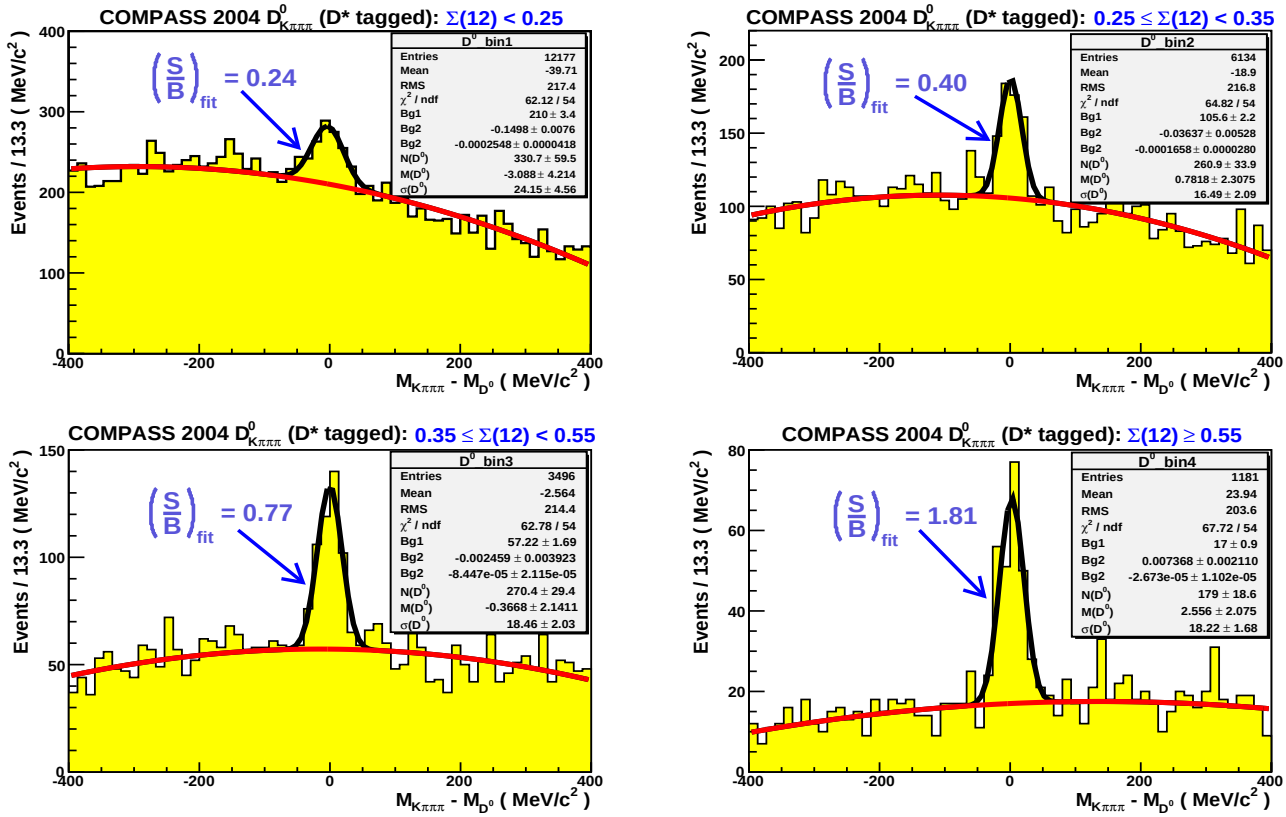

Figure 7.24: $D^*_{K\pi\pi\pi}(2004)$ mass spectrum in bins of D^0 probability (Σ).

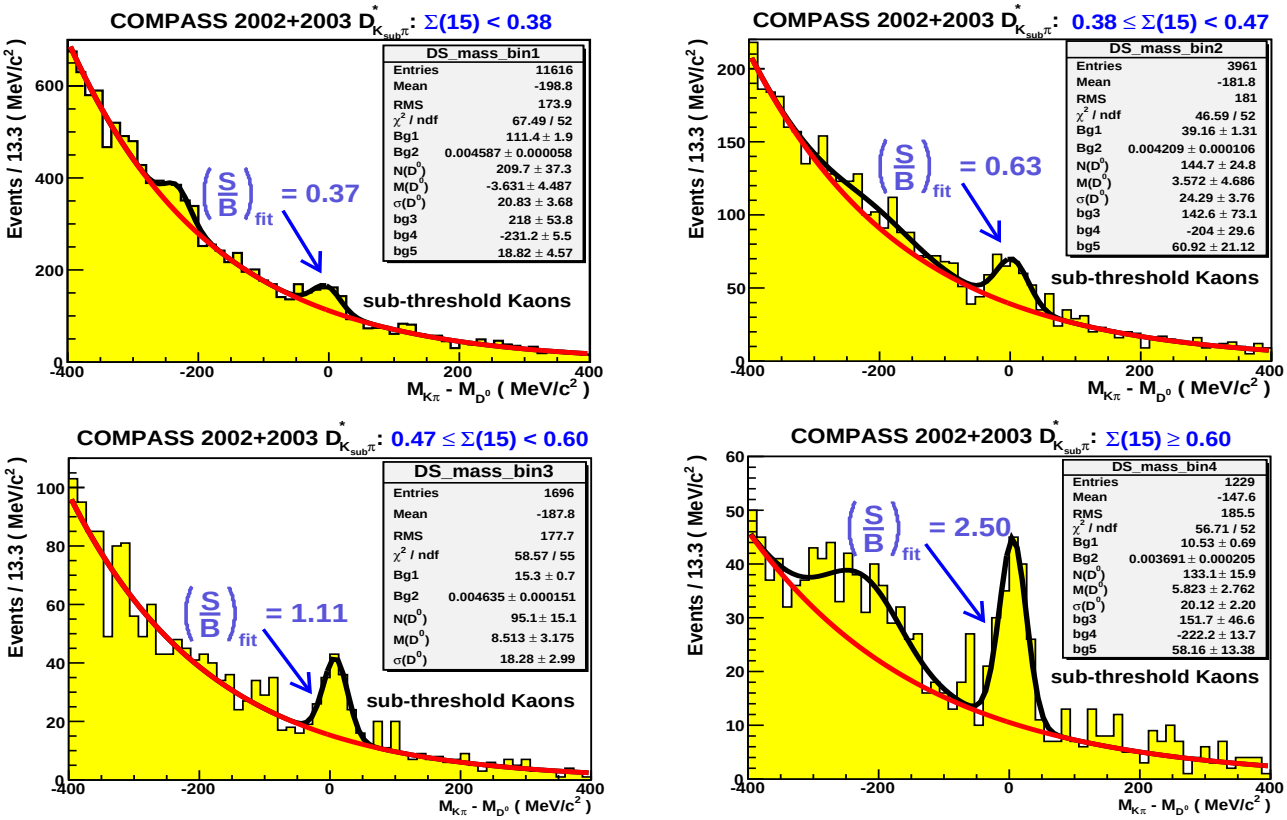

Figure 7.25: $D^*_{K_{sub}\pi}(2002+2003)$ mass spectrum in bins of D^0 probability (Σ).

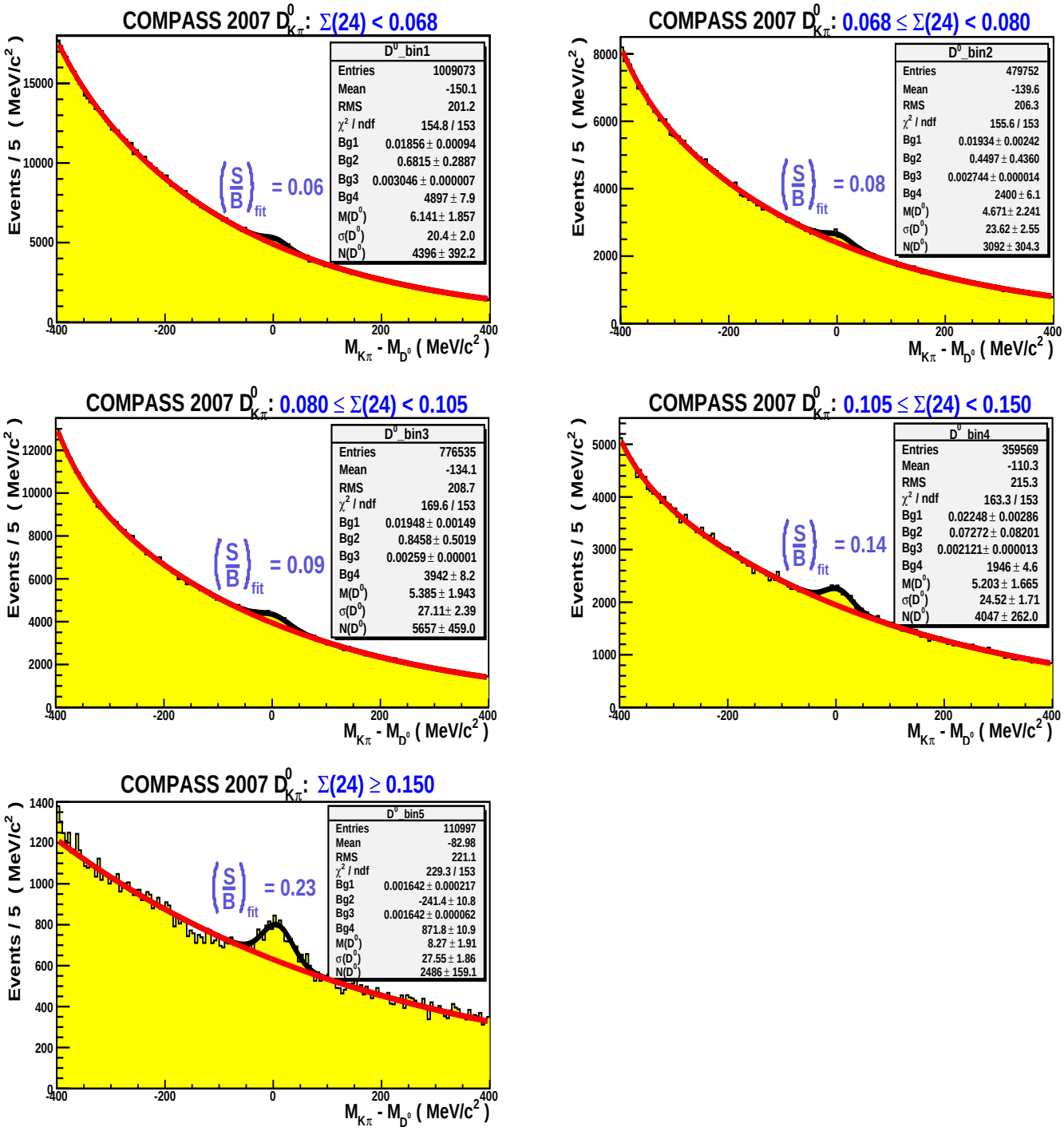

Figure 7.26: $D^0_{K\pi}(2007)$ mass spectrum in bins of D^0 probability (Σ).

7.5 Impact of Σ in the analysis

In Table 7.2 it is quantified the impact of the Σ parameterisation in the FOM $\equiv S^2/(S+B)$ of all D^0 mass spectra. For the case of the $D^0_{K\pi}$ channels (tagged and untagged) the FOM is not improved by a cut in the Neural Network response and, therefore, the cut in o_1 is not used for these samples. Although their signal purities can be increased through the use of such cut in o_1

(mostly combinatorial background is removed), no cut value is found to increase their FOM [4]. Regarding the $D^*_{K\pi}$ channel, the kinematic selection of D^0 events (see Tab. 5.8) gives rise to a very clean peak (cf. Fig. 5.15). Therefore, the application of a cut in o_1 is not very helpful for the golden channel. On the other hand, the main problem of the untagged $D^0_{K\pi}$ samples is the absence of a dedicated Σ-parameterisation. As a result, the huge combinatorial background cannot be removed without affecting significantly the signal.

The improvements introduced by Σ in the analysis can also be seen qualitatively in Fig. 7.27, where the final mass spectra (yellow plots - after a cut in o_1) are shown together with the Σ-weighted mass spectra (green distributions): by comparing the scales of both mass spectra, it is clear that the signal-to-background ratios (S/B) are increased by the Σ-parameterisations. In a more quantitative approach we can determine the gain in the FOM, for each channel, by fitting the signal of the Σ-weighted mass spectra with a Gaussian function. The integral of the Gaussian fit corresponds to the FOM that is achieved by the use of Σ. The results obtained can then be compared to the FOM coming from the yellow mass spectra (cf. Tab. 7.2 and Fig. 7.27). Using the numbers from the 4$^{\text{th}}$ column of Tab. 7.2, we can directly compare the relative contributions of the 5 channels to the extraction of the gluon polarisation:

$$\delta\left(\frac{\Delta G}{G}\right) = \frac{1}{P_\mu \cdot P_T \cdot f \cdot D \cdot \langle a_{LL}\rangle} \times \frac{1}{\sqrt{\text{FOM}}} \tag{7.25}$$

The low purity channels of low statistics ($D^*_{K\pi\pi^0}$, $D^*_{K\pi\pi\pi}$ and $D^*_{K_{sub}\pi}$) and all samples from the 2007 proton data are analysed for the first time in this open-charm analysis.

Data	**Channel**	**FOM (2σ) $\equiv$ S^2/(S+B)**		
		Mass spectra with o_1 cut	**Final mass spectra**	**Σ-weighted mass spectra**
2002-2006	$D^*_{K\pi}$	-	5967	+14%
	$D^*_{K\pi\pi^0}$	+17%	1986	+29%
	$D^*_{K\pi\pi\pi}$	+16%	1170	+34%
	$D^*_{K_{sub}\pi}$	+32%	818	+65%
	$D^0_{K\pi}$	-	3170	+20%
2007	$D^*_{K\pi}$	-	3021	+11%
	$D^*_{K\pi\pi^0}$	+6%	1074	+8%
	$D^*_{K\pi\pi\pi}$	+13%	393	+26%
	$D^*_{K_{sub}\pi}$	+39%	239	+13%
	$D^0_{K\pi}$	-	1909	+27%

Table 7.2: Improvements introduced by the parameterisations of $\frac{S}{S+B}$ in the FOM of all D^0 mass spectra. The illustrated gains are calculated by using the same mass windows where o_1 and Σ were built. The penultimate column shows the final FOM obtained for each channel.

[4] Note that a smaller percentage of the signal is also removed with a cut in o_1.

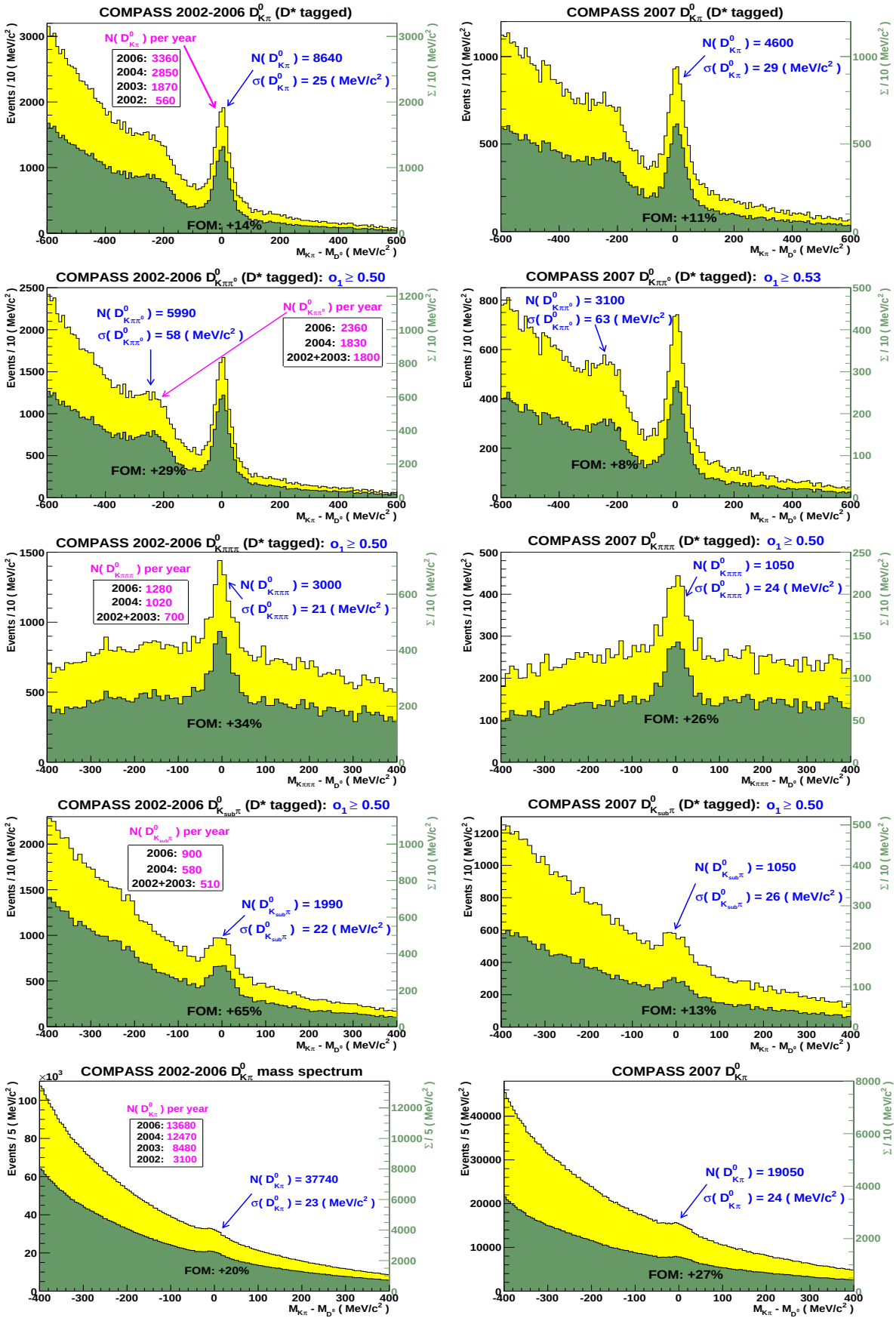

Figure 7.27: Final samples used for the asymmetry calculation (in yellow). Each channel can be seen per line, for the deuteron (first column) and proton (second column) data. The green distributions, shown with their own scales on the right, correspond to the Σ-weighted events: by fitting the signal of these distributions we obtain the FOM corresponding to the use of Σ.

7.6 The analysing power

The muon-gluon analysing power for the charm production, a_{LL}, is dependent on the full knowledge of the partonic kinematics. Therefore, this partonic asymmetry is not experimentally accessible, on the event-by-event basis, because the information associated with one of the charm quarks is lost. Even in the unlikely event where two D^0 candidates can be reconstructed, the probability that at least one of them belongs to the combinatorial background is non-negligible. Qualitatively, one can easily understand this statement by considering all the requirements for a double D^0 reconstruction:

1. In a PGF event, it is necessary that the two charm quarks do fragment into the same kind of D meson (D^0 or D^*) with the same D^0 decay mode (both candidates need to be in the same mass spectrum).

2. All particles in the final state need to be in the experimental acceptance imposed by the solenoid surrounding the target.

3. With the exception of the slow-pion, all particles in the final state must have a momentum high enough in order to be reconstructed (above the RICH thresholds for PID, cf. Fig. 3.9):

   - $p(K) > 9.0$ GeV/c ($p(K) > 2.5$ GeV/c for the $D^*_{K_{sub}\pi}$ channel)
   - $p(\pi) > 2.5$ GeV/c

Clearly, it is very unlikely to have two D^0 in the same event decaying to one out of the three final states considered in the analysis. For example, being the branching ratio of a D^0 decay into a $K\pi$ pair 3.89% [16], we obtain a probability of only 0.16% for a double $D^0_{K\pi}$ production in the same event. Moreover, as a result from the PGF interaction, these open-charm mesons are produced with a high-transverse momentum. Consequently, if a second D^0 is required, the number of reconstructed events is significantly reduced: the probability for all the decay products to be in the acceptance window is obviously lower. Even if those two conditions are fulfilled, all the particles in the final state (twice more) need to enter the RICH detector with the required momenta (cf. section 3.3.2). After the kinematic and RICH selection (Chapter 5), the number of events with two D^0 candidates correspond only to 7% of the total statistics, for the untagged channel, and less than 2 % for the D*-tagged samples. In addition to that, as explained above, most of these events contain a contribution from the combinatorial background.

In the best scenario we can partially separate the signal from the background in the D^0 mass spectra, by performing a proper kinematic parameterisation (cf. section 7.3) which attributes to every D^0 candidate a probability to be indeed a D^0 meson. Nevertheless, even if the background contamination is efficiently removed (under the resonance), the resulting statistics to calculate a_{LL} is only a small fraction of 2% (or 7%) of the total number of selected events. Therefore, the only solution is to obtain the partonic asymmetry with the help of a Monte Carlo generator for heavy flavours. Events containing the charmed mesons are generated with AROMA [73], processed with COMGEANT [5] [75] to simulate the full response of the COMPASS spectrometer, and finally reconstructed with CORAL [6] and PHAST [7] using the same analysis chain as for real

[5] **COM**pass Monte Carlo simulation program based on GEANT 3.21.

[6] **CO**mpass **R**econstruction **AL**gorithm: used for the event reconstruction, involving the definition of the beam track, the scattered muon and the vertex of the interaction.

[7] **PH**ysics **A**nalysis **S**oftware **T**ools: used to read the output of CORAL and to perform the physics analysis.

events. After this full Monte Carlo chain the muon-gluon asymmetry is calculated, for every generated event, using the reconstructed partonic variables. The explicit kinematic dependence of a_{LL}, using a leading order QCD approximation, can be verified from eq. 2.87 to eq. 2.93. The general formula, including the next-to-leading order corrections, is partially available in [52, 53, 54, 55, 56] and also upon request [57]. In order to use the generated values of a_{LL} in the real data, a Neural Network [79] is used to parameterise this partonic asymmetry in terms of mensurable kinematic variables:

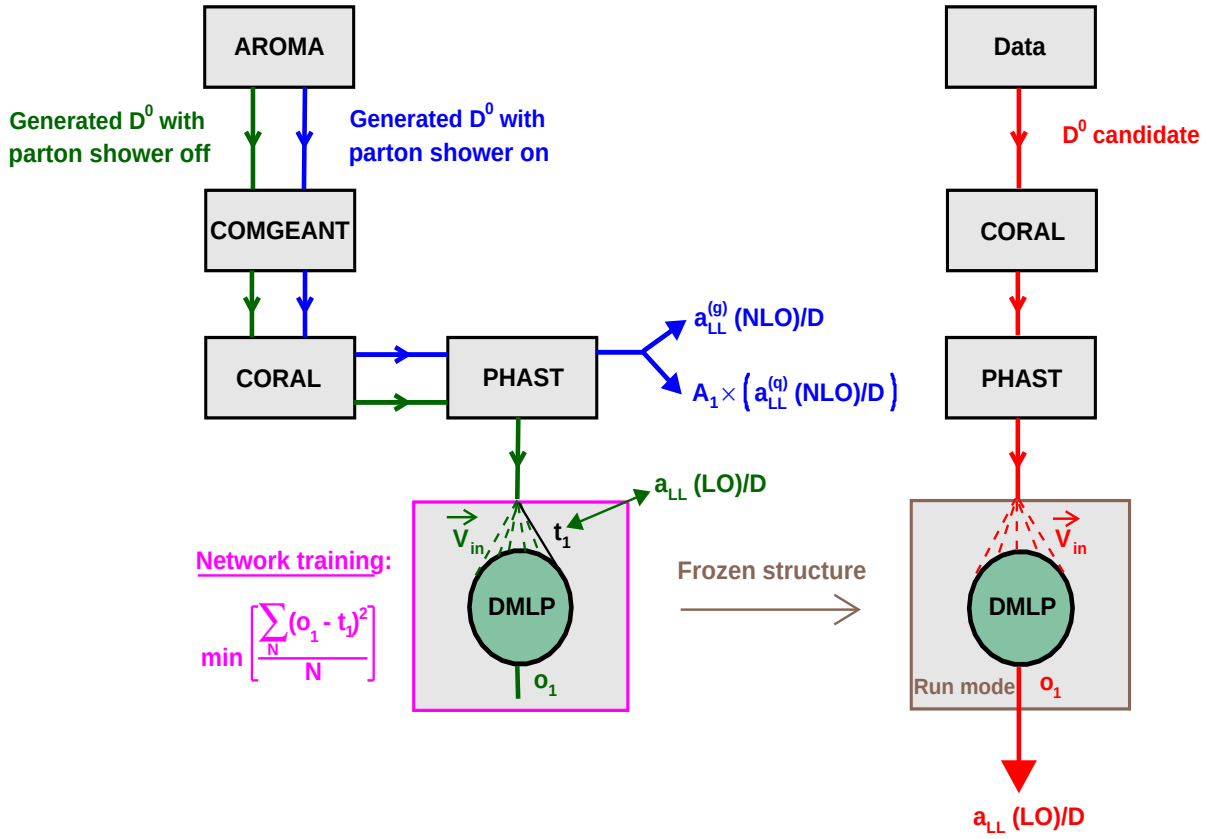

Figure 7.28: Scheme of the procedure used to obtain the photon-gluon asymmetry, a_{LL}/D.

To the left of Fig. 7.28 one can see a flowchart representing the full Monte Carlo chain, from AROMA to the Dynamic Multi-Layer Perceptrons (DMLP) Network, illustrating all the needed ingredients for the Neural Network parameterisation. This last step is of crucial importance to determine the values of the partonic asymmetries to be used in real data. The procedure is very similar to the one described for the signal purities, $S/(S+B)$, with one exception: instead of an event classification based on a multidimensional kinematic comparison, here the Network acts as an event predictor based on the underlying kinematics. For a proper understanding of this new mode of the Network operation, a very brief summary of the $S/(S+B)$ parameterisation is now presented.

The Neural Network classification of events:

The D^0 probabilities are parameterised by a kinematic comparison of two real data samples, gcc and wcc, where the latter is used as a background model. This sample has the obvious expectation value of $t_1(wcc) = 0$, whereas the data sample containing the D^0 events and com-

binatorial background is labelled with $t_1(gcc) = 1$. What the Network does is to parameterise a two-value classification function [8] with the aim of minimising the following two deviations:

$$\frac{\sum_{i=1}^{N(wcc)} [o_{1,i}(wcc) - t_{1,i}(wcc)]^2}{N(wcc)} \tag{7.26}$$

$$\frac{\sum_{i=1}^{N(gcc)} [o_{1,i}(gcc) - t_{1,i}(gcc)]^2}{N(gcc)} \tag{7.27}$$

There is one important consequence imposed by eq. 7.26: those gcc candidates that are kinematically similar to the wcc events are interpreted (by the Neural Network) as members of the combinatorial background and, as a result, they are assigned with lower $o_1(gcc)$ values when compared to the real D^0 mesons. To the latter the Neural Network assigns $o_1(gcc)$ values close to 1, due to their unmatched kinematics and to the existence of the condition given by eq. 7.27. Finally, for those indistinguishable gcc events (when compared to the wcc sample) an answer around 0.5 is computed by the Network. The result of this parameterisation is the classification of the gcc events according to their kinematic similarities. Consequently, using the $o_1(gcc)$ spectrum we are able to distinguish part of the signal from the combinatorial background.

7.6.1 Neural Network parameterisation of a_{LL} at LO

As already stated above, for the parameterisation of a_{LL} the Neural Network acts as an event predictor. The expectation variable, t_1, changes its values for every event: $t_1 = a_{LL}/D$ (generated). Since the depolarisation factor D is basically dependent on y, $D(y)$ (cf. eq. 2.35), it is chosen to parameterise the photon-gluon asymmetry (instead of the muon-gluon one) to take advantage of this extra kinematic dependence. The Neural Network takes as an input a vector containing some generated kinematic variables (experimentally accessible), and then the event information contained in t_1 is used to obtain the correlation between a_{LL}/D and those kinematic variables. If the correlation is high, it means that the Network prediction for the photon-gluon asymmetry is very close from the truth: in other words, if the correlation is high the deviation between the prediction (o_1) and the expected output (t_1) is small. As for the signal purities, the Neural Network tries to minimise the following quantity:

$$\frac{\sum_{i=1}^{N^{gen}} (o_{1,i} - t_{1,i})^2}{N^{gen}} \tag{7.28}$$

In order to ensure an unbiased parameterisation, a control sample is also used here. The procedure is identical to the one represented in Fig. 7.3, except for the fact that now only one sample is used in the training and in the testing sets. Consequently, the output o_1 of the Network is a single spectrum of predictions for the a_{LL}/D corresponding to each event. Several learning vectors are tested, and the one originating the highest correlation between o_1 and t_1 is selected. The kinematic variables considered for the parameterisation are:

$$Q^2 \ , \quad x_{Bj} \ , \quad y \ , \quad z_{D^0} \quad \text{and} \quad p_T(D^0)$$

The same initial neural structure as represented in Fig. 7.1 is used. The weights associated to the variable-neuron and to the neuron-neuron connections are randomly initialised, and

[8] In the definition of the classification function the two values which distinguish between the wcc and the gcc samples are arbitrary ones. The choice of 0 and 1, respectively, simplifies the interpretation of the Neural Network output in terms of probabilities.

thereafter they are all iteratively adjusted to minimise eq. 7.28. As before, the sigmoid function represented in Fig. 7.2 is used as a neuron activation function: every neuron computes an answer $f_{\text{act}}(\vec{V}\cdot\vec{W}^T) = o_1$ using the sigmoid function, where $\vec{V}$ and $\vec{W}$ represent the corresponding input and weight vectors. After each iteration, the weights associated to every hidden neuron are modified to produce the desired answer of the final neuron in the output layer (Neural Network response). The independent control sample ensures that the result of this parameterisation is not artificial: the same stable minimum is found for the training and for the testing sets (see section 7.2 for details). At the end of the parameterisation, the Network structure is frozen to allow for its use on the real data. It consists on several weight vectors $\vec{W}$ belonging to each of the hidden neurons that survived to the training procedure. Using this trained structure we are able to feed the Neural Network with the same reconstructed kinematic variables (from real data), and as an output the Network computes a prediction of a_{LL}/D for every single data event. The illustration of the full procedure can be seen on the right side of Fig. 7.28. Finally, the conversion of the photon-gluon asymmetry to the muon-gluon asymmetry is trivial:

$$a_{LL} = a_{LL}^{\mu g} = \left(a_{LL}^{\gamma^* g} \times D(y)\right) \tag{7.29}$$

The depolarisation factor is given by eq. 2.35 and, due to its exclusive dependence on y, it is a quantity that is experimentally accessible on an event-by-event basis. In Fig. 7.29 one can see the quality of the a_{LL} parameterisations (purple box in Fig. 7.28).

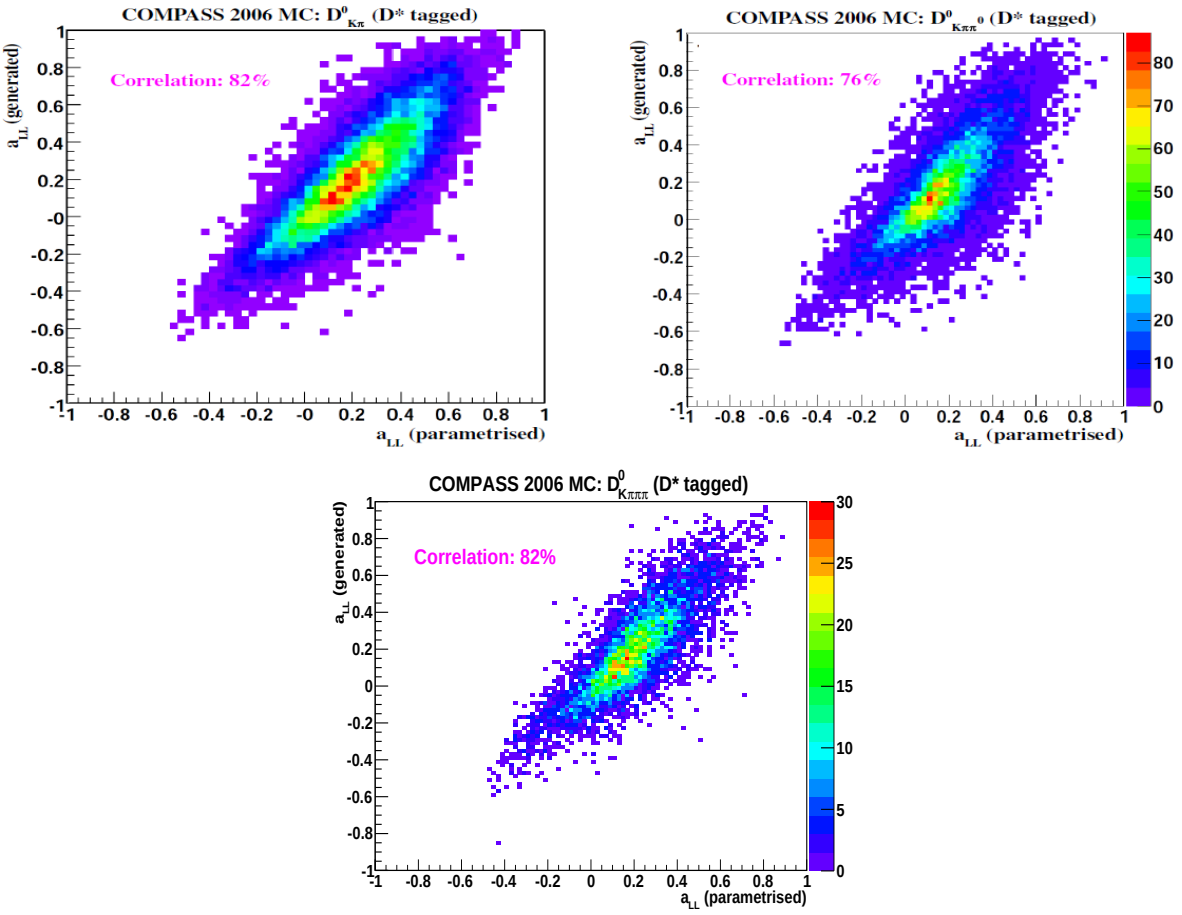

Figure 7.29: Example of the correlation between the generated analysing power and the a_{LL} parameterised by the Neural Network, for the 3 D^0 decay modes considered in the analysis.

A total of 6 parameterisations are built for all the samples considered in the analysis: three for each D^0 decay mode using the COMGEANT description of the 2006 spectrometer (cf. Fig. 7.29), and another three using the description of the spectrometer as it was in 2004. The idea is to account for the different experimental acceptances, because these constraints may affect the corresponding a_{LL} distributions in different ways. The target acceptance for a D^0 candidate was increased from 70 mrad to 180 mrad during the year of 2005 (by replacing the target solenoid by a new one), cf. Fig. 3.3. Nevertheless, it is found for the events collected in 2004 that the obtained muon-gluon asymmetry is practically the same when one uses the parameterisation of 2004 or 2006. As a result from this observation, it was decided to use only two parameterisations to account for the impact of the different experimental acceptances in a_{LL}: for the data collected in 2007 (2002 and 2003) the parameterisation of 2006 (2004) is used. The different D^0 decay modes are also considered for a separate parameterisation of the partonic asymmetry, because the reconstruction of those events containing more particles in the final state may be more affected by the acceptance constraints.

7.6.2 The analysing power a_{LL} obtained at NLO

Only the leading order a_{LL}/D is considered for the Neural Network parameterisation, with the aim of using it event-by-event in the real data (cf. the full procedure in procedure in Fig. 7.28). For the next-to-leading order analysis the generated photon-gluon asymmetry is directly applied on the data. The justification for that lies on the weak correlation found between the analysing power and the available kinematic variables for reconstruction:

- $\left(\frac{a^q_{LL}(NLO)}{D}\right)$ $\rightarrow$ 52% of correlation (between $o_1(a^{par}_{LL})$ and $t_1(a^{gen}_{LL})$)
- $A_1 \times \left(\frac{a^q_{LL}(NLO)}{D}\right)$ $\rightarrow$ 23% of correlation

The second item is needed to account for the physical background that exists in the NLO interpretation of the open-charm production (cf. Fig. 2.19). With such low correlations achieved by the Neural Network parameterisations, the statistical benefits of a_{LL} inside the signal weight are lost. Consequently, the next-to-leading order analysis is performed in several kinematic bins ($p_T^{D^0}$ and E_{D^0}) where the average values of the generated a_{LL}/D can be used (see section 8.3). The use of this method instead of an event-by-event analysis, results in a loss of precision in the order of 6% on the measurement of the gluon polarisation. This was verified in the leading order analysis where both methods can be applied (cf. section 8.2).

Determination of a_{LL} at NLO:

The phase-space needed for the NLO real gluon emission processes, $\gamma^* g \rightarrow c\bar{c}g$ (cf. Fig. 2.20), is simulated through parton showers included in the standard LO AROMA generator [9]. For every simulated event, the energy of parton showers (if present in the event) defines the upper limit of integration over the energy of the unobserved gluon in the NLO emission process. This

[9] The parton showers are considered in the initial and final states of the PGF interaction originating an open-charm meson.

integration reduces the differential cross-section for a three–body final state ($c\bar{c}g$) into a two–body one ($c\bar{c}$), and thus we can combine it with the LO cross-section ($c\bar{c}$, PGF), plus the two–body virtual and soft NLO corrections. This procedure guarantees a correct cancellation of the infra-red divergence [53, 54]. Therefore, the total partonic cross-section, at NLO, is calculated on an event-by-event basis, for the unpolarised case as well as for the polarisation dependent cross-section and, as a consequence, a new a_{LL} in NLO-QCD approximation is obtained. The same procedure is applied for the correction originating from a light-quark (cf. Fig. 2.19), but in this case the integration is performed over an unobserved final state light-quark. However, a LO generator with parton showers cannot properly describe the full phase-space corresponding to the NLO processes due to the approximations used when simulating the parton showers. Also, the normalisation of the event distributions is based on the LO cross-section. In order to estimate the systematic effect on a_{LL} related to the approximations used in the parton shower concept, a simplified Monte Carlo is employed. The events with and without real gluon emissions are generated using uniformly distributed partonic kinematic variables. Afterwards, the events are re-weighted according to the correct unpolarised NLO cross-section containing all the corrections: virtual, soft and real gluon emissions. This procedure guarantees a correct NLO normalisation. The gluon polarisation based on the events obtained from the LO AROMA with parton showers, is well approximated by the result based on the re-weighted events obtained from the simplified Monte Carlo. Here the comparison is done at the generator level, i.e. without simulating the detector acceptance. Therefore, the usage of LO AROMA with parton showers to simulate the phase-space for NLO processes is completely justified. To end this section, two examples corresponding to the LO and NLO distributions of a_{LL} are presented in Fig. 7.30. From this figure, we conclude that the NLO corrections to the muon-gluon asymmetry are quite important. Therefore, the gluon polarisation should also be extracted at the NLO approximation.

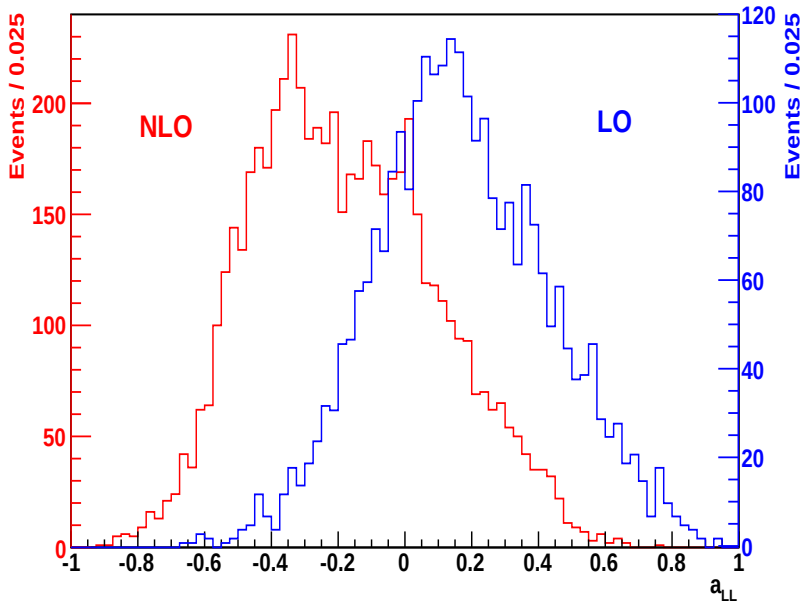

Figure 7.30: Distributions of the analysing power a_{LL} in the LO-QCD and in the NLO-QCD approximations. Observe the different normalisations of the LO and NLO samples. The 2006 target setup is considered for these distributions. The LO distribution results from the AROMA generator without parton showers, whereas for NLO the parton shower concept is applied. Both distributions are obtained after the full Monte Carlo chain.

Chapter 8

Results for $\Delta G/G$ and A_{bg}

The results of the gluon polarisation measurement from the open-charm production are presented in this chapter. Firstly, the values of $\langle \Delta G/G \rangle$ and $\langle A_{bg} \rangle$, obtained in a LO-QCD approximation, will be given for each of the five channels under analysis. Thereafter, the combined virtual-photon asymmetries for the D^0 production, $A^{\gamma^* N \to D^0 X}$, will be presented in bins of the D^0 transverse momentum and energy. These asymmetries are totally independent of any theoretical interpretation as they correspond only to the measurement of the experimental spin-asymmetries. Therefore, the obtained results on $A^{\gamma^* N}$ can be used by theorists to constrain their fit models of ΔG in a global analysis (using the world data). To enable an unbiased use of these asymmetries, they are provided in bins within which the acceptance of the COMPASS spectrometer is roughly flat for the PGF process. Finally, results for $\langle \Delta G/G \rangle$ and $\langle A_{bg} \rangle$, obtained in the NLO-QCD approximation, will also be shown and discussed.

8.1 Leading Order results for the gluon polarisation

Values for the $\langle \Delta G/G \rangle$ and the $\langle A_{bg} \rangle$ are obtained for each of the 48 weeks of data taking and, separately, for each of the five channels of analysis. The method used for this extraction is described in section 6.1.2. The results are summarised in the Tables 8.1 and 8.2 in terms of the weighted means (per year). The background asymmetries are consistent with zero.

Year	$\Delta G/G$				
	$D^*_{K\pi}$	$D^*_{K\pi\pi^0}$	$D^*_{K\pi\pi\pi}$	$D^*_{K_{sub}\pi}$	$D^0_{K\pi}$
2002	-1.506 ± 1.509	$+0.844 \pm 1.288$	-4.530 ± 2.549	-4.396 ± 2.027	-3.207 ± 1.864
2003	$+0.152 \pm 0.746$				$+0.106 \pm 1.014$
2004	$+0.106 \pm 0.570$	$+0.622 \pm 1.259$	-1.747 ± 1.701	$+2.403 \pm 1.668$	$+0.827 \pm 0.755$
2006	-0.612 ± 0.542	-1.236 ± 0.996	$+2.925 \pm 1.175$	$+2.147 \pm 1.687$	-0.574 ± 0.742
2007	$+0.036 \pm 0.702$	-1.159 ± 1.132	$+0.403 \pm 2.135$	-0.872 ± 4.292	$+0.548 \pm 1.017$
Total	-0.192 ± 0.305	-0.414 ± 0.575	$+0.628 \pm 0.833$	$+0.497 \pm 0.995$	$+0.020 \pm 0.415$

Table 8.1: Results per channel and per year for the gluon polarisation extracted from the full weighted analysis. The quoted errors are statistical.

Year	A_{bg}				
	$D^*_{K\pi}$	$D^*_{K\pi\pi^0}$	$D^*_{K\pi\pi\pi}$	$D^*_{K_{sub}\pi}$	$D^0_{K\pi}$
2002	-0.107 ± 0.107	-0.149 ± 0.068	-0.048 ± 0.084	-0.190 ± 0.101	$+0.019 \pm 0.014$
2003	-0.055 ± 0.067				$+0.001 \pm 0.009$
2004	$+0.052 \pm 0.056$	$+0.088 \pm 0.061$	$+0.057 \pm 0.067$	$+0.139 \pm 0.129$	-0.014 ± 0.008
2006	$+0.051 \pm 0.056$	$+0.146 \pm 0.069$	$+0.000 \pm 0.060$	-0.015 ± 0.071	-0.008 ± 0.007
2007	$+0.055 \pm 0.072$	$+0.157 \pm 0.088$	-0.046 ± 0.093	$+0.164 \pm 0.105$	-0.004 ± 0.009
Total	$+0.019 \pm 0.029$	$+0.051 \pm 0.035$	$+0.002 \pm 0.037$	$+0.004 \pm 0.047$	-0.005 ± 0.004

Table 8.2: Results per channel and per year for the background asymmetry. The quoted errors are statistical.

We can also compare these results in a graphical way from Fig. 8.2 to Fig. 8.4. The values of $\langle \Delta G/G \rangle$ are all distributed around zero, with larger fluctuations for the low purity channels due to the small statistics available (cf. Fig. 8.4). The final value of the gluon polarisation is the weighted mean of the five channel results shown in Tab. 8.1, and amounts to:

$$\left\langle \frac{\Delta G}{G} \right\rangle^{\text{LO}} = -0.08 \pm 0.21 \text{ (stat.)} \pm 0.08 \text{ (syst.)} \tag{8.1}$$

The details about the systematic error are given in Chapter 9.

Assuming that $[\Delta G/G](x_g)$ is approximately a linear function of x_g in the range covered by the present data, the above result is the gluon polarisation $\Delta G/G$ at $\langle x_g \rangle_{\omega^2}$, where the latter is the weighted average calculated using the signal weights (eq. 6.44). The average value of x_g probed by this analysis, in the LO approximation, is:

$$\langle x_g \rangle_{\omega^2} = 0.11^{+0.08}_{-0.04} \qquad @\langle \mu^2 \rangle_{\omega^2} = 13 \text{ (GeV/}c\text{)}^2 \tag{8.2}$$

The limits defined by the above x_g interval are determined from Fig. 8.1, using the following equation:

$$\begin{aligned} \text{AL} \quad &= \quad 10^{(\ \text{Log}_{10}\langle x_g \rangle\ \pm\ \text{RMS}\ )} \\ &\overset{(\text{RMS}\ =\ 0.22)}{=} \quad \{\underbrace{0.06}_{-}\ ,\ \underbrace{0.19}_{+}\} \end{aligned} \tag{8.3}$$

where AL are the **A**symmetric **L**imits of 1σ that result from the logarithmic (symmetric) distribution of x_g. The result quoted in eq. 8.1 represents the cleanest (and most direct) measurement ever made of the gluon polarisation. The obtained value is displayed in Fig. 8.5 together with all the world $\langle \Delta G/G \rangle$ measurements. Note the difference in the scale used to obtain each of the experimental results: the open-charm point is measured at a scale of $\langle \mu^2 \rangle = 13$ (GeV/c)^2 whereas the remaining points are determined at a scale of $\langle \mu^2 \rangle = 3$ (GeV/c)^2. In the case of the open-charm analysis, the perturbative treatment of the hard photon-gluon process is completely ensured by the much higher scale considered. Concerning the high-p_T results, they all have associated some theoretical uncertainties related to the existence of a physical background. Therefore, the quality of these experimental (high-p_T) points rely on the existence

of a Monte Carlo describing very well the data. All results show a good compatibility among them: they are all consistent with small values of $\Delta G/G$ within a range of $x_g \sim [0.05, 0.25]$. The previous sentence is the most fair conclusion that one can draw from Fig. 8.5, because not even the sign of ΔG can be inferred from all the $\langle \Delta G/G \rangle$ measurements (due to the existence of large statistical errors). The results are also compatible with zero, i.e. the gluons do not contribute to the nucleon spin in this x_g range.

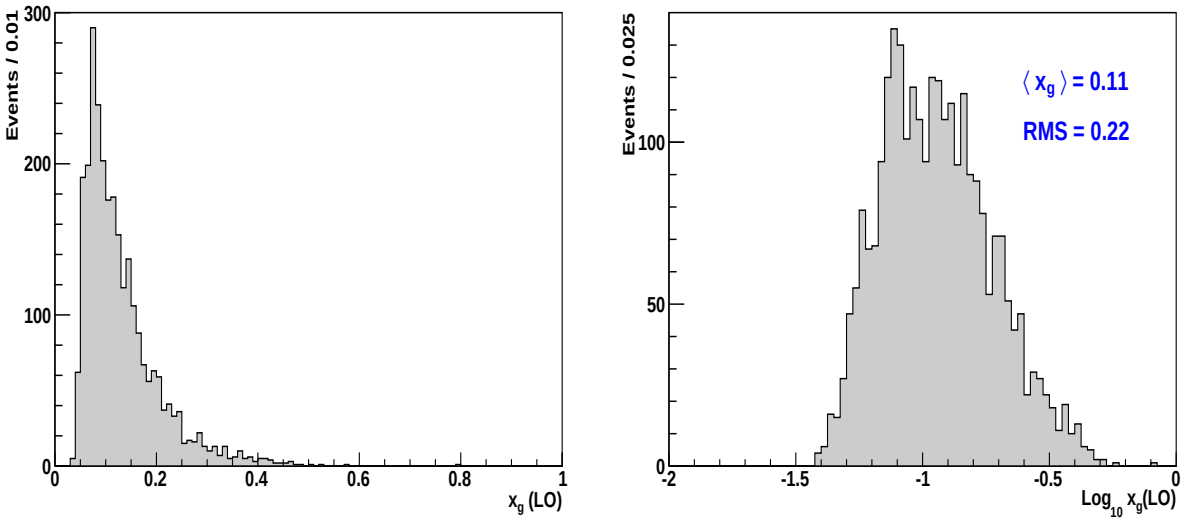

Figure 8.1: Distribution of x_g, obtained in the LO approximation, in linear (left) and logarithmic (right) scales. The latter is much more symmetric and therefore it is suited for the estimation of the x_g interval.

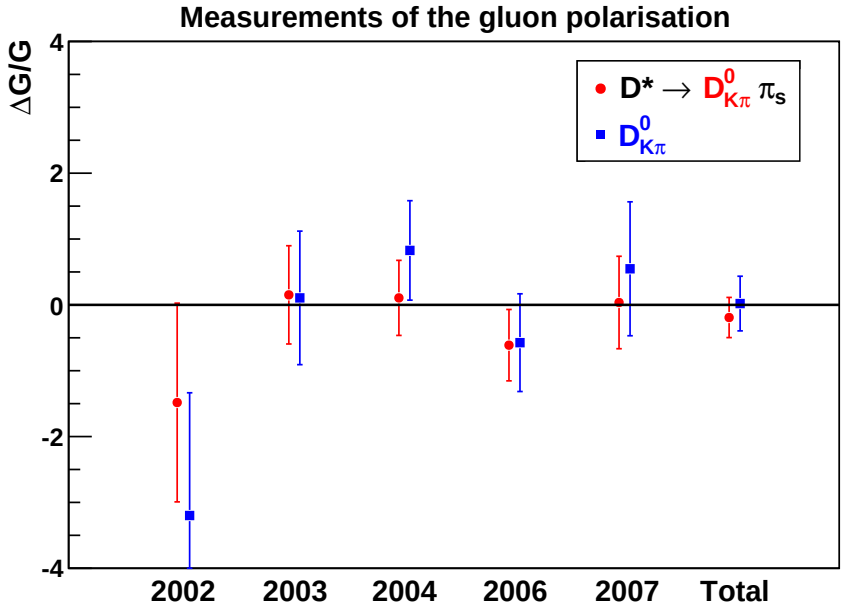

Figure 8.2: Comparison among the ΔG/G results, year by year, obtained from the main channels of analysis ($D^*_{K\pi}$ and $D^0_{K\pi}$). Only the statistical error is quoted.

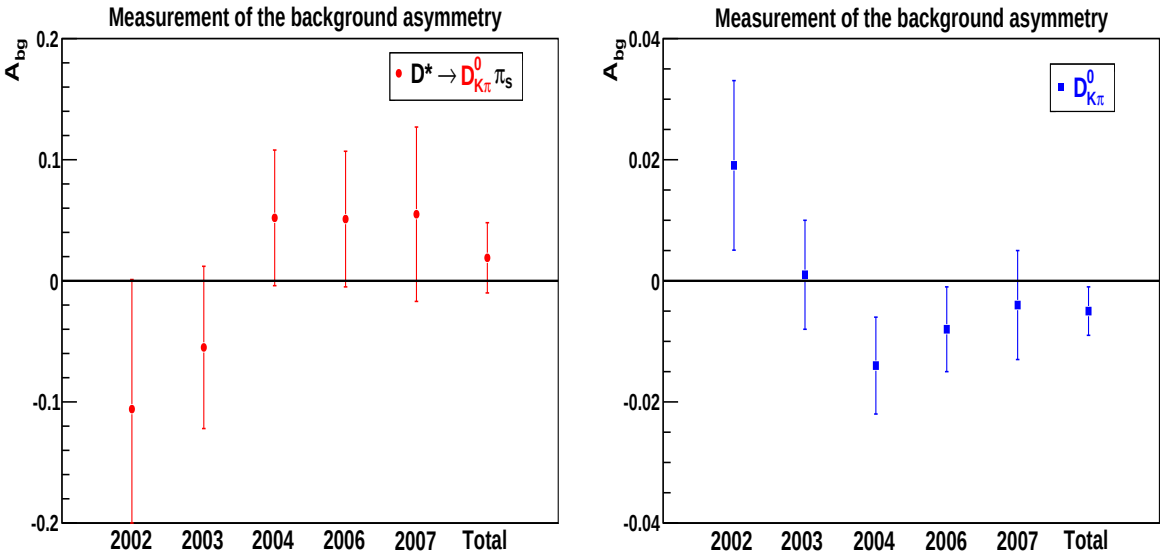

Figure 8.3: Summary of the A_{bg} results obtained from the $D^*_{K\pi}$ (left) and $D^0_{K\pi}$ (right) channels. Note that these background asymmetries are simultaneously extracted with $\Delta G/G$ for each week of data. No significant deviations from zero are found, as attested by the illustrated averaged results.

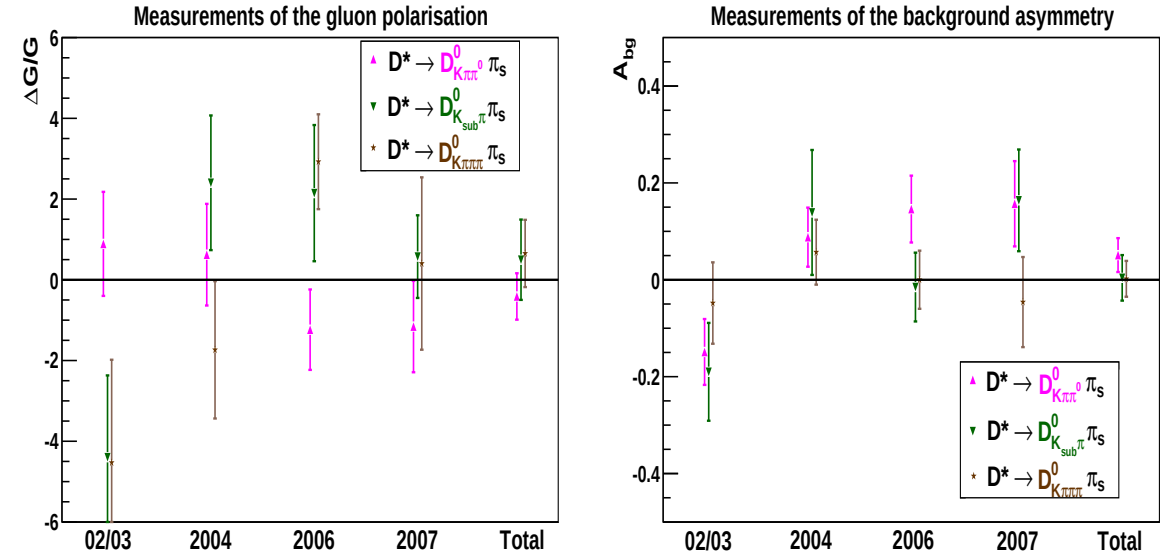

Figure 8.4: Comparison of the $\Delta G/G$ (left) and A_{bg} (right) results obtained from the low purity channels of analysis ($D^*_{K\pi\pi^0}$, $D^*_{K_{sub}\pi}$ and $D^*_{K\pi\pi\pi}$).

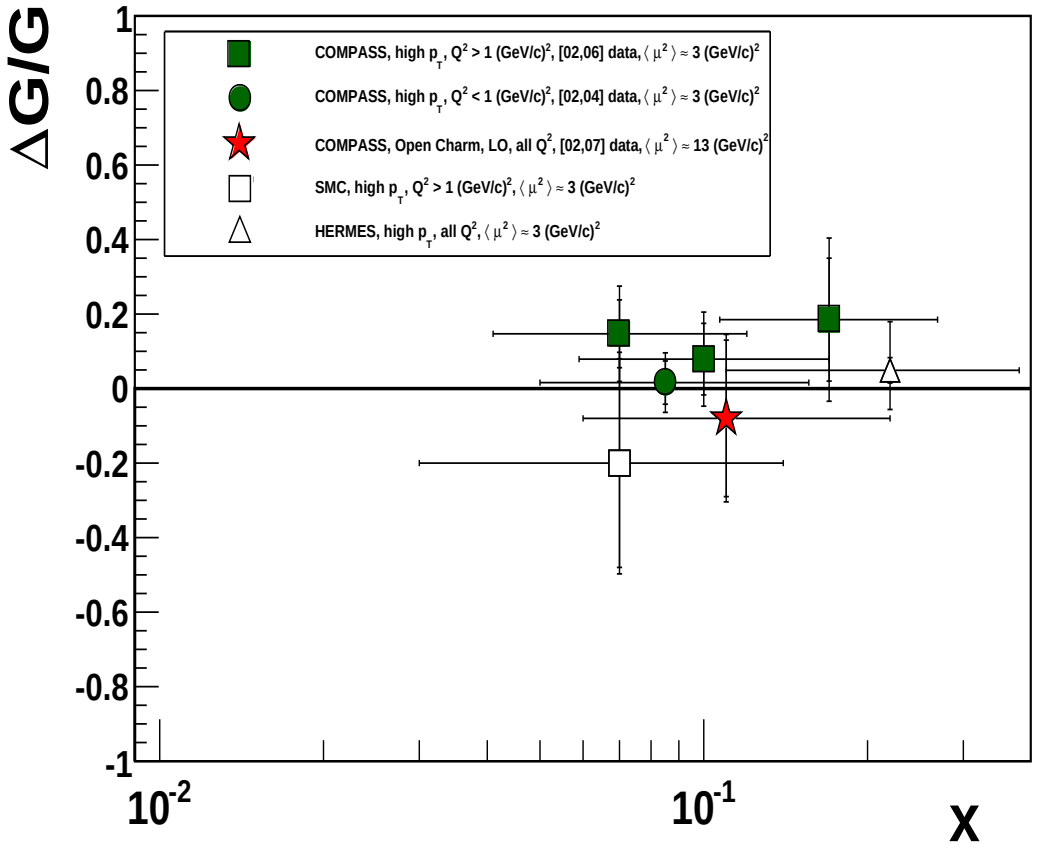

Figure 8.5: Summary of the world measurements on $\langle \Delta G/G \rangle$. Due to the large statistics available in the COMPASS high-p_T analysis, the result obtained for $Q^2 > 1$ (GeV/c)^2 is divided in three bins of x_g [43, 83]. The open-charm point is the only one obtained at a scale of $\langle \mu^2 \rangle = 13$ (GeV/c)^2. It represents also the only result for which the theoretical framework is well established.

8.2 Determination of the photon-nucleon asymmetries

The data described in Chapter 5 also allow us to determine the photon-nucleon asymmetry resulting from the D^0 production, $A^{\gamma^* N \to D^0 X} = A^{\mu N \to D^0 X}/D = (a_{LL} \times \Delta G/G)/D$. The experimental result of this asymmetry is used to constrain the values of $\Delta G(x_g)$, in a global analysis fit, because it does not depend on any QCD interpretation. To maximise the impact of $A^{\gamma^* N}$ in the QCD fits of $\Delta G(x_g)$, the asymmetry is extracted in bins of the transverse momentum of the D^0 with respect to the virtual-photon, $p_T^{D^0}$, and also in bins of the energy carried by the D^0 in the laboratory frame, E_{D^0}. There are two major criteria for the choice of the binnings. The first one has a pure statistical basis: the number of bins is maximised according to the available statistics, and they are chosen in such a way that the variation of a_{LL}/D is small (within each bin) when compared to the variation over the whole domain. The latter is important because averaging a_{LL}/D over the full kinematic range would result in a large dilution of the photon-nucleon asymmetry [1], caused by the large dispersion of a sign changing

[1] This fact is relevant only if we want to extract $\Delta G/G$ from $A^{\gamma^* N}$.

a_{LL} (cf. Fig. 7.29). But, above all, the most important requirement for the definition of those $(p_T^{D^0}, E_{D^0})$ bins is the minimisation of the asymmetry dependence on the experimental acceptance. If this is ensured, the asymmetries $A^{\gamma^* N}(\langle p_T^{D^0}\rangle, \langle E_{D^0}\rangle)$ can be used without major bias by the theorists outside of the COMPASS collaboration. In principle, $A^{\gamma^* N}$ also depends on the inclusive variables y and Q^2. These dependencies are accounted for by the depolarisation factor D, which is used in the new definition of the signal weight. In fact, this represents the only modification introduced in the method used to extract $\langle \Delta G/G\rangle$ (cf. section 6.1.2). The partonic asymmetry, a_{LL}, is replaced by the depolarisation factor D in the signal weight:

$$\omega_S = P_\mu f D \frac{S}{S+B} \tag{8.4}$$

The justification of the above ω_S is given as follows. By definition, the removal of a_{LL} from ω_S is equivalent to extract a muon-nucleon asymmetry: $A^{\mu N} = a_{LL} \times \Delta G/G$. However if we insert the depolarisation factor D into the signal weight, ω_S, we extract $A^{\gamma^* N}$ instead of $A^{\mu N}$ [2].

As explained before, the asymmetry $A^{\gamma^* N \to D^0 X}$ is extracted simultaneously with the background asymmetry for each $(p_T^{D^0}, E_{D^0})$ bin of the selected data. These values are obtained per channel and per year of data taking, except for the low purity channels with low statistics ($D^*_{K\pi\pi^0}$, $D^*_{K_{sub}\pi}$ and $D^*_{K\pi\pi\pi}$). In these 3 channels, the data taken in the years with the same target setup (2002-2004 and 2006-2007) are merged for some bins. Final results of $A^{\gamma^* N}$ for each D^0 decay mode are presented in Tables 8.5-8.7, together with the average values of relevant kinematic variables. In total, fifteen $(p_T^{D^0}, E_{D^0})$ bins are defined for the asymmetries extraction. As stated above, by construction, within these bins the dependence on the experimental acceptance is negligible. All averages are calculated using ω_S^2 as the weight. The justification for the use of ω_S^2 to calculate the averages of the kinematic variables is given as follows. Not considering any weights in the analysis implies the evaluation of those averages using the following analysing power [3]: $P_\mu f D S/(S+B)$. The use of the latter is needed to properly account for the small contribution of events with low signal purities (and vice-versa). Therefore, if an additional weight ω_S is considered, all averages are determined as:

$$\langle v\rangle = \frac{\sum_i \left(P_\mu f D \frac{S}{S+B}\right)_i^2 v_i}{\sum_i \left(P_\mu f D \frac{S}{S+B}\right)_i^2} \tag{8.5}$$

for a generic variable v and a weight $\omega_S = P_\mu f D S/(S+B)$.

Finaly, the extraction of the gluon polarisation, from each $A^{\gamma^* N}$ measurement (see Tables 8.5-8.7), is performed by using the equation 8.6 (true at LO):

$$\left\langle \frac{\Delta G}{G} \right\rangle (\langle p_T^{D^0}\rangle, \langle E_{D^0}\rangle) = \frac{A^{\gamma^* N}(\langle p_T^{D^0}\rangle, \langle E_{D^0}\rangle)}{\langle a_{LL}/D\rangle (\langle p_T^{D^0}\rangle, \langle E_{D^0}\rangle)} \tag{8.6}$$

By combining all the fifteen $\Delta G/G$ $(\langle p_T^{D^0}\rangle, \langle E_{D^0}\rangle)$ results we obtain a value for the gluon polarisation corresponding to each D^0 decay mode. The only requirement is the knowledge of $\langle a_{LL}/D\rangle$ for each $(p_T^{D^0}, E_{D^0})$ bin. All these quantities are determined from the data using

[2] Note that $A^{\mu N} = D \times A^{\gamma^* N}$.

[3] Apart from the target polarisation P_t (time-dependent variable), this factor corresponds to the variable β_S which is defined in eq. 6.11. This important factor relates the number of D^0 mesons to the gluon polarisation.

eq. 2.35 (with R = 0), eqs. 2.87-2.93 (at LO-QCD) and using also the procedure described in section 7.6. The resulting average values of a_{LL}/D are shown in Tab. 8.9. The corresponding average values at NLO are also presented and they will be discussed in section 8.3. The stability of the $\Delta G/G$ results obtained from $A^{\gamma^* N}$ can be verified by comparing them with the ones resulting from the full weighted analysis (summarised in Tab. 8.1). The results of both methods are presented in Tab. 8.3[4].

Channels	$\langle \Delta G/G \rangle$	
	Full weighted analysis	$\mathbf{A^{\gamma^* N}}$ **in bins of** $(\mathbf{p}_T^{D^0}, \mathbf{E}_{D^0})$
$\mathbf{D^* \rightarrow D^0_{K\pi}\pi_s}$	-0.192 ± 0.305	-0.252 ± 0.319
$\mathbf{D^* \rightarrow D^0_{K\pi\pi^0}\pi_s}$	-0.414 ± 0.575	-0.370 ± 0.643
$\mathbf{D^* \rightarrow D^0_{K_{sub}\pi}\pi_s}$	$+0.497 \pm 0.995$	$+0.565 \pm 1.057$
$\mathbf{D^* \rightarrow D^0_{K\pi\pi\pi}\pi_s}$	$+0.628 \pm 0.833$	$+0.584 \pm 0.853$
Untagged $\mathbf{D^0_{K\pi}}$	$+0.020 \pm 0.415$	-0.040 ± 0.446

Table 8.3: $\langle \Delta G/G \rangle$ results obtained from the two applied method.

The judgement whether the two measurements are compatible, for each channel quoted in Tab. 8.3, is obtained from the difference of their mean value and from the error of the difference:

Channels	**Difference in** $\langle \Delta G/G \rangle$	**Error**
$\mathbf{D^* \rightarrow D^0_{K\pi}\pi_s}$	-0.060	$\sqrt{0.319^2 - 0.305^2} = 0.093$
$\mathbf{D^* \rightarrow D^0_{K\pi\pi^0}\pi_s}$	$+0.047$	$\sqrt{0.643^2 - 0.575^2} = 0.288$
$\mathbf{D^* \rightarrow D^0_{K_{sub}\pi}\pi_s}$	$+0.068$	$\sqrt{1.057^2 - 0.995^2} = 0.357$
$\mathbf{D^* \rightarrow D^0_{K\pi\pi\pi}\pi_s}$	-0.044	$\sqrt{0.853^2 - 0.833^2} = 0.184$
Untagged $\mathbf{D^0_{K\pi}}$	-0.060	$\sqrt{0.446^2 - 0.415^2} = 0.163$

Table 8.4: Comparison of the $\langle \Delta G/G \rangle$ results shown in Tab. 8.3.

From Tables 8.3 and 8.4 we see that both methods lead to a compatible result, with a minimum loss in the precision when using the asymmetries. The slightly bigger statistical error corresponding to the latter method is justified by the absence of a_{LL} inside the signal weight: the statistical benefits introduced by a variable that shows a large dispersion are lost.

[4]Note that for this comparison the asymmetries obtained from the individual channels $D^*_{K\pi}$, $D^*_{K_{sub}\pi}$ and $D^0_{K\pi}$ are used. However, since all these channels share the same D^0 decay mode only their combined asymmetries are shown in Tab. 8.5.

Bin limits		$A^{\gamma^* N}$	$\langle y \rangle$	$\langle Q^2 \rangle$	$\langle p_T^{D^0} \rangle$	$\langle E_{D^0} \rangle$	$\langle D \rangle$
$p_T^{D^0}$ (GeV/c)	E_{D^0} (GeV)			(GeV/c)^2	(GeV/c)	(GeV)	
0-0.3	0-30	-0.90 ± 0.63	0.50	0.46	0.19	24.3	0.62
0-0.3	30-50	-0.19 ± 0.48	0.60	0.69	0.20	39.1	0.74
0-0.3	> 50	$+0.07 \pm 0.68$	0.69	1.17	0.20	59.2	0.84
0.3-0.7	0-30	-0.18 ± 0.37	0.51	0.47	0.51	24.6	0.63
0.3-0.7	30-50	$+0.10 \pm 0.26$	0.60	0.62	0.51	39.5	0.75
0.3-0.7	> 50	-0.04 ± 0.36	0.69	0.73	0.51	59.0	0.83
0.7-1	0-30	-0.42 ± 0.44	0.50	0.45	0.85	24.7	0.62
0.7-1	30-50	-0.36 ± 0.29	0.61	0.60	0.85	39.2	0.75
0.7-1	> 50	$+1.49 \pm 0.42$	0.69	0.76	0.84	58.6	0.83
1-1.5	0-30	-0.30 ± 0.35	0.54	0.41	1.23	25.3	0.66
1-1.5	30-50	$+0.13 \pm 0.23$	0.64	0.55	1.24	39.2	0.77
1-1.5	> 50	-0.20 ± 0.33	0.71	0.73	1.24	58.3	0.85
> 1.5	0-30	$+0.38 \pm 0.49$	0.56	0.47	1.84	25.6	0.69
> 1.5	30-50	-0.00 ± 0.25	0.65	0.70	1.92	39.9	0.79
> 1.5	> 50	$+0.36 \pm 0.33$	0.69	0.60	1.95	59.9	0.86

Table 8.5: The asymmetries $A^{\gamma^* N}$ for the $D^*_{K\pi}$, $D^*_{K_{sub}\pi}$ and $D^0_{K\pi}$ combined samples in bins of ($p_T^{D^0}$, E_{D^0}), together with the weighted averages of several kinematic variables (weighted with ω_S^2). Only the statistical error is given.

Bin limits		$A^{\gamma^* N}$	$\langle y \rangle$	$\langle Q^2 \rangle$	$\langle p_T^{D^0} \rangle$	$\langle E_{D^0} \rangle$	$\langle D \rangle$
$p_T^{D^0}$ (GeV/c)	E_{D^0} (GeV)			(GeV/c)^2	(GeV/c)	(GeV)	
0-0.3	0-30	-0.63 ± 1.29	0.52	0.75	0.19	24.4	0.65
0-0.3	30-50	$+0.27 \pm 1.17$	0.67	0.65	0.20	38.8	0.81
0-0.3	> 50	-2.55 ± 2.00	0.72	1.12	0.19	59.3	0.86
0.3-0.7	0-30	-0.24 ± 0.80	0.53	0.51	0.52	24.3	0.65
0.3-0.7	30-50	$+0.49 \pm 0.69$	0.65	0.65	0.51	39.0	0.79
0.3-0.7	> 50	-1.28 ± 1.03	0.72	0.77	0.51	59.1	0.86
0.7-1	0-30	$+0.55 \pm 0.95$	0.53	0.41	0.84	24.6	0.65
0.7-1	30-50	-0.53 ± 0.76	0.63	0.53	0.86	39.4	0.77
0.7-1	> 50	-0.17 ± 1.00	0.73	0.80	0.85	58.2	0.88
1-1.5	0-30	$+1.35 \pm 0.86$	0.54	0.38	1.24	25.4	0.67
1-1.5	30-50	-0.11 ± 0.51	0.64	0.59	1.25	39.6	0.78
1-1.5	> 50	-0.05 ± 0.78	0.74	0.62	1.25	58.3	0.88
> 1.5	0-30	-0.19 ± 1.14	0.56	0.52	1.80	25.7	0.70
> 1.5	30-50	-0.23 ± 0.51	0.66	0.66	1.88	40.0	0.80
> 1.5	> 50	$+0.26 \pm 0.90$	0.74	0.88	1.92	57.3	0.88

Table 8.6: The asymmetries $A^{\gamma^* N}$ for the $D^*_{K\pi\pi^0}$ sample in bins of ($p_T^{D^0}$, E_{D^0}) together with the weighted averages of several kinematic variables (weighted with ω_S^2). Only the statistical error is given.

Bin limits		$A^{\gamma^* N}$	$\langle y \rangle$	$\langle Q^2 \rangle$	$\langle p_T^{D^0} \rangle$	$\langle E_{D^0} \rangle$	$\langle D \rangle$
$p_T^{D^0}$ (GeV/c)	E_{D^0} (GeV)			(GeV/c)^2	(GeV/c)	(GeV)	
0-0.3	0-30	$+7.03 \pm 4.74$	0.46	0.38	0.22	27.7	0.58
0-0.3	30-50	-2.05 ± 1.10	0.60	0.72	0.20	40.6	0.74
0-0.3	> 50	$+0.17 \pm 1.83$	0.69	0.88	0.20	59.1	0.84
0.3-0.7	0-30	-0.59 ± 1.74	0.52	0.31	0.53	27.8	0.71
0.3-0.7	30-50	$+1.00 \pm 0.54$	0.61	0.44	0.52	39.7	0.80
0.3-0.7	> 50	-1.75 ± 0.84	0.68	0.70	0.51	60.2	0.84
0.7-1	0-30	$+2.91 \pm 2.61$	0.45	0.26	0.84	27.7	0.61
0.7-1	30-50	$+1.42 \pm 0.57$	0.64	0.57	0.85	40.9	0.81
0.7-1	> 50	$+1.69 \pm 0.81$	0.69	0.58	0.86	60.9	0.84
1-1.5	0-30	-1.89 ± 2.64	0.46	0.31	1.22	27.7	0.64
1-1.5	30-50	-0.45 ± 0.51	0.63	0.58	1.23	41.1	0.79
1-1.5	> 50	$+1.06 \pm 0.66$	0.71	0.77	1.24	61.8	0.86
> 1.5	0-30	$+1.64 \pm 3.52$	0.46	0.40	1.84	28.1	0.72
> 1.5	30-50	$+0.44 \pm 0.68$	0.65	0.75	1.95	42.2	0.78
> 1.5	> 50	$+0.08 \pm 0.63$	0.74	0.77	2.03	64.4	0.88

Table 8.7: The asymmetries $A^{\gamma^* N}$ for the $D^*_{K\pi\pi\pi}$ sample in bins of ($p_T^{D^0}$, E_{D^0}) together with the weighted averages of several kinematic variables. Only the statistical error is given.

Bin limits		$\langle x_g^{NLO} \rangle$		
$p_T^{D^0}$(GeV/c)	E_{D^0}(GeV)	$D^*_{k\pi}$, $D^*_{k_{sub}\pi}$ and $D^0_{k\pi}$	$D^*_{k\pi\pi^0}$	$D^*_{k\pi\pi\pi}$
0-0.3	0-30	-9.48	0.47	0.41
0-0.3	30-50	0.56	0.44	0.51
0-0.3	> 50	0.34	0.33	0.36
0.3-0.7	0-30	0.48	0.33	0.45
0.3-0.7	30-50	0.30	0.27	0.31
0.3-0.7	> 50	0.23	0.23	0.26
0.7-1	0-30	0.29	0.27	0.34
0.7-1	30-50	0.25	0.25	0.26
0.7-1	> 50	0.23	0.22	0.23
1-1.5	0-30	0.29	0.28	0.28
1-1.5	30-50	0.25	0.26	0.26
1-1.5	> 50	0.24	0.24	0.24
> 1.5	0-30	0.33	0.32	0.34
> 1.5	$30 - 50$	0.31	0.30	0.30
> 1.5	> 50	0.27	0.29	0.28

Table 8.8: The average of x_g obtained at NLO in bins of ($p_T^{D^0}$, E_{D^0}) and for each D^0 decay mode. The weighted average of x_g is computed using as a weight: $\omega = \left(a_{LL}^{(g)} \times D\right)$.

Bin limits		**Photon-gluon asymmetry**								
		$D^*_{k\pi}$, $D^*_{k_{sub}\pi}$ and $D^0_{k\pi}$			$D^*_{k\pi\pi^0}$			$D^*_{k\pi\pi\pi}$		
$p_T^{D^0}$	E_{D^0}	LO	NLO		LO	NLO		LO	NLO	
(GeV/c)	(GeV)	$\left\langle \frac{a_{LL}^{(g)}}{D} \right\rangle$	$\left\langle \frac{a_{LL}^{(g)}}{D} \right\rangle$	$\langle A_{corr} \rangle$	$\left\langle \frac{a_{LL}^{(g)}}{D} \right\rangle$	$\left\langle \frac{a_{LL}^{(g)}}{D} \right\rangle$	$\langle A_{corr} \rangle$	$\left\langle \frac{a_{LL}^{(g)}}{D} \right\rangle$	$\left\langle \frac{a_{LL}^{(g)}}{D} \right\rangle$	$\langle A_{corr} \rangle$
0-0.3	0-30	0.65	0.00	0.01	0.62	-0.11	0.01	0.37	-0.09	0.01
0-0.3	30-50	0.68	-0.06	0.01	0.65	-0.08	0.01	0.47	-0.08	0.01
0-0.3	> 50	0.76	-0.12	0.02	0.74	-0.11	0.02	0.62	-0.09	0.01
0.3-0.7	0-30	0.46	-0.08	0.01	0.42	-0.17	0.01	0.27	-0.10	0.02
0.3-0.7	30-50	0.50	-0.19	0.02	0.46	-0.23	0.02	0.33	-0.20	0.02
0.3-0.7	> 50	0.56	-0.22	0.02	0.53	-0.18	0.02	0.44	-0.21	0.02
0.7-1	0-30	0.26	-0.26	0.01	0.19	-0.29	0.02	0.15	-0.19	0.01
0.7-1	30-50	0.26	-0.29	0.01	0.21	-0.32	0.02	0.20	-0.31	0.02
0.7-1	> 50	0.29	-0.33	0.03	0.26	-0.36	0.03	0.25	-0.32	0.03
1-1.5	0-30	0.00	-0.35	0.01	-0.06	-0.40	0.02	0.01	-0.36	0.02
1-1.5	30-50	0.01	-0.40	0.02	-0.05	-0.44	0.03	0.03	-0.41	0.02
1-1.5	> 50	0.05	-0.43	0.03	-0.02	-0.42	0.04	0.07	-0.45	0.03
> 1.5	0-30	-0.23	-0.49	0.02	-0.29	-0.52	0.02	-0.19	-0.49	0.03
> 1.5	$30 - 50$	-0.26	-0.53	0.03	-0.31	-0.50	0.04	-0.18	-0.54	0.03
> 1.5	> 50	-0.27	-0.53	0.04	-0.31	-0.49	0.05	-0.19	-0.54	0.05

Table 8.9: The photon-gluon asymmetries, a_{LL}/D, in bins of ($p_T^{D^0}$, E_{D^0}) and for each D^0 decay mode used in the analysis. The values at LO use a_{LL}/D from real data events, obtained from a Neural Network parameterisation, and thus they are weighted with ω_S^2. In the NLO approximation, the presented averages are obtained from a full Monte Carlo chain and therefore they are weighted only with the quantity D^2.

8.3 Next-to-Leading Order results for $\Delta G/G$

In this section, an alternative method to obtain $\langle \Delta G/G \rangle$ at NLO is presented. The simultaneous extraction of $\langle \Delta G/G \rangle$ and $\langle A_{bg} \rangle$ can be done using a similar method to the one used for the LO analysis. The complete formalism is described in section 6.2. To access the gluon polarisation, at NLO, the additional requirements are the knowledge of the inclusive asymmetry A_1, $a_{LL}^{(g)}$ and $a_{LL}^{(q)}$ for each real data event. Like for the LO approximation this can be achieved by a Neural Network parameterisation. However, as it was already discussed in section 7.6.2, the correlation between the generated and the parameterised a_{LL}/D turned out to be much smaller than in the LO analysis. This is obvious, since the partonic kinematics is much more complicated at NLO (*e*.g., there are 3 particles in the final state of the real gluon emission processes). Consequently, the expected gain in the precision of $\Delta G/G$ when using the full weighted method (cf. section 6.2) is lower at NLO. Due to this fact, the photon-nucleon asymmetries $A^{\gamma^* N}(\langle p_T^{D^0} \rangle, \langle E_{D^0} \rangle)$ are used to obtain the gluon polarisation result at NLO. To accomplish that, we just need to use the following NLO interpretation of $A^{\gamma^* N}$:

$$A^{\gamma^* N} = \left\langle \frac{\Delta G}{G} \right\rangle \left\langle \frac{a_{LL}^{(g)}}{D} \right\rangle + \langle A_{corr} \rangle \tag{8.7}$$

where

$$A_{corr} = \left\langle A_1^d \frac{a_{LL}^{(q,d)}}{D} + \beta^p A_1^p \frac{a_{LL}^{(q,p)}}{D} \right\rangle \tag{8.8}$$

In addition to the diagrams shown in Fig. 2.14, the quantity $a_{LL}^{(g)}/D$ contains also contributions from the processes illustrated in Fig. 2.20. The correction term, A_{corr}, is needed to account for the physical background which is introduced by the processes shown in Fig. 2.19. Since this background originates from interactions with polarised quarks, the soft part of the muon-nucleon scattering is replaced by the inclusive asymmetry A_1 (instead of $\Delta G/G$). Two terms are considered in eq. 8.8 due to the two types of nuclear targets used in this analysis: deuterons (2002-2006 data) and protons (2007 data). Therefore, the respective asymmetries A_1^d and A_1^p are needed. The quantity ζ^p accounts for the **F**igure **O**f **M**erit (FOM) of the proton data. The weight of each target material in the whole data is:

$$\zeta^d = \left(\frac{\mathrm{FOM}^d}{\mathrm{FOM}^d + \mathrm{FOM}^p} \right) = 0.775 \quad \text{and} \quad \zeta^p = \left(\frac{\mathrm{FOM}^p}{\mathrm{FOM}^d + \mathrm{FOM}^p} \right) = 0.225$$

The quantity ζ^d does not appear explicitly in eq. 8.8 because it is hidden inside the asymmetry $a_{LL}^{(q,d)}/D$. Indeed, these photon-gluon and photon-quark asymmetries do not have the same interpretation as a_{LL}/D at LO. To see why, we must look to the following definitions of the polarised and unpolarised cross-sections (in the NLO approximation):

$$\begin{aligned} \sigma_{\mu N} &= \left(G \otimes \hat{\sigma}_{\mu g} + \zeta^d \sum_q q \otimes \left[\hat{\sigma}_{\mu c} + \frac{5}{18} \hat{\sigma}_{\mu q} \right] + \zeta^p \left[\sum_q q \otimes \hat{\sigma}_{\mu c} + \sum_q e_q^2 q \otimes \hat{\sigma}_{\mu q} \right] \right) \otimes F \\ &= \left(G \otimes \hat{\sigma}_{\mu g} + \sum_q q \otimes \hat{\sigma}_1 + \zeta^p \sum_q e_q^2 q \otimes \hat{\sigma}_{\mu q} \right) \otimes F \end{aligned} \tag{8.9}$$

$$\Delta\sigma_{\mu N} = \left(\Delta G \otimes \Delta\hat{\sigma}_{\mu g} + \sum_q \Delta q \otimes \Delta\hat{\sigma}_1 + \zeta^p \sum_q e_q^2 \Delta q \otimes \Delta\hat{\sigma}_{\mu q} \right) \otimes F \tag{8.10}$$

using

$$\hat{\sigma}_{\mu g} = \hat{\sigma}_{\mu g}^{0\ (PGF)} + \hat{\sigma}_{\mu g}^{1\ (PGF)} \qquad \text{and} \qquad \hat{\sigma}_1 = \hat{\sigma}_{\mu c} + \frac{5}{18}\zeta^d \hat{\sigma}_{\mu q} \tag{8.11}$$

where c stands for the charm quark (cf. (a) and (b) in Fig. 2.19), q represents any of the light-quarks (diagrams (c) and (d) in Fig. 2.19) and F is the fragmentation function. Therefore, the muon-nucleon asymmetry can be written as:

$$\begin{aligned} A_{c\bar{c}}^{\mu N} &= \frac{\left(\frac{\Delta G}{G} G \otimes \Delta\hat{\sigma}_{\mu g} + A_1^d \sum_q q \otimes \Delta\hat{\sigma}_1 + A_1^p \zeta^p \sum_q e_q^2 q \otimes \Delta\hat{\sigma}_{\mu q} \right) \otimes F}{\sigma_{\mu N}} \\ &= \left\langle \frac{\Delta G}{G} a_{LL}^{(g)} + A_1^d a_{LL}^{(q,d)} + \zeta^p A_1^p a_{LL}^{(q,p)} \right\rangle \\ &= \left\langle \frac{\Delta G}{G} \right\rangle \left\langle a_{LL}^{(g)} \right\rangle + \left\langle A_1^d a_{LL}^{(q,d)} + \zeta^p A_1^p a_{LL}^{(q,p)} \right\rangle \end{aligned} \tag{8.12}$$

where

$$a_{LL}^{(g)} = \frac{G\Delta\hat{\sigma}_{\mu g}}{\hat{\sigma}} \qquad a_{LL}^{(q,p)} = \frac{\sum_q e_q^2 q \Delta\hat{\sigma}_{\mu q}}{\hat{\sigma}} \qquad a_{LL}^{(q,d)} = \frac{\sum_q q \Delta\hat{\sigma}_1}{\hat{\sigma}} \tag{8.13}$$

and

$$\hat{\sigma} = G\hat{\sigma}_{\mu g} + \sum_q q\hat{\sigma}_1 + \zeta^p \sum_q e_q^2 q \hat{\sigma}_{\mu q} \tag{8.14}$$

Finally, using the definition of the photon-nucleon asymmetry, $A^{\gamma^* N} = A^{\mu N}/D$, we reproduce eqs. 8.7-8.8. From the latter we can estimate the gluon polarisation for each $(p_T^{D^0}, E_{D^0})$ bin. The ingredients needed ($A^{\gamma^* N}$, $a_{LL}^{(g)}/D$ and A_{corr}) are all available, per bin, in Tables 8.5-8.7 and in Tab. 8.9. All quantities shown in Tab. 8.9 are weighted only with D^2 because they are pure Monte Carlo quantities ($S/(S+B) = 1$). To obtain A_{corr} the following two parameterisations are used:

$$A_1^d = x^{1.24} \qquad \text{and} \qquad A_1^p = x^{0.67} \tag{8.15}$$

These parameterisations are determined from a fit to the world data on the inclusive asymmetries A_1^d and A_1^p (see Refs.[5, 32]).

Summary of the $\langle \Delta G/G \rangle$ results:

The $\Delta G/G$ measurements at NLO, obtained from eq. 8.7, are shown in the last column of Tab. 8.10 [5]. The corresponding LO results are also presented for comparison. We see that the LO

[5] Note that only the combined asymmetries of the $D^*_{K\pi}$, $D^*_{K_{sub}\pi}$ and $D^0_{K\pi}$ channels are shown in Tab. 8.5. However, to obtain the results shown in Tab. 8.10 the asymmetries $A^{\gamma^* N}$ are considered separately.

Channels	$\langle \Delta G/G \rangle$		
	LO		NLO
	Full weighted analysis	$A^{\gamma^* N}$ in bins	$A^{\gamma^* N}$ in bins
$D^* \rightarrow D^0_{K\pi}\pi_s$	-0.19 ± 0.31	-0.25 ± 0.32	$+0.04 \pm 0.32$
$D^* \rightarrow D^0_{K\pi\pi^0}\pi_s$	-0.41 ± 0.58	-0.37 ± 0.64	$+0.12 \pm 0.55$
$D^* \rightarrow D^0_{K_{sub}\pi}\pi_s$	$+0.50 \pm 1.00$	$+0.57 \pm 1.06$	-0.34 ± 1.21
$D^* \rightarrow D^0_{K\pi\pi\pi}\pi_s$	$+0.63 \pm 0.83$	$+0.58 \pm 0.85$	-0.96 ± 0.56
Untagged $D^0_{K\pi}$	$+0.02 \pm 0.42$	-0.04 ± 0.45	-0.34 ± 0.41
Total	-0.08 ± 0.21	-0.11 ± 0.23	-0.20 ± 0.21

Table 8.10: Summary of all the $\langle \Delta G/G \rangle$ results in these analyses. The values in the last two columns represent the weighted means of the fifteen $\Delta G/G$ results in bins of $(p_T^{D^0}, E_{D^0})$.

extraction of $\Delta G/G$ from $A^{\gamma^* N}$ leads to a compatible result with the one obtained from the full weighted analysis, with a minimum loss of precision. Therefore, the NLO determination of $\Delta G/G$ from $A^{\gamma^* N}$ is well justified. It can also be seen that the NLO results have a different sign when compared to the LO ones. The exception is the untagged D^0 channel for which the $\Delta G/G$ result is very close to zero (the LO value fluctuates in the same direction as the NLO value). The justification for this sign change is given by the different muon-gluon asymmetry distributions at LO and at NLO (cf. Fig. 7.30). At NLO, the distribution peaks on the negative side of a_{LL}, contrary to the LO one. Since these partonic asymmetries are given as functions of $p_T^{D^0}$ and E_{D^0}, a two-dimensional distribution of a_{LL} is also presented in Figs. 8.6-8.7. The $p_T^{D^0}$ distribution is very different in the two analyses (the average p_T is higher at NLO - cf. also Fig. 7.30). One can also observe that within each bin the muon-gluon asymmetry is approximately constant.

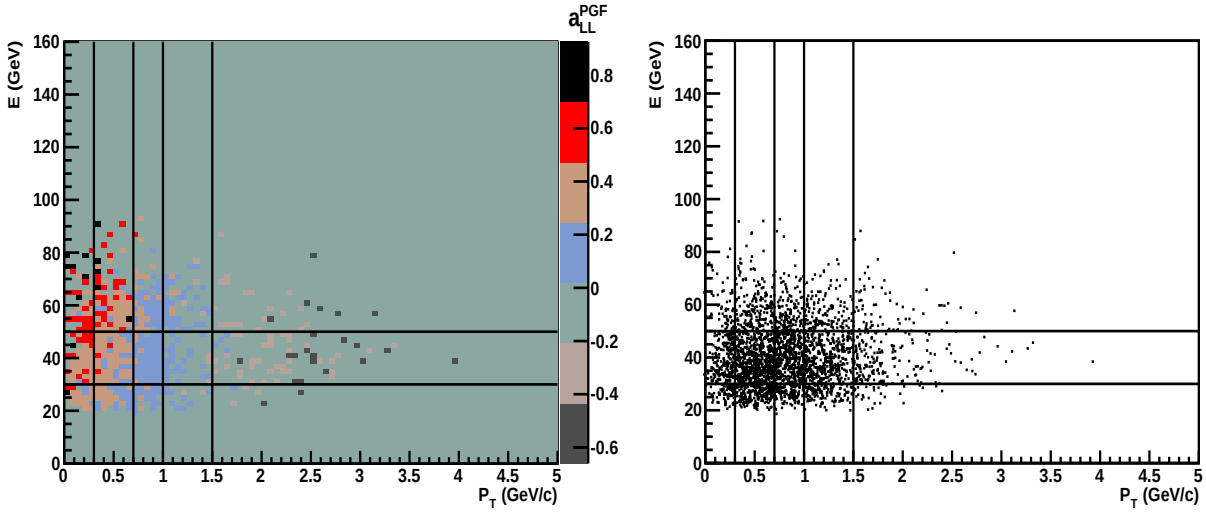

Figure 8.6: Distribution of a_{LL} in bins of ($p_T^{D^0}$, E_{D^0}) (left) and the corresponding AROMA events (right), in the LO-QCD approximation. Lines define the bins used in the analysis (see section 8.2 for details).

The final result on the gluon polarisation, at NLO, is obtained from the combination of the five values shown in Tab. 8.10 and amounts to:

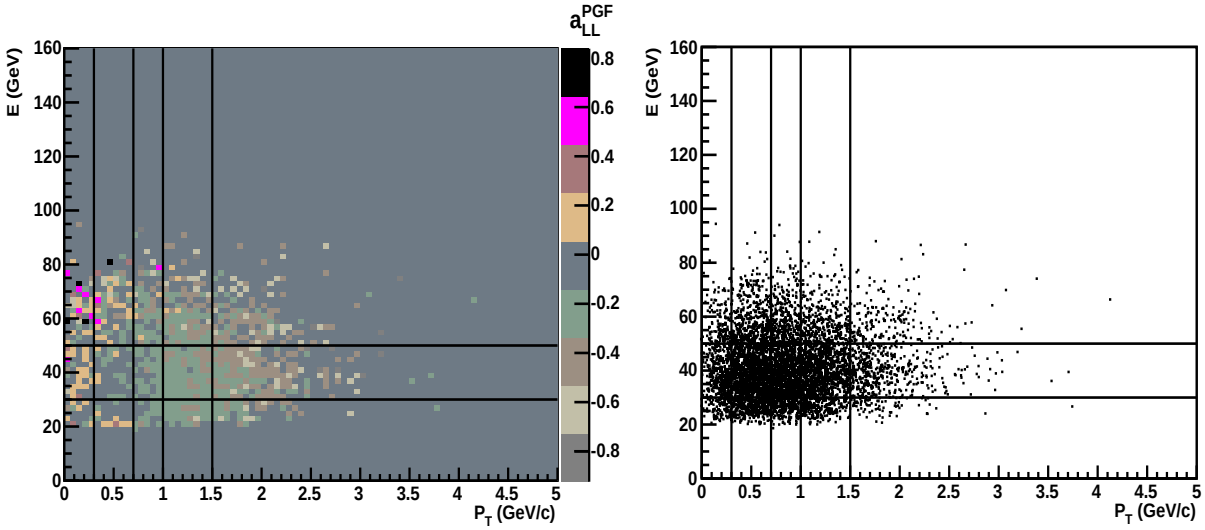

Figure 8.7: Distribution of a_{LL} in bins of ($p_T^{D^0}$, E_{D^0}) (left) and the corresponding AROMA events (right), in the NLO-QCD approximation. Lines define the bins used in the analysis (see section 8.2 for details).

$$\left\langle \frac{\Delta G}{G} \right\rangle^{\text{NLO}} = -0.20 \pm 0.21 \text{ (stat.)} \pm 0.09 \text{ (syst.)} \tag{8.16}$$

As for the LO result, the systematic error is discussed in Chapter 9. The NLO calculations have also led to the important observation that the x_g average value of (at which the gluon polarisation is probed) is dependent on the sign of a_{LL} and, consequently, on the QCD approximation used in the analysis [6]. Moreover, due to the real gluon emissions in the NLO approximation, the energy in the photon-gluon centre-of-mass system is higher than at LO. These two effects lead to a higher x_g average value at which the gluon polarisation is determined. The individual results obtained per each bin and per decay-mode are presented in Tab. 8.8. The value of -9.48 is non-physical and results from a statistical fluctuation coming from averaging events with slightly negative and slightly positive values of a_{LL}. Nevertheless, at NLO, that particular ($p_T^{D^0}$, E_{D^0}) bin does not contribute to the final result of $\Delta G/G$. The reason for this lies on the zero value obtained for $a_{LL}^{(g)}/D$, which makes it impossible to estimate the gluon polarisation. The final value of $\langle x_g \rangle$ is determined by the weighted average of all bins, using the statistical error of $\Delta G/G$ as a weight:

$$\langle x_g \rangle_{\omega^2} = 0.28^{+0.19}_{-0.10} \qquad @\langle \mu^2 \rangle_{\omega^2} = 13 \text{ (GeV}/c)^2 \tag{8.17}$$

Again, as in the LO case, the limits defined by the above interval are determined from Fig. 8.8. Using eq. 8.3, we obtain the x_g domain corresponding to the present measurement: [0.18, 0.47]. The result given in eq. 8.16 is also shown in Fig. 8.9 together with the available NLO-QCD fits for $\Delta G/G$ (DSSV [84, 85], LSS [86] and COMPASS [87]). The open-charm point represents

[6] The general expression for $\langle x_g \rangle$ is given by eq. 6.40. Here, at NLO, we extract $\Delta G/G$ from $A^{\gamma^* N}$. Therefore, in eq. 6.40 we need to replace a_{LL} by a_{LL}/D, and as a weight we use the quantity D^2 (because x_g is a pure Monte Carlo quantity). As a result, the average of x_g is determined using the following global weight: $\omega^2 = a_{LL} \times D$.

the first direct measurement ever made for $\Delta G/G$ at the NLO approximation.

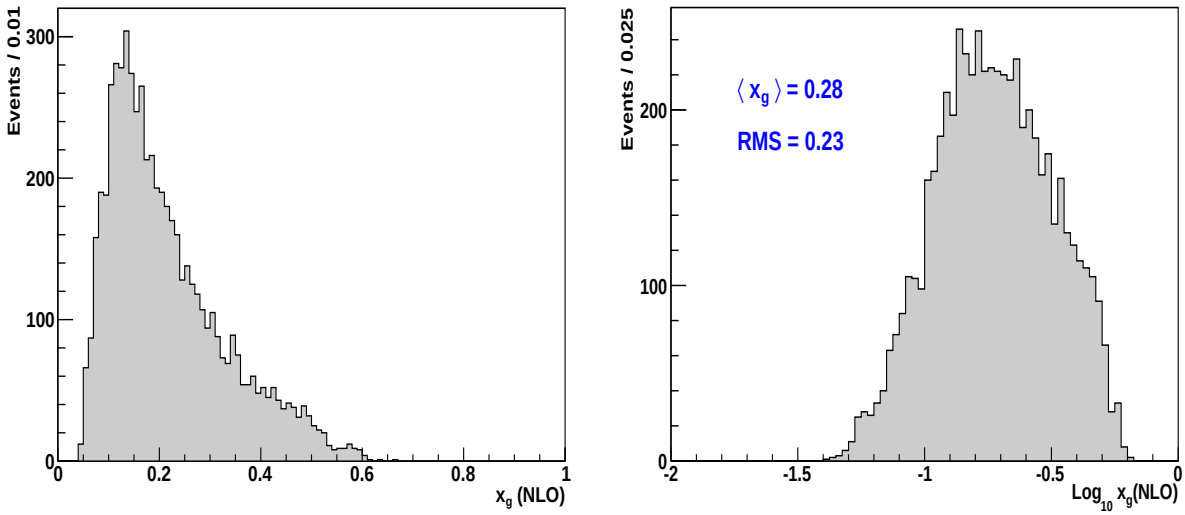

Figure 8.8: Distribution of x_g, obtained in the NLO approximation, in linear (left) and logarithmic (right) scales. The latter is much more symmetric and therefore it is suited for the estimation of the x_g interval.

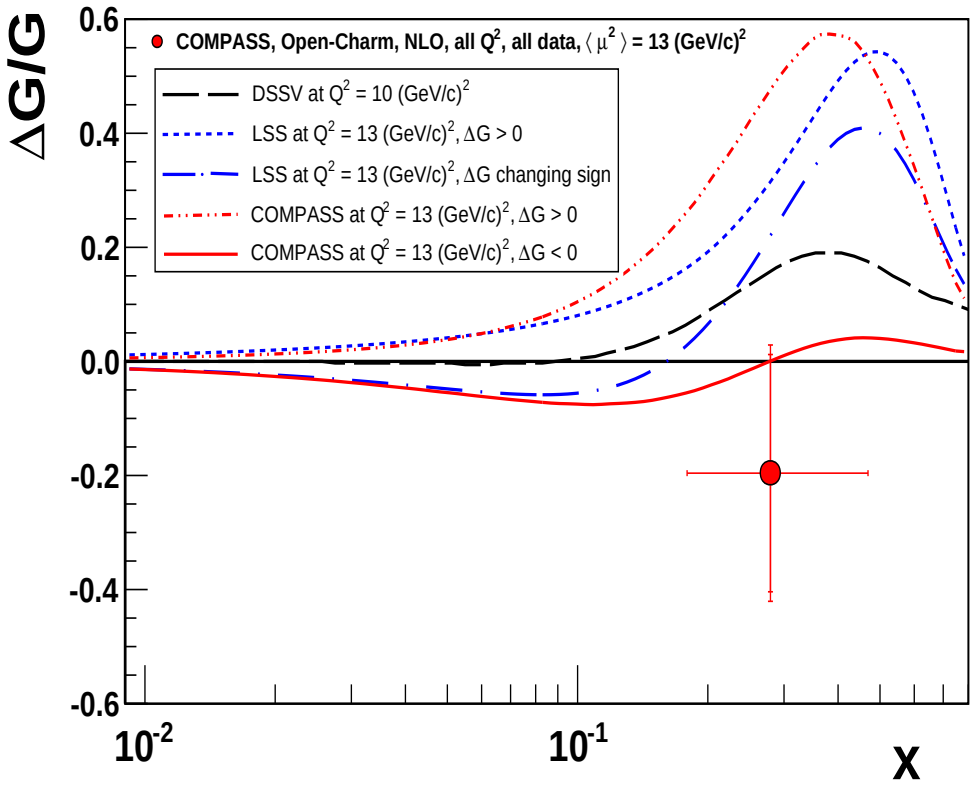

Figure 8.9: Result of the open-charm measurement using the NLO-QCD approximation. The illustrated fits are also obtained in the NLO approximation.

Chapter 9

Studies on the Systematic Error

The main contributions to the systematic error of $\langle \Delta G/G \rangle$ are listed in Table 9.1:

Source	$\delta\left(\langle \Delta G/G \rangle^{\mathbf{LO}}\right)$	$\delta\left(\langle \Delta G/G \rangle^{\mathbf{NLO}}\right)$
False Asymmetry	0.080	0.080
$S/(S+B)$	0.006	0.014
a_{LL}	0.008	0.036
Dilution Factor	0.002	0.004
Target Polarisation	0.004	0.010
Beam Polarisation	0.004	0.010
Total	0.081	0.090

Table 9.1: Systematic errors for the LO and the NLO analyses. Aside from the false asymmetries and the target polarisation, the remaining contributions enter in the signal weight used in the analysis (the extraction of ΔG/G is done exclusively based on the event weights). The total results are obtained by adding all the listed contributions in quadrature.

The experimental factors related to the beam and target polarisations, P_μ and P_t, are parameterised with a relative error of 5%, whereas the dilution factor f is parameterised with a relative error of 2% (cf. Chapter 3). These uncertainties are included to the systematic error of the gluon polarisation as a fraction of the $\langle \Delta G/G \rangle$ value. The other contributions are discussed below. The quantities $S/(S+B)$ and a_{LL} are just multiplicative factors between the muon-nucleon asymmetry and $\Delta G/G$. Consequently, possible errors in their description will result in an error which is also a fraction of the measured $\langle \Delta G/G \rangle$. We may evaluate these systematic errors from the spread of the $\langle \Delta G/G \rangle$ values, originated by a change in the description of $S/(S+B)$ and a_{LL}. However, in the open-charm analysis this method is completely dominated by statistical fluctuations. There is a much better approach. For the study of the systematic error, one must compare the default analysis using a weight ω_0 with other analyses dealing with other weights ω_i (containing different $S/(S+B)$ or a_{LL} values). This can be accomplished through the use of the following equation [1] [88]:

[1] Using eq. 7.6 (with $\omega = \omega_0$) in eq. 7.8 results in the following weighted asymmetry: $A_{\omega_0} = \frac{\sum_j A^{\mathrm{raw}} \omega_{0_j} n_j}{\sum_j \omega_{0_j}^2 n_j}$, where $A^{\mathrm{raw}} = \sum_j \omega_{0_j} A_j$. The use of the latter definition implies an unbiased analysis, i.e. $\langle A_{\omega_0} \rangle = A_j$. However, if the correct weight is ω_i instead of ω_0, i.e. $A^{\mathrm{raw}} = \sum_j \omega_{i_j} A_j$, we have: $\langle A_{\omega_0} \rangle = \frac{\langle \omega_i \cdot \omega_0 \rangle}{\langle \omega_0^2 \rangle} A_j$

$$\langle A_{\omega_0} \rangle = \frac{\langle \omega_i \cdot \omega_0 \rangle}{\langle \omega_0^2 \rangle} \frac{\Delta G}{G} \tag{9.1}$$

where the expectation value of the asymmetry A is identified with the gluon polarisation. Therefore, the quantity $\langle \omega_i \cdot \omega_0 \rangle / \langle \omega_0^2 \rangle$ gives the relative systematic error [2] introduced by a different analysis of weight ω_i.

9.1 Systematic error associated with S/(S+B)

Several changes were introduced in the parameterisation procedure of the signal purity in order to determine the contribution of $S/(S+B)$ to the systematic error. In total, more than 50 parameterisations (around 3 per sample/year) are built for each of the following steps:

- **Parameterisation window:** Different mass intervals are considered for the Neural Network parameterisation.
- **Fitting procedure:** Different functional forms are tried to fit the background of the mass spectra in the hybrid-method approach (in bins of the $fP_\mu a_{LL}$ and also in bins of the NN_{o1}). These background fits are also used to control the uncertainties resulting from the introduction of the mass dependence in $S/(S+B)$.
- **Binning:** The impact of a different number of bins in the mass spectra is analysed.

Concerning the fitting procedure, only the background description is changed, with one exception: the real bumpy shape of the $D^*_{K\pi\pi^0}$ signal (obtained from Monte Carlo) is also tested to fit the distribution containing these D^0 mesons. However, the impact of this function in the parameterisation of $S/(S+B)$ is completely negligible:

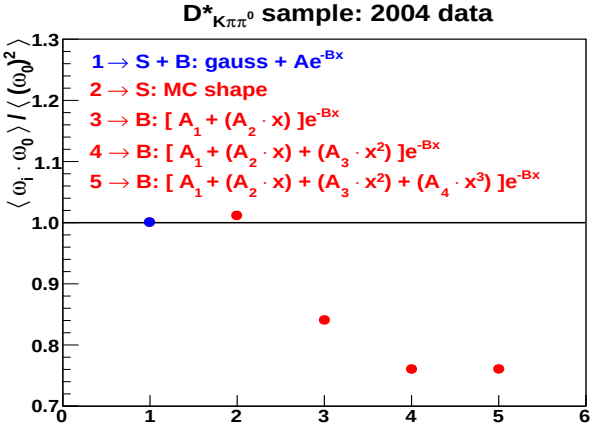

Figure 9.1: Example of the spread of weights generated by the use of a different fitting procedure. The first point corresponds to the default analysis, i.e. $\omega_i = \omega_0$. The remaining points use a different signal purity, $[S/(S+B)]_i$, which is obtained through the use of new fitting functions to the signal (2) or to the background (3, 4, 5) of the mass spectra. Consequently, a new weight ω_i is determined and used to estimate the systematic error. The variable x in those functions is the reconstructed mass of a D^0 candidate.

[2] The final error is given by the average spread of weights around 1 ($\omega_i = \omega_0$), taken as a fraction of $\Delta G/G$.

One can conclude from Fig. 9.1 that the signal of the $D^*_{K\pi\pi^0}$ sample is well approximated by a Gaussian distribution. In Fig. 9.2 it is displayed all the systematic studies performed for the sample that reveals the worst parameterisation of $S/(S+B)$, i.e. $D^0_{K\pi}(2006)$, the sample for which there is the biggest uncertainty in the weight definition (highest spread of weights). As in the previous case, the first point in each plot corresponds to the default analysis of weight ω_0. All the remaining points generate a systematic error which is given by their difference to the default analysis (in the y-coordinate). For this particular sample, the biggest uncertainty introduced by a parameterisation of $S/(S+B)$ corresponds to 11% of the $\langle \Delta G/G \rangle$ value.

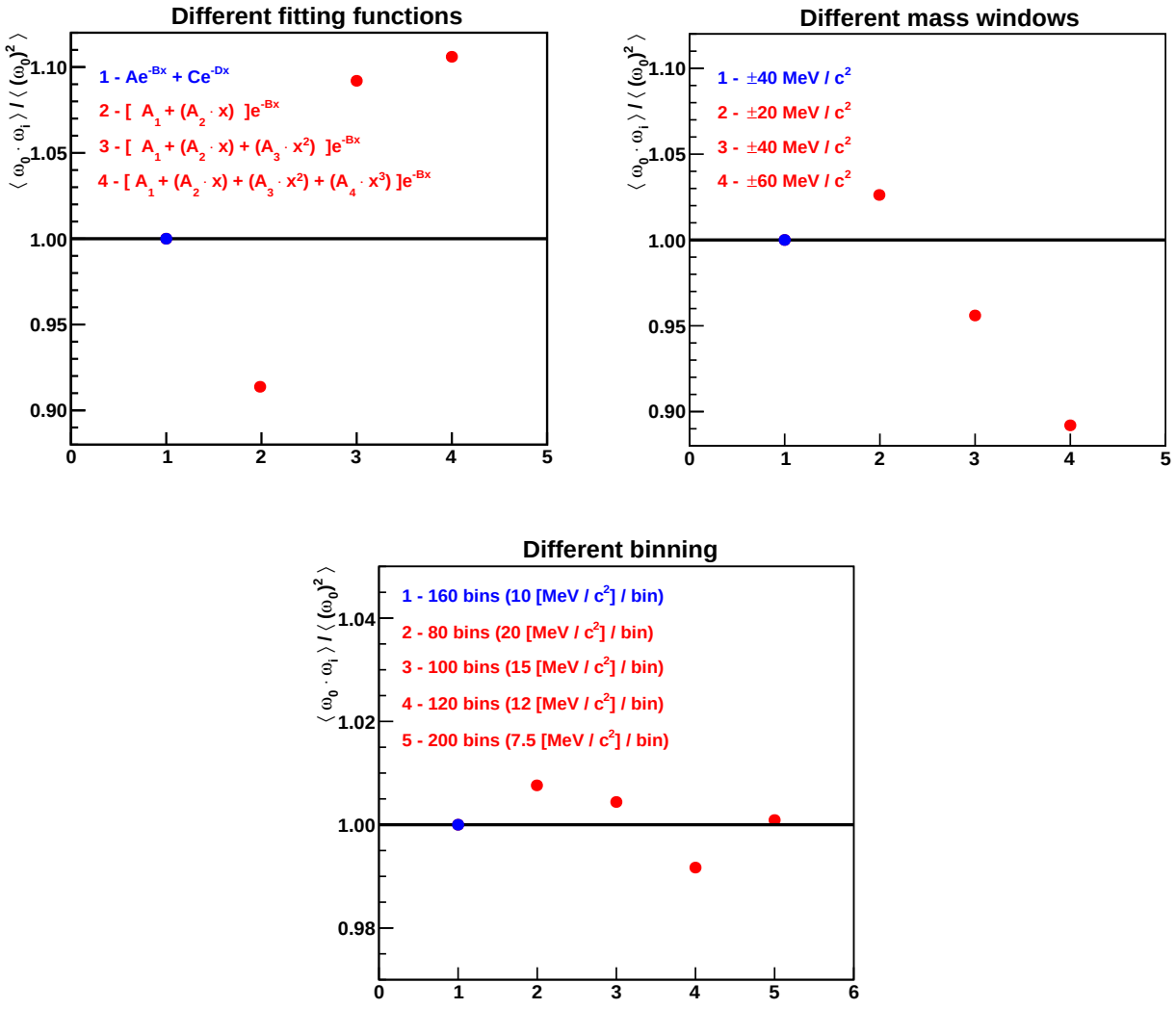

Figure 9.2: Example of the systematic studies done for $S/(S+B)$, in the $D^0_{K\pi}$ (2006) sample.

The final uncertainty associated with $S/(S+B)$ is obtained from the weighted average of all the systematic spreads belonging to all samples considered in the analysis (5 channels from 5 years). The statistical errors of $\langle \Delta G/G \rangle$ are used as a weight to this average. In this way, the different impact that each sample has in the final result is taken into account. The averages are determined separately for each step of the parameterisation, i.e. for the different mass windows considered, the different fitting procedures and the different binnings. The three results obtained are added in quadrature to produce the final dispersion which amounts to 7%. Therefore, at LO, the uncertainty assigned to $S/(S+B)$ in the determination of the gluon polarisation is 0.006 (0.014 at NLO).

9.2 Systematic error associated with a_{LL}

Analogously to the parameterisation of $S/(S+B)$, several modifications are introduced in the procedure used to determine the partonic asymmetry a_{LL}. This study is divided in two parts: the Monte Carlo PGF simulator and the Neural network procedure. The most important one is focused on the uncertainties generated by the Monte Carlo simulation of the PGF process. These contributions to the systematic error are obtained from the spread of the signal weights originated by the use of different PDFs (**P**arton **D**istribution **F**unctions), different masses of the charm quark and different scales. For each of these systematic studies, the AROMA generator [73] is used to produce a new set of PGF events (with (NLO) and without (LO) parton showers). The produced D^0 mesons are constrained to the COMPASS acceptance through a full simulation of the spectrometer, and thereafter they are reconstructed like real events. Using the Monte Carlo information on both charm quarks we can calculate a new a_{LL}^i (for every generated event) and, consequently, a new ω_i is obtained as a signal weight. The final results are shown in Fig. 9.3.

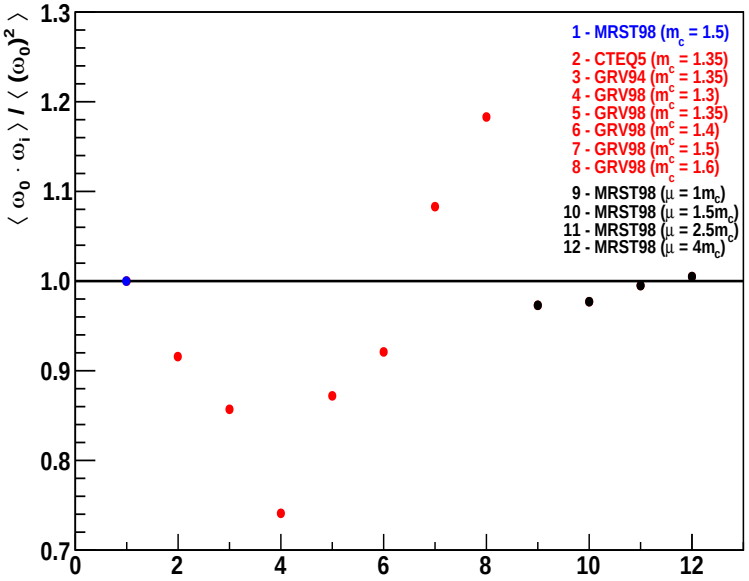

Figure 9.3: The spread introduced in the signal weight by all the systematic studies related to the Monte Carlo dependence of a_{LL} (at LO). All data is included. The default analysis is given by the first point (in blue). The remaining points correspond to the use of a different combination of PDFs, charm masses (m_c in GeV/c^2), and scales ($\mu^2 = (2m_c^T)^2$), during the generation of the PGF events.

The second part of this study is devoted to the systematic error introduced by the Neural Network in the parameterisation of a_{LL}. To this aim, the initial conditions of the Neural Network are changed and, as a result, a new parameterisation is obtained. With the help of the latter a different a_{LL}^i is calculated for each real data event. The resulting spread of the signal weights can be seen in Fig. 9.4. The final uncertainty associated to this partonic asymmetry is calculated from the two averages of spreads (from Fig. 9.3 and Fig. 9.4) added in quadrature. The dispersion obtained amounts to 9% of the $\langle \Delta G/G \rangle$ value, which corresponds to an uncertainty of 0.008 introduced by a_{LL} in the LO determination of the gluon polarisation. Regarding the NLO analysis, a conservative value of 18% is assumed to account for the contributions of $a_{LL}^{(q)}$. This dispersion represents an uncertainty of 0.036 to the NLO determination of $\Delta G/G$.

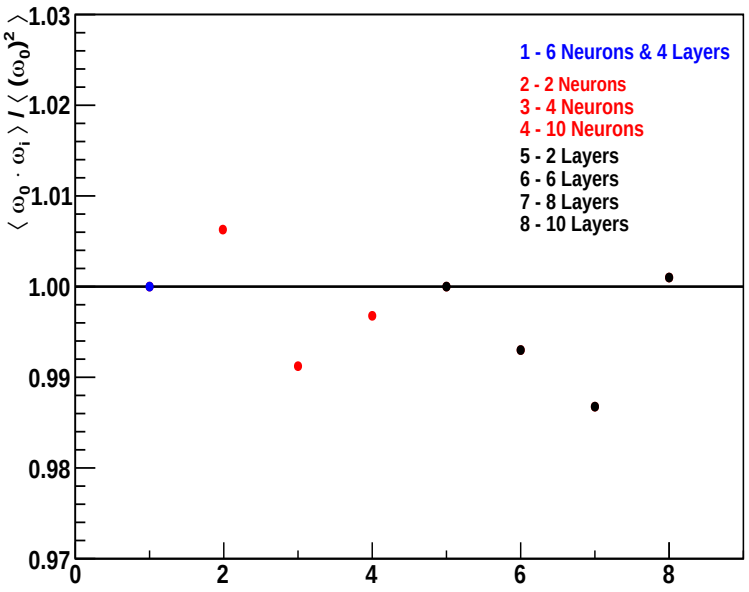

Figure 9.4: The spread introduced in the signal weight by all the systematic studies related to the Neural Network parameterisation of a_{LL} (at LO). All data is included. The default analysis is given by the first point (blue). The remaining points correspond to the use of a different set for the initial conditions of the Neural Network structure, i.e. a different number of neurons and a different number of layers are used.

9.3 False Asymmetries

The asymmetry extraction relies on the following assumption:

$$K = \frac{a_u n_u \times a_{d'} n_{d'}}{a_{u'} n_{u'} \times a_d n_d} = 1 \tag{9.2}$$

where a is the acceptance and n is the number of target nucleons in the upstream (u) or in the downstream (d) cells, before and after (') the field rotation. Variations with time of a and n may generate false asymmetries but, in general, a global change cancels in K. However, a small change of efficiency in a given part of the spectrometer will not affect the target cells in the same way: since they are not at same distance from the detectors, these inefficiencies will not cancel in K.

We can consider two kinds of false asymmetries depending whether the source of the asymmetry is or is not correlated with the solenoid field (surrounding the polarised target) direction. Uncorrelated sources are essentially time variations of the spectrometer efficiency. The latter false asymmetries will not really bias the measured asymmetries but rather enlarge their variance. They can be studied by measuring the asymmetries dispersion (the so-called pulls), and we call them random false asymmetries.

There are at least two sources correlated with the magnetic field: the displacement of the target induced by the solenoid field rotation and some subtle effects resulting from the interference between the fields of the solenoid and of the SM1 magnet. The latter may originate a small tilt of the target (caused by a force that tends to anti-align the two fields) and, as a

result, the number of target nucleons is changed inside the fiducial volume ($K \neq 1$). These kind of false asymmetries are called reproducible false asymmetries. Their sign is changed when the microwave (μW) settings in the two cells are exchanged to reverse the polarisation. Therefore, they can be studied by comparing the asymmetries measured with the two μW settings.

9.3.1 Random False Asymmetries

These kind of uncertainties are studied with the help of the following pulls:

$$p_i = \frac{\langle \Delta G/G \rangle_i - \langle \Delta G/G \rangle}{\sigma_i} \tag{9.3}$$

where $\langle \Delta G/G \rangle_i$ corresponds to the results on the gluon polarisation (per channel) obtained for each of the 48 weeks (periods) of data taking. For the channels of low statistics ($D^*_{K\pi\pi^0}$, $D^*_{K\pi\pi\pi}$ and $D^*_{K_{sub}\pi}$) some periods of data with same acceptance are merged for the asymmetry extraction. The factors σ_i and $\langle \Delta G/G \rangle$ are the statistical errors and the final value of the gluon polarisation. The pulls obtained from the main channels of analysis are shown in Fig. 9.5:

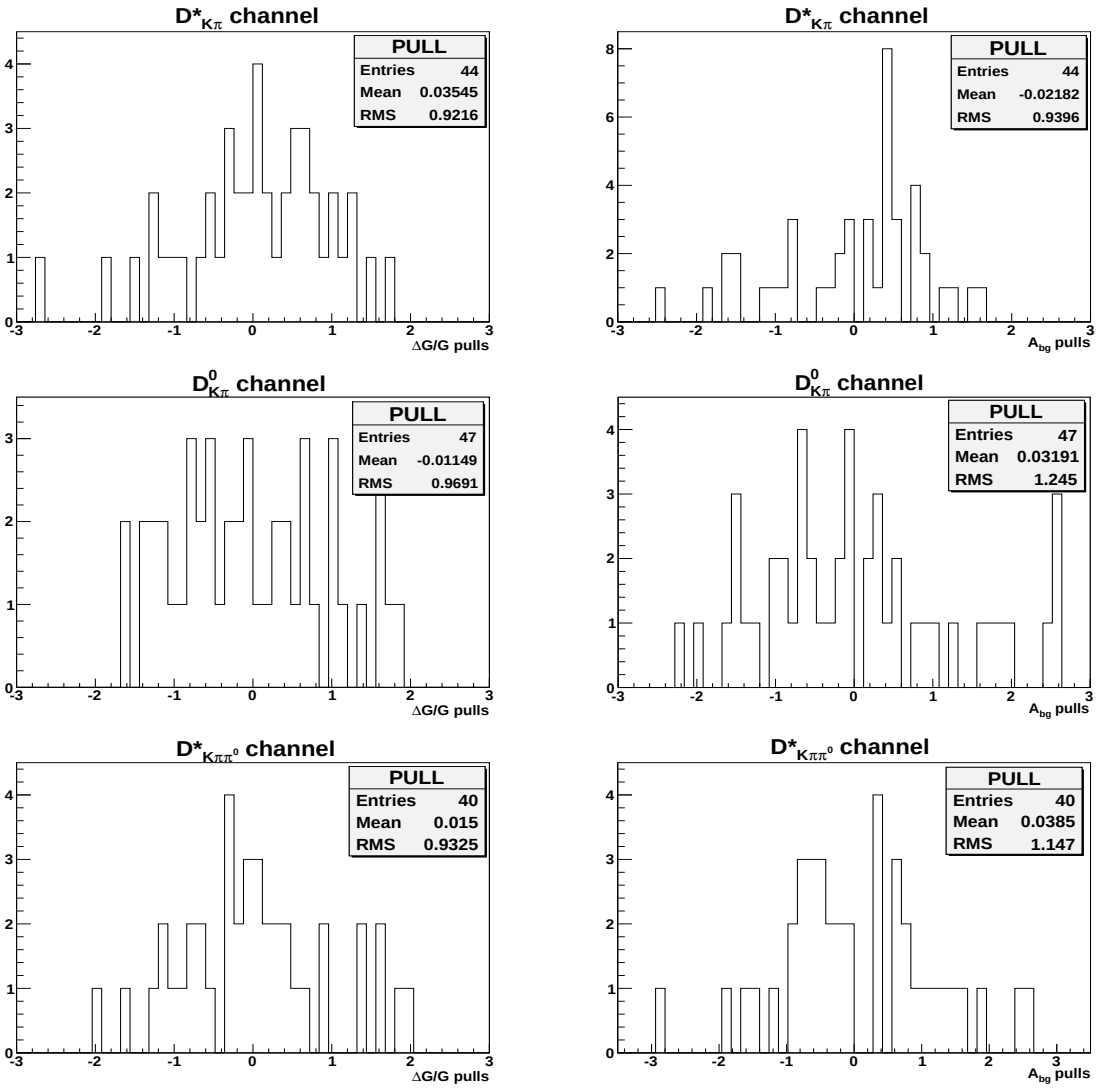

Figure 9.5: Pulls of ΔG/G (left) and A_{bg} (right) related to the $D^*_{K\pi}$, $D^0_{K\pi}$ and $D^*_{K\pi\pi^0}$ channels.

The statistical error associated to the RMS of the pulls is $\delta_{\mathrm{RMS}} = \mathrm{RMS}/\sqrt{2(N-1)}$, where N is the total number of weeks (44 for the $D^*_{K\pi}$ case). By defining $\sigma^2_{\mathrm{tot}} = \sigma^2_{\mathrm{stat}} + \sigma^2_{\mathrm{syst}}$, where σ_{syst} denotes the systematic error due to the random false asymmetries, we get a 1-σ upper limit for σ_{tot} of $(\max(\mathrm{RMS}, 1) + \delta_{\mathrm{RMS}}) \times \sigma_{\mathrm{stat}}$. This result implies the following upper limit:

$$\sigma_{\mathrm{syst}} \leq \sqrt{(\max(\mathrm{RMS}, 1) + \delta_{\mathrm{RMS}})^2 - 1} \times \sigma_{\mathrm{stat}} \tag{9.4}$$

The absence of this kind of false asymmetries is verified if the pulls are centred at zero with an RMS = 1. In Fig. 9.5, a result compatible with this assumption is seen (left plots). We can also verify the absence of correlation among the pulls of the different channels, in Fig. 9.6. The latter is also a good indication for the non existence of random false asymmetries in the present analysis.

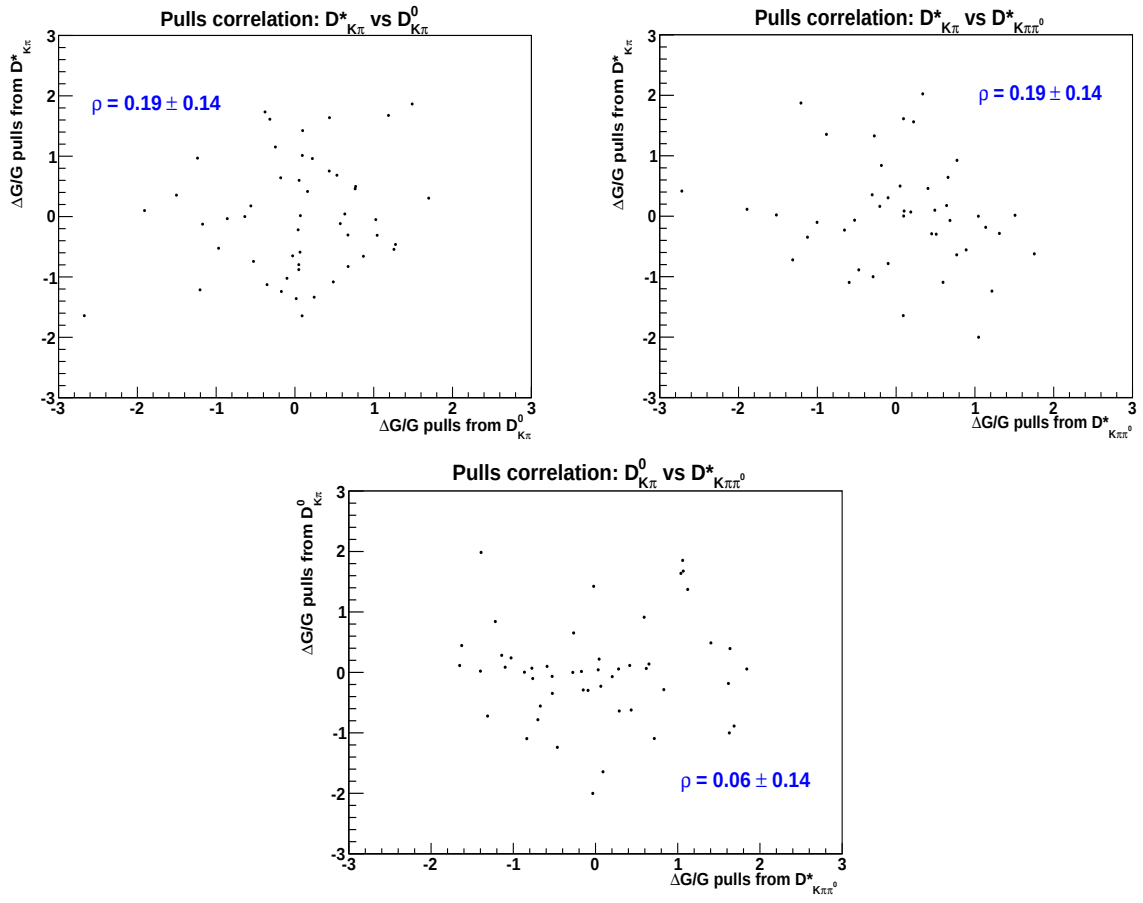

Figure 9.6: Correlation (ρ) among the pulls of ΔG/G corresponding to the $\mathrm{D}^*_{K\pi}$, $\mathrm{D}^0_{K\pi}$ and $\mathrm{D}^*_{K\pi\pi^0}$ channels. In all cases the correlation is compatible with zero.

The upper limit obtained for σ_{syst}, as defined in eq. 9.4, is quite high. Considering the $D^*_{K\pi}$ channel as an example, we obtain the following uncertainty for an RMS = 1: $\sigma_{\mathrm{syst}} \leq 0.48 \times \sigma_{\mathrm{stat}}$. In order to get a smaller upper limit, instead of $\Delta G/G$ we consider the pulls from the background asymmetries which have much more statistics (cf. Fig. 9.5-right). Thereafter, the obtained results need to be translated to $\Delta G/G$. The following discussion describes the procedure to get $\sigma_{\mathrm{syst}}(\langle \Delta G/G \rangle)$ from $\sigma_{\mathrm{syst}}(\langle A_{bg} \rangle)$. Let's consider K_S and K_B to be the double ratio of acceptances, $a_u a_{d'}/a_d a_{u'}$, for the signal and for the background events. The generalisation of eq. 6.12 (double ratio of events) to include the background asymmetry is given by the following

equation (for simplicity of notation we have $\Delta G/G$ for $\langle \Delta G/G \rangle$):

$$r_C = K_C \frac{(1 - \langle \beta_{u,S} \rangle_{\omega_C} \frac{\Delta G}{G} - \langle \beta_{u,B} \rangle_{\omega_C} A_{bg})(1 - \langle \beta_{d',S} \rangle_{\omega_C} \frac{\Delta G}{G} - \langle \beta_{d',B} \rangle_{\omega_C} A_{bg})}{(1 - \langle \beta_{d,S} \rangle_{\omega_C} \frac{\Delta G}{G} - \langle \beta_{d,B} \rangle_{\omega_C} A_{bg})(1 - \langle \beta_{u',S} \rangle_{\omega_C} \frac{\Delta G}{G} - \langle \beta_{u',B} \rangle_{\omega_C} A_{bg})} \tag{9.5}$$

where C = S, B

Using $-\langle \beta_S \rangle_{\omega_C} = -\langle \beta_{u,S} \rangle_{\omega_C} = -\langle \beta_{d',S} \rangle_{\omega_C} = \langle \beta_{u',S} \rangle_{\omega_C} = \langle \beta_{d,S} \rangle_{\omega_C}$ and $-\langle \beta_B \rangle_{\omega_C} = -\langle \beta_{u,B} \rangle_{\omega_C} = -\langle \beta_{d',B} \rangle_{\omega_C} = \langle \beta_{u',B} \rangle_{\omega_C} = \langle \beta_{d,B} \rangle_{\omega_C}$, we obtain for eq. 9.5:

$$\begin{aligned} r_C &= K_C \frac{(1 + \langle \beta_S \rangle_{\omega_C} \frac{\Delta G}{G} + \langle \beta_B \rangle_{\omega_C} A_{bg})^2}{(1 - \langle \beta_S \rangle_{\omega_C} \frac{\Delta G}{G} - \langle \beta_B \rangle_{\omega_C} A_{bg})^2} \\ &\approx K_C \left(1 + 4 \langle \beta_S \rangle_{\omega_C} \frac{\Delta G}{G} + 4 \langle \beta_B \rangle_{\omega_C} A_{bg} \right) \end{aligned} \tag{9.6}$$

The above approximation is justified by the small asymmetries ($\langle \beta_S \rangle_{\omega_C} \Delta G/G \ll 1$ and $\langle \beta_B \rangle_{\omega_C} A_{bg} \ll 1$) observed in COMPASS. The following system of equations is obtained from eq. 9.6 [89]:

$$\begin{pmatrix} \xi_S \\ \xi_B \end{pmatrix} = \begin{pmatrix} \Delta G/G \\ A_{bg} \end{pmatrix} \begin{pmatrix} \langle \beta_S \rangle_{\omega_S} & \langle \beta_B \rangle_{\omega_S} \\ \langle \beta_S \rangle_{\omega_B} & \langle \beta_B \rangle_{\omega_B} \end{pmatrix} \tag{9.7}$$

where $\xi_C = \frac{1}{4} \left(\frac{r_C}{K_C} - 1 \right)$. The solution of this system is:

$$\begin{pmatrix} \Delta G/G \\ A_{bg} \end{pmatrix} = \frac{1}{[\langle \beta_S \rangle_{\omega_S} \langle \beta_B \rangle_{\omega_B} - \langle \beta_B \rangle_{\omega_S} \langle \beta_S \rangle_{\omega_B}]} \times \begin{pmatrix} \langle \beta_B \rangle_{\omega_B} \xi_S - \langle \beta_B \rangle_{\omega_S} \xi_B \\ -\langle \beta_S \rangle_{\omega_B} \xi_S + \langle \beta_S \rangle_{\omega_S} \xi_B \end{pmatrix} \tag{9.8}$$

There are two ways to translate the random false asymmetries from A_{bg} to $\Delta G/G$:

1- <u>Assuming $K_S = K_B$</u>:

From eq. 9.8 we obtain:

$$\frac{\delta(\Delta G/G)|_{K_S}}{\delta(A_{bg})|_{K_B}} = \left(\frac{\frac{\partial \Delta G/G}{\partial K_S} \cdot \delta(K_S)}{\frac{\partial A_{bg}}{\partial K_B} \cdot \delta(K_B)} \right) = \left| \frac{-\langle \beta_B \rangle_{\omega_B} + \langle \beta_B \rangle_{\omega_S}}{\langle \beta_S \rangle_{\omega_B} - \langle \beta_S \rangle_{\omega_S}} \right| \tag{9.9}$$

where the assumptions of $K_S = K_B = 1$ and $r_C \approx 1$ are used. Inserting eq. 9.4 into eq. 9.9 (and replacing δ by σ_{syst}), we have:

$$\sigma_{\text{syst}}(\Delta G/G)|_{K_S} = \left| \frac{-\langle \beta_B \rangle_{\omega_B} + \langle \beta_B \rangle_{\omega_S}}{\langle \beta_S \rangle_{\omega_B} - \langle \beta_S \rangle_{\omega_S}} \right| \times \sqrt{(\max(\text{RMS}, 1) + \delta_{RMS})^2 - 1} \times \sigma_{\text{stat}}(A_{bg}) \tag{9.10}$$

Therefore, this uncertainty on $\Delta G/G$ can be estimated from the knowledge of the factors $\langle \beta_C \rangle_{\omega_C}$

together with the RMS information associated to the A_{bg} pulls. The present hypothesis is the most realistic one because it only assumes an equal influence of the detector instabilities on the signal and background events.

2- Assuming that $\rho(K_S,\ K_B) = 0$:

Using a much more conservative approach, we can also consider the scenario where K_S and K_B are totally uncorrelated. With this assumption we obtain for the systematic error:

$$\sigma_{\rm syst}(\Delta G/G)|_{K_S} = \left| \frac{\langle\beta_B\rangle^2_{\omega_B} + \langle\beta_B\rangle^2_{\omega_S}}{\langle\beta_S\rangle^2_{\omega_B} + \langle\beta_S\rangle^2_{\omega_S}} \right| \times \sqrt{(\max(\mathrm{RMS},1) + \delta_{RMS})^2 - 1}\ \times \sigma_{\rm stat}(A_{bg}) \quad (9.11)$$

using

$$\frac{\delta(\Delta G/G)|_{K_S}}{\delta(A_{bg})|_{K_B}} = \frac{\langle\beta_B\rangle^2_{\omega_B} + \langle\beta_B\rangle^2_{\omega_S}}{\langle\beta_S\rangle^2_{\omega_B} + \langle\beta_S\rangle^2_{\omega_S}} \quad (9.12)$$

Clearly this hypothesis corresponds to an extreme case. Nevertheless, it is useful to set an upper limit that takes into account possible small deviations between K_S and K_B (caused by instabilities of the spectrometer). The final results obtained for the random false asymmetries are shown in Table 9.2

	Channels			
	$D^*_{K\pi}$	$D^0_{K\pi}$	$D^*_{K\pi\pi^0}$	$D^*_{K_{sub}\pi} + D^*_{K\pi\pi\pi}$
$\left\lvert\frac{-<\beta_B>_{\omega_B}+<\beta_B>_{\omega_S}}{<\beta_S>_{\omega_B}-<\beta_S>_{\omega_S}}\right\rvert$	1.388	2.492	0.857	1.678
$\frac{<\beta_B>^2_{\omega_B}+<\beta_B>^2_{\omega_S}}{<\beta_S>^2_{\omega_B}+<\beta_S>^2_{\omega_S}}$	2.524	29.609	7.168	6.729
$\sqrt{(\max(\mathrm{RMS},1)+\delta_{\rm RMS})^2-1}$	0.279	0.950	0.812	0.277
$\sigma_{\rm syst}(A_{bg})$	0.008	0.004	0.028	0.008
$\sigma_{\rm syst}(\Delta G/G)$	0.011 (0.021)	0.009 (0.107)	0.024 (0.203)	0.013 (0.054)
$\frac{\sigma_{\rm syst}(\Delta G/G)}{\sigma_{\rm stat}(\Delta G/G)}$	4% (7%)	2% (26%)	4% (35%)	2% (8%)

Table 9.2: Summary of the random false asymmetries estimated for each channel of the analysis. The channels $D^*_{K_{sub}\pi}$ and $D^*_{K\pi\pi\pi}$ are merged due to statistical limitations. All the factors needed in eqs. 9.10-9.11 are listed here. The final systematic error (accounting for this kind of uncertainty) is shown for $K_S = K_B$ and also for the case where $\rho(K_S,\ K_B) = 0$ (in parenthesis).

9.3.2 Reproducible False Asymmetries

This contribution to the systematic error is estimated from the comparison of asymmetries obtained with the two microwave settings, i.e. $A^{rep}_{bg} = (A^+_{bg} - A^-_{bg})/2$. All asymmetries A^{rep}_{bg}, summarized in Table 9.3, are compatible with zero. Therefore, there is no evidence that points

to the existence of reproducible false asymmetries in the data. Still a 1-σ upper limit is defined: $|A_{bg}^{rep}| + \delta(A_{bg}^{rep})$. As before, this result must be transformed to an upper limit for $(\Delta G/G)^{rep}$. This can be accomplished by applying the same multiplicative factors used for the random false asymmetries (cf. eq. 9.9 and eq. 9.12). Thereafter, the final systematic error introduced by reproducible false asymmetries is obtained from the following equation:

$$\sigma_{\rm syst}\left(\frac{\Delta G}{G}\right)^{rep} = \frac{(\delta^+)^2 - (\delta^-)^2}{(\delta^+)^2 + (\delta^-)^2}\left(\frac{\Delta G}{G}\right)^{rep} \tag{9.13}$$

where $\delta^{+/-} = 1/[\sigma_{\rm stat}^{+/-}(\Delta G/G)]^2$ is computed from the data collected with a positive (+) or with a negative (−) microwave configuration. The uncertainty resulting from eq. 9.13 is even more diluted as a consequence of averaging the asymmetries over the two μW-settings. The results for this kind of false asymmetries are presented in Table 9.3.

Channels	A_{bg}^{+}	A_{bg}^{-}	A_{bg}^{rep}	$\sigma_{\rm syst}(\Delta G/G)^{rep}$
$D^*_{K\pi}(02-04)$	-0.016 ± 0.055	-0.002 ± 0.057	-0.009 ± 0.040	0.003 (0.005)
$D^*_{K\pi}(2006)$	-0.025 ± 0.094	-0.093 ± 0.069	-0.059 ± 0.058	0.047 (0.086)
$D^*_{K\pi}(2007)$	0.183 ± 0.104	-0.061 ± 0.099	0.122 ± 0.072	0.014 (0.025)
$D^0_{K\pi}(02-04)$	-0.003 ± 0.007	0.006 ± 0.007	-0.004 ± 0.005	0.002 (0.020)
$D^0_{K\pi}(2006)$	0.015 ± 0.012	-0.017 ± 0.009	-0.016 ± 0.055	0.021 (0.251)
$D^0_{K\pi}(2007)$	0.006 ± 0.012	-0.014 ± 0.012	0.010 ± 0.009	0.002 (0.020)
$D^*_{K\pi\pi^0}$ $(02-04)$	0.018 ± 0.070	-0.014 ± 0.068	0.016 ± 0.049	0.002 (0.016)
$D^*_{K\pi\pi^0}$ (2006)	0.017 ± 0.116	-0.218 ± 0.087	-0.100 ± 0.072	0.042 (0.351)
$D^*_{K\pi\pi^0}$ (2007)	0.243 ± 0.127	0.076 ± 0.123	0.084 ± 0.088	0.005 (0.041)
$D^*_{K_{sub}\pi} + D^*_{K\pi\pi\pi}$ $(02-04)$	-0.059 ± 0.095	0.049 ± 0.063	-0.054 ± 0.057	0.073 (0.294)

Table 9.3: Summary of the reproducible false asymmetries estimated for each channel of the analysis. The study is done separately for the two different solenoids (2002-2004 and 2006-2007) and for the two different targets (2002-2006 and 2007) used in the COMPASS experiment. This kind of contribution to the systematic error is shown for $K_S = K_B$ and also for the case where $\rho(K_S,\ K_B) = 0$ (in parenthesis).

9.3.3 Final results

The final uncertainty coming from possible false asymmetries is calculated from the components summarized in the Table 9.4. A value of 0.077 is obtained from the weighted average (using the statistical error as weight) of the individual channels total results. The latter are determined in two steps. In the first step, the averages of the results obtained under the assumptions $K_S = K_B$ and $\rho(K_S,\ K_B) = 0$ are calculated per channel and separately for the random and reproducible false asymmetries. In the final step, these averages are added in quadrature to reproduce the uncertainties shown in the last line of Table 9.4.

False Asymmetry	Channels			
	$D^*_{K\pi}$	$D^0_{K\pi}$	$D^*_{K\pi\pi^0}$	$D^*_{K_{sub}\pi} + D^*_{K\pi\pi\pi}$
$\sigma_{\rm syst}(\Delta G/G)^{ran}$	0.016	0.058	0.114	0.034
$\sigma_{\rm syst}(\Delta G/G)^{rep}$	0.030	0.053	0.076	0.184
Total	0.034	0.079	0.137	0.187

Table 9.4: Final false asymmetries resulting from the random and reproducible contributions added in quadrature.

9.3.4 Additional False Asymmetry studies

The efficiency stability and the homogeneity of the detector are an essential assumption of this analysis. In order to control the consistency of the data recorded, one last test was performed:

- Left-Right and Top-Bottom stability of the spectrometer.

For this study two samples of similar statistics are considered. This division is done based on the data containing a D^0 candidate going to the left (L) or to the right (R) in the spectrometer (similar case for the top (T) / bottom (B) samples). The slow pion coming from a D^* decay (together with a D^0) is used for this test, since it is more interesting to see the effect on the magnetic bending plane. For each of those two samples the gluon polarisation is simultaneously extracted with the polarised background asymmetry (after applying all standard cuts of the analysis). The consistency of the data collected from all parts of the spectrometer can be evaluated through the following difference:

$$(\Delta G/G)_F^{L-R\ (T-B)} = (\Delta G/G)_F^{L\ (T)} - (\Delta G/G)_F^{R\ (B)} \tag{9.14}$$

This difference should be compatible with zero within the accuracy of the statistical error, evaluated by:

$$\sigma\left(\Delta G/G\right)_F^{L-R\ (T-B)} = \sqrt{\left(\sigma\left(\Delta G/G\right)_F^{L\ (T)}\right)^2 \ + \ \left(\sigma\left(\Delta G/G\right)_F^{R\ (B)}\right)^2} \tag{9.15}$$

The results for each year of data taking are shown in Fig. 9.7. No significant inconsistencies are observed, as all the points are compatible with zero, within two standard deviations. However, concerning the top-bottom compatibility a small systematic effect is observed: all experimental points have the same asymmetry signal. Clearly, this effect has its origin in the lack of statistics available because it is completely washed out from the $(A_{bg})_F^{T-B}$ asymmetry. The latter is extracted with much more statistics from the same data. A similar problem is observed for the left-right compatibility study. Unfortunately, there are no more data available to confirm or deny the validity of such false asymmetry (seen in $(A_{bg})_F^{L-R}$). Therefore, using a conservative approach we can consider the final point of $(A_{bg})_F^{L-R}$, 0.06, as an upper limit for the false asymmetry contribution to the systematic error. Assuming that $K_S = K_B$, this limit is translated to $\Delta G/G$ with a value of 0.08. The latter is precisely the result obtained from the previous discussion on random and reproducible false asymmetries. Since these two results

are totally correlated, only one of them is considered as a contribution to the final uncertainty associated to the measured $\Delta G/G$.

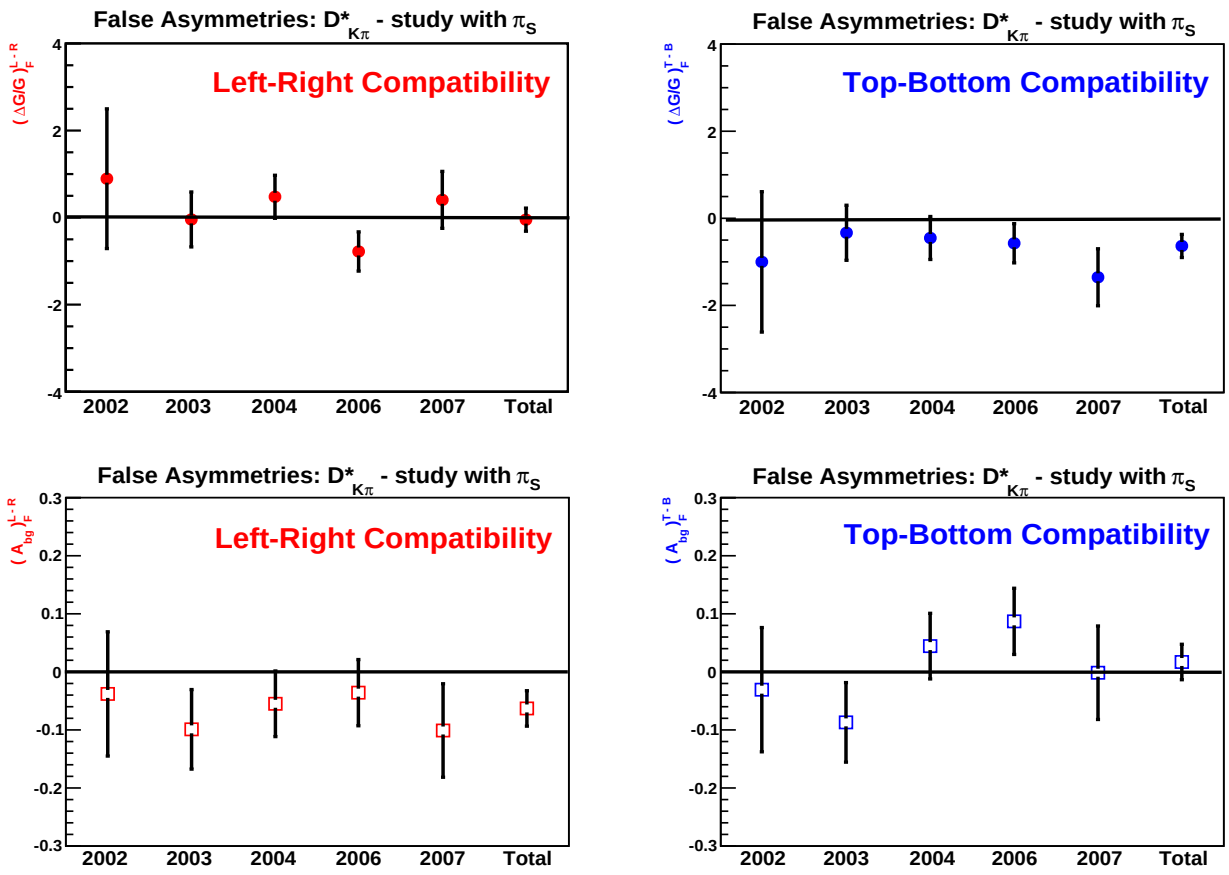

Figure 9.7: Stability tests to the performance of the spectrometer. The differences in ΔG/G (top-figures) and in A_{bg} (bottom-figures) are calculated from two independent samples of each year of data taking: the π_{slow} coming from a D^* decay (together with a $D^0_{K\pi}$) is reconstructed in the left/right (left-figures) or in the top/bottom (right-figures) parts of the spectrometer. The absence of false asymmetries is verified if these differences are compatible with zero.

Chapter 10

Summary and Conclusions

The unpolarised structure of the nucleon is nowadays very well known. It is the result of a series of successful **D**eep **I**nelastic lepton-nucleon **S**cattering experiments, DIS, that have been performed at CERN, SLAC and DESY. The resulting data allowed a very precise determination of the unpolarised structure functions over a wide kinematic range. From these measurements one can easily extract the quark (per flavour) and gluon densities inside the nucleon. In particular, the structure function which describes the gluon was accurately determined from a QCD fit to the world data on F_2.

Concerning the spin structure of the nucleon, the situation is completely different. The concept of spin is extremely important for many areas of science, from quantum computing to medical applications such as the magnetic resonance. Therefore, it would be useful (and advisable) to know in detail the origin of the nucleon spin. In the last years, a considerable effort has been made to understand how the spin of $\hbar/2$ is decomposed in terms of contributions of quarks and gluons. Up to now, it was only possible to determine with good accuracy the contribution of quarks to the nucleon spin. The obtained result shows that only 30% of the nucleon spin is due to the intrinsic spin of the quarks. At the first glance the most obvious solution to this spin puzzle lies in the contribution of gluons, i.e. ΔG. However, the QCD fit is poorly constrained for the structure function describing the gluon helicity. This fact is justified by the scarce information available on the polarised data. The latter are available in a rather limited kinematic range, since the corresponding measurements have been performed mainly by fixed-target experiments. Therefore, a direct measurement of ΔG is needed to solve the puzzle of the nucleon spin.

This thesis is dedicated to the determination of the gluon polarisation in the nucleon. The process on which this measurement is based is the **P**hoton-**G**luon **F**usion (PGF). It can be tagged by the open-charm meson production, assuming that the intrinsic charm content of the nucleon is negligible. In the presented analysis, D^0 mesons are used to directly measure $\Delta G/G$ from the polarised data of COMPASS. These mesons are identified via the reconstruction of their invariant mass, without distinction between the production and the decay vertices (the polarised target of COMPASS does not permit the use of dedicated vertex detectors with the needed resolution, i.e. ≈ 1 mm). Nevertheless, the impact of the combinatorial background is significantly reduced through the use of an innovative method based on Neural Networks. The remaining ingredient, needed for the extraction of $\Delta G/G$, is the analysing power, a_{LL}, which is defined by the ratio of the spin-dependent and the spin-independent muon-gluon cross-sections. This quantity cannot be determined from the data because it depends on the unknown partonic kinematics: typically, only one D^0 of the two charmed hadrons produced is reconstructed from each PGF event in COMPASS. Therefore, a_{LL} is determined from events resulting from a

dedicated Monte Carlo simulation. The final result for the gluon polarisation is obtained at LO-QCD (a_{LL} is calculated in **L**eading **O**rder approximation of α_S) and also, for the first time, at NLO-QCD (**N**ext-to-**L**eading **O**rder approximation). These two values are determined at the scale of $\mu^2 = 13$ (GeV/c)^2, and amount to:

$$\left\langle \frac{\Delta G}{G} \right\rangle^{\mathrm{LO}} = -0.08 \pm 0.21(\mathrm{stat.}) \pm 0.08(\mathrm{syst.}) \qquad @\langle x_g \rangle = 0.11^{+0.11}_{-0.05} \tag{10.1}$$

$$\left\langle \frac{\Delta G}{G} \right\rangle^{\mathrm{NLO}} = -0.20 \pm 0.21(\mathrm{stat.}) \pm 0.09(\mathrm{syst.}) \qquad @\langle x_g \rangle = 0.28^{+0.19}_{-0.10} \tag{10.2}$$

The uncertainty of these results is completely dominated by their statistical errors. The amount of the systematic errors is considerably much smaller. Therefore, in despite of the large statistical uncertainties, these results are of great relevance as they are almost independent of theoretical models. The dependence on the assumptions introduced in the Monte Carlo simulations represents only a small fraction of the total systematic errors.

The final question we want to answer is the contribution of gluons to the nucleon spin (cf. eq. 1.5), i.e. ΔG. That can be accomplished with the help of Fig. 10.1:

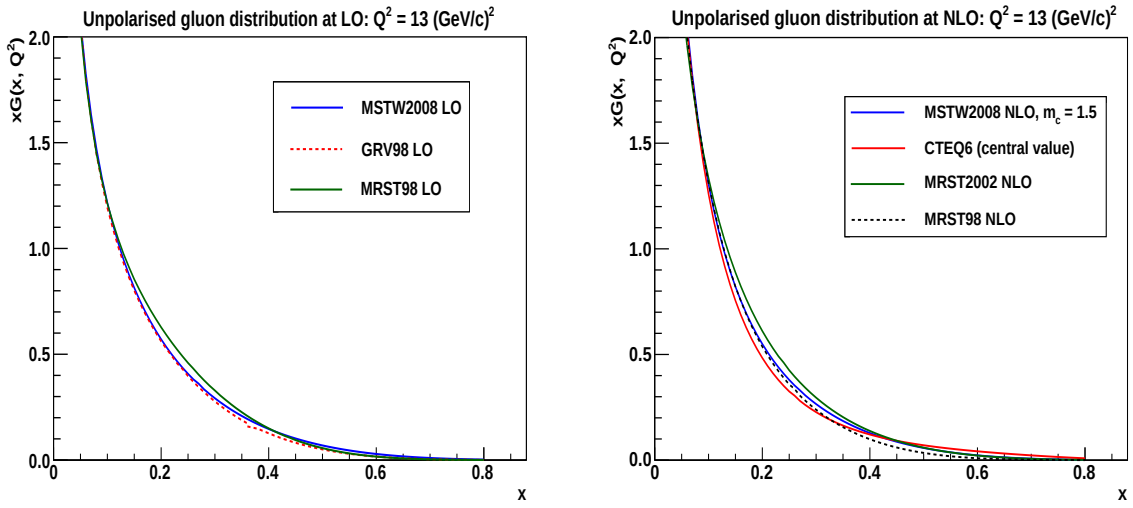

Figure 10.1: Examples of some parameterisations for $xG(x, Q^2)$ obtained in the LO-QCD (left) and in the NLO-QCD (right) approximations.

One can easily obtain ΔG by using the proper $xG(x, Q^2)$ value corresponding to the x_g of the $\Delta G/G$ measurement. By using the same parameterisation that is used in the analysis (for the estimation of a_{LL}), MRST 98, one obtains:

$$\langle \Delta G \rangle^{\mathrm{LO}} = -0.83 \pm 2.30 \qquad @\langle x_g \rangle = 0.11^{+0.11}_{-0.05} \tag{10.3}$$

$$\langle \Delta G \rangle^{\mathrm{NLO}} = -0.20 \pm 0.23 \qquad @\langle x_g \rangle = 0.28^{+0.19}_{-0.10} \tag{10.4}$$

The uncertainties shown in these two equations contain both the statistical and the systematic errors, added in quadrature (multiplied by $G(x, Q^2)$ from MRST 98). An additional error

related to the choice of $G(x, Q^2)$ should also be assigned. However, as one can see from Fig. 10.1 the impact of this choice is completely negligible as compared to the error values already estimated (cf. eq. 10.3 and eq. 10.4). This contribution is therefore neglected. Final results for $x\Delta G$ are shown in Fig. 10.2:

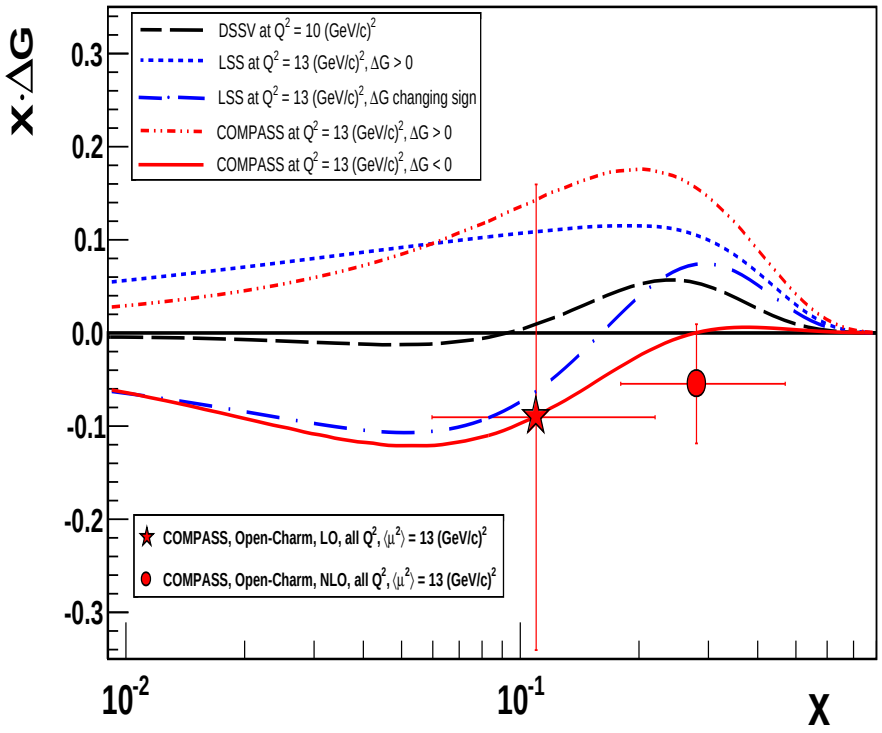

Figure 10.2: Parameterisations of $x\Delta G(x, Q^2)$ together with the LO and the NLO results obtained from the open-charm analysis.

In Fig. 10.2 it is also displayed the COMPASS fits performed at the NLO approximation in QCD, using all the world inclusive DIS data ($Q^2 > 1$ (GeV/c)^2). Thirty values of A_1^d and A_1^p are used to constrain the fits in the range of $0.004 < x < 0.7$. Two solutions with comparable χ^2 probability are found, one with $\Delta G > 0$, the other with $\Delta G < 0$. These two fits are also constrained by the result obtained for $\langle \Delta G/G \rangle^{\rm NLO}$ from the open-charm analysis performed in this work. The impact of the open-charm point in the COMPASS fits can be verified in the following table:

	$\Delta G > 0$	$\Delta G < 0$
No open-charm point	$\Delta G_1 = 0.39 \pm 0.07$ $\chi^2/NDF = 250/235$	$\Delta G_1 = -0.32 \pm 0.11$ $\chi^2/NDF = 261/235$
Open-charm point included	$\Delta G_1 = 0.27 \pm 0.09$ $\chi^2/NDF = 260/236$	$\Delta G_1 = -0.34 \pm 0.12$ $\chi^2/NDF = 262/236$

Table 10.1: Summary of the first moments of ΔG: $\Delta G_1 = \int_0^1 \Delta G(x)\, dx$.

One can see from Tab. 10.1 that the negative solution is practically not affected by the open-charm result. On the other hand, the first moment of the positive solution is reduced by 30%.

The experimental points for $x\Delta G$ reveal a good compatibility with the negative COMPASS fit (cf. Fig. 10.2) [1]. In fact, if we consider only the golden channel for this analysis, $D^*_{K\pi}$, the result that we obtain is $x\langle\Delta G\rangle^{\rm NLO} = +0.01 \pm 0.09$ at $x = 0.28$, which is precisely the place where the fit crosses zero. The addition of the remaining channels change this result, but nevertheless it is still compatible with zero. It is worthwhile to recall that the NLO-point from open-charm has no impact on the COMPASS fit with $\Delta G < 0$. The use of this fit implies a contribution of gluons to the nucleon spin of $\Delta G_1 = -0.34$. This number is clearly too small to solve the spin puzzle evidenced by eq. 1.5 (note that $\Delta\Sigma \approx 0.3$). Therefore, from the available results, we may conclude that the missing spin is in the orbital angular momentum of quarks and gluons (at least partially). This conclusion is not strict due to the large errors associated to the experimental points. Nevertheless, the COMPASS solution for $\Delta G > 0$ is strongly unfavoured: the point for $x\langle\Delta G\rangle^{\rm NLO}$ is 2.7σ below the curve, even after the constraint imposed on the fit by the open-charm result. The first moment, corresponding to the positive fit of ΔG, has the needed value for the solution of the spin puzzle (cf. Tab. 10.1 and eq. 1.5). Unfortunately this fit is not confirmed by the direct measurements of $\Delta G/G$ obtained from the open-charm analysis.

The remaining fits shown in Fig. 10.2 (non COMPASS fits) were not yet constrained by the open-charm asymmetries (cf. section 8.2). They are 1.5σ, 2σ and 2.5σ above the point obtained for $x\langle\Delta G\rangle^{\rm NLO}$. Their integrals reveal a first moment of ΔG whose absolute value is considerably closer to zero. If we take also into account the experimental points from the high-p_T analyses (cf. Fig. 8.5), we are tempted to support the conclusion made above: the gluon contribution to the nucleon spin is small and compatible with zero.

Another conclusion we can draw is that the contribution of quarks to the nucleon spin is indeed 30%. A possible reconciliation with the theoretical preditictions of $\Delta\Sigma \approx 0.60$ is completely excluded. In the AB scheme, $\Delta\Sigma$ is related to ΔG_1 according to the following equation:

$$\Delta\Sigma^{\rm AB} = a_0(Q^2) + \frac{n_f\alpha_S(Q^2)}{2\pi}\Delta G_1(Q^2) \tag{10.5}$$

In order to reconcile a $\Delta\Sigma^{AB} \approx 0.60$ with the measurement of $a_0 \approx 0.30$, we would need to have a $\Delta G_1 \approx 2.5-3$. The latter scenario is completely ruled out by the experimental measurements of $\Delta G/G$. Therefore, since ΔG_1 is small we have $\Delta\Sigma \approx a_0$ for all factorisation schemes.

The future program of COMPASS [90] includes the determination of the so-called **G**eneralised **P**arton **D**istributions (GPDs). Each of these functions contain the corresponding PDF, together with the additional information on the transverse localisation of a parton as a function of the fraction it carries of the nucleon's longitudinal momentum. Obtaining such a 3-dimensional nucleon picture is sometimes referred to as "nucleon tomography". It is quite obvious that the GPDs will be a major breakthrough for the understanding of the nucleon structure. Moreover, it was already shown [90] that the total angular momentum of a given parton species, J_q for quarks ($q = u,\ d,\ s$) or J_g for gluons, is related to the second moment of the sum of two GPDs (H and E). Therefore, the experimental measurement of the quark GPDs will allow us to constrain the quark component J_q of the nucleon spin. Such data may provide the answer to the question whether the missing spin in the nucleon is due to the orbital angular momentum of partons (L_q or L_g) or not.

[1] The comparison of the LO-point from open-charm with the NLO fits may be misleading. However, we can see from Fig. 10.1 that the different parameterisations of xG are very similar, either if we consider the LO or the NLO approximation in QCD. Therefore, we assume that the same is valid for $x\Delta G$.

Bibliography

[1] EMC, J. Ashman et al., Nucl. Phys. B 328 (1989) 1; Phys. Lett. B 206 (1988) 364

[2] S. Bass, *The Spin Structure of the Proton*, Word Scientific Publishing (2007).

[3] SMC, B. Adeva et al., *Next-to-leading order QCD analysis of the spin structure function* g_1, Phys. Rev. D 58 (1998) 112001.

[4] J. Ellis and R. Jaffe, , Phys. Rev. 9 d (1974) 1444; *ibid.* 10 (1974) 1669.

[5] COMPASS, V. Yu Alexakhin et al., *Spin asymmetry* A_1^d *and the spin-dependent structure function* g_1^d *of the deuteron at low values of* x *and* Q^2, Phys. Lett. B 647 (2007) 8.

[6] E155, P. L . Anthony et al, *Measurement of the Deuteron Spin Structure Function* $g_1^d(x)$ *for 1* $(GeV/c)^2 < Q^2 < 40$ $(GeV/c)^2$, Phys. Lett. B463 (1999) 339.

[7] HERMES, A. Airapetian et al., *Precise determination of the spin structure function g1 of the proton, deuteron, and neutron*, Phys. Rev. D 75 (2007) 012007; erratum ibid. D 76 (2007) 039901.

[8] CLAS, K. V. Dharmawardane et al, *Measurement of the* x *and* Q^2 *Dependence of the Spin Asymmetry A1 on the Nucleon*, Phys. Lett. B641 (2006) 11.

[9] PHENIX, A. Adere et al., *Gluon-Spin Contribution to the Proton Spin from the Double-Helicity Asymmetry in Inclusive* π^0 *Produciton in Polarized p+p Collisions at* $\sqrt(s) = 200$ GeV, Phys. Rev. Lett. 103 (2009) 012003.

[10] STAR, B. I. Abelev et al., *Longitudinal Double-Spin Asymmetry for Inclusive Jet Production in p+p Collisions at* $\sqrt{s} = 200$ GeV, Phys. Rev. Lett. 100 (2008) 232003.

[11] HERMES, A. Airapetian et al., *Leading-Order Determination of the Gluon Polarization from high-p(T) Hadron Electroproduction.*, JHEP 1008:130 (2010); arXiv:1002.3921 [hep-ex].

[12] SMC, B. Adeva et al., *Spin asymmetries for events with high pT hadrons in DIS and an evaluation of the gluon polarization*, Phys. Rev. D 70 (2004) 012002.

[13] COMPASS, E. S. Ageev et al. et al, *Gluon polarization in the nucleon from quasi-real photoproduction of high-pT hadron pairs*, Phys. Lett. B633 (2006) 25.

[14] COMPASS, M. G. Alekseev et al. et al, *Gluon Polarisation in the Nucleon and Longitudinal Double Spin Asymmetries from Open Charm Muoproduction*, Phys. Lett. B676 (2009) 31-38.

[15] E. Leader, *Spin in Particle Physics*, Cambridge University Press, 2004.

[16] K. Nakamura et al, *Review of Particle Physics*, Journal of Physics G 37 075021 (2010).

[17] A. V. Manohar, *An Introduction to Spin Dependent Deep Inelastic Scattering*, Lectures given at Lake Louise Winter Inst., Lake Louise, Canada, 1992, hep-ph/9204208v1.

[18] M. Anselmino, A. Efremov and E. Leader, *The Theory and Phenomenology of Polarised Deep Inelastic Scattering*, Phys. Rep. 261 (1995) 1-124.

[19] R. L . Jaffe, *g_2: The Nucleon's Other Spin Dependent Structure Function*, Comments Nucl. Part. Phys. 19 (1990) 239.

[20] G. K. Mallot, *The Spin Structure of the Nucleon from the SMC Experiments*, Habilitation Thesis, Fachbereich Physik der Johannes Gutenberg-Universitat Mainz Mainz, 1996. http://wwwcompass.cern.ch/compass/publications/theses/2007_hab_mallot.ps.gz.

[21] A. Airapetian et al, *First Measurement of the Tensor Structure Function b_1 of the Deuteron*, Preprint, hp-ex/0506018 (2005).

[22] M. von Hodenberg, *First Measurement of the GLuon Polarisation in the Nucleon using D Mesons at COMPASS*, PhD thesis, Albert-Ludwigns-Universitat Freiburg, 2005. http://wwwcompass.cern.ch/compass/publications/theses/2005_phd_von_hodenberg.ps.gz.

[23] H1, C. Adloff et al, Eur. Phys. J. C21 (2001) 33.

[24] ZEUS, S. Chekanov et al, Eur. Phys. J. C21 (2001) 443.

[25] BCDMS, A. C. Benvenuti et al, Phys. Lett. B223 (1989) 485.

[26] E665, M. R. Adams et al, Phys. Rev. D54 (1996) 3006.

[27] NMC, M. Arneodo et al, Nucl. Phys. B483 (1997) 3.

[28] SLAC, L. W. Whitlow et al, Phys. Lett. B282 (1992) 475.

[29] E143, K. Abe et al, *Measurements of the Proton and Deuteron Spin Structure Functions g_1 and g_2*, Phys. Rev. D58 (1998) 112003.

[30] CLAS, Y. Prok et al, *Moments of the Spin Structure Functions g_1^p and g_1^d for $0.05 < Q^2 < 3.0$ $(GeV/c)^2$*, Phys. Lett. B672 (2009) 12.

[31] COMPASS, V.Yu. Alexakhin et al, *The Deuteron Spin-dependent Structure Function g_1^d and its First Moment*, Phys. Lett. B647 (2007) 8-17.

[32] COMPASS, M. G. Alekseev et al, *The spin-dependent structure function of the proton g_1^p and a Test of the Bjorken Sum Rule*, Phys. Lett. B690 (2010) 466-472.

[33] F. E. Close, *An Introduction to Quarks and Partons*, Academic Press (1979).

[34] R. D. Carlitz, J. C. Collins, A. H. Mueller, *The Role of the Axial Anomaly in Measuring Spin Dependent Parton Distributions*, Phys. Lett. B214 (1988) 229.

[35] G. Altarelli, G. G. Ross, *The Anomalous Gluon Contribution to Polarized Leptoproduction*, Phys. Lett. B212 (1988) 391.

[36] F. Halzen, A. Martin, *Quarks & Leptons: An Introductory Course in Modern Particle Physics*, Wiley, (1984).

[37] J. Kodaira, S. Matsuda, K. Sasaki, and T. Uematsu, Nucl. Phys. B159 (1979) 99.

[38] R. Mertig, W. L. van Neerven, Z. Phys. C70 (1996) 637.

[39] W. Vogelsang, Phys. Rev. D54 (1996) 2023.

[40] S. Adler and W. Bardeen, *Absence of Higher Order Corrections in the Anomalous Axial Vector Divergence Equation*, Phys. Rev. 182 (1969) 1517.

[41] S. Heidicke, *Determination of the Gluon Polarisation in the Nucleon using Hadron Pairs with high Transverse Momentum at COMPASS*, PhD thesis, Albert-Ludwigns-Universitat Freiburg, 2005. http://wwwcompass.cern.ch/compass/publications/theses/2005_phd_heidicke.pdf.

[42] K. Klimaszewski, *Determination of the Gluon Polarisation in the Nucleon using Hadron Pairs with high Transverse Momentum at COMPASS*, PhD thesis, Albert-Ludwigns-Universitat Freiburg, 2005. http://wwwcompass.cern.ch/compass/publications/theses/2010_phd_Klimaszewski.pdf.

[43] L. Silva, *Measurement of The Gluon Polarisation through High p_T Hadron Production in COMPASS*, PhD thesis, Instituto Superior Técnico, 2011. http://wwwcompass.cern.ch/compass/publications/theses/2011_phd_silva.pdf.

[44] EMC, J.J. Aubert et. al*The Intrinsic Gluon Component of the Nucleon*, Nucl. Phys. B213 (1983) 31.

[45] B. W. Harris, J. Smith and R. Vogt, *Reanalysis of the EMC charm production data with extrinsic and intrinsic charm at NLO*, Hep-ph/9508403.

[46] Johan Alwall, *Quark Asymmetries and Intrinsic Charm in Nucleons*, Hep-ph/0508126.

[47] S. J. Brodsky, P. Hoyer, C. Peterson and N. Sakai, *The intrinsic charm of the proton*, Phys. Lett. B93 (1980) 451.

[48] A. Bravar, K. Kurek, R. Windmolders, *POLDIS: A Monte Carlo for POLarized (semi-inclusive) Deep Inelastic Scattering*, (1997) Hep-ph/9704313v1.

[49] J. Pretz, *The Gluon Polarization in the Nucleon from the COMPASS Experiment*, Habilitation Thesis, Mathematisch-Naturwissenschaftliche Fakultat der Universitat Bonn, 2007. http://wwwcompass.cern.ch/compass/publications/theses/2007_hab_pretz.pdf.

[50] M. Klein, *Structure Functions in Deep Inelastic Lepton-Nucleon Scattering*, Preprint, hep-ex/0001059 (2000).

[51] R. Windmolders, *QCD fits of $g_1(x, Q^2)$ updated with the open charm result on $\Delta G/G$*, private communication, June 2011.

[52] I. Bojak, *NLO QCD Corrections to the Polarized Photo- and Hadroproduction of Heavy Qaurks*, PhD thesis, Abteilung Physik der Universitat Dortmund, 2001.

[53] W. Beenakker, H. Kuijf, W.L .Neerven, J. Smith, Phys. Rev. D 40 (1989) 54.

[54] J. Smith, W.L. Neerven, Nucl. Phys. B 374 (1992) 36.

[55] I. Bojak and M. Stratmann, Phys. Lett.B 433 (1998) 411.

[56] I. Bojak and M. Stratmann, Nucl. Phys.B 540 (1999) 345.

[57] M. Stratmann, private communications.

[58] By STAR Collaboration (Pibero Djawotho for the collaboration), *Gluon polarization and jet production at STAR*, Published in J.Phys.Conf.Ser.295:012061, 2011. 4pp.

[59] By PHENIX Collaboration (Paul Kline for the collaboration), *Accessing Gluon Polarization in the Proton with Direct Photons at PHENIX*, Published in J.Phys.Conf.Ser.295:012073, 2011. 4pp.

[60] COMPASS, P. Abbon et al., *The COMPASS Experiment at CERN*, NIMA 577 (2007) 455-518

[61] J-M Le Goff, *Evaluation of D^0 and D^* channels for the measurement of $\Delta G/G$*, COMPASS Internal Note 2002-2.

[62] B. Adeva et al, *Measurement of the Polarization of a High-Energy Muon Beam*, Nucl. Instr. and Meth. A343 (1994) 636.

[63] D. Adams et al, *Measurement of the SMC Muon Beam Polarization using the Asymmetry in the Elastic Scattering of Polarized Electrons*, Nucl. Instr. and Meth. A443 (2000) 1.

[64] A. Abragam and M. Goldman, *Nuclear Magnetism: Order and Disorder*, Clarendon Press, Oxford, 1982.

[65] K. Gustafsson, *Computation of the Dilution Factor for the Year 2002 COMPASS Data*, COMPASS Internal Note 2003-3.

[66] K. Kurek et al, *An algorithm for track reconstruction in the large-angle spectrometer of the COMPASS experiment*, NIMA 485 (2002) 720.

[67] Y. Bedfer, S. Gerassimov, A. Korzenev and R. Windmolders, *COMPASS's track reconstruction algorithm*, COMPASS Internal Note 2004-1.

[68] M. Gardner (October 1970), Scientific American, ISBN 0894540017.

[69] M. S. Grewal, *Kalman Filtering: Theory & Practice*, Englewood Cliffs, NJ: Prentice-Hall, 1993.

[70] K. Fujii, *Extended Kalman Filter*, http://www-jlc.kek.jp/subg/offl/kaltest/doc/ReferenceManual.pdf.

[71] S. Gorbunov and I. Kisel, *An Analytic Formula for Track Extrapolation in an Non-Homogeneous Magnetic Field*, NIMA 559 (2006) 148-152.

[72] P. Abbon, et al, *Particle identification with COMPASS RICH-1*, Nucl. Instr. and Meth. A 631 (2010) 26.

[73] G. Ingelman et al, *AROMA 2.2 - A Monte Carlo Generator for Heavy Flavour Events in ep Collisions*, Comput. Phys. Commun. 101 (1997) 135; see http://www.isv.uu.se/thep/aroma/ for recent updates.

[74] http://wwwcompass.cern.ch/compass/software/offline/input/stab/index.html

[75] V. Alexakhine, *COMGEANT web page*, http://wwwcompass.cern.ch/compass/software/offline/welcome.html

[76] B. Andersson, *The Lund Model*, Cambridge University Press, 1989.

[77] J.M. Le Goff and J. Pretz, *Statistical errors and correlations for semi-inclusive asymmetries*, COMPASS note 2004-4.

[78] J. Pretz and J.M. Le Goff, *Simultaneous Determination of Signal and Background Asymmetries*, Nucl. Instr. and Meth. A 602 (2009) 594.

[79] See. http://www.ire.pw.edu.pl/∼rsulej/NetMaker/

[80] R. Sulej, K. Zaremba, K. Kurek and E. Rondio, *Application of the neural networks in events classification in the measurement of spin structure of the deuteron*, Measur.Sci.Tech.18: 2486-2490.

[81] F. Robinet, *Measure de la polarisation des gluon dans le nucléon par la muo-production de mésons charmés à COMPASS*, PhD thesis, Université PARIS DIDEROT (Paris 7), 2008. http://wwwcompass.cern.ch/compass/publications/theses/2007_phd_robinet.pdf.

[82] F. Robinet, J-M Le Goff, *Including the Signal Strength in the D^0 Event Weight*, COMPASS Internal Note 2007-8.

[83] COMPASS, M. G. Alekseev et al., *Leading order determination of the gluon polarisation from DIS events with high-p_T hadron pairs*, to be submitted to Phys. Lett. B.

[84] D. de Florian, R. Sassot, M. Stratmann, W. Vogelsang, Phys.Rev. Lett. 101 (2008) 072001; arXiv:0804.0422 [hep-ex].

[85] D. de Florian, R. Sassot, M. Stratmann, W. Vogelsang, Phys.Rev. D80 (2009) 034030; arXiv:0904.3821 [hep-ex].

[86] E. Leader, A. V. Sidorov, D. B. Stamenov, Phys.Rev. D82 (2010) 114018; arXiv:1010.0574 [hep-ex].

[87] COMPASS, M. G. Alekseev et al., *Leading and Next-to-Leading Order Gluon Polarisation in the Nucleon and Longitudinal Double Spin Asymmetries from Open Charm Muoproduction*, to be submitted to Phys. Rev. D.

[88] J-M Le Goff, *Asymmetry extraction*, COMPASS Internal Note 2004-3.

[89] J-M Le Goff, J. Pretz, F. Robinet *Systematic Error due to False Asymmetries in the Open Charm Measurement*, COMPASS Internal Note 2008-4.

[90] http://wwwcompass.cern.ch/compass/proposal/compass-II_proposal/compass-II_proposal.pdf